



HAL
open science

Modélisation numérique d'impacts de vagues sur un mur: prise en compte de la présence d'air dans l'eau

Louis-Romain Plumerault

► **To cite this version:**

Louis-Romain Plumerault. Modélisation numérique d'impacts de vagues sur un mur: prise en compte de la présence d'air dans l'eau. Sciences de la Terre. Laboratoire de Sciences Appliquées au Génie Civil et Côtier, 2009. Français. NNT: . tel-00410870v2

HAL Id: tel-00410870

<https://theses.hal.science/tel-00410870v2>

Submitted on 8 Sep 2009 (v2), last revised 4 Jun 2010 (v4)

HAL is a multi-disciplinary open access archive for the deposit and dissemination of scientific research documents, whether they are published or not. The documents may come from teaching and research institutions in France or abroad, or from public or private research centers.

L'archive ouverte pluridisciplinaire **HAL**, est destinée au dépôt et à la diffusion de documents scientifiques de niveau recherche, publiés ou non, émanant des établissements d'enseignement et de recherche français ou étrangers, des laboratoires publics ou privés.

--	--	--	--	--	--	--	--	--	--

THÈSE

PRÉSENTÉE À

L'UNIVERSITE DE PAU ET DES PAYS DE L'ADOUR

ECOLE DOCTORALE DES SCIENCES EXACTES ET DE LEURS
APPLICATIONS

PAR

Louis-Romain PLUMERAULT

POUR OBTENIR LE GRADE DE

DOCTEUR

Spécialité:
Génie Civil

Modélisation numérique d'impacts de vagues sur un mur: prise en compte de la présence d'air dans l'eau.

Soutenu le 4 juin 2009

Après avis de

Hocine OUMERACI	Rapporteur
Philippe FRAUNIE	Rapporteur

Devant la Commission d'examen formée de :

Philippe FRAUNIE	Président
Hocine OUMERACI	Examineur
Dominique ASTRUC	Examineur
Mathieu MORY	Examineur
Philippe MARON	Examineur
Philippe VILLEDIEU	Examineur

Numerical modelling of aerated-water wave impacts
on a coastal structure.

L.-R. Plumerault

Abstract

This work presents a numerical model designed for the simulation of water wave impacts on a structure when aeration of the liquid phase is considered. The model is based on a multifluid Navier-Stokes approach in which fluids are compressible. The numerical methods are a finite volume algorithm in space and a second order Runge-Kutta method in time, the interface is tracked through a pressure relaxation method. A validation of this model is performed. It shows a good accuracy for acoustic and shock wave propagation in a bubbly liquid and for wave breaking. Then results from wave impact on a vertical wall are analysed. The influences of the air content and of the wave breaking distance from the wall are investigated. The oscillation of the entrapped air pocket showed to be linked to the oscillations of the pressure at the wall. The presence of strong gradients in front of wall is highlighted.

Résumé

On présente un modèle numérique conçu pour la simulation d'impact de vagues sur une structure avec prise en compte de l'aération de la phase liquide. Ce modèle est fondé sur une approche multifluide résolvant les équations de Navier-Stokes dans le cas compressible. Les méthodes numériques sont un algorithme de volumes finis pour l'espace et une méthode de Runge-Kutta d'ordre 2 pour l'avancement en temps. L'interface est suivie par une méthode de relaxation. On réalise une validation de ce modèle qui donne des résultats satisfaisants pour la propagation d'ondes acoustiques et de choc dans un mélange d'eau et de bulles et pour le déferlement de vague. Ensuite les résultats de l'application aux impacts de vague sur un mur vertical sont analysés. On étudie l'influence de la teneur en air dans l'eau et de la distance au mur du déferlement. Les oscillations de la poche d'air sont corrélées aux oscillations de la pression au mur. La présence de forts gradients devant le mur est mise en évidence.

Remerciements

Je souhaite tout d'abord remercier Philippe Maron qui a obtenu cette bourse de thèse. Philippe, je te suis reconnaissant pour m'avoir fait confiance et pour m'avoir permis de travailler de manière autonome. Je te remercie aussi pour ton intégrité et pour la relation amicale que nous avons entretenue.

Je souhaite à présent remercier Dominique Astruc. Dominique tu as été mon encadrant et m'as aidé à concevoir ce projet de thèse et surtout à le mener à bien. La relation que j'ai entretenue avec toi est une relation de "maître à disciple" en ce sens que tu as essayé de me transmettre ton savoir faire avec amitié et bienveillance. C'est toi, Dominique, qui m'a poussé dans l'autocritique et la rigueur du raisonnement. Avec constance, tu as fait preuve d'un professionnalisme toujours cordial et respectueux. Les rapports que nous avons eu dans le travail ont été des échanges, c'est à dire que tu as fait un vrai travail d'encadrement en ce sens que tu m'as guidé et proposé tes idées sans jamais tenter de les imposer. Chaque décision a fait l'objet d'un véritable échange. Cette attitude respectueuse que tu as eu à mon égard est un des principaux facteurs qui ont alimenté ma motivation et mon enthousiasme tout au long de ce projet. Je te suis donc profondément reconnaissant de m'avoir initié à la recherche dans de si bonnes conditions.

Je souhaite aussi remercier Olivier Thual. Olivier c'est le stage que j'ai effectué sous ta direction qui m'a donné l'envie de mordre un peu plus dans la pomme de la recherche. Ton enthousiasme, ton énergie et ta positivité font que quiconque se place à tes côtés avec une bonne foi se retrouve propulsé par l'élan que tu es capable de donner.

Philippe Villedieu, bien qu'ayant été attaché à ce projet à travers une simple collaboration, a beaucoup contribué à son bon fonctionnement. Philippe je souhaite te remercier pour m'avoir fait confiance en me confiant le produit d'un de tes travaux numériques. Je te remercie aussi pour ta disponibilité lorsque j'avais besoin d'expertise numérique. Enfin ta personnalité agréable est venue ajouter à notre collaboration une teneur particulièrement sympathique.

Je remercie aussi Christian La Borderie pour m'avoir accueilli dans son laboratoire ainsi que Stéphane Abadie pour son soutien.

Enfin je remercie vivement les membres du jury et en particulier les rapporteurs Philippe Fraunié et Hocine Oumeraci qui ont accepté de travailler sur mon manuscrit ainsi que de se déplacer pour ma soutenance.

Dans un contexte plus personnel, je remercie de tout coeur mes parents qui m'ont permis de poursuivre les études de mon choix en me soutenant malgré que quelques une de mes décisions furent parfois difficiles. Je remercie aussi mon ami Tom pour ses précieuses corrections linguistiques. Pour finir je remercie profondément ma compagne qui par son constant soutien a fait preuve d'une grande compréhension et d'une grande patience.

Contents

List of Figures	iv
List of Symbols	viii
1 General introduction	2
2 Bibliographic review of sea-wave impacts on coastal protection structures	4
2.1 Introduction	4
2.2 Impact types	4
2.2.1 Sloping bottom	5
2.2.2 Impact on a vertical wall	6
2.3 Pressure field	15
2.4 The influence of air in water	19
2.4.1 Air pockets	19
2.4.2 Entrained air	21
2.4.3 Air bubble rates	28
2.5 Conclusion	30
3 The original SLOSH model	31
3.1 Introduction	31
3.2 Numerical methods for wave breaking	31
3.3 Navier-Stokes free-surface flow models	32
3.3.1 Incompressible Navier-Stokes one-fluid models	33
3.3.2 Diffuse interface models	34
3.3.3 Compressible multifluid models	35
3.4 Derivation of the continuous multifluid model	37
3.4.1 Single phase Navier-Stokes equations	37
3.4.2 Macroscopic scale: averaged equations	38
3.4.3 Model closure: Relaxation terms	44
3.4.4 Another derivation path from model (BN)	45
3.4.5 Mixture dynamic viscosity	48
3.4.6 External forces	49
3.5 Numerical method	50
3.5.1 Relaxation model (R)	50

3.5.2	Numerical scheme for the hyperbolic part of the model: Fractional-step method	51
3.5.3	Numerical scheme for the diffusion term	54
3.6	Conclusion	57
4	Extended model	58
4.1	Introduction	58
4.2	Principle	59
4.3	Governing equations	60
4.3.1	Conservation equations	60
4.3.2	Pressure equilibria	61
4.3.3	Transformation equations	61
4.3.4	Acoustics of the bubbly water (fluid 2)	63
4.4	Numerical implementation	66
4.4.1	Transport step: numerical flux (Godunov)	66
4.4.2	Relaxation step	67
4.5	Conclusion	68
5	Extended model: Validation	69
5.1	Introduction	69
5.2	Acoustic wave propagation in a bubbly liquid	69
5.2.1	Set-up	69
5.2.2	Sound speed	72
5.2.3	The influence of grid resolution	73
5.2.4	Wave attenuation	74
5.3	Shock tube	75
5.4	Deep water breaking Stokes Wave at the incompressible limit	80
5.5	Conclusion	80
6	Wave impact on a wall	81
6.1	Introduction	81
6.2	Numerical set-up for impact	81
6.3	Wave impact dynamics	84
6.3.1	Free-surface dynamics	84
6.3.2	The vertical jet along the wall	88
6.3.3	The air pocket	90
6.3.4	Flow Mach number	92
6.3.5	Spatio-temporal pressure evolution	93
6.3.6	Evolution of the pressure distribution at the wall: Oscillations	95
6.4	Forces	106
6.4.1	Forces on the wall	106
6.4.2	Estimation of the forces on an object located in front of the wall	111
6.5	Conclusion	115
7	Conclusion and perspectives	117

A	Appendices	120
A.1	Similarities between pressure equilibrium and the transport equation for the volume fraction	121
A.2	Mathematical properties of the model (E)	123
A.3	Mathematical properties of the model (R)	124
A.4	Connection between models (E) and (R): Chapman-Enskog type development	125
A.5	Resolution of the Riemann problem associated with model (R)	127
A.6	An analytical solution for a multiphase shock tube	127

List of Figures

2.1	Classification of breaking wave impact types according to (Schmidt, Oumeraci & Partenscky 1992).	7
2.2	Four categories of breakers found by (Oumeraci & Partenscky 1991) (scheme from (Hull & Muller 2002)).	7
2.3	Classification of breaking wave impact types according to (Kirkgoz 1995).	8
2.4	Free-surface elevation profiles at different times during flip-through impact (Peregrine 2003).	9
2.5	The four breaking cases from Hull & Muller (2002). Superimposed pictures at three different instants.	11
2.6	Experimental flip-through, record rate 4000 Hz (Lugni, Brocchini, Dolcini, Palladino, Bulgarelli & Faltinsen 2005).	11
2.7	Air cavity formation during flip-through impact, just after fast rising jet at the wall. The impinged wall is on the left side. (Lugni et al. 2005).	12
2.8	Lugni, Brocchini & Faltinsen's (2006) case (c): Flip-through.	13
2.9	Example of perfect breaking impact, courtesy G. Müller.	13
2.10	Illustration of the "filling flow"	14
2.11	Time history of impact force on the wall by (Oumeraci & Partenscky 1991) for the different impact types of Oumeraci's classification (figure 2.2).	15
2.12	Typical time evolution of the force on the wall for the different impact types (Oumeraci & Partenscky 1991).	16
2.13	Idealized impact of a wave on a vertical wall	16
2.14	Illustration of pressure gradient due to wave impact and object lying on the sea bed.	18
2.15	Sound speed in mixture according to Wood's (1941) law, for $P_0 = 1 \text{ bar}$.	22
2.16	Sound speed in mixture according to Wood's (1941) law, for $P_0 = 1 \text{ bar}$, plotted versus air mass fraction y .	22
2.17	Sound speed in mixture according to Wood's (1941) law for different reference pressure P . The lines are iso- y plots.	23
2.18	Results of simulations from (Peregrine, Bredmose, Bullock, Obhrai, Muller & Wolters 2005)	25
2.19	Sketches of wave impacts: (a) flip-through, (b) and (c) two different supersonic impacts with small and large contact point accelerations, respectively (Peregrine & Thais 1996).	27
3.1	Free-surface Navier-Stokes models.	35

3.2	Diagram showing the path and stages for the derivation of the model.	39
4.1	Air-water mixture sound speed, comparison between model (R) and physical.	58
4.2	Resulting equation of state of fluid 2 for several fixed values of y	64
5.1	Silberman (1957) case's scheme.	70
5.2	Pressure field example	72
5.3	Sound speed versus frequency and air content.	73
5.4	Wave attenuation versus resolution for a standing linear pressure wave, $\beta = 3.77 \cdot 10^{-4}$	74
5.5	Attenuation versus altitude, $\beta = 3.77 \cdot 10^{-4}$, frequency = 2012 Hz	74
5.6	Attenuation versus frequency, $\beta = 3.77 \cdot 10^{-4}$	75
5.7	Comparison of a numerical simulation of the mixture shock tube with 800 cells to the analytical solution, for $P_L/P_R = 10$ and $\beta_0 = 0.01$	77
5.8	Comparison of the numerical simulation of the mixture shock tube with 800 cells to the analytical solution, for $P_L/P_R = 10$ and different values of β_0	78
5.9	Free-surface dynamics for the breaking of Stokes wave	79
6.1	Numerical set-ups.	82
6.2	Free-surface profiles at impact for $\beta = 0.001$ and $D = 0.08$	84
6.3	Free-surface profiles at impact for $\beta = 0.01$ and $D = 0.08$	85
6.4	Free-surface profiles at impact for $\beta = 0.05$ and $D = 0.08$	85
6.5	Influence of β on the free-surface position before the impact, $t = 0.3292$ and $D = 0.08$	86
6.6	Free-surface profiles at impact for $\beta = 0.05$ and $D = 0.10$	86
6.7	Free-surface profiles at impact for $\beta = 0.05$ and $D = 0.06$	87
6.8	Free-surface profiles at impact for $\beta = 0.05$ and $D = 0.04$	87
6.9	Influence of the air content on the altitude of the vertical jet at the wall, for $D = 0.08$	89
6.10	Influence of D on the altitude of the liquid jet at the wall. Extrapolated data after the end of simulations (vertical line).	89
6.11	Air-pocket lower and upper extremities position at the wall for $\beta = 0.001$ and $D = 0.08$	90
6.12	Fourier transforms of waterline position.	91
6.13	Relative Pressure field sequences for $\beta = 0.05$ and $D = 0.08$	94
6.14	Evolution of the distribution of pressure $P - P_0$ at the wall for all β values and for $D = 0.08$	96
6.15	Free-surface position (dotted line) and altitude of the primary maximum pressure at the wall (solid line) for all β values and $D = 0.08$	96
6.16	Primary pressure P maximum value for all β values and $D = 0.08$	97
6.17	Evolution of the distribution of pressure $P - P_0$ at the wall for all D values.	99
6.18	Free-surface position (dotted line) and altitude of the primary maximum pressure at the wall (solid line) for all D values and $\beta = 0.05$	99

6.19	Primary pressure P maximum value for all D values.	100
6.20	Pressure P history on the wall at the altitude of the first maximum pressure for all β values and for $D = 0.08$	101
6.21	Fourier transform of the pressure history at the location of primary maximum pressure for all β values and for $D = 0.08$	101
6.22	Pressure history on the wall at the altitude of the first maximum pressure for different D values and $\beta = 0.05$	103
6.23	Fourier transform of the pressure history at the location of primary maximum pressure for all D values and $\beta = 0.05$	104
6.24	Figures from Schmidt et al. (1992).	105
6.25	Dominant frequency for all the simulated cases.	106
6.26	Lineic effort on the wall for all β values and for $D = 0.08$	106
6.27	Lineic effort on the wall for all D values and for $\beta = 0.05$	107
6.28	Lineic moment on the wall for all $beta$ values.	107
6.29	Lineic moment on the wall for D values and for $\beta = 0.05$	108
6.30	Fourier transform of the forces on the wall for all β values and $D = 0.08$	110
6.31	Fourier transform of the forces on the wall for all D values and for $\beta = 0.05$	110
6.32	Definition scheme of an immersed block.	111
6.33	Pressure variation threshold to exceed for the lifting of a concrete block.	112
6.34	Critical altitude and time for $\beta = 0.001$ and $D = 0.08$	113
6.35	Critical altitude and time for $\beta = 0.01$ and $D = 0.08$	113
6.36	Critical altitude and time for $\beta = 0.05$ and $D = 0.08$	113
6.37	Critical altitude and time for $D = 0.10$ and $\beta = 0.05$	114
6.38	Critical altitude and time for $D = 0.06$ and $\beta = 0.05$	114
6.39	Critical altitude and time for $D = 0.04$ and $\beta = 0.05$	114

List of Symbols

α	Volume fraction of fluid 1
α_k	Volume fraction of fluid k
β	Volume fraction of fluid a within fluid 2
C	Volume fraction
c_k	Sound speed in fluid k ($m.s^{-1}$)
$C_{i,j,k}$	Volume of grid cell i, j, k
$c_{k,0}$	Sound speed in fluid k at standard pressure ($m.s^{-1}$)
CFL	Courant-Friedrichs-Lewy constant
Δt^n	Time step
$\Delta x_i, \Delta y_i, \Delta z_i$	Cell grid dimensions in the three directions
D	Non-dimensional wave breaking distance from the wall
ϵ	Relaxation time
\underline{F}_c	Capillary forces
F	Flux vector along x
f	Frequency (Hz)
f_0	Air-pocket eigen frequency (Hz)
f_k	Body force volume density for fluid k
f_t, f_l	Transverse and longitudinal mode frequencies (Hz)
$f_{p,j,k}$	flux through the face of abscissa x_p in the x direction
γ	Constant for the Stiffened-Gas equation of state
$\Gamma_k, \underline{M}_k$	Interfacial source terms
G	Flux vector along y

g	Gravity density ($m.s^{-2}$)
$g_{p,j,k}$	flux through the face of abscissa x_p in the y direction
H	Flux vector along z
$h_{p,j,k}$	flux through the face of abscissa x_p in the z direction
\underline{I}	Identity matrix
k	Polytropic constant
ka	Wave steepness
λ	Wavelength (m)
μ	Mixture dynamic viscosity ($Pa.s$)
μ_k	Dynamic viscosity of fluid k ($Pa.s$)
\underline{M}_k^d	Interfacial force density
\underline{M}_m	force due to the surface tension at the interface
m_k	Mass of fluid k (kg)
∇X_k	Dirac vector function peaking at the interface
\underline{n}	Unit vector normal to the interface
n	number of quarter wavelength from the free surface to the node or antinode in question
π	Constant for the Stiffened-Gas equation of state
P'	Pressure without hydrostatic contribution (Pa)
P_0	Standard pressure (Pa)
P_k	Pressure in fluid k (Pa)
P_{hyd}	Hydrostatic pressure (Pa)
$P_{k,i}$	interfacial pressure of the k th phase (Pa)
P_{k0}	Standard pressure in fluid k (Pa)
P_{rms}	Root mean square pressure (Pa)
ρ	Mixture density ($kg.m^3$)
ρ_k	Density of fluid k ($kg.m^3$)

ρ_{i0}	Density of fluid i at standard pressure ($kg.m^3$)
R_0	Air-pocket steady state radius (m)
σ	Surface tension ($N.m^{-1}$)
\underline{S}	Viscous stress tensor
S	Source term
SWL	Still water level
τ_k	Viscous stress tensor of fluid k
\underline{T}_k	Stress tensor for fluid k
T	Wave period (s)
\underline{u}	Average velocity ($m.s^{-1}$)
u, v, w	Velocity in each direction ($m.s^{-1}$)
\underline{V}_i	Velocity of the interface ($m.s^{-1}$)
\underline{V}_k	Velocity of fluid k ($m.s^{-1}$)
$\underline{V}_{k,i}$	interfacial velocity of the kth phase ($m.s^{-1}$)
V_k	Volume of fluid k
V_{tot}	Volume of the total mixture (mixture of fluid 1 and fluid 2) (m^3)
W	Vector of conservative variables
$X_k(\underline{x}, t)$	Presence rate of fluid k
y	Mass fraction of fluid a within fluid 2

Chapter 1

General introduction

In the regions of the world where coasts undergo strong constraints from the sea, the protection of inhabited coastal areas is of major concern. Great deteriorations of artificial structures that preserve these zones from the direct assault of the sea are often observed. The building or preservation of such barriers that protect the coast from wave-induced hazards is at stake, particularly in the current context of global warming, which has empowered natural hazards and over-population, forcing people to live in more exposed areas. Thus coastal structures are of first importance in their role of protecting human heritage. Often presenting a great vulnerability regarding the sea forces, these structures have been studied by engineers for a long time. Strong structural damage like breaks or cracks in masonry works are attributed to the force of the waves. For hybrid rubble mound structures including armour units, these can even disintegrate or be removed several meters away from their initial place under the force of water flows. But wave impacts on structures involve several classes of physical processes as well as a wide range of scales, and the processes that are responsible for such damages are still not fully understood.

However, it has been observed that successive wave breaking events in the vicinity of coastal structures can entrap a considerable quantity of air within the water over a layer of a few meters below the free surface. Indeed, it has been shown that the air volume fraction under breaking waves ranges approximately between 0.1% and a few percent (Hoque & Aoki 2005), and air volume fractions above 20% have been observed by (Lamarre & Melville 1991) to be sustained near the surface up to half a wave period after breaking. The presence of air is known to drastically modify the compressibility of the mixture. The presence of a few percent of air can lead to a decrease in the sound speed of more than an order of magnitude. The increased compressibility is expected to lead to the presence of pressure gradients of large amplitude and long lasting time. These gradients might be the cause for damage to the structure or objects motion in the vicinity of the structure. Thus even a small amount of air might drastically change the dynamics of impact in the vicinity of the structure. Therefore this great change in the compressibility of the liquid medium leads us to a different approach regarding the models used to represent such flows and compressibility should be accounted for in the models for wave impacts on structures.

The aim of the present work is to analyse the fluid flow in the vicinity of a structure impacted by a breaking wave, and evaluate the role played by the presence of air within water and its influence on the dynamics of wave impacts.

As a first approximation, in the literature, the fluid was modeled as being incom-

pressible and most of the numerical analysis have been based on incompressible flow modelling. However the role played by the presence of air has recently been investigated from different points of view (Peregrine 2003). Laboratory experiments have been undertaken but the multi-physics aspect of wave impacts makes them difficult to analyse in a reduced lab model. And a few studies involving numerical simulations have also been undertaken to gain knowledge about the small scale mechanisms.

In order to provide a description of air in the liquid medium, a numerical model suitable for fully compressible two-fluid flows is presented here. The numerical code, SLOSH, which was first developed by (Chanteperdrix 2004), is extended for wave impacts in this work. This code is based on what is called a "multifluid" approach. The method solves the Navier-Stokes equations in both water and air for compressible flows. The numerical method is based on a finite volume algorithm, an exact Riemann solver with a Godunov scheme for which the second order is obtained by the MUSCL method, and a second order Runge-Kutta method. The transport of the volume fractions is achieved through the so called "relaxation method", which consists in the pressure relaxation of both fluids to the equilibrium.

In chapter 2, we present a bibliographic review about wave breaking and wave impacts. The main properties of wave breaking are recalled as a basis for the introduction to wave impacts. Then we review state of the art research regarding wave impacts, discussing the different classification of impact types found in the literature. Finally, the main point of this bibliographic review is to address the issue of the presence of air within water, which is the key element of the present study.

In chapter 3, a short review of free-surface flow models is presented. Then we introduce the mathematical model used in SLOSH in its original version (Chanteperdrix 2004). Finally the numerical methods used to solve the model in SLOSH are described.

In chapter 4, we describe the improvements we made on the SLOSH model. The model was previously unable to properly represent the acoustics of a mixture of air and water so we extended it by including a third phase. This allows us to simulate dispersed phase flows with proper acoustic properties. We then detail the numerical methods used in the new model.

In chapter 5, the new model is tested for a case of acoustic wave propagation in a column filled with bubbly water. Then we estimate the ability of the code to represent shock waves in mixtures. Finally, a breaking Stokes wave is computed in the incompressible limit of the new model to evaluate its ability to simulate complex free-surface topologies.

In chapter 6, we analyse the results of wave impacts simulations. The numerical set-up we chose to generate impacts is an unstable Stokes wave breaking on a vertical wall. We then varied two parameters, the level of aeration of the water and the relative position of the impacting wave to the wall. Firstly, the influence of these two parameters on the dynamics at impact is evaluated. The free-surface behaviour and the pressure distribution at the wall are investigated in detail. Secondly, we evaluate the forces applied to the structure and how they are influenced by the two parameters.

Finally, chapter 7 sums up the main results of this study and prospective investigations are proposed.

Chapter 2

Bibliographic review of sea-wave impacts on coastal protection structures

2.1 Introduction

The current state of investigations about wave actions on breakwaters is reviewed here. The general case of a composite breakwater is of interest here. It is made of an impermeable caisson, which we will refer to as the "wall", and it is protected by layers of armour units. The incident waves propagate over either a permeable or impermeable bed with singular topography, with various angles relative to the normal direction to the wall. The purpose here is to introduce the reader to phenomena that could be powerful enough to be responsible for the movements of armour layer units. There are some questions that this review is prone to answer. In water wave impacts against structures, what could be responsible for great damages like cracks in the wall or movements of armour units? What are the most critical conditions in terms of the geometry of the structure, geometry of the wave, the presence of air in the water, for damages to occur?

As a preliminary, the first section is devoted to wave breaking. The second section sets out a key theoretical description of the pressure field at impact. This description introduces how the pressure field can cause great damage to coastal structures. Finally, the third section talks about the main concern of this study: the presence of air in water at impact in the form of air bubbles (entrained air) and air pockets. This raises the complex issue of multiphase flow dynamics.

2.2 Impact types

Wave breaking is known to cause serious damages to structures (Oumeraci 1994, Melby & Kobayashi 1998, Medina & Hudspeth 2000).

As waves approach the coast, their height and steepness increase as water depth decreases until their wave length reaches a limiting value. The wave then experiences

an instability called "bathymetric breaking" through which energy is dissipated. The region called the "surf zone" is the zone in which the breaking is the dominant hydrodynamic process. It extends from the seaward outermost breaking wave to the "swash zone", which is the part of the beach that is alternatively covered and uncovered by water under the action of waves. Bathymetric breaking occurs when the depth is not sufficient to let the wave propagate. The parameter that controls the breaking is the ratio between the wave height and the water depth.

There is another type of breaking, which occurs in deep water. In this case, the instability process is due to an increase in the steepness of the wave which may be caused by the interaction of multiple waves, the interaction between wind and waves or the interaction between currents and waves.

The third case of wave breaking is the breaking on a structure. This can occur when a wave propagates over a bathymetry variation like a step, or over a complex geometry like for example the armour layer of a breakwater. This type of breaking is similar to bathymetric breaking although it is due to more sudden changes in the bathymetry.

Although this section's main objective is to explore the issue of the classification of wave impact types on a structure, it first seems necessary to say a few words about the different types of breaking waves.

The breaking process has been thoroughly investigated during past years and this is not an exhaustive review. For more details, the reader can for instance refer to (Peregrine 1983, Duval 2007). In the present section, we only introduce the notion of onset of breaking and simple breaking classification.

2.2.1 Sloping bottom

2.2.1.1 Breaking criterion

Several empirical criteria have been proposed to characterize the water depth or the steepness at which the wave breaking process occurs. A common used criterion for the onset of breaking on a sloping beach is the criterion defined by Miche (1944):

$$\frac{H_b}{\lambda} = 0.142 \tanh\left(2\pi \frac{d_b}{\lambda}\right) \quad (2.1)$$

meaning that the breaking instability occurs when the ratio between the incident local wave height H_b at breaking point and wavelength λ reaches a value depending on the water depth at breaking point d_b . Miche's criterion gives a good estimation for beaches of gentle slope. Indeed, Tsai, Chen, Hwung & Huang (2005) carried out experiments and showed that this criterion was accurate for a slope of 1/10 but overestimates the breaking height by 50% and 60% for beaches of slope 1/3 and 1/5.

In the presence of a reflective structure, the onset of breaking is lowered. Indeed, the reflected waves increase the local steepness of the wave, making it break at smaller values of the ratio $\frac{H}{\lambda}$ than for a gentle sloping beach.

Investigations by (Iwata & Kiyono 1985) led to the following semi-empirical relationship:

$$\frac{H_b}{L_b} = \left(0.109 + 0.033 \frac{1 - K_r}{1 + K_r}\right) \tanh\left(2\pi \frac{d_b}{L_b}\right) \quad (2.2)$$

where K_r is the reflection coefficient of the structure. For a non reflective structure, $K_r = 0$ and this relationship is equivalent to Miche's criterion.

Several other breaking criteria are available in the literature (e.g. Weggel 1972, Grilli, Svendsen & Subramanya 1997). For a detailed review of these criteria and breaking mechanisms, please refer to (Duval 2007).

2.2.1.2 Breaking types

The surf similarity parameter initially proposed by (Iribarren 1949):

$$\xi = \frac{\tan \alpha}{\sqrt{\frac{H_0}{\lambda_0}}} \quad (2.3)$$

where α is the slope angle, H_0 is the incident wave height at the toe of the slope and $\lambda_0 = \frac{gT^2}{2\pi}$ is the deep-water wavelength. It constitutes a suitable discriminator for the types of breakers. Battjes (1974) proposed a classification of breaker types on sloping beaches or mild-slope structures based on the the value of the Iribarren number:

<i>Spilling breaker</i>	$\xi < 0.4$	
<i>Plunging breaker</i>	$0.4 < \xi < 2.3$	
<i>Collapsing breaker</i>	$2.3 < \xi < 3.2$	
<i>Surging breaker</i>	$3.2 < \xi$	(2.4)

2.2.2 Impact on a vertical wall

Now let us review the attempts of classification of wave impact types on a vertical wall found in the literature. For a wave impact on a vertical wall after a propagation on a slope, Schmidt et al. (1992) distinguished 7 types of impacts (figure 2.1) established from large-scale flume wave experiments. These types depend on the type of wave breaking (plunging or spilling) and on the relative position of the breaker to the vertical wall. Their classification is based on the parameter $\frac{H_b}{d_w}$ where H_b is the breaker height and d_w is the Still Water Level (SWL).

From experiments Oumeraci & Partenscky (1991) and Oumeraci, Klammer & Partenscky (1993) distinguished four impact types depending on the distance from the vertical wall at which it breaks. They observed that a gradual increase in the incident wave height results in a breaking occurring further offshore and thus in four different types of wave impact (figure 2.2):

- (a) turbulent foamy bore,
- (b) well developed plunging breaker entrapping a large air pocket,
- (c) plunging breaker entrapping a small air pocket,
- (d) non-breaking upward deflected wave, for which the waterline at the wall rises very rapidly, reaching the anticipated wave-crest impact point just before this former overturns and hits the wall. This latter type is similar to the "flip-through" impact (Cf. figure 2.4), which is reviewed further.

The difference between type (c) and type (d) is that in type (c) the overturning


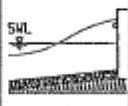
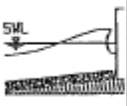
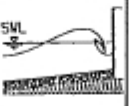
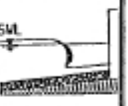

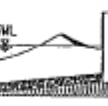
Plunging breaker					Spilling breaker	
upward deflected	well developed		broken		well de-veloped	broken
$\frac{H_b}{d_w} = 0,92$	$\frac{H_b}{d_w} = 0,99$	$\frac{H_b}{d_w} = 1,06$	$\frac{H_b}{d_w} = 1,14$		$\frac{H_b}{d_w} = 0,99$	$\frac{H_b}{d_w} = 1,14$
						
Type 1	Type 2	Type 3	Type 4	Type 5	Type 6	Type 7

Figure 2.1: Classification of breaking wave impact types according to (Schmidt et al. 1992).

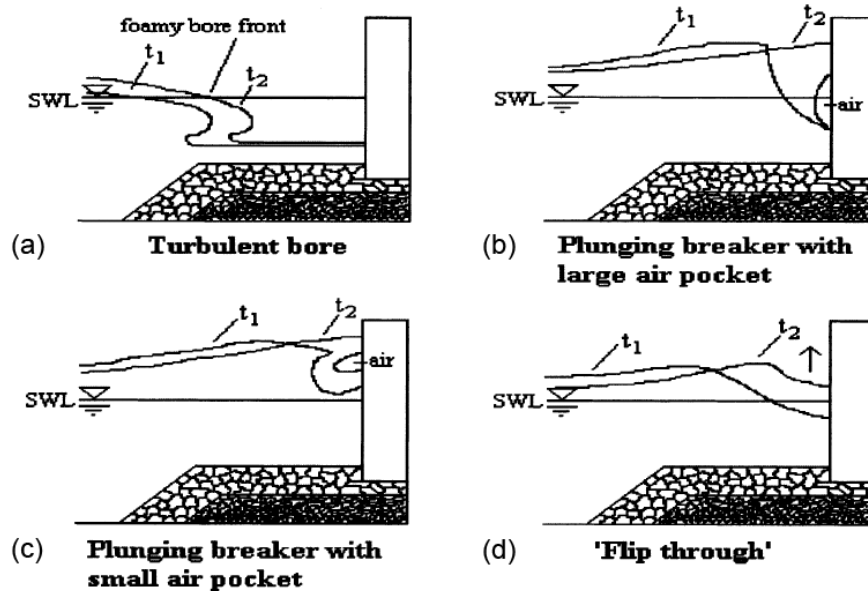


Figure 2.2: Four categories of breakers found by (Oumeraci & Partensky 1991) (scheme from (Hull & Muller 2002)).

wave crest hits the wall and in type (d) it does not. The highest pressures at the wall during the impact are observed for type (c) and its value is decreasing for type (b). It decreases even more for type (d) and its minimum is observed for type (a).

Kirkgoz (1995) also proposed a classification of breaking wave impacts on a vertical wall, where three types are distinguished (figure 2.3):

- "early breaking": the breaking wave front was vertical when it reached the wall. Thus the wall is impacted by the plunging wave crest, which entraps an air pocket. They distinguish the case when air stays entrapped (figure 2.3(a)) and the case when air escapes (figure 2.3(b)).

- "perfect breaking" (Nagai 1960): the wave reaches the vertical wall when the front of the wave is vertical at the instant of impact (figure 2.3(d)).

- "late" breaking: the wave front is not vertical yet when it reaches the wall (figure 2.3(c)).

As they also investigated the effect of the wall inclination angle, they underlined that

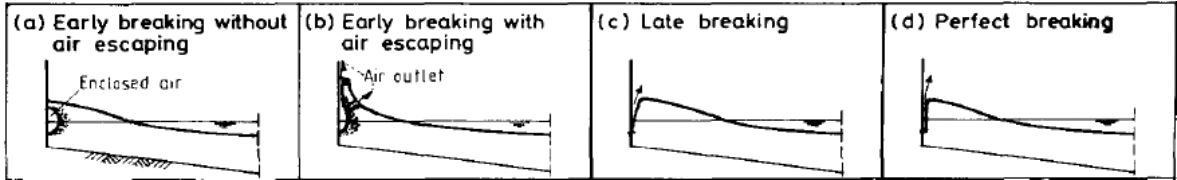


Figure 2.3: Classification of breaking wave impact types according to (Kirkgoz 1995).

perfect breaking can also occur on inclined walls when the wave front is parallel to the wall at the impact. They observed that in the presence of a vertical or inclined wall the breaking point is slightly shifted shoreward compared to the case of a sloping beach without a wall. They proposed an empirical relationship between the breaking depth on a sloping beach d_b and the breaking depth in the presence of a wall d_{bw} , based on the experiments of (Kirkgoz 1991): $\frac{d_{bw}}{d_b} = 1 - 0.3 \tanh\left(\frac{20H_0}{L_0}\right)$ where H_0 and L_0 are the deep water wave height and length.

Whillock (1987) and Kirkgoz (1991) found that measured maximum impact pressures are greater for certain wall inclination angles than for a vertical wall. The maximum impact pressure was observed not only to be a function of the relative position between the breaker and the wall at the instant of the impact but also to depend on the local plunger/wall geometry.

The experiments led by (Kirkgoz & Akoz 2005) focused on the perfect breaking on a structure composed of an armour layer and a caisson. They explored $\frac{1}{2}$, $\frac{1}{4}$ and $\frac{1}{6}$ slopes for the armour layer, and, several distances between the summit of the armour layer and the caisson's vertical front wall (berm width). They adjusted water depth in the channel thanks to a video camera checking the occurrence of a "breaker becoming almost vertical at the instant of impact". In order to generate waves likely to generate perfect breaking they estimated the wave conditions in open sea thanks to a linear theory. The Iribarren number based on the wave height at breaking point in the presence of the wall was in the range characteristic of a plunging breaker on a slope. They observed that the wave height at the breaking point, the wave crest altitude, and the breaking depth in front of the wall, all increase with relative berm width whereas the

armour layer slope and the corresponding deep water wave height do not seem to have an effect. But due to the lack of data the tendency was not very pronounced. Despite the experiments of (Kirkgoz & Akoz 2005), the existence of the "perfect breaking" type is controversial.

One can find in the literature a definition of another impact type that seems to be very similar to perfect breaking but this is defined in different terms. Cooker & Peregrine (1992) introduced the "flip-through" impact. It is also a case for which the wave front is vertical at the impact and the wave does not overturn, but they underline that in this case, the point of contact between the waterline and the wall accelerates upward, flips through the crest level and forms a jet like flow going upward along the wall. An example of "flip-through" impact is shown in figure 2.4. Cooker & Peregrine (1992)

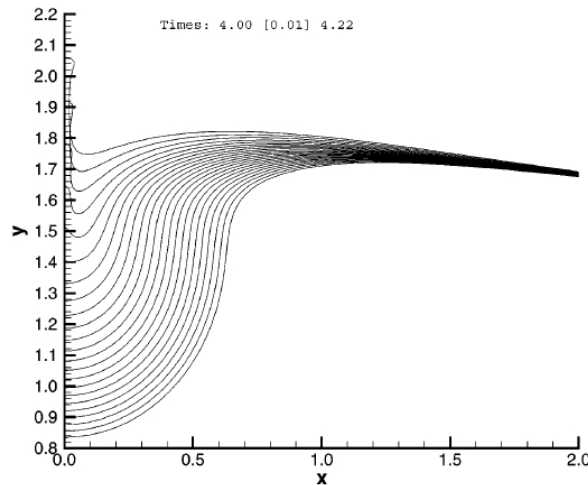


Figure 2.4: Free-surface elevation profiles at different times during flip-through impact (Peregrine 2003).

modelled this flow with a two-dimensional unsteady potential flow model. (Peregrine 2006) suggested that flip-through and perfect breaking seem to be the same thing. The idea of flip-through is related to the rising of the waterline whereas Kirkgoz (1995) did not mention this feature for perfect breaking. Moreover in flip-through the air entrapped between the wave face and the wall must necessarily be expelled in the upward direction, and not through the water as in the "early breaking" type of Kirkgoz (1995) illustrated in figure 2.3(b). Very few observations of flip-through exist. A record of a flow that seems similar to the flip-through situation can be found in the Chan & Melville's (1988) experiment. The impact case (d) from the observations of Oumeraci et al. (1993) mentioned above seems to be similar to flip-through too, even though the frame rate of the video observation was not high enough to identify the rise of the waterline along the wall. However, Peregrine (2003) added that the incident waves involved were very different. Indeed Cooker & Peregrine (1990*b*) in their computations used a large shallow-water wave that steepened due to the higher portion of the wave overtaking the front of the wave. Whereas Chan & Melville (1988) used the frequency dispersion of deep-water waves to focus wave energy into a breaking wave event. In

addition, the 'wall' described in (Chan & Melville 1988) was a vertical plate that did not penetrate to the bottom of the wave tank. This shows that flip-through is independent of global geometry and dynamics and is a local phenomenon. The occurrence of flip-through in reality does not seem to be fully acknowledged in the community as it is a local phenomenon and in most of the physical cases the free surface is too disturbed for it to be observed. Although Chan & Melville (1988) recorded images at 1100 frames per second, they mentioned that a video experiment at a high frame rate was needed to observe a flip-through impact in detail.

Hull & Muller (2002) also performed experimental investigations on the shape of waves breaking on a vertical wall. After a propagation over a 1:10 slope before reaching the wall. Tests were run for different offshore wave heights H_0 ranging between 0.5 and 0.81 times the water depth at the wall. They confirmed the classification of Oumeraci et al. (1993) (figure 2.2) which was already established for a horizontal bottom and in the presence of a berm, and identified four different impact types on the wall (from small to large values of H_0):

Type (i) non-breaking wave sloshing up the wall. Hull & Muller (2002) could not identify a distinct upward moving jet close to the wall in the impact zone and during the impact but only after the impact of the crest on the wall. So this type cannot be confirmed to be a flip-through. This may be due to the fact that the image-acquisition frequency was 20 Hz making them unable to see the incipient motion of the waterline along the wall (figure 2.5(a)). This type corresponds to type (d) in figure 2.2.

Type (ii) plunging breaker with small air pocket (figure 2.5(b)). This type corresponds to type (c) in figure 2.2.

Type (iii) well developed plunging breaker with large air pocket (figure 2.5(c)). This type corresponds to type (b) in figure 2.2.

Type (iv) already broken wave (having broken very close to the wall) as turbulent foamy bore (figure 2.5(d)). This type corresponds to type (a) in figure 2.2.

Let us mention that the existence of "flip-through" and "perfect breaking" are not confirmed in this paper.

In effect, although the definition of perfect breaking seems quite clear in theory (Nagai 1960): the impacting wave face is perfectly parallel to the wall at the instant of impact; this case may be purely theoretical, as the wave face is never 'perfectly' flat. Unclear references to perfect breaking may be found in the literature. For instance Kirkgoz & Akoz (2005) mentioned the presence of an air pocket in a case of perfect breaking.

Lugni et al. (2005) and Lugni et al. (2006) did perform video records at high frequency (4000 Hz) to monitor experimental flip-through in a 0.1 m wide channel (figure 2.6). They found that in a flip-through impact after the jet quickly rises up the wall a small air cavity can form (see figure 2.7). This small air cavity forms a different topology compared to cases (b) and (c) of Oumeraci et al. (1993) because here the air cavity is not in direct contact with the wall. They found that the velocity of the pressure peak along the wall is almost constant and approximately equal to the speed of the wave trough (point of the free surface with the lowest altitude). The speed of the

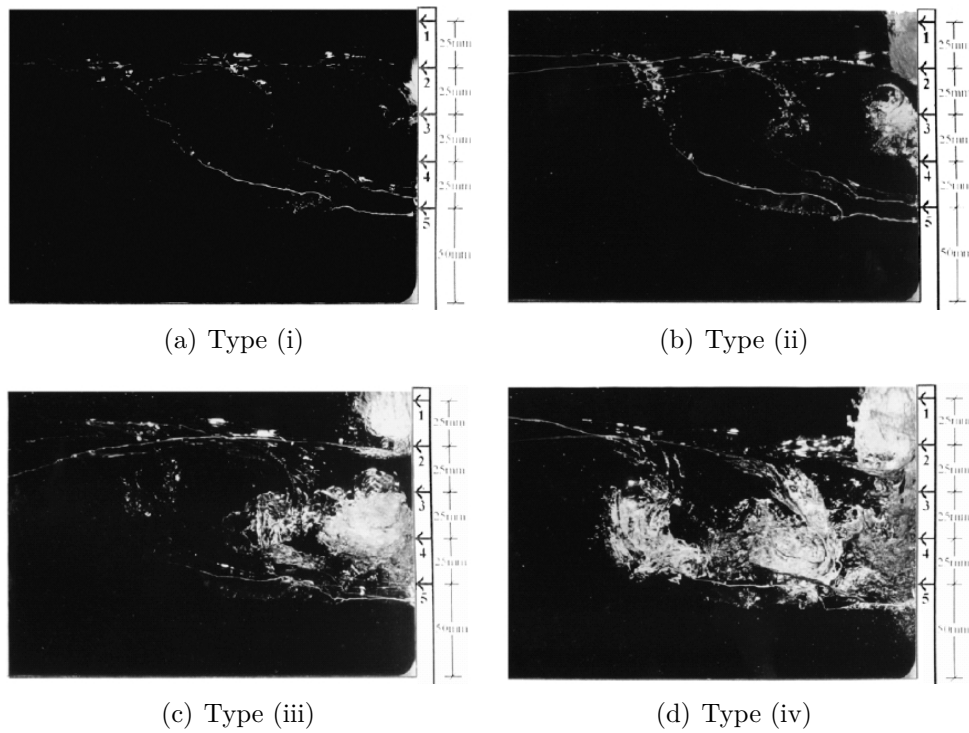


Figure 2.5: The four breaking cases from Hull & Muller (2002). Superimposed pictures at three different instants.

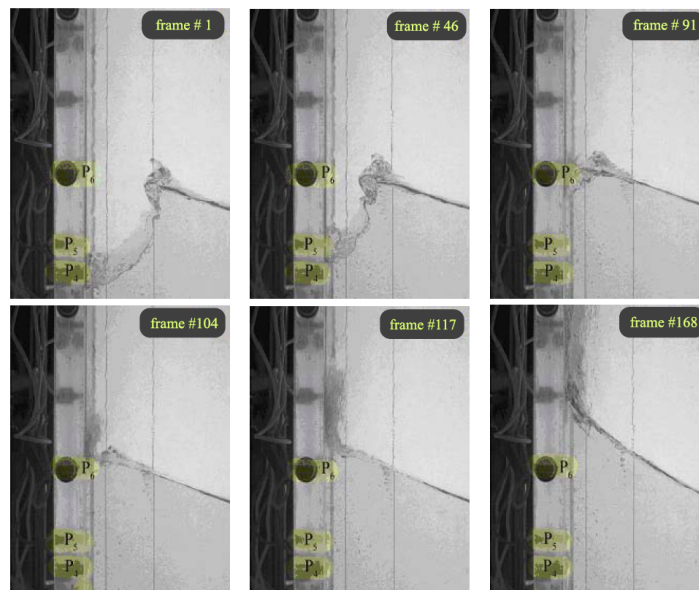


Figure 2.6: Experimental flip-through, record rate 4000 Hz (Lugni et al. 2005).

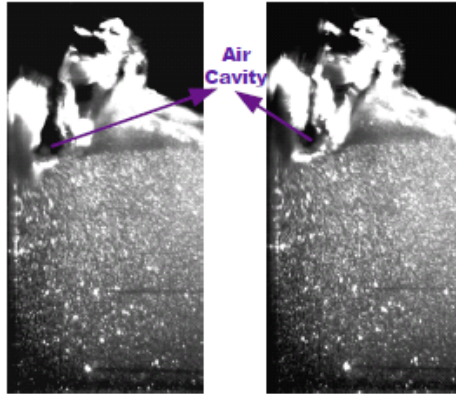
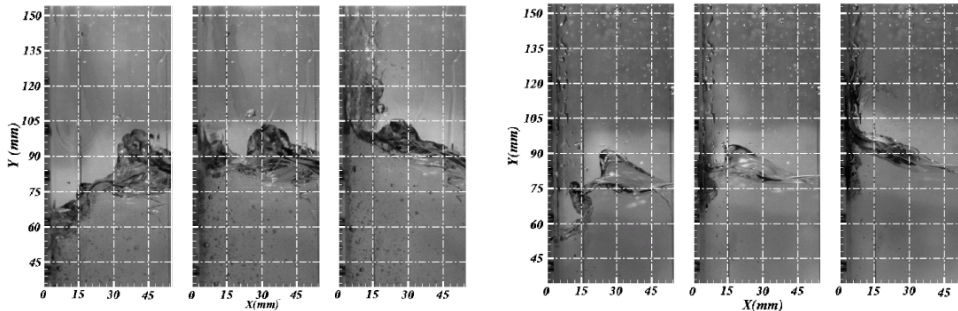


Figure 2.7: Air cavity formation during flip-through impact, just after fast rising jet at the wall. The impinged wall is on the left side. (Lugni et al. 2005).

flip-through jet at the wall was ten times larger than the velocity of the approaching wave. And the acceleration of the flip-through jet was measured up to $1500g$. They proposed a classification of flip-through events into three different modes:

- Mode (a) flip-through with no air entrapment (figure 2.8(a)),
- Mode (b) flip-through with entrapment of a single small air cavity (no phase mixing) (figure 2.8(b)),
- Mode (c) flip-through with entrapment of a large amount of minute bubbles (air/water mixing) (figure 2.8).

However they mentioned that the third case is obtained with an approaching wave



(a) Flip-through mode (a) according to (b) Flip-through mode (b) according to Lugni et al. (2006).

that already has a turbulent front. Let us clarify here that case (c) is a case of flip-through with air entrainment and not with an air pocket entrapment. This case is for a flip-through that occurs when the wave already contained entrained air before the impact. They also highlighted that the most important kinematic flow variable to analyse is the duration of the meeting between the approaching wave crest and the near-wall jet, which they called the "impact duration".

Figure 2.9 is courtesy of G. Müller. Given the slope of the wave front before the impact in figure 2.9, it is likely that we are in the presence of a severe impact. However, G. Muller reported that this wave did not generate strong impact pressures nor an

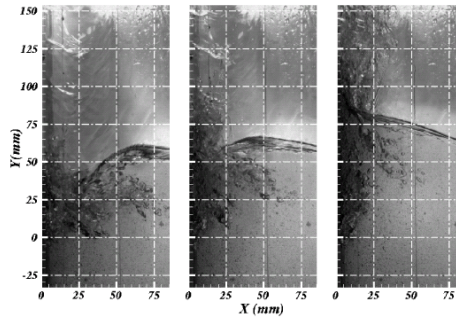


Figure 2.8: Lugni et al.'s (2006) case (c): Flip-through.

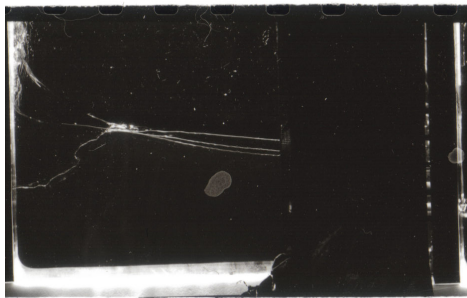


Figure 2.9: Example of perfect breaking impact, courtesy G. Müller.

audible slapping noise. Perhaps the controversy around 'flip-through' is also a matter of terminology and Peregrine and his co-workers would call this an impact, although it did not create a very high pressure. It is likely that H.D. Peregrine considered flip-through as an impact whereas G. Müller did not. For the latter, what is described as an upward jet in the flip-through is likely only to be a "contact of an oblique-faced horizontally moving body of fluid with a vertical wall" (personal communication). The different feature being that in the case of the flip-through the rising jet front at the wall is at a larger altitude than the trough, which is not the case for a simple oblique moving liquid body impact. To discriminate this issue, it would have been necessary to see the intermediate images, around the moment of the impact itself. This would have allowed to see the dynamics of the waterline point. Another point is that in Müller's experiment the water depth is only 10cm. So a flow in such a small tank can add scaling issues to the interpretation of impact dynamics (further details on scaling issues in wave impacts will be reviewed in section 2.4). The pictures in (Oumeraci et al. 1993) shows the exact same flow during impact as this one. They called it an "upward deflected wave" impact.

The work of Lugni et al. (2006) clarifies certain points about the flip-through. However, it is still difficult to distinguish perfect breaking of Nagai (1960) and flip-through of Cooker & Peregrine (1992). The existence of perfect breaking of Nagai (1960) is not totally acknowledged, as Hull & Muller (2002) were not able to observe it. The definition of "wave face" is not made clear by Kirkgoz (1995), nor by Kirkgoz & Akoz (2005) who do not state how they characterize perfect breaking other than mentioning

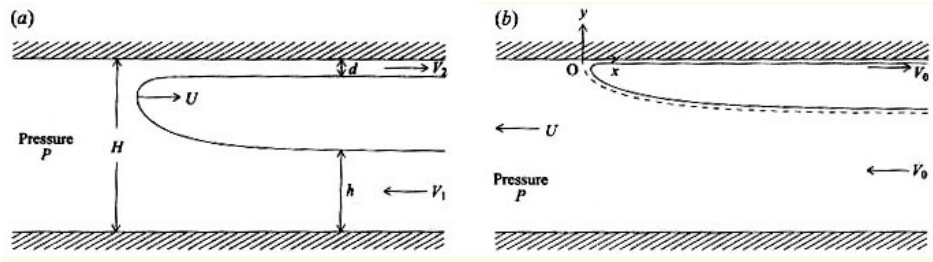


Figure 2.10: Illustration of the idealized configuration of the "filling flow", the impacted wall is represented by the top boundary, so the fast uprising jet in the reality is heading right ward in this scheme:(a) in a stationary frame, for $h = 0.468H$, $d = 0.1H$; (b) in the moving reference frame where the flow is steady including the dividing streamline —, for $h = 0.709H$, $d = 0.025H$. (Peregrine & Kalliadasis 1996)

that "the breaker becomes almost vertical at the instant of impact". Moreover, the case of perfect breaking is only an ideal case considering that the wave face is never totally flat, but concave especially in the case of a plunging breaker. Therefore "perfect breaking" and "flip-through" are not proved to actually differ/exist. This controversy is a proof that the kinematics of waves breaking on structures is not fully understood.

The modelling of the flip-through: the filling flow

In the case of the flip-through, the impact region is defined as the uncovered part of the wall's front face before the impact and then impacted by the wave. As detailed in section 2.3, the standard approach of pressure impulse theory is unable to model the flow in the impact region. In order to achieve such modelling, Peregrine & Kalliadasis (1996) introduced the "filling flow". This approach allows us to estimate the pressure at the surface of a confined space impinged by jets as sketched in figure 2.10. For instance, such a space can be a slot underneath an armour stone. The reason for such a study is to estimate if the filling flow pressure could be great enough to lift an armour block unit. In this configuration of confined space, a thin stream flows along the lower border of a smooth-surface slot with a velocity V_1 and a depth h , hits the dead end of the slot, and, if the inflow is fast and thin enough, turns around in the dead end and shoots back out along the upper border with a velocity V_2 and depth d . This creates a jet like outflow, similar to the jet rising from the impact region in the flip-through impact case. Such a flow is considered steady, incompressible, inviscid and the model does not account for the jets breaking into drops and entraining air, nor for jets directly entrapping an air pocket. However the authors made an attempt to investigate the case where the confined space initially contains an air pocket at its closed end. If a crack in the structure has appropriate length, high pressures from filling flow can last significantly longer than high pressures from direct wave impacts. Moreover they suggested that high filling pressures can be more common than high direct impact pressures.

2.3 Pressure field

As the pressure is a way forces manifest in the flow, we are required to investigate it thoroughly. However, it is relevant here to introduce a simple theory that provides insights on the characteristics of the pressure field below an impact.

First let us introduce a particular magnitude, the "pressure impulse", that was first investigated by De Rouville (1938), who was the first to achieve reliable wall pressure recordings of wave impacts on a structure. Most of the investigators (Denny 1951, Nagai 1960, Richert 1968, Kirkgoz 1982, Furhboter 1986, Kirkgoz 1991) report a wide scatter in their measurements of peak pressures at the wall (maximum pressure over the duration of impact at a given location). For a given wave condition, at a given point of the wall, the peak pressure and its rising time vary unpredictably for apparently identical wave impacts (see figure 2.11).

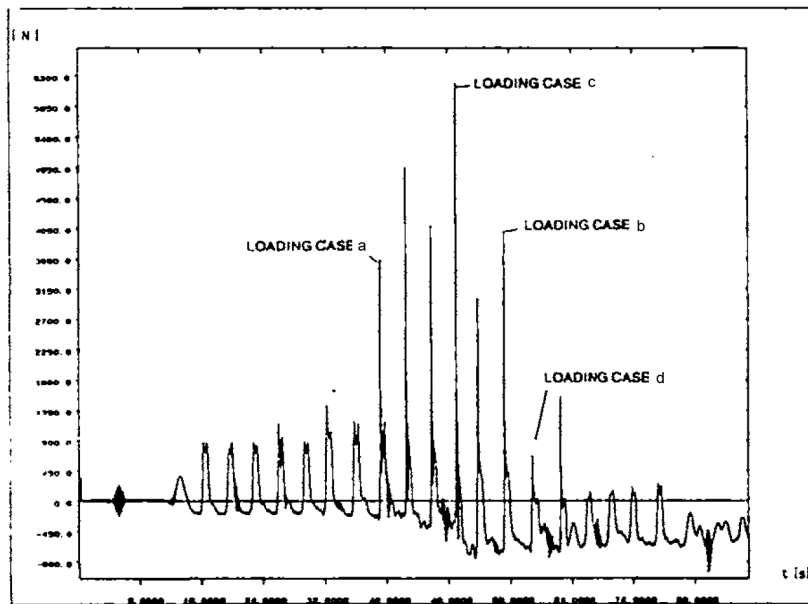


Figure 2.11: Time history of impact force on the wall by (Oumeraci & Partensky 1991) for the different impact types of Oumeraci's classification (figure 2.2).

Figure 2.11 shows that impact type (c) in Oumeraci's classification (figure 2.2) is the one that induces the impact force with the highest intensity and the shortest duration. Figure 2.12 shows the typical force histories for the different impact types of Oumeraci's classification. In figure 2.12, the typical intensity history of case (c) is referred in the literature as the "cathedral shape" pressure history. For this particular shape, from the beginning of the impact duration, the pressure first rises fast, then it attains its peak pressure value, then it decreases fast to reach a local minimum, and then there a little slow increases and it finally decreases to the end of the impact duration. Although the peak pressure and the impact duration experience great variability, Bagnold (1939) showed experimentally that the pressure integrated over the duration of impact:

$$P(x) = \int_{t_a}^{t_b} p(x, t) dt \quad (2.5)$$

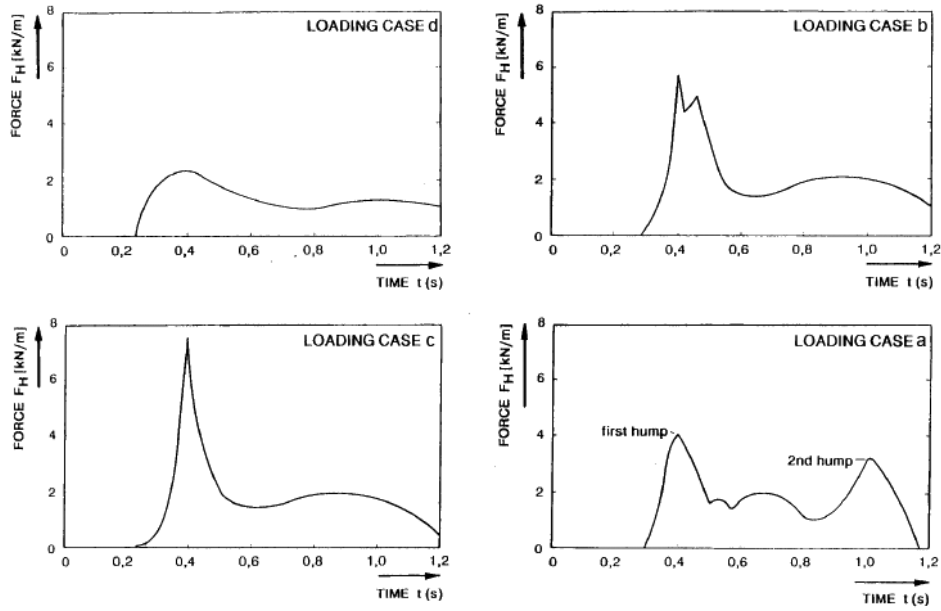


Figure 2.12: Typical time evolution of the force on the wall for the different impact types (Oumeraci & Partensky 1991).

is approximately constant. In this definition t_b and t_a are the times immediately before and after impact respectively and x represents the spatial coordinates. This quantity is called the "pressure impulse" or "impulsive pressure".

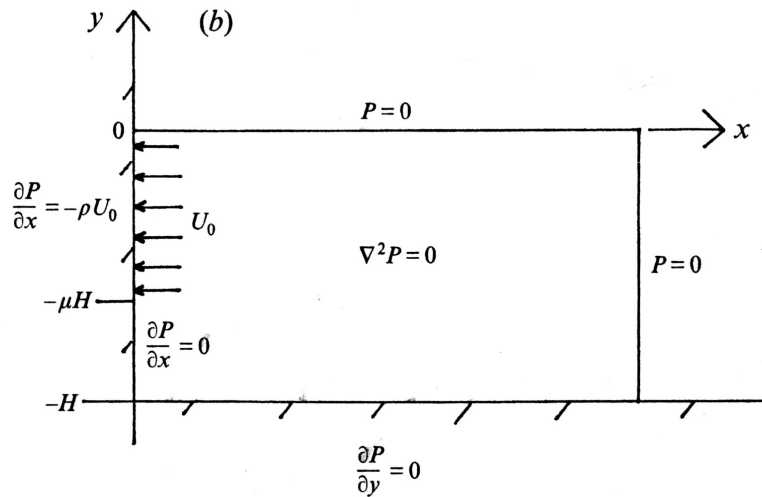


Figure 2.13: Impact of a wave on a vertical wall idealized as a two-dimensional boundary value problem for the impact of a rectangle of fluid on a vertical wall located at $x=0$. The distance from the bed to rest is denoted by H , and the wave strikes a fraction μ of this height. The normal component of impact velocity is modeled as a constant: $U_0 > 0$ at the wall $x=0$, on the part of wall that is subject to impact $-\mu H \leq y \leq 0$. (Fig.2 of (Cooker & Peregrine 1995))

Relying on the work of Lamb (1932) and Cooker & Peregrine (1990*a*), Cooker & Peregrine (1995) showed that pressure impulse can be interpreted as a potential outside of the close impact zone. Although they mentioned that the compressibility plays a dominant role in wave impact, this theory is derived under the assumptions of incompressibility, linearity, inviscid and inelastic collision. Indeed, the non-linear convective term in the equation of motion is considered negligible compared with the time derivative, as long as the change in velocity during the impulsive event takes place over a short time. This leads to the following linearised equation:

$$\frac{\partial U}{\partial t} = -\frac{1}{\rho}\nabla p \quad (2.6)$$

By integrating it with respect to time over $[t_a; t_b]$ and using the definition in equation (2.5) for the pressure impulse, one obtains:

$$\underline{U}_a - \underline{U}_b = -\frac{1}{\rho}\nabla P \quad (2.7)$$

Taking the divergence of this, $\nabla \cdot \underline{U}_a$ and $\nabla \cdot \underline{U}_b$ both vanish and the pressure impulse satisfies Laplace's equation:

$$\nabla^2 P = 0 \quad (2.8)$$

The model obtained is a two-dimensional boundary value problem. At the free surface the pressure is constant and taken to be a zero reference pressure so that $P = 0$. At a rigid boundary in contact with the liquid before and after the impulse, the normal velocity is unchanged so that: $\partial P / \partial n = 0$. At a solid boundary struck by the liquid during the impact, the change in normal velocity gives the normal derivative of the pressure impulse. For a stationary rigid boundary: $u_{nb} = \frac{1}{\rho} \partial P / \partial n$, where u_{nb} is the normal component of the velocity of the impacting liquid immediately before the impact.

An inelastic impact is assumed. Such a problem is sketched in figure 2.13. Thanks to this approach, (Cooke & Peregrine 1995) show that the momentum lost by a wave during impact comes from that part of the liquid domain that is near the wall. Indeed, introducing a "momentum length", they show that its value is half the water depth at the crest H . Thus, the whole pressure-impulse field is insensitive to wave-shape variations located at distances greater than half the water depth from the impact region. This indicates that as long as the basic properties of the wave near impact can be estimated, most other details of wave shape are unimportant. They also highlight the presence of a gradient of pressure impulse along the bed capable of moving bodies seaward. In addition, the model leads to the conclusion that pressure generated by impacts that occur in confined spaces are much greater than when impact is unconfined. Thus higher pressure impulses may be expected in yet more confined spaces like cracks, slots or deep masonry joints in a structure, or wave-cut notch in a cliff.

Thanks to this model Cooker & Peregrine (1992) introduced the flip-through type of impact and report, for this impact type, the presence of an important gradient in the pressure field acting along the sea bed and away from the wall. They also showed that the pressure impulse theory introduced by Cooker & Peregrine (1990*a*)

and described in detail by Cooker & Peregrine (1995) also predicts this significant pressure gradient along the bed and directed seaward, as reviewed by Peregrine (2003) (see figure 2.14(a)). Cooker & Peregrine (1992) examined the strong seaward force led by this pressure gradient on bodies lying on the sea bed as illustrated in figure 2.14(b). The impulse on a body, which is the pressure impulse integrated on its surface

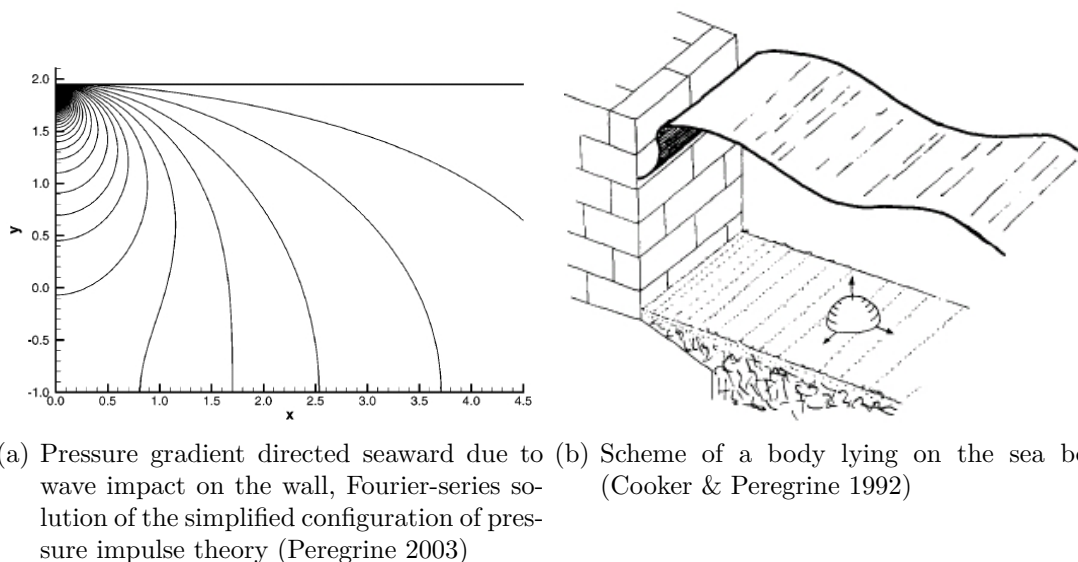


Figure 2.14: Illustration of pressure gradient due to wave impact and object lying on the sea bed.

or the integral of the force with respect to time, depends on its shape as long as its presence distorts the pressure field. This impulse is particularly strong for long thin bodies lying with their great axis parallel to the wall. Particularly a log-like shaped object experiences an upward vertical impulse that is one fifth the horizontal impulse. Moreover, this pressure gradient force may, as calculated for the hemispherical boulder, dominate other forces such as weight, friction with the bed and even drag due to wave-induced flow. In addition, whereas the drag force varies with the square of the object's radius, the impulse varies with the cube of the radius. Therefore, bodies large enough to be unresponsive to drag force can be expected to be moved by a nearby wave impact. Moreover, non flat based bodies as illustrated by the example of a log can experience a strong upward vertical impulse.

(Muller & Wolters 2000) led laboratory experiments on forces on the sea bed induced by wave impact on a wall. They showed that not only the wave impact but also the downfall of the vertical jet along the wall can create pressure peaks critical for the structure. They confirmed that strong pressures can propagate from the impact zone on the wall to the sea bed and they identified three types of pressures on the sea bed in front of the vertical wall:

1. Impact induced pressures, propagating away from the sea wall immediately after the impact,
2. Impact pressure oscillations, probably created during the initial stage of the down-rush of the water mass upwardly projected by the wave impact, 0.2 wave periods after

the impact.

3. Small pressure oscillations probably caused by the downfall of water droplets, 0.5 wave periods after the impact.

Cox & Cooker (1999) theoretically investigated the pressure impulse force on a body lying in front of a vertical wall. They found that for a 10-m-high wave, a spherical body of radius greater than half a metre will be moved as the impulsive force from the wave impact overcome the frictional forces of the body. They also investigated the case of a spherical body on a gently sloping bottom. They showed that the velocity of the body only depends on its shape and not on its volume but that larger bodies can move over a longer distance.

Cox & Cooker (2001) theoretically investigated the pressure impulse within fluid-filled cracks. They consider a wave impact on a wall in which there is a fluid-filled crack whose roof is piecewise linear. Their main result is that a large block forming the roof of the crack can be lifted due to the impulse exerted by the fluid in the crack beneath it. This means that impulses in cracks can cause considerable damage to the surrounding blockwork or armour structure.

In this section the pressure impulse theory has been introduced. The main result for our study is that, due to impacts, strong pressure gradients acting seaward can form. Those gradients are shown to be able to remove objects lying on the sea bed in front of the structure. However the issue of air content in the water was not considered.

2.4 The influence of air in water

The presence of air in water is of high interest when considering wave impacts. In this section the two distinct ways for air to be present in wave impacts are reviewed. Firstly air can be entrapped in air pockets. Secondly air can be entrained in water as small bubbles.

Moreover, in the study of wave impacts, there has long been problems in scaling experimental data from laboratory to real scales. This is partly due to the oversight of the presence of air in the attempt to find scaling laws. For instance the natural choice of Froude scaling gives unrealistically large prototype forces. This issue is also presented along this section.

2.4.1 Air pockets

Air pockets can be trapped between the impacting wave face and the structure. Typically, this phenomenon occurs when a wave overturns just before impact on a wall. This air pocket entrapment is illustrated in cases (b) and (c) of figure 2.2, and figures 2.5(b) and 2.5(c). The questioning around air pocket entrapment is how does it modify the pressure on the wall. Hayashi & Hattori (1958), Chan & Melville (1988) and Hattori, Arami & Yui (1994) found that the magnitude of the peak pressure decreases with the amount of entrapped air whereas the pressure rise time increases. They found that both small and large air pockets can produce large impact pressures. In addition

to its effect on pressure maxima, the trapped air interacts with the surrounding fluid in a pulsating motion wherein the fluid energy is alternately stocked and released. This causes pressure oscillations (Schmidt et al. (1992) found a frequency of 13 Hz) that are typically modulated by a damping mechanism. (Cooker & Peregrine 1992) observed a phenomenon of leakage of the trapped air and disintegration of the air pocket into a mixture of bubbly flow. In the context of a deep water plunging breaker impacting a wall, it is proposed by Zhang, Yue & Tanizawa (1996) to model the flow at impact by a self-similar solution of a non-symmetric oblique impacting jet, extending the standard methods for symmetric normal impacts. They found that the potential energy stored in the air pocket can be a significant part (15%) of the total fluid energy at impact. Zhang et al. (1996) also develop scaling laws for the maximum impact pressure on the wall and its rise time for impacts involving a trapped air pocket. A comparison with Chan & Melville's (1988) experiments of deep water wave impacts showed that free surface profiles and velocities are in good agreement for their scaling laws. Maximum impact pressures and rise times compare quite well with experiments provided that corrections to the model were applied to account for particular effects due to the experimental set-up of Chan & Melville (1988).

Wood, Peregrine & Bruce (2000) improved the "filling flow" theoretical model reviewed in section 2.2 by assuming that the presence of an air pocket may bounce the impinging water backward. Indeed they added to the "filling flow" the modeling of the bounce back due to the presence of a trapped air pocket that produces oscillatory pressures. Although strong simplifications made such a model not very realistic, the pressure distribution on the wall and on the bed compared well from experimental data.

The large scale model tests carried out by Obhrai, Bullock, Muller, Wolters, Peregrine, Bredmose & Grüne (2004) confirmed the idea that large impulses can occur with the presence of a trapped air pocket, although it resulted in lower pressures than when there was no air pocket for most of the tests they made. Therefore, they highlighted that air pockets increase spatial extend and duration of the impulse. They also mentioned that pressure oscillations after impact are due to the compression/expansion of the aerated water or air pocket.

Although some of the authors cited in section mentioned that, generally, lower pressures occur in the presence of an entrapped air pocket, this has not been confirmed yet as some authors found otherwise. For instance, Bagnold (1939) mentioned that "shock pressures occur only when the shape of the advancing wave front is such as to enclose an air cushion between it and the wall", or Richert (1968), Partenscky (1988) and Hattori et al. (1994) observed the most severe pressures at the wall when the wave hits the wall with a shape somewhere between the perfect breaking and the case with a very thin lens shaped air pocket. Another example is the work of Oumeraci, Bruce, Klammer & Easson (1995) who found that the case with a large air pocket (figure 2.2(b)) resulted in the highest pressures, and the case with small air pocket (figure 2.2(c)) gave the largest overall forces.

2.4.2 Entrained air

It is well known that successive breaking events lead to air bubble entrainment within water into the impact zone. Concerning wave impacts, the corresponding questioning is whether the presence of air increases or decreases the severity of impacts? Let us consider here entrained air in the form of bubbles. This mixture behaves as a compressible flow, which may be characterised by its sound speed.

2.4.2.1 Acoustics in bubbly flows

Wood (1941) derived a simple expression for the speed of acoustic waves in a bubbly mixture. He assumed that the mixture was homogeneous with a bulk density and compressibility. This assumption is valid only when the frequency of the pressure wave is well below the resonant frequency of the largest bubbles in the mixture (see Commander & Prosperetti 1989). The interactions between bubbles are not considered. Assume a mixture at a pressure P_0 composed of air with density ρ_{a0} and sound speed c_{a0} dispersed in water of density ρ_{w0} and sound speed c_{w0} . The volume fraction of air within the mixture is β and therefore the volume fraction of water is $1 - \beta$. The mixture density ρ reads at any pressure:

$$\rho = \beta\rho_a + (1 - \beta)\rho_w \quad (2.9)$$

Wood (1941) established the following expression for the sound speed in the mixture c_0 at pressure P_0 :

$$\frac{1}{\rho_0 c_0^2} = \frac{\beta_0}{\rho_{a0} c_{a0}^2} + \frac{1 - \beta_0}{\rho_{w0} c_{w0}^2} \quad (2.10)$$

This formula can also be written in terms of the air mass fraction $y = m_a/m$ where m_a is the mass of air and m is the mass of mixture in a control volume. Indeed at a given pressure P_0 , using the fact that $\beta_0\rho_{a0} = y\rho_0$ and $(1 - \beta_0)\rho_{w0} = (1 - y)\rho_0$, one can write:

$$\rho_0 = \frac{\rho_{a0}\rho_{w0}}{y\rho_{w0} + (1 - y)\rho_{a0}} \quad (2.11)$$

$$\beta_0 = \frac{y\rho_{w0}}{(1 - y)\rho_{a0} + y\rho_{w0}} \quad (2.12)$$

These relations allow us to write c_0^2 as a function of y , ρ_{a0} and ρ_{w0} :

$$\frac{1}{c_0^2} = \left(\frac{\rho_{a0}\rho_{w0}}{(1 - y)\rho_{a0} + y\rho_{w0}} \right)^2 \left(\frac{y}{\rho_{a0}^2 c_{a0}^2} + \frac{1 - y}{\rho_{w0}^2 c_{w0}^2} \right) \quad (2.13)$$

Figure 2.15 shows how the sound speed in mixture c varies with β at a given pressure: Figure 2.16 is the same mixture sound speed but plotted versus air mass fraction y . The major point to highlight in this expression is the following. Although it would be natural to think that the air-water mixture sound speed takes values between pure air sound speed and pure water sound speed, it is not so. One can note in figure 2.15 that for β great enough (greater than 0.124 %), the sound speed in the mixture is actually

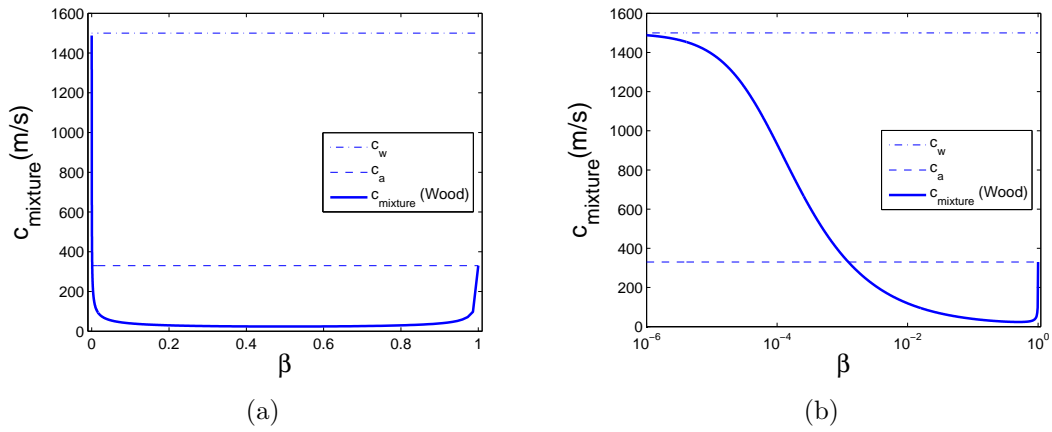


Figure 2.15: Sound speed in mixture according to Wood's (1941) law, for $P_0 = 1 \text{ bar}$.

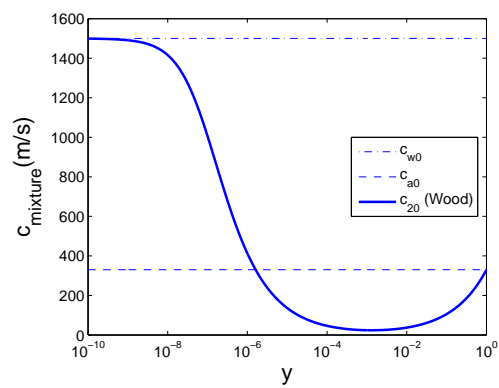


Figure 2.16: Sound speed in mixture according to Wood's (1941) law, for $P_0 = 1 \text{ bar}$, plotted versus air mass fraction y .

lower than the sound speed in pure air. The minimum mixture sound speed is attained for $\beta = 0.5006$, and is 23.7686 m/s .

The compressibility of air complicates the situation by causing the velocity to be both pressure and aeration dependent. Figure 2.17 represents the variation of figure 2.15(b) with reference pressure.

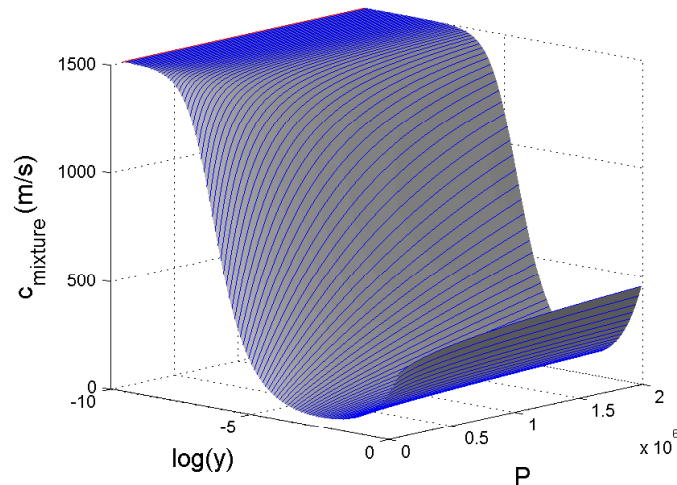


Figure 2.17: Sound speed in mixture according to Wood’s (1941) law for different reference pressure P . The lines are iso- y plots.

This description of the drastic reduction of sound speed with the rate of air in the mixture shows that the pressure dynamics can be greatly modified by the injection of air in the liquid.

In particular, this strong sound speed reduction is responsible for making pressure gradients last longer. Indeed the pressure relaxation times are conversely proportional to the sound speed in the medium. Therefore, in the presence of air, the pressure gradients in front of structure that have been computed in the pressure impulse theory (see section 2.3) would last longer. And thus, even if the intensity of the pressure gradient remains the same, the force exerted on an object lying on the bed would last longer too, causing the displacement of the object to be greater. Indeed, a constant pressure gradient resulting in a constant external force applied to an object leads to a displacement that is a quadratic function of duration of application of the force. So a decrease in sound speed in the liquid medium leads to an increase in the duration of application of the force to the object and this leads to an increase in the displacement of an object. We can consider that when approaching such a case with incompressible models the time relaxation of pressure gradients is so brief that the displacement of the object is too small to be relevant.

2.4.2.2 The influence of entrained air in wave impacts

Bullock, Crawford, Hewson, Walkden & Bird (2001) carried out both laboratory and field tests to characterize the influence of air on wave impacts. They carried out an

experiment to evaluate the effect of the air content on the pressure in a water bulk impacted by a piston, they reported field data from Admiralty Breakwater in Alderney Island and they conducted laboratory experiments using a 1:25 scale two-dimensional model of the Admiralty breakwater. They conclude that entrained air reduces the maximum impact pressure and increases the rise times in laboratory tests. However they did not properly control the aeration level in the physical model for wave impacts because reluctances of bubbles in saltwater and freshwater are different. Indeed they used fresh- and saltwater successively in order to investigate the influence of salt in water on pressure scaling. Thanks to an analysis of pressure reduction factors (maximum pressures recorded with aerated water divided by the average of the corresponding maximum pressures recorded with unaerated water), they were able to predict pressures for seawater impact from freshwater impact pressure at model scale. But they highlight that the variation of the air volume fraction is subject to a scaling effect beyond the scope of either the Froude or Cauchy scaling laws, therefore conversion to full scale has yet to be resolved. The critical effect that lies beyond this is the fact that the size of bubbles in saltwater is much smaller than those in freshwater (Scott 1975). This means that bubbles coalesce less easily. Thus they remain of small diameter, rise more slowly and so persist much longer in saltwater, which leads to higher volume fraction of air over longer durations, increasing compressibility.

Bullock, Obhrai, Peregrine & Bredmose (2007) performed large scale tests of wave impacts on vertical and sloping walls. They identified four types of impact. The "Slightly breaking" type corresponds to the transition between near breaking waves and well developed impact conditions. The "low-aeration" occurs when their measurements indicated that the water adjacent to the wall contained relatively little air (voids ratio $\leq 5\%$) and corresponds to the flip-through (figure 2.2(d)). The "high aeration" type, is for high voids ratios ($\geq 5\%$) and corresponds to the entrapment of pockets or dense clouds of bubbles. They first found that the highest impact pressures occur near still water level (SWL) for all the types of impact they investigated. They also found that low-aeration impacts led to more spatially localised pressure maxima and to shorter rise time and maximum duration than for high-aeration impacts. Bullock et al. (2007) mentioned that both low and high aeration can create high pressures of similar magnitude. Therefore the level of aeration of the liquid does not seem to influence the magnitude of the maximum impact pressure.

Bullock et al. (2007) also concluded from analytical and numerical studies that a potential benefit for the structure of aeration (pressure 'cushioning' effect) would anyway decrease as impact pressure increased. Moreover, even if the pressures during a high-aeration impact are lower, the fact that the impact is generally less spatially localised than a low-aeration impact reduces the chance of the resultant force being lower. Moreover, as this is combined with longer durations of rise and fall times typical of a high-aeration impact, the pressure impulse (equation (2.5)) associated with the impact may well be higher. The authors then noticed that consequently a 'cushioning' effect afforded by aeration due to the increased compressibility is not necessarily a dominant effect. They mentioned this is of particular relevance to the interpretation of freshwater hydraulic model studies as it suggests that the greater persistence of air in seawater waves may not help to protect full-scale structures from impact damage as

is often assumed.

Another important feature Bullock et al. (2007) observed is that in high-aeration cases sub-atmospheric pressures can occur, which can create a strong seaward force if combined with a high pressure event within the structure. Thus this can lead to practical damage risk like for instance the removal of masonry parts in the structure due to peak pressure propagation in a crack. In the same way, if the liquid medium is aerated enough (compressible enough) at the time of occurrence of such sub-atmospheric pressures or simply low pressures at SWL, then the sound speed can be low enough for the previous maximum pressure to have propagated down and be located at the foot of the structure. This means that a vertical gradient directed upward from the sea bed to the impact zone can appear. And therefore an object lying on the bed or part of the armour of the structure can experience a lifting force. This is of real relevance when considering the pressure impulse approach introduced above in section 2.3.

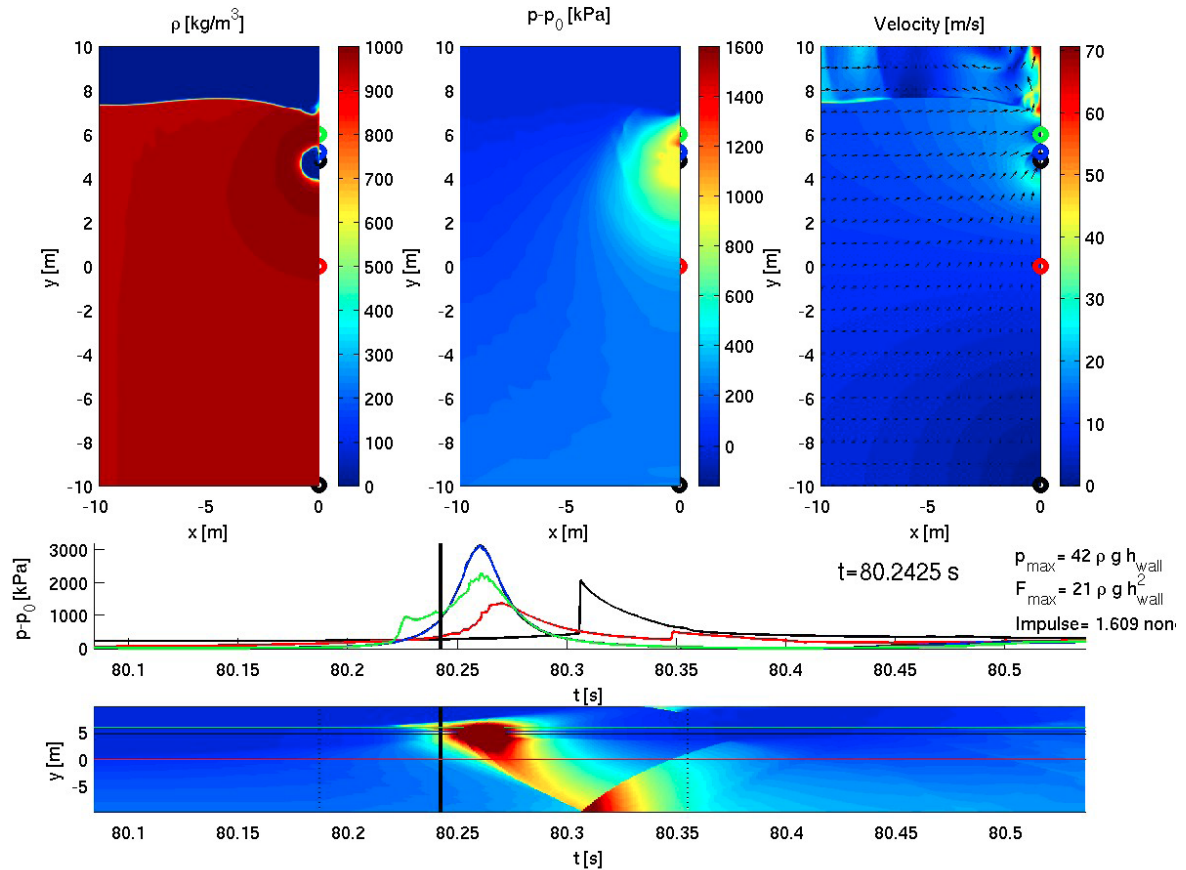


Figure 2.18: The three upper panels show density, pressure and velocity magnitude fields at a time close to that of maximum pressure. The middle strip shows pressure as a function of time for four points on the wall, marked as semi-circles in the graphs of the upper panels. The bottom panel shows pressure on the wall as a function of time. Figure 5 of (Peregrine et al. 2005).

Peregrine et al. (2005) performed the simulation of wave impacts on a vertical wall using a two-dimensional unsteady compressible flow model. The results from a previous

incompressible potential flow computation are used for initial conditions. Computations were carried out for flip-through type impacts (figure 2.2(d)) and for plunging breakers (figure 2.2(c)). The results shown in figure 2.18 are from an overturning wave for which the initial air fraction is of 5% in the water. They found that the pressure in the air pocket can fall below the atmospheric pressure. After the impact, a pressure wave propagates from the impact region down the base of the wall as one can see on the bottom strip of figure 2.18. This pressure wave steepens to become a shock wave by the time it reaches the bed. Reflection of the shock wave by the impermeable sea bed leads to a significant amplification of the sea bed pressure, occurring at the base of the wall a short time after the impact of the wave on the vertical wall. It is also important to notice that the maximum pressure at the bed occurs at the same time as the minimum pressure higher up the wall, applying a strong turning moment on the wall towards the sea.

2.4.2.3 Entrained air in the "filling flow" model

The work of Peregrine & Thais (1996) extended the study of the "filling flow" model reviewed in section 2.2, which was designed for the modeling of the flip-through, to the case where the filling liquid is an air-water mixture. This means that the air was entrapped in the water before the impact. The reader can refer to the configuration scheme in figure 2.10. The behaviour of bubbly liquid, subject to substantial pressure change, is considered here. Homogeneously dispersed bubbles are introduced in the filling flow. They assume that the gas density is negligible compared to the liquid density. A polytropic equation of state $P_g \rho_g^{-\kappa} = constant$ is used for the gas part. They perform an asymptotic development according to the small parameter $\epsilon = 1 - h/H$ where H is the height of the slot and h is the height of the incoming flow. This allows them to compare the first order solution to the exact solution computed numerically. And it shows that this first order solution is accurate for the case where the height of the inflow is large. Therefore this asymptotic theory can be useful to estimate the influence of cushioning effects on the pressure in practical applications. While the speed of sound relates to moderate pressure perturbations, the compressibility described here is applicable to substantial changes of pressure.

In their study they used the following expression for the sound speed in a bubbly mixture (Hsieh & Plesset 1961):

$$c = \left[\frac{\kappa P}{\rho_l \beta (1 - \beta)} \right]^{\frac{1}{2}} \quad (2.14)$$

where P is the pressure, β is the air volume fraction, ρ_l denotes density of water and κ is the constant in the polytropic law. With this expression, if the air fraction β is 5% with the conditions $\rho_l = 1025 kg/m^3$, $P = 1bar$ and $\kappa = 1.4$, the sound of speed is $54m/s$, while the speed of sound in non-aerated seawater is about $1500 m/s$. Thus even a small fraction of air can dramatically lower the sound of speed and the high pressures encountered in violent confined flows. Moreover they build a Mach number based on the inflow velocity, which, in relation to a wave impact on a wall, corresponds to the waterline velocity. They mentioned that if the air content in the water is enough, the jet along the wall may be supersonic.

Thanks to this approach, Peregrine & Thais (1996) showed that pressures on the wall for a filling flow can be reduced by an order of magnitude by a cushioning effect. But this applies only in large scale flows, for which the velocity is great whereas it is not in small scale flows. This is a phenomenon that can be part of scaling problems. It is mentioned that the maximum pressures at the entrance of the slot are more reduced than the background pressures far in the slot. And those background pressures are likely to be comparable to the pressure below the impact region in the flip-through. Although the choice of an appropriate reference frame makes the flow steady in it, it is actually unsteady as the stagnation point, which is the point where inflow's free surface and outflow's free surface are connected, moves towards the entrance of the slot as it is filled. Therefore this velocity of filling is influenced by the incoming air content. As air is more present in the inflow mixture, the velocity of filling decreases. Indeed, the fluid, being compressed by high pressure, experiences a volume reduction due to its compressibility, hence reducing the effective filled volume. This flow is relevant to the description of the flip-through impact. Moreover the transient process of transonic flow

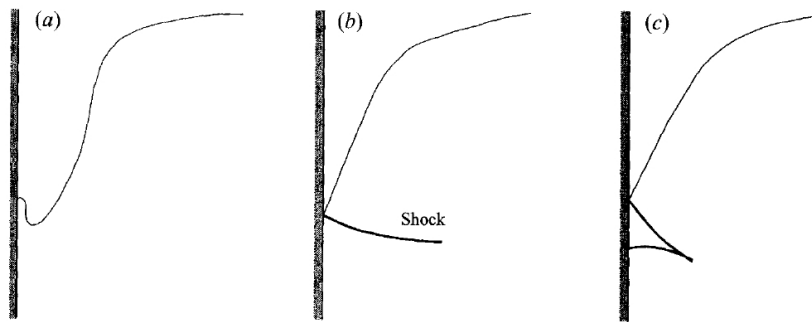


Figure 2.19: Sketches of wave impacts: (a) flip-through, (b) and (c) two different supersonic impacts with small and large contact point accelerations, respectively (Peregrine & Thais 1996).

for flip-through impacts has been figured out (figure 2.19). However the filling flow has not been made accurate for supersonic filling velocities. This model can represent a practical interest on the condition that the incoming air volume fraction is determined.

Muller, Wolters & Cooker (2003) investigated experimentally the propagation of pressure pulses through water-filled cracks. They performed an experiment in which they generated pressure pulses with a piston at the entrance of a crack model, which can then propagate through the crack. They found that the pressure wave propagation speed in the crack is five times lower than the sound speed in pure water, yet they did not inject air on purpose. They mentioned that no air bubbles were visible in the water-filled crack. However, they related this reduction of speed to the presence of micro air bubbles stuck in the micro crevices of the containment. This illustrates that a very small amount of air can drastically modify the pressure dynamics within a crack. Moreover significantly larger air volume fractions than what they worked with can be expected in natural wave impacts making this effect even more dominant. Therefore high pressures may build up inside breakwater or cliffs cracks or underneath armour units while the impinging wave impact pressure has already disappeared, leading to outward or upward

forces. They also observed that attenuation in cracks with widths larger than 3 mm is lower, which makes structures with wider cracks more susceptible for damage. Moreover they found that complex crack geometry does not reduce pressure pulses, so large internal forces may be present in cracks containing cavities.

Wolters, Müller, Bullock, Obhrai, Peregrine & Bredmose (2005) investigated wave-impact induced pressure pulses propagation in cracks filled with an air-water mixture at large scale and full scale. They implemented this research area with new data that show that pressure pulses within can reach extreme magnitudes. For the large scale in the laboratory, at which they were able to investigate more critical conditions than at full scale for technical reasons, pressure attained 550 kPa for an aeration rate in the range of 0.01 to 16%. They found seaward pressures (pressure gradients acting outward from the crack) up to 250 kPa at large scale. This clearly demonstrates that damage occurring in masonry cracks are very likely to be due to this effect. They also mention that scale effects between the field and the laboratory are of first importance.

2.4.3 Air bubble rates

It is obvious that successive breaking events generate entrapment of air within water. However it is complicated to get a good estimation of the effective rate of air under a breaking wave. Indeed, accurate measurement of the air volume fraction due to a breaking wave is not easy. Lamarre & Melville (1995) developed a technique for measuring low-frequency-sound speed in the ocean at depths of 0.5m and greater. From sound speed measurements under the surface of an ocean experiencing 8m/s wind, they estimated the corresponding entrapped air volume fractions through Wood's (1941) law. They found air volume fractions up to 10^{-5} at 0.5 m below the surface, and only $2 \cdot 10^{-6}$ at 1 m below the surface, which is very small regarding figure 2.15(b).

Then Buckingham (1997) studied the theoretical shape of vertical profile of air fraction beneath the free surface. They proposed a model explaining an inverse-square profile, assuming a uniform injection of air through the sea surface so that bubble concentration immediately beneath the free surface varies with depth but not with horizontal range. Air is injected according to a wind speed parameter only and is carried down through a process of turbulent diffusion. Such a one-dimensional diffusion model is inadequate to describe the bubble plumes generated by breaking, which are strongly non uniform in the vertical as well as in the horizontal direction. They suggest that a short-term exponential-profile plume generated by a breaking wave near the free surface would be superimposed to a longer-lived inverse-square profile plume that remains in the background due to the diffusion of bubbles to a greater depth.

The bubble creation process was investigated by Deane & Stokes (2002), however they do not say much about volume fractions. They proposed two different mechanisms of bubble creation. The first is the fragmentation of the air pocket formed by the plunging jet of the breaker, which generates bubbles larger than 1 mm. The second is the impact of the jet and of drops on the free surface, generating smaller bubbles. They identified the discrimination in bubble radius distribution as the Hinze scale.

Real bubble fraction values are still difficult to estimate. For instance Cox & Shin (2003) conducted laboratory measurements of air fractions under 10 cm waves breaking

in freshwater and found peak void fractions up to 20%, which is a large ratio of air considering figure 2.15(b). Whereas Deane (1997) carried out in-situ measurements of air fraction in the surf zone and found air fractions up to 0.3-0.4.

Deane & Stokes (1999) mentioned the terminology of Monahan (1993) who introduced the terms " α plume", " β plume" and " γ plume" to describe the various stages of plume evolution. They focused their investigation on α plumes, which persist for a second or so after wave breaking and are characterized by high void fractions (order 10% volume fraction of air) and a broad spectrum of bubble sizes (millimeters to tens of microns). They concluded that mechanisms are responsible for two large scale air entrainments in water: jet intrusions and the crushing of air cavities. Then they distinguished two small scale mechanisms of bubble formation. The first is the unstable breaking of very thin filaments of air (a few hundreds of microns wide and millimetres long). The second process is the splitting of large bubbles.

Lamarre & Melville (1992) made field measurements of air volume fractions beneath the surface with wind up to 14.9 m/s and under breaking waves of height ranging between 1.7 m and 2.8 m. They found a basis of low aeration, lower than 0.005 and a maximum aeration close to the surface of 0.24. Void fractions above 0.005 were found to be only sporadic peak signals at depth of 20 cm, and absent at depth of 80 cm. The authors recommend to perform accurate measurements of lower values of void fractions (10^{-5} to 10^{-3}). They seem to introduce the idea that there is an average, long lasting aeration, to which sporadic peaks are superimposed.

Several void fraction measurement techniques were developed. Vagle & Farmer (1998) reviewed four linear acoustic techniques applicable to the surf zone to the open ocean. Whereas Stokes & Deane (1999) developed an optical imaging system for high volume fraction measurement and applied it to the field. They found void fractions ranging between 0.003 and 0.271, 20 cm beneath the free surface, attached to a buoy drifting in the open ocean. The buoy experienced the white cap impacts and the waves were around 30 cm high.

Terril, Melville & Stramski (2000) carried out field measurements using one of the methods reviewed by Vagle & Farmer (1998). They performed measurements of void fraction at Scripps San Diego pier, in the surf zone in water of 6 m depth. They found void fraction up to 10^{-5} . However they do not mention wave height during the recording campaign. This campaign was extended to measurements of void fractions beneath the free surface at an offshore location (Terril, Melville & Stramski 2001). They tried to relate surface wind speed to air volume fraction and found air volume fractions up to $3 \cdot 10^{-4}$ at 0.7 m beneath surface for a 17 m/s wind speed. However it is difficult from this study to evaluate the influence on wave breaking. Indeed, they do not mention whether they were in the fetch zone with rather small height waves or in a zone where waves were already well propagated and thus with bigger amplitudes.

The studies found in the literature do not allow us to conclude clearly on an air volume fraction under waves. Some mention very high fractions whereas others mention very low ones. This can be related to the two different mechanisms that Deane & Stokes (2002) propose.

2.5 Conclusion

In this chapter we have introduced the reader to the state of the art in the research area of wave impacts. A review of classifications of wave impact has been made to throw the basis of the frame of this work. Some theoretical points have been presented in relations to wave impacts. Then we presented the problems related to the presence of air within water at the moment of the impact.

While setting the physical context of wave impacts, we have shown that this phenomenon is still not fully understood. More particularly their effect on the structure on which they impact or on the surrounding environment in the presence of air need more investigation. The work presented here aims to gain knowledge on the influence of air on the effect of wave impacts on objects within a structure or close to the impact zone. This issue will be investigated through performing numerical simulations of a breaking wave in a water-air mixture impacting a rigid wall. The model used to perform such simulations is presented in chapters 3 and 4. However, before we introduce the method we used in this study, chapter 3 begins with the numerical methodologies available in the literature to approach such an issue as wave impacts on coastal structures and from which we chose ours.

Chapter 3

The original SLOSH model

3.1 Introduction

The main objective of this chapter is to introduce the original multifluid model and the underlying numerical methods used in SLOSH, which is the base model from which we have developed an extension that will be presented in chapter 4.

But firstly, in order for the reader to gain a good overview of the relations between this multifluid model and the other models found in the literature, we present in section 3.2 a very short review of numerical approaches classically used for the simulation of wave breaking. Then a more precise description of Navier-Stokes free-surface-flow models is proposed in section 3.3. Only then in section 3.4 the model for free-surface compressible two-fluid flows used in SLOSH is derived. Finally the underlying numerical methods are presented in section 3.5.

3.2 Numerical methods for wave breaking

Several models can be used to simulate wave breaking. Some detailed reviews of different models for wave breaking can be found in the literature (e.g. Helluy, Golay, Caltagirone, Lubin, Vincent, Drevard, Marcer, Fraunié, Seguin, Grilli, Lesage, Dervieux & Allain 2005). Although most of the approaches are based on a Eulerian representation of the flow, there are attempts to use Lagrangian approaches. For instance, the Smoothed Particle Hydrodynamics (SPH) method has been used recently. This method belongs to meshfree particle methods (MPM) and was first proposed in the field of astrophysical problems by Lucy (1977), Gingold & Monaghan (1977) and Monaghan (1992). In this method the state of a system is represented by a set of particles. Each particle possesses individual material properties and moves in interaction with the others according to the governing conservation equations. Its major advantage and certainly its most attractive feature is that it can handle problems with large deformations. The SPH method has been recently used to study breaking waves by (Yang & Tryggvason 1997, Monaghan & Kos 1999, Liu & Shao 2002, Lo & Shao 2002, Dalrymple & Rogers 2006).

One can also find hybrid Eulerian/Lagrangian approaches, like for instance, the

Trackers method. This method computes the velocity and pressure fields through a two-phase Navier-Stokes model on a fixed grid. But the interface is localized by Lagrangian particles. Those particles allow for the tracking of the interface position through its deformation over time. This technique allows for the computation of the deformations of the interface at a subgrid scale. Those methods are reviewed among others in (Scardovelli & Zaleski 1999) and are particularly used for the simulation of wave breaking (e.g. Lee & Heo 2005). Song & Sirviente (2004) used a hybrid method between a front capturing and a front tracking technique to study wave breaking dynamics. Gomez-Gesteira & Dalrymple (2004) investigated the three-dimensional impact of a dam break wave on a vertical parallelepiped using a compressible SPH method. They compared their simulations to an experiment and found good agreement for the velocity field in front of the structure and the force exerted by the wave on the structure. Gomez-Gesteira, Cerqueiro, Crespo & Dalrymple (2005) used the same method and studied waves overtopping a flat deck parallel and just above the surface. They also found good agreement for the dynamics when comparing to experimental data.

Regarding Eulerian methods, one can find several approaches in the literature. Bredmose, Brocchini, Peregrine & Thais (2003) used a Boussinesq model to investigate steep-wave sloshing in a tank and compared it to an experiment. Biauxser, Grilli & Fraunié (2004) used a pseudo-compressible method, which is a coupled VOF/Boundary element method. They extended it for three-dimensional flows and studied wave breaking dynamics. There was an attempt to improve the incompressible one-fluid (detailed in section 3.3.1) VOF method, by Wemmenhove (2006), as they accounted for the compressibility of one of the phases. They performed simulations of hydrodynamic loading with this two-phase model with compressible air. They took the compressibility of air into account by setting its density as a function of pressure through an adiabatic transformation law: $\frac{\rho_a}{\rho_{a0}} = \left(\frac{P}{P_0}\right)^{\frac{1}{\gamma}}$. They performed two test cases for hydrodynamic loading, a falling water mass and the classic dam break test, for which they found a medium accuracy when comparing them with experiments.

3.3 Navier-Stokes free-surface flow models

In this section we review models based on the Navier-Stokes equations that have been developed for the simulation of free-surface flows. Although some non Navier-Stokes models have been used to represent surface waves, they are not in the range of this study which focuses on wave breaking and wave impacts. For a summary of those models the reader can refer to Duval (2007).

Let us notice that the terms "free-interface" or "free-surface" refer in this document to separated-phase flows. In such flows there is a unique interface separating two zones occupied respectively by each fluid. In contrast the flows called "dispersed phase flows" contain several interfaces (like bubble interfaces) whose spatial extent is at a smaller scale.

3.3.1 Incompressible Navier-Stokes one-fluid models

The most common approach for the modeling of free-surface flows is the resolution of a Navier-stokes "incompressible one-fluid model". Such a model is based on incompressible Navier-Stokes equations in each phase and on stress and momentum continuity conditions at the interface. An averaging procedure (Drew 1983) is undertaken to obtain a unique set of incompressible Navier-Stokes equations describing the flow of both phases in the entire domain. (The reader will notice that this procedure is used further in this document (section 3.4.2) to develop the so called "multifluid model" used in the present work). The resulting unique set of equations reads:

$$\begin{aligned} \nabla \cdot \underline{u} &= 0 \\ \frac{\partial \rho \underline{u}}{\partial t} + \nabla \cdot (\rho \underline{u} \underline{u}) &= \nabla \cdot (-P \underline{I} + 2\mu \underline{S}) + \rho g + \underline{F}_c \end{aligned} \quad (3.1)$$

where ρ , \underline{u} , P are the average density, velocity and pressure, g is the gravity acceleration, \underline{S} the viscous stress tensor, μ the dynamic viscosity and σ the surface tension. \underline{F}_c are the capillary forces. The model (3.1) implicitly assumes no slip between phases (there is a unique velocity field), no description of dynamics at the subgrid scale and no mass transfer between phases at the interface.

Now for this unique fluid to represent separated-phase flows, it is necessary to track the interface between the two phases in order to know which phase is where. One can distinguish two types of methods for interface tracking: Eulerian and Lagrangian. Hybrid methods mixing both Eulerian and Lagrangian approaches can also be found. The Lagrangian approach can lead to severe difficulties when the interface topology becomes complex, thus it will not be reviewed here. In the case of the Volume-Of-Fluid (VOF) methods (Hirt & Nichols 1981), which are widely used, a fraction function C is transported by the flow velocity. This function can be interpreted as the volume fraction of one of the fluids. In such a Eulerian approach the volume fraction C is defined in the process of averaging. It indicates the amount of phase 1 and phase 2 at a given point in space and time and is equal to 0 (resp. 1) where phase 1 (resp. 2) is present. This volume fraction obeys:

$$\frac{\partial C}{\partial t} + \underline{u} \cdot \nabla C = 0 \quad (3.2)$$

The numerical diffusion may cause the jump in C at an interface to thicken, making an accurate estimation of the localization of the interface difficult. In Level-Set methods introduced by (Osher & Sethian 1988) the extra magnitude allowing to track the interface is no more the volume fraction but the distance to the interface, which is thus defined by the points where this quantity vanishes. However the equation governing this distance field is complex making its resolution difficult. And even with accurate schemes losses of mass can be experienced.

In the particular field of wave breaking the one-fluid model (3.1) is widely used. For instance Kleefsman, Fekken, Veldman, Iwanowski & Buchner (2005) used an incompressible VOF based method to simulate wave impact problem. They ran different impact test cases (dam break, water entry of wedge) to evaluate their method and

found good accuracy. Hieu & Tanimoto (2006) performed simulations of wave breaking over an immersed breakwater. They used a VOF-based two phase method in which air and water are considered incompressible. The equation to distinguish the zones filled with air from the ones filled with water is a VOF equation (Hirt & Nichols 1981), with a source term for the fraction function in order to emulate a wave maker that minimize the wave reflection at its boundary. The algorithm for this equation is of PLIC type. They found results in good agreement with laboratory experiments for a wave breaking on a sloping bottom. For a wave breaking over a submerged porous breakwater, they also compared their model to laboratory tests, and found good agreement. However they do not focus on precise dynamics of the breaking process or on the pressure field induced by breaking. Very recently Karim, Tanimoto & Hieu (2009) applied a VOF method to the investigation of non-breaking wave dissipation in porous structures.

To face the difficulties inherent to classic VOF and Level-Set methods, some authors propose some improvements: the interface reconstruction for VOF methods and the re-distanciation and the Ghost-Fluid method for the Level-Set methods (Fedkiw, Aslam, Merriman & Osher 1999). Let us also remark that in the same way the volume average of Drew (1983) is applied to incompressible Navier-Stokes equations, it can be applied to Reynolds Averaged (time averaged) Navier-Stokes (RANS) equations. For instance Lin & Liu (1998) presented a 2D Reynolds averaged Navier-Stokes (RANS) equation model coupled with the k - ϵ model to study periodic and solitary wave breaking in the surf zone. Comparisons between their numerical results and experimental data were satisfactory. Lara, Garcia & Losada (2006) also use a RANS approach for interactions with submerged permeable structures. Losada, Lara, Christensen & Garcia (2005) compared RANS and Large eddy Simulation (LES) for the simulation of waves breaking over a low crested breakwater. Other examples of investigations of LES can be found in (Watanabe & Saeki 1999, Christensen 2006). These approaches provide a fine and accurate description of turbulence for wave interactions with porous or complex structures.

3.3.2 Diffuse interface models

Another way to face the difficulties of Eulerian methods is to go back over the mathematical model. A solution is to directly introduce in the model an interface thickness, which can be worthwhile for the consideration of surface tension effects and phase changes. This leads to the so-called "diffuse interface models" (Anderson, McFaden & Wheeler 1998), which is not to be mistaken for "diffuse interface methods", which is a generic terminology referring to all methods in which interfaces are unfortunately diffused (figure 3.1). The derivation of the diffuse interface models is carried out according to a thermodynamical approach, a major point being the choice of the mixture free energy. Among these models, let us mention the Second-Gradient approach (Jamet, Lebaigue, Coutris & Delhay 2001) wherein the mixture free energy is expressed as a function of the mixture density and its gradient, and the Phase-Field approach (Penrose & Fife 1993, Jacqmin 1999) where the free energy is defined from a potential with two extrema, which corresponds to the equilibrium of each phase.

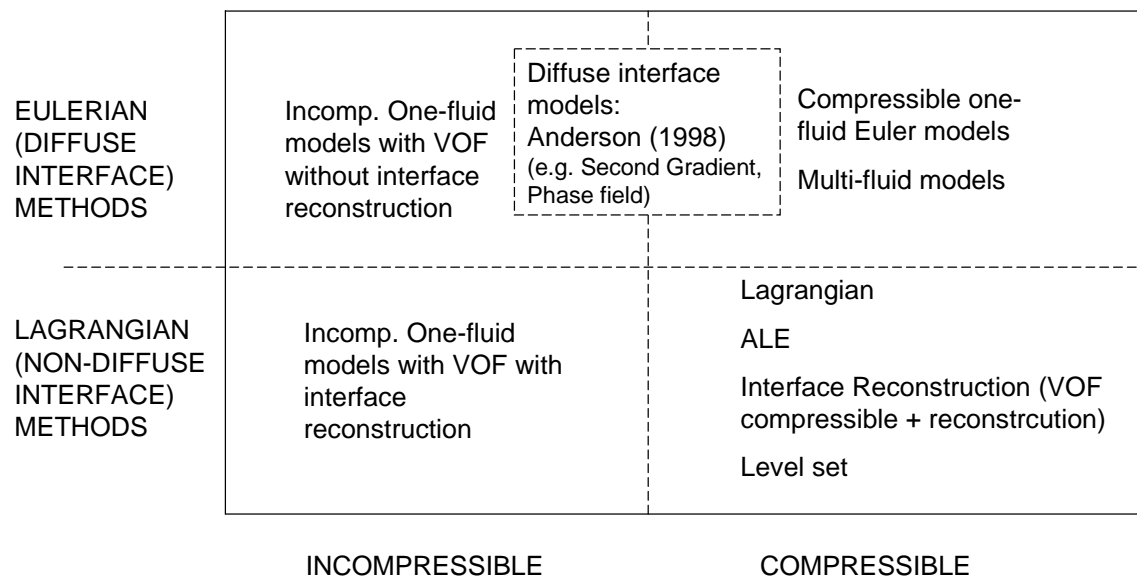


Figure 3.1: Free-surface Navier-Stokes models.

3.3.3 Compressible multifluid models

It has been shown in section 2.4 that air bubbles and air pockets are present in wave impacts and that they induce compressibility. Therefore the compressibility should be taken into account for an accurate model of wave impacts. Therefore the standard incompressible one-fluid method should be extended to include compressibility effects. We review here two classes of compressible models.

3.3.3.1 Models based on compressible Euler equations (non-viscous fluids)

These models are based on the Euler equations, which are solved in each pure phase. The model then is supplemented by equations that provide the evolution of the position of the phases. Firstly, Karni (1994) proposed a method based on the Euler equations in each pure phase with a transport equation for the mass fraction. Based on the work of Karni (1994), Abgrall (1996) and Shyue (1998) developed a method for the resolution of the 1D Euler equations with an ideal-gas equation of state. They simulated multi-fluid compressible flows with interfaces between two gases of different ratios of specific heats and they called this approach a "multi-species approach". A numerical method based on this model is proposed by Saurel & Abgrall (1999a) for structured grids. They also extended this approach to several dimensions and to fluids governed by a stiffened gas equation of state. In this case the pressure and the internal energy are related through the Stiffened-Gas equation of state:

$$P = (\gamma - 1)\rho e - \gamma\pi \quad (3.3)$$

where γ is an empirically determined constant and π is a constant representing the molecular attraction between molecules for the considered materials. Then transport equations for the parameters γ and π are added to the Euler equations to represent

multi-phase flows. This numerical method was then extended to unstructured grids by Abgrall, Nkonga & Saurel (2003).

The advantages of such approaches is that they are accurate, robust and simple to program. However they can show conservation errors regarding the partial mass of the various fluids leading to inaccurate internal energies and temperatures at the interface. Moreover for the applications of interest here inviscid equations are not suitable.

3.3.3.2 Models based on multi-phase Navier-Stokes equations

Saurel & Abgrall (1999*b*), following Baer & Nunziato (1986), introduced a new class of methods to simulate two-phase compressible flows. This approach is a method able to solve the same governing equations with the same numerical methods in the whole computation domain (for both fluids), for reasons of simplicity and efficiency. Which is not the case for example for front tracking methods (see Cocchi & Saurel 1997). In this approach the average procedure of (Drew 1983, Drew & Passman 1998) is applied to compressible Navier-Stokes equations. This results in the model called "multifluid model", which is a set of 7 equations (when dealing with two phases): two mass, two momentum, two energy conservation equations (one for each phase) and one topological equation (transport equation for the volume fraction of one phase). This model then deals with two pressures, two velocities, that allows for the determination of the thermodynamic and kinematic variables of each fluid (or phase).

Such a model can deal with very general equations of state and is conservative for the mixture. It allows for the treatment of interface problems (separated phase flows) as well as homogeneous two-phase flows (dispersed phase flows) and is accurate for internal energy and temperature. Multifluid models have been used for the modelling of shock waves in compressible mixtures, detonation waves in heterogeneous materials (Saurel & LeMetayer 2001). This model is also able to dynamically create interfaces, which may be suitable for the simulation of cavitating flows.

Let us make a short remark on terminology. (Saurel & Abgrall 1999*b*) defined separated-phase flows as "multi-fluid flows" and dispersed-phase flows as "multi-phase flows". However a case where several phases are flowing separately, like for example the case of a water wave propagating at a free-surface, should preferably be called a multi-fluid (air/water) multi-phase (liquid/gas) flow. In contrast cases where a mixture of several fluids is flowing homogeneously can be found. For example an emulsion of liquid water and liquid oil should preferably be called a multi-fluid flow rather than a multi-phase flow, because two fluids and only one phase are present, even though the flow is dispersed (many interfaces within a control volume). In separated-phase or separated-fluid flows, almost all control volumes only contain a pure phase or fluid, except the ones around the interface. In this work, like in most of the studies found in the litterature, the distinction will not be made, so we will call by abuse "multifluid" or "multiphase" flows, flows of either different phases or different fluids.

Let us also remark that such a multifluid model can also be used for more than two-phase flows, for instance (Saurel & LeMetayer 2001) extended the multifluid model to n phases. The multifluid model is designed for applications in which the compressibility plays an important role. In such a model it is relevant to notice that the interface is

represented by a contact discontinuity. Thus numerical methods able to deal with contact discontinuities are requested. However these contact discontinuities are thickened by the numerical diffusion, which thus, in the case of separated-phase flows, creates a numerical mixture between fluids. Also for these models the choice of relevant mixture laws for the densities and the viscosities is crucial especially if interface reconstruction is chosen not to be performed. These mixture laws are actually very important from a mathematical point of view as they influence the hyperbolicity and the thermodynamical consistency of the model. Moreover, for multifluid models, additional links with thermodynamics can be established, such as the ones of which Second-Gradient and Phase-Field approaches benefit.

This is a "multifluid" approach that is used in the SLOSH code, although it is restricted to a unique velocity field. A detailed derivation of multifluid models is given in section 3.4.

3.4 Derivation of the continuous multifluid model

The model that we present in this chapter is the model included in the original SLOSH model developed by Chantepedrix (2004). An overview of the derivation of the model is to be given here. For this purpose we chose to present the derivation of the macroscopic equations using an averaging process, which is a classic technique to introduce multifluid models. Firstly we start from the scale at which both phases can be distinguished. Then we apply the averaging process. Finally, through different derivation paths, we obtain a set of different macroscopic models that account for two-phase flows. These models are schematized in figure 3.2. Finally, we focus on the model that has been chosen for the SLOSH code for modelling reasons and we present the numerical methods implemented to solve it on a fixed grid.

The reader will notice that the energy conservation equation is not taken into account in the following mathematical derivation, because the model actually used in this work presupposes a constant temperature.

3.4.1 Single phase Navier-Stokes equations

In the following k refers to phase 1 or phase 2. We suppose we are at a scale small enough to consider that both phases are not mixed. If we assume that each phase k can be described as a continuum, its motion is governed by the compressible Navier-Stokes equations:

$$\frac{\partial \rho_k}{\partial t} + \nabla \cdot \rho_k \underline{V}_k = 0 \quad \text{Mass conservation} \quad (3.4)$$

$$\frac{\partial \rho_k \underline{V}_k}{\partial t} + \nabla \cdot \rho_k \underline{V}_k \otimes \underline{V}_k = \nabla \cdot \underline{T}_k + \rho_k \underline{f}_k \quad \text{Momentum conservation} \quad (3.5)$$

where ρ_k is the density of fluid k , \underline{V}_k is the velocity of fluid k , \underline{T}_k is the stress tensor and \underline{f} is the body force volume density.

In addition, the assumption of barotropic fluids is made. It means that the isopycnic ($\rho = cst$) lines are lined up with the isobaric lines, thus the pressure P_k in fluid k only depends on its density ρ_k :

$$P_k = P_k(\rho_k) \quad (3.6)$$

At this stage the model is at the continuum level. The materials are separated by an interface across which there is a jump in mass and momentum:

$$\begin{aligned} [[\rho(\underline{V} - \underline{V}_i) \cdot \underline{n}]] &= 0 \\ [[\rho \underline{V}(\underline{V} - \underline{V}_i) \cdot \underline{n} - \underline{T} \cdot \underline{n}]] &= \sigma \kappa \underline{n} \end{aligned} \quad (3.7)$$

where $[[\]]$ denotes the jump in a variable across the interface, \underline{V}_i is the velocity of the interface, σ is the surface tension, κ is the mean curvature of the interface and \underline{n} is the unit normal to the interface.

At the microscopic scale (the scale considered in this section), for two immiscible phases, at a given time, each point in space is either in phase 1 or 2. Thus let us define a function $X_k(\underline{x}, t)$ that indicates the presence of phase k at every instant t and location \underline{x} :

$$X_k(\underline{x}, t) = \begin{cases} 1 & \text{if phase } k \text{ is at time } t \text{ in location } \underline{x} \\ 0 & \text{otherwise.} \end{cases} \quad (3.8)$$

Function X_k is "attached" to phase k therefore its material derivative along the interface vanishes:

$$\frac{\partial X_k}{\partial t} + \underline{V}_i \cdot \nabla X_k = 0 \quad (3.9)$$

The reader will notice that ∇X_k is zero except at the interface. Thus ∇X_k is a Dirac vector function peaking at the interface and its direction is the normal interior to phase k . So ∇X_k can be written:

$$\nabla X_k = -\underline{n}_k \delta_i \quad (3.10)$$

where δ_i is the Dirac function peaking at the interface.

3.4.2 Macroscopic scale: averaged equations

Now the averaging procedure of Drew (1983) is applied to equations derived in section 3.4.1.

Let us consider a volume of this two-phase mixture large enough for this two-phase mixture to be described as a continuum but small enough to still provide a local or continuous description of the flow. Let $\langle \ \rangle$ denote the averaging operator over the considered volume. The average process acts like a smoothing filter in space in the sense that no details appear in the averaged variables. It is assumed to satisfy the

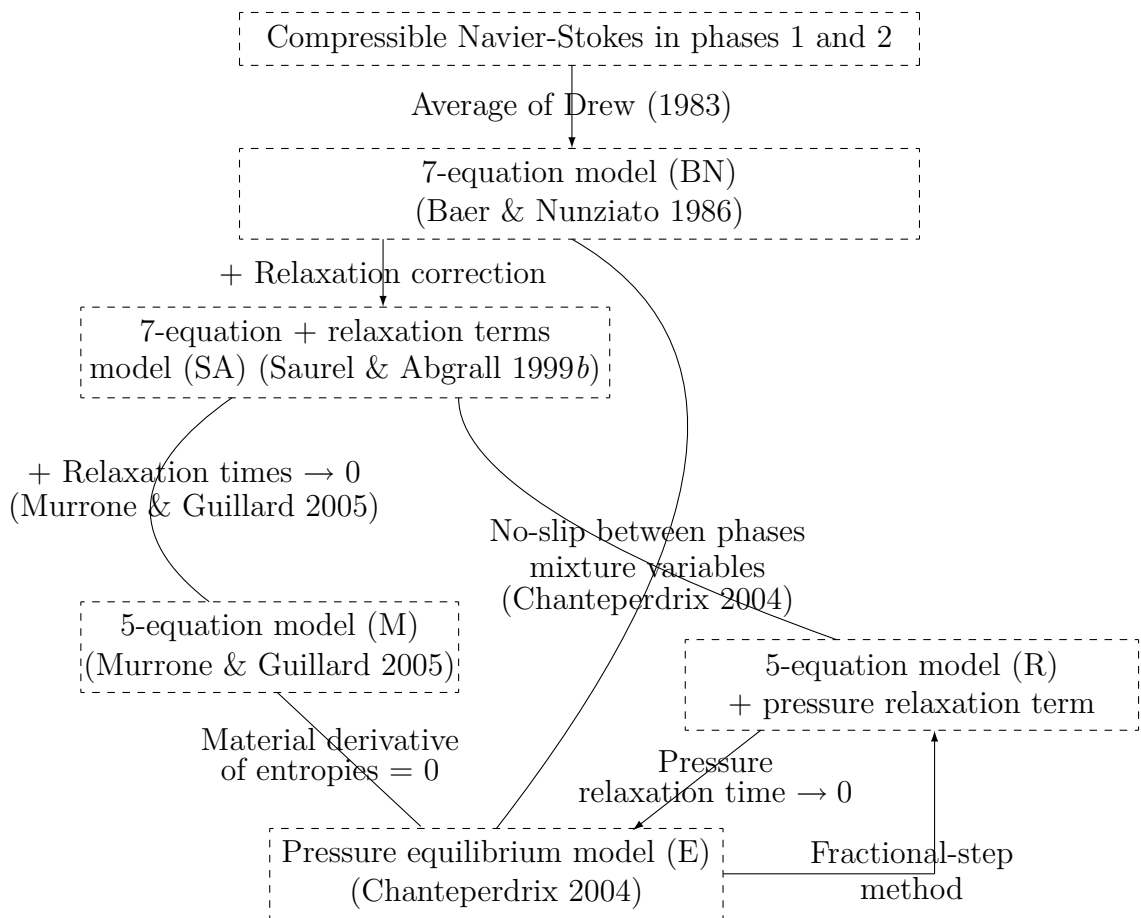


Figure 3.2: Diagram showing the path and stages for the derivation of the model.

following rules:

$$\begin{aligned}
\langle a + b \rangle &= \langle a \rangle + \langle b \rangle \\
\langle \langle a \rangle b \rangle &= \langle ab \rangle \\
\langle a \rangle &= a \\
\langle \frac{\partial a}{\partial t} \rangle &= \frac{\partial \langle a \rangle}{\partial t} \\
\langle \frac{\partial a}{\partial x_i} \rangle &= \frac{\partial \langle a \rangle}{\partial x_i}
\end{aligned} \tag{3.11}$$

Conservation equations (3.5) for phase k are only valid where phase k is present. In order to make them valid in the whole domain, we multiply them by X_k :

$$X_k \frac{\partial \rho_k}{\partial t} + X_k \nabla \cdot \rho_k \underline{V}_k = 0 \quad \text{Mass conservation} \tag{3.12}$$

$$X_k \frac{\partial \rho_k \underline{V}_k}{\partial t} + X_k \nabla \cdot \rho_k \underline{V}_k \otimes \underline{V}_k = X_k \nabla \cdot \underline{T}_k + X_k \rho_k \underline{f}_k \quad \text{Momentum conservation} \tag{3.13}$$

Then by using equation (3.9) and some algebra, one can make X_k enter the differential operators and one obtains:

$$\begin{aligned}
\frac{\partial X_k \rho_k}{\partial t} + \nabla \cdot X_k \rho_k \underline{V}_k &= \rho_k (\underline{V}_k - \underline{V}_i) \nabla \cdot X_k \\
\frac{\partial X_k \rho_k \underline{V}_k}{\partial t} + \nabla \cdot (X_k \rho_k \underline{V}_k \otimes \underline{V}_k) &= \nabla \cdot X_k \underline{T}_k + X_k \rho_k \underline{f}_k + (\rho_k \underline{V}_k (\underline{V}_k - \underline{V}_i) - \underline{T}_k) \cdot \nabla X_k
\end{aligned} \tag{3.14}$$

By averaging the transport equation for X_k (equation (3.9)), one obtains:

$$\frac{\partial \langle X_k \rangle}{\partial t} + \nabla \cdot \langle (\underline{V}_i X_k) \rangle = \langle X_k \nabla \cdot (\underline{V}_i) \rangle \tag{3.15}$$

and from the conservation equations (3.14), using the averaging operator one obtains:

$$\begin{aligned}
\frac{\partial \langle X_k \rho_k \rangle}{\partial t} + \nabla \cdot \langle X_k \rho_k \underline{V}_k \rangle &= \Gamma_k \\
\frac{\partial \langle X_k \rho_k \underline{V}_k \rangle}{\partial t} + \nabla \cdot \langle (X_k \rho_k \underline{V}_k \otimes \underline{V}_k) \rangle &= \nabla \cdot \langle X_k \underline{T}_k \rangle + \langle X_k \rho_k \underline{f}_k \rangle + \underline{M}_k
\end{aligned} \tag{3.16}$$

where the terms

$$\Gamma_k = \langle \rho_k (\underline{V}_k - \underline{V}_i) \nabla \cdot X_k \rangle \tag{3.17}$$

$$\underline{M}_k = \langle (\rho_k \underline{V}_k (\underline{V}_k - \underline{V}_i) - \underline{T}_k) \cdot \nabla X_k \rangle \tag{3.18}$$

are the interfacial source terms. They represent the creation of phase k in the macroscopic average volume due to the mass transfer across the interface at the microscopic scale. Thus the first of these terms represents phase changes and the second one represents the momentum transfers due to mass transfers.

Now before applying the averaging operator to the jump conditions (3.7), we multiply them by δ_i , using equation (3.10) and recognizing that $\underline{n}_1 = -\underline{n}_2 = \underline{n}$:

$$\begin{aligned} & \rho_1(\underline{V}_1 - \underline{V}_i) \cdot \nabla X_1 + \rho_2(\underline{V}_2 - \underline{V}_i) \cdot \nabla X_2 = 0 \\ (\rho_1 \underline{V}_1 (\underline{V}_1 - \underline{V}_i) - \underline{T}_1) \cdot \nabla X_1 + (\rho_2 \underline{V}_2 (\underline{V}_2 - \underline{V}_i) - \underline{T}_2) \cdot \nabla X_2 &= \sigma \kappa \nabla X_1 \end{aligned} \quad (3.19)$$

By applying the averaging operator to these equations and using (3.17) and (3.18) one obtains:

$$\begin{aligned} \sum_{k=1}^2 \Gamma_k &= 0 \\ \sum_{k=1}^2 \underline{M}_k &= \sigma \langle \kappa \nabla X_1 \rangle = \underline{M}_m \end{aligned} \quad (3.20)$$

\underline{M}_m is the force due to the surface tension at the interface.

Now let us defined the volume fraction of phase k :

$$\alpha_k = \langle X_k \rangle \quad (3.21)$$

At the macroscopic scale α_k can be interpreted as a "volume density of volume of fluid k " within the meaning of continuum mechanics:

$$V_k = \int_V \alpha_k dV \quad (3.22)$$

The fact that the fluids fill the whole volume of the domain results in the saturation constraint:

$$\sum_k \alpha_k = 1, \text{ at each point.} \quad (3.23)$$

Although the fluids considered are immiscible, the assumption is made that both fluids are present at each point of the domain. This means that neither α_1 nor α_2 can reach the value 0 or 1. This is a necessary condition for further developments using laws in which division by α_k are undertaken (e.g. equation (3.59)).

Under the assumption of immiscible fluids, leading to infinitely-thin interfaces, the volume fraction indicates exactly the volume effectively occupied by the corresponding fluid.

The volume fractions verify the following properties:

$$\left\langle \frac{\partial X_k}{\partial t} \right\rangle = \frac{\partial \alpha_k}{\partial t} \quad (3.24)$$

and

$$\langle \nabla X_k \rangle = \nabla \alpha_k \quad (3.25)$$

We also define the X_k -weighted average of a given magnitude A to be:

$$\tilde{A}_k = \frac{\langle X_k A \rangle}{\alpha_k} \quad (3.26)$$

and the mass-weighted average by:

$$\widehat{A}_k = \frac{\langle X_k \rho_k A \rangle}{\alpha_k \widetilde{\rho}} \quad (3.27)$$

Now by using equations (3.21) to (3.27) and accounting for the interfacial terms (3.17) and (3.18), the equation for the transport of function X_k (3.15) and conservation equations (3.16) become:

$$\begin{aligned} \frac{\partial \alpha_k}{\partial t} + \nabla \cdot \alpha_k \widetilde{V}_i &= \alpha_k \widetilde{\nabla \cdot (V_i)} \\ \frac{\partial \alpha_k \widetilde{\rho}_k}{\partial t} + \nabla \cdot \alpha_k \widetilde{\rho}_k \widetilde{V}_k &= \Gamma_k \\ \frac{\partial \alpha_k \widetilde{\rho}_k \widehat{V}_k}{\partial t} + \nabla \cdot (\alpha_k \widetilde{\rho}_k \widehat{V}_k \otimes \widehat{V}_k) &= \nabla \cdot \alpha_k \widetilde{T}_k + \alpha_k \widetilde{\rho}_k \widehat{f}_k + \underline{M}_k \end{aligned} \quad (3.28)$$

Now let us split the stress tensor \widetilde{T}_k into terms of pressure and extra stresses (viscous):

$$\underline{T}_k = -P_k \underline{I} + \tau_k \quad (3.29)$$

$$\widetilde{\underline{T}}_k = -\widetilde{P}_k \underline{I} + \widetilde{\tau}_k \quad (3.30)$$

We define the interfacial velocity of the k th phase $\underline{V}_{k,i}$ by:

$$\Gamma_k \underline{V}_{k,i} = \langle (\rho_k \underline{V}_k (\underline{V}_k - \underline{V}_i)) \cdot \nabla X_k \rangle \quad (3.31)$$

and the interfacial pressure of the k th phase by

$$P_{k,i} |\nabla \alpha_k|^2 = \langle P_k \nabla X_k \rangle \cdot \nabla \alpha_k \quad (3.32)$$

Then the term \underline{M}_k defined by equation (3.18) becomes:

$$\underline{M}_k = \Gamma_k \underline{V}_{k,i} - P_{k,i} \nabla \alpha_k + \underline{M}_k^d \quad (3.33)$$

where $\underline{M}_k^d = \langle (P_k - P_{k,i}) \nabla X_k - \tau_k \cdot \nabla X_k \rangle$ is the interfacial force density. In the following we neglect its contribution. The system (3.28) becomes:

$$\begin{aligned} \frac{\partial \alpha_k}{\partial t} + \nabla \cdot \alpha_k \widetilde{V}_i &= \alpha_k \widetilde{\nabla \cdot (V_i)} \\ \frac{\partial \alpha_k \widetilde{\rho}_k}{\partial t} + \nabla \cdot \alpha_k \widetilde{\rho}_k \widetilde{V}_k &= \Gamma_k \\ \frac{\partial \alpha_k \widetilde{\rho}_k \widehat{V}_k}{\partial t} + \nabla \cdot (\alpha_k \widetilde{\rho}_k \widehat{V}_k \otimes \widehat{V}_k + \alpha_k \widetilde{P}_k \underline{I}) &= \nabla \cdot (\alpha_k \widetilde{\tau}_k) + \alpha_k \widetilde{\rho}_k \widehat{f}_k + \Gamma_k \underline{V}_{k,i} - P_{k,i} \nabla \alpha_k \end{aligned} \quad (3.34)$$

Let us notice that, as $\alpha_2 = 1 - \alpha_1$, the first equation of system (3.34) written for phase 2 reads:

$$\frac{\partial \alpha_1}{\partial t} - \nabla \cdot \widetilde{V}_i + \nabla \cdot \alpha_1 \widetilde{V}_i = -\widetilde{\nabla \cdot (V_i)} + \alpha_1 \widetilde{\nabla \cdot (V_i)} \quad (3.35)$$

then by using the same equation written for phase 1, one obtains:

$$\widehat{\nabla \cdot (\underline{V}_i)} = \nabla \cdot \widetilde{\underline{V}_i} \quad (3.36)$$

Thus when considering the two-phase system (3.34) reads:

$$\begin{aligned} \frac{\partial \alpha_1}{\partial t} + \widetilde{\underline{V}_i} \nabla \cdot \alpha_1 &= 0 \\ \frac{\partial \alpha_1 \widetilde{\rho}_1}{\partial t} + \nabla \cdot \alpha_1 \widetilde{\rho}_1 \widetilde{\underline{V}_1} &= \Gamma_1 \\ \frac{\partial \alpha_2 \widetilde{\rho}_2}{\partial t} + \nabla \cdot \alpha_2 \widetilde{\rho}_2 \widetilde{\underline{V}_2} &= \Gamma_2 \\ \frac{\partial \alpha_1 \widetilde{\rho}_1 \widetilde{\underline{V}_1}}{\partial t} + \nabla \cdot (\alpha_1 \widetilde{\rho}_1 \widetilde{\underline{V}_1} \otimes \widetilde{\underline{V}_1} + \alpha_1 \widetilde{P}_1 \underline{I}) &= \nabla \cdot (\alpha_1 \widetilde{\tau}_1) + \alpha_1 \widetilde{\rho}_1 \widetilde{\underline{f}_1} + \Gamma_1 \underline{V}_{1,i} - P_{1,i} \nabla \alpha_1 \\ \frac{\partial \alpha_2 \widetilde{\rho}_2 \widetilde{\underline{V}_2}}{\partial t} + \nabla \cdot (\alpha_2 \widetilde{\rho}_2 \widetilde{\underline{V}_2} \otimes \widetilde{\underline{V}_2} + \alpha_2 \widetilde{P}_2 \underline{I}) &= \nabla \cdot (\alpha_2 \widetilde{\tau}_2) + \alpha_2 \widetilde{\rho}_2 \widetilde{\underline{f}_2} + \Gamma_2 \underline{V}_{2,i} - P_{2,i} \nabla \alpha_2 \end{aligned} \quad (3.37)$$

From here average symbols are omitted for clarity. We assume that $P_{1,i} = P_{2,i}$. With the additional assumption that there is no mass transfer at the interface (no phase change), system (3.37) reads:

$$(BN) \left\{ \begin{aligned} \frac{\partial \alpha_1}{\partial t} + \underline{V}_i \nabla \cdot \alpha_1 &= 0 \\ \frac{\partial \alpha_1 \rho_1}{\partial t} + \nabla \cdot \alpha_1 \rho_1 \underline{V}_1 &= 0 \\ \frac{\partial \alpha_2 \rho_2}{\partial t} + \nabla \cdot \alpha_2 \rho_2 \underline{V}_2 &= 0 \\ \frac{\partial \alpha_1 \rho_1 \underline{V}_1}{\partial t} + \nabla \cdot (\alpha_1 \rho_1 \underline{V}_1 \otimes \underline{V}_1 + \alpha_1 P_1 \underline{I}) &= \\ &P_i \nabla \alpha_1 + \nabla \cdot (\alpha_1 \tau_1) + \alpha_1 \rho_1 \underline{f}_1 \\ \frac{\partial \alpha_2 \rho_2 \underline{V}_2}{\partial t} + \nabla \cdot (\alpha_2 \rho_2 \underline{V}_2 \otimes \underline{V}_2 + \alpha_2 P_2 \underline{I}) &= \\ &-P_i \nabla \alpha_2 + \nabla \cdot (\alpha_2 \tau_2) + \alpha_2 \rho_2 \underline{f}_2 \end{aligned} \right. \quad (3.38)$$

This model with the energy conservation equations (7 equations) was proposed by Baer & Nunziato (1986).

Then Saurel & Abgrall (1999b), from a case of multi-shock problems presenting multidimensional interfaces, showed that model (BN) (3.38) leads to an incorrect representation of relaxation processes. They also showed that model (BN) is not closed for problems with an interface separating two pure fluids and similarly for problems with an interface separating a two-phase mixture and a pure-fluid zone, which is of interest here. Thus model (BN) is ill adapted as it does not represent well relaxation phenomena behind shocks and pressure waves in two-phase mixtures and interface conditions between pure fluids or mixtures. Therefore correction terms must be added to the system (3.38) in order to represent the relaxation processes behind shocks and pressure waves and to restore boundary conditions at the interface. This closure procedure is presented in section 3.4.3.

3.4.3 Model closure: Relaxation terms

Saurel & Abgrall (1999b) proposed to add correction terms in the transport equation for α and in the momentum conservation equations in order to restore boundary conditions at the interface, and to account for relaxation processes behind shocks or pressure waves. Then model (BN) (equations (3.38)) reads:

$$(SA) \left\{ \begin{array}{l} \frac{\partial \alpha_1}{\partial t} + \underline{V}_i \nabla \cdot \alpha_1 = \frac{P_2 - P_1}{\epsilon} \quad (3.39) \\ \frac{\partial \alpha_1 \rho_1}{\partial t} + \nabla \cdot (\alpha_1 \rho_1 \underline{V}_1) = 0 \quad (3.40) \\ \frac{\partial \alpha_2 \rho_2}{\partial t} + \nabla \cdot (\alpha_2 \rho_2 \underline{V}_2) = 0 \quad (3.41) \\ \frac{\partial \alpha_1 \rho_1 \underline{V}_1}{\partial t} + \nabla \cdot (\alpha_1 \rho_1 \underline{V}_1 \otimes \underline{V}_1 + \alpha_1 P_1 \underline{I}) = \\ \quad P_i \nabla \alpha_1 + \nabla \cdot (\alpha_1 \tau_1) + \alpha_1 \rho_1 \underline{f}_1 + \frac{V_2 - V_1}{\zeta} \quad (3.42) \\ \frac{\partial \alpha_2 \rho_2 \underline{V}_2}{\partial t} + \nabla \cdot (\alpha_2 \rho_2 \underline{V}_2 \otimes \underline{V}_2 + \alpha_2 P_2 \underline{I}) = \\ \quad -P_i \nabla \alpha_2 + \nabla \cdot (\alpha_2 \tau_2) + \alpha_2 \rho_2 \underline{f}_2 - \frac{V_2 - V_1}{\zeta} \quad (3.43) \end{array} \right.$$

where $\frac{1}{\epsilon}$ and $\frac{1}{\zeta}$ are the relaxation parameters (relaxation speeds). $\frac{1}{\epsilon}$ is called the "dynamic compaction viscosity". While the pressures in phase 1 and 2 are controlled by appropriate equations of state that will be detailed further, the pressure P_i and the velocity \underline{V}_i represent the average values of the pressure and the velocity at the interface over the control volume. Both must be modelled.

However such models must lead to a well posed hyperbolic problem. There are several models proposed in the literature. For a review see (Saurel & Abgrall 1999b). It was chosen in SLOSH to use the modelling of Saurel & Abgrall (1999b) who consider that the averaged interface pressure P_i is equal to the "mixture pressure":

$$P_i = \alpha_1 P_1 + \alpha_2 P_2 \quad (3.44)$$

and that the averaged interface velocity \underline{V}_i is equal to the velocity of the center of mass:

$$\underline{V}_i = \sum_{k=1}^2 \alpha_k \rho_k \underline{V}_k / \sum_{k=1}^2 \alpha_k \rho_k \quad (3.45)$$

However in many physical situations and particularly the ones of interest in this work, it is reasonable to assume that pressure tends to equilibrium instantaneously, which corresponds to ϵ and ζ tending towards zero. Thus the solution is computed by first making it evolve over time by the strictly hyperbolic part of the system, which is the system without the relaxation terms, and then followed by a relaxation step. But this numerical procedure will be detailed further in section 3.5.2. This is completely different to assuming pressure equilibrium in the original equations and trying to solve

such equations because the corresponding system would not be hyperbolic (Saurel & Abgrall 1999b).

In the sequel to this, Murrone & Guillard (2005) conducted an asymptotic study of model (SA) (equations (3.39) to (3.43)) for relaxation times tending towards zero. This asymptotic study results in the following reduced system:

$$(M) \left\{ \begin{array}{l} \frac{\partial \alpha_1}{\partial t} + \underline{V} \nabla \cdot \alpha_1 = \alpha(1 - \alpha) \frac{\rho_2 c_2^2 - \rho_1 c_1^2}{\alpha \rho_2 c_2^2 + (1 - \alpha) \rho_1 c_1^2} \nabla \cdot \underline{V} \quad (3.46) \\ \frac{\partial \alpha_1 \rho_1}{\partial t} + \nabla \cdot \alpha_1 \rho_1 \underline{V}_1 = 0 \quad (3.47) \\ \frac{\partial \alpha_2 \rho_2}{\partial t} + \nabla \cdot \alpha_2 \rho_2 \underline{V}_2 = 0 \quad (3.48) \\ \frac{\partial \rho \underline{V}}{\partial t} + \nabla \cdot (\rho \underline{V} \otimes \underline{V} + P \underline{I}) = \nabla \cdot (\alpha_1 \tau_1 + \alpha_2 \tau_2) + \alpha_1 \rho_1 \underline{f}_1 + \alpha_2 \rho_2 \underline{f}_2 \quad (3.49) \end{array} \right.$$

We call this set of equations model (M). In this model there is only one pressure, because P_1 and P_2 are relaxed to a common value, and similarly there is a unique velocity \underline{V} . The procedure to obtain model (M) is similar to the one used by Kapila, Menikoff, Bdzil, Son & Stewart (2001). Massoni, Saurel, Nkonga & Abgrall (2002) and Allaire, Clerc & Kokh (2002) derived a similar form of the multifluid model but the transport equation for the volume fraction had a zero right side ($\frac{\partial \alpha_1}{\partial t} + \underline{V}_i \nabla \cdot \alpha_1 = 0$). Murrone & Guillard (2005) specified that the transport equation for α with a zero right side is not compatible with the isentropic constraint along material trajectories for each phase $Ds_k/Dt = 0$.

3.4.4 Another derivation path from model (BN)

Model (M) of (3.49) can also be obtained by undertaking another derivation proposed by Chantepredrix (2004).

The asymptotic study of Murrone & Guillard (2005) where the velocity relaxation time tends to zero corresponds to the assumption of no-slip between phases. This means that we can note the common velocity $\underline{V} = \underline{V}_1 = \underline{V}_2$ and introduce it in model (BN) (equations (3.38)). This is a strong assumption that implies that for instance in the case of gas bubbles dispersed in a liquid, the bubbles cannot rise because of the Archimede effect.

Concerning the pressures, assuming that the relaxation times tend towards zero corresponds to the assumption that pressures in both phases are instantaneously equal, so it means that:

$$P_1 = P_2 \quad (3.50)$$

This second assumption implies that in the case of gas bubbles dispersed in a liquid, the model does not account for acoustical effect in bubbles.

Another derivation path rejoining model (M) can be taken by applying these assumptions directly into model (BN) (3.38) instead of through the asymptotic study of (Murrone & Guillard 2005) (see figure 3.2).

Hence from the system (3.38) we directly assume no-slip between phases so we set $\underline{V} = \underline{V}_1 = \underline{V}_2$ and we sum the two momentum balance equations:

$$\begin{aligned}
\frac{\partial \alpha_1}{\partial t} + \underline{V} \nabla \cdot \alpha_1 &= 0 \\
\frac{\partial \alpha_1 \rho_1}{\partial t} + \nabla \cdot \alpha_1 \rho_1 \underline{V} &= 0 \\
\frac{\partial \alpha_2 \rho_2}{\partial t} + \nabla \cdot \alpha_2 \rho_2 \underline{V} &= 0 \\
\frac{\partial (\alpha_1 \rho_1 + \alpha_2 \rho_2) \underline{V}}{\partial t} + \nabla \cdot ((\alpha_1 \rho_1 + \alpha_2 \rho_2) \underline{V} \otimes \underline{V} + (\alpha_1 P_1 + \alpha_2 P_2) \underline{I}) &= \\
&= \nabla \cdot (\alpha_1 \underline{\tau}_1 + \alpha_2 \underline{\tau}_2) + \alpha_1 \rho_1 \underline{f}_1 + \alpha_2 \rho_2 \underline{f}_2
\end{aligned} \tag{3.51}$$

The "mixture density" naturally appears in the conservation equations, it reads:

$$\rho = \alpha_1 \rho_1 + \alpha_2 \rho_2 \tag{3.52}$$

Although there is no effective "mixture" at the continuum level as long as fluids are immiscible, ρ is called here by abuse *volume density of mass of mixture* and obeys $\frac{\partial \rho}{\partial t} + \nabla \cdot (\rho \underline{V}) = 0$. But this single variable is not sufficient, as the pressure will depend on both densities ρ_1 and ρ_2 . Therefore one will keep both mass conservation equations in the model, one for each fluid. Let us notice that this model degenerates into one-fluid equations at locations where the volume fraction tends to 0 or 1. Laws like equation (3.52) are called by abuse "mixture laws" even if there is no real "mixture" at the microscopic scale, because they are the expression of magnitudes that are common to both fluids in function of the corresponding magnitudes of each fluid.

From now on the model (3.51) can be rewritten:

$$\frac{\partial \alpha_1}{\partial t} + \underline{V} \nabla \cdot \alpha_1 = 0 \tag{3.53}$$

$$\frac{\partial \alpha_1 \rho_1}{\partial t} + \nabla \cdot \alpha_1 \rho_1 \underline{V} = 0 \tag{3.54}$$

$$\frac{\partial \alpha_2 \rho_2}{\partial t} + \nabla \cdot \alpha_2 \rho_2 \underline{V} = 0 \tag{3.55}$$

$$\frac{\partial \rho \underline{V}}{\partial t} + \nabla \cdot (\rho \underline{V} \otimes \underline{V} + (\alpha_1 P_1 + \alpha_2 P_2) \underline{I}) = \nabla \cdot (\alpha_1 \underline{\tau}_1 + \alpha_2 \underline{\tau}_2) + \alpha_1 \rho_1 \underline{f}_1 + \alpha_2 \rho_2 \underline{f}_2 \tag{3.56}$$

The assumption of no slip between phases has allowed to write a single equation of momentum balance, in which:

$$P = \alpha P_1 + (1 - \alpha) P_2 \tag{3.57}$$

is the "mixture pressure", P_1 is the pressure in fluid 1 and P_2 is the pressure in fluid 2.

From now on we define the following conservative variable for lighter notation:

$$\tilde{\rho}_k \equiv \alpha_k \rho_k \tag{3.58}$$

In consequence when developing the equations of state the chosen closure law for mixture pressure reads:

$$P(\tilde{\rho}_1, \tilde{\rho}_2) = \alpha P_1\left(\frac{\tilde{\rho}_1}{\alpha}\right) + (1 - \alpha) P_2\left(\frac{\tilde{\rho}_2}{1 - \alpha}\right) \quad (3.59)$$

Then the model (3.56) becomes:

$$\frac{\partial \alpha_1}{\partial t} + \underline{V} \nabla \cdot \alpha_1 = 0 \quad (3.60)$$

$$\frac{\partial \alpha_1 \rho_1}{\partial t} + \nabla \cdot \alpha_1 \rho_1 \underline{V} = 0 \quad (3.61)$$

$$\frac{\partial \alpha_2 \rho_2}{\partial t} + \nabla \cdot \alpha_2 \rho_2 \underline{V} = 0 \quad (3.62)$$

$$\frac{\partial \rho \underline{V}}{\partial t} + \nabla \cdot (\rho \underline{V} \otimes \underline{V} + (P) \underline{I}) = \nabla \cdot (\alpha_1 \tau_1 + \alpha_2 \tau_2) + \alpha_1 \rho_1 \underline{f}_1 + \alpha_2 \rho_2 \underline{f}_2 \quad (3.63)$$

It is worth mentioning P_1 and P_2 are not "partial pressures". However, the pressure P_1 (respectively P_2) is only defined in zones where fluid 1 (respectively fluid 2) is present. Therefore it is necessary to extend its definition at points where fluid 1 (resp. fluid 2) is absent in order to be able to compute the mixture pressure. In such zones, we choose to set the value of pressure of the absent fluid to the value of pressure of the present fluid. In other words, where fluid 1 is absent we set P_1 to P_2 and where fluid 2 is absent we set P_2 to P_1 , i.e. we set:

$$P_1 = P_2 \text{ everywhere in the domain.} \quad (3.64)$$

The choice of closure for pressure in equation (3.64) is arbitrary and another one could have been made, but it leads to convenient mathematical properties of the model such as hyperbolicity. Moreover, it corresponds to the minimization of total energy (see section A.3 for details) and it corresponds to the derivation of model (M), which is based on a pressure relaxation speed tending towards infinity. The influence of pressure closures on mathematical properties of such models have been studied by Coquel, Gallouët, Hérard & Seguin (2002).

Then the unknown $\alpha = \alpha(\tilde{\rho}_1, \tilde{\rho}_2)$ is controlled by equation (3.64). It is the variable used to compute the pressures. For this purpose the equilibrium relationship between the two pressures described above is used to compute α instead of the transport equation in the system. Therefore α is the solution of:

$$P_1\left(\frac{\tilde{\rho}_1}{\alpha}\right) = P_2\left(\frac{\tilde{\rho}_2}{1 - \alpha}\right) \quad (3.65)$$

where $\tilde{\rho}_1$ and $\tilde{\rho}_2$ are constant.

The model (3.63) can now be written:

$$(E) \left\{ \begin{array}{l} P_1\left(\frac{\tilde{\rho}_1}{\alpha}\right) = P_2\left(\frac{\tilde{\rho}_2}{\alpha_2}\right) \quad (3.66) \\ \frac{\partial \alpha_1 \rho_1}{\partial t} + \nabla \cdot \alpha_1 \rho_1 \underline{V} = 0 \quad (3.67) \\ \frac{\partial \alpha_2 \rho_2}{\partial t} + \nabla \cdot \alpha_2 \rho_2 \underline{V} = 0 \quad (3.68) \\ \frac{\partial \rho \underline{V}}{\partial t} + \nabla \cdot (\rho \underline{V} \otimes \underline{V} + (P) \underline{I}) = \nabla \cdot (\alpha_1 \tau_1 + \alpha_2 \tau_2) + \alpha_1 \rho_1 \underline{f}_1 + \alpha_2 \rho_2 \underline{f}_2 \quad (3.69) \end{array} \right.$$

This is model (E) ("E" stands for the "equilibrium" $P_1 = P_2$). This is the model that is implemented in the original version of the SLOSH code. However another model will be introduced within the process of numerical resolution of (E). This will be detailed in section 3.5.

Equation (3.65) admits a unique solution α for each couple $(\tilde{\rho}_1, \tilde{\rho}_2)$ whatever the equations of state $P_k(\rho_k)$ as long as they verify a few non-restrictive assumptions (regular enough, convexes and increasing). α thus is defined implicitly as a function of $\tilde{\rho}_1$ and $\tilde{\rho}_2$, which are two of the conservative variables of the system.

Let us remark that the equilibrium between pressures (equation (3.66)) can lead to a partial derivative equation for α . Indeed Murrone & Guillard (2005) demonstrates that from equilibrium (3.66) and by assuming $Ds_k/Dt = 0$, one can find the following transport equation for the volume fraction:

$$\frac{\partial \alpha}{\partial t} + \underline{V} \cdot \nabla \alpha = \alpha(1 - \alpha) \frac{\rho_2 c_2^2 - \rho_1 c_1^2}{\alpha \rho_2 c_2^2 + (1 - \alpha) \rho_1 c_1^2} \nabla \cdot \underline{V} \quad (3.70)$$

However in the models we manipulate in this work no energy conservation equation is accounted for, so this demonstration is made explicit without considering the entropy in appendix A.1. This demonstration proposed by (Chanteperdrix 2004) proves the existence and uniqueness of the solution of the pressure equilibrium equation (3.66) and introduces the partial derivative equation (3.70). Equation (3.70) is the transport equation that is in model (M)(equation (3.46)).

The most general feature of this remark is that from model (E) one can derive model (M) of Murrone & Guillard (2005) by assuming that the material derivative of the phase entropies are zero. This is illustrated in the scheme in figure 3.2.

3.4.5 Mixture dynamic viscosity

In model (E), the momentum conservation equation contains the viscous stress tensor of fluid 1 and fluid 2 τ_1 and τ_2 .

Assuming that each fluid behaves like a Newtonian fluid and neglecting the associated "viscosity coefficient of Lamé", one can assume that their viscous stress tensor is proportional to the strain tensor, which is the symmetric part of the velocity field gradient:

$$\tau_k = \mu_k \left(\nabla \underline{V} + {}^t \nabla \underline{V} \right) \quad (3.71)$$

where μ_k is the dynamic viscosity of fluid 1.

Now we choose to introduce what we call the "mixture dynamic viscosity" μ , which reads:

$$\mu = \alpha\mu_1 + (1 - \alpha)\mu_2 \quad (3.72)$$

With this definition model (E) (equations (3.66) to (3.69)) can be rewritten:

$$P_1\left(\frac{\tilde{\rho}_1}{\alpha}\right) = P_2\left(\frac{\tilde{\rho}_2}{\alpha_2}\right) \quad (3.73)$$

$$\frac{\partial\alpha_1\rho_1}{\partial t} + \nabla \cdot \alpha_1\rho_1\underline{V} = 0 \quad (3.74)$$

$$\frac{\partial\alpha_2\rho_2}{\partial t} + \nabla \cdot \alpha_2\rho_2\underline{V} = 0 \quad (3.75)$$

$$\frac{\partial\rho\underline{V}}{\partial t} + \nabla \cdot (\rho\underline{V} \otimes \underline{V} + P\underline{I}) = \nabla \cdot (\mu(\nabla\underline{V} + {}^t\nabla\underline{V})) + \alpha_1\rho_1\underline{f}_1 + \alpha_2\rho_2\underline{f}_2 \quad (3.76)$$

Let us remark that this choice for modeling the mixture dynamic viscosity is not the only one possible. Others could have been made, like for instance $\mu = \rho\nu = \alpha_1\rho_1\nu_1 + \alpha_2\rho_2\nu_2$ based on kinematic viscosities ν_1 and ν_2 of fluids 1 and 2 and on the "mixture kinematic viscosity" $\nu = \mu/\rho$.

However this *mixture dynamic viscosity* μ and others are tested on simple isothermal test cases by Jamet, Vila, Villedieu & Chantepedrix (2003) but the results do not shed light on whether to choose one particular model or another.

3.4.6 External forces

The external volume forces terms \underline{f}_k include gravity acceleration \underline{g} and a volume density of capillary forces \underline{f}_c . However, although the capillary effects are available in the code, they will not be taken into account in the simulations presented in this work because for the physical processes we investigate they are negligible. Therefore the momentum source term only reads:

$$\underline{f}_k = \underline{g} \quad (3.77)$$

Now model (E) reads:

$$P_1\left(\frac{\tilde{\rho}_1}{\alpha}\right) = P_2\left(\frac{\tilde{\rho}_2}{1 - \alpha}\right) \quad (3.78)$$

$$\frac{\partial\alpha_1\rho_1}{\partial t} + \nabla \cdot \alpha_1\rho_1\underline{V} = 0 \quad (3.79)$$

$$\frac{\partial\alpha_2\rho_2}{\partial t} + \nabla \cdot \alpha_2\rho_2\underline{V} = 0 \quad (3.80)$$

$$\frac{\partial\rho\underline{V}}{\partial t} + \nabla \cdot (\rho\underline{V} \otimes \underline{V} + P\underline{I}) = \nabla \cdot (\mu(\nabla\underline{V} + {}^t\nabla\underline{V})) + \rho\underline{g} \quad (3.81)$$

Mathematical properties of model (E) can be found in appendix A.2.

3.5 Numerical method

3.5.1 Relaxation model (R)

Model (E) is a model in which the relaxation process regarding pressure is assumed to be instantaneous. Although model (E) has already quite good properties for numerical implementation (hyperbolicity and existence of Lax entropy), Chantepredrix (2004) introduces another model, model (R) whose solutions are very close to the ones of model (E). Model (R) is easier to numerically implement because it has the advantage of leading to a simple Riemann problem whereas the Riemann problem associated to model (E) would be very difficult to solve. This feature of model (R) allows us to use an exact Godunov scheme for its numerical implementation, which is one of the most robust non-centered schemes. The Godunov scheme will be presented in section 3.5.2.2.

In order to introduce this model (R), we go back over model (SA) of Saurel & Abgrall (1999b) (equations (3.39) to (3.43)) and we assume that the pressure relaxation time is not zero but that the velocity relaxation time is zero (no-slip between phases), so there is a unique velocity field. We also introduce mixture density $\rho = \alpha_1\rho_1 + \alpha_2\rho_2$, mixture pressure $P = \alpha_1P_1 + \alpha_2P_2$, mixture dynamic viscosity $\mu = \alpha_1\mu_1 + \alpha_2\mu_2$ and use the model in the equation (3.71) for stress tensor. Then we obtain the following equations:

$$(R) \left\{ \begin{array}{l} \frac{\partial \alpha_1}{\partial t} + \underline{V} \nabla \cdot \alpha_1 = \frac{P_2 - P_1}{\epsilon} \quad (3.82) \\ \frac{\partial \alpha_1 \rho_1}{\partial t} + \nabla \cdot \alpha_1 \rho_1 \underline{V} = 0 \quad (3.83) \\ \frac{\partial \alpha_2 \rho_2}{\partial t} + \nabla \cdot \alpha_2 \rho_2 \underline{V} = 0 \quad (3.84) \\ \frac{\partial \rho \underline{V}}{\partial t} + \nabla \cdot (\rho \underline{V} \otimes \underline{V} + P \underline{I}) = \nabla \cdot (\mu (\nabla \underline{V} + {}^t \nabla \underline{V})) + \rho \underline{g} \quad (3.85) \end{array} \right.$$

where $\frac{1}{\epsilon}$ is the "relaxation speed". We call this set of equations model (R). "R" stands for "relaxation". The reader will notice that this model is similar to model (SA) with a unique velocity field. For model (R) to have the same solutions than model (E), this parameter will be intended to tend to infinity so that relaxation is instantaneous.

To convince oneself of the natural relationship that exists between the models (E) and (R), one can notice that by multiplying equation (3.82) by ϵ and by making it tend to 0, one exactly meets the pressure-equilibrium equation $P_1 = P_2$, which defines the equilibrium volume fraction α .

Considering the mass conservation equations (3.83) and (3.84), equation (3.82) can be written:

$$\frac{\partial \rho \alpha}{\partial t} + \nabla \cdot (\rho \alpha \underline{V}) = \rho \frac{P_1 - P_2}{\epsilon} \quad (3.86)$$

Although it looks like a balance equation, it cannot be interpreted as such because it is difficult to give a precise meaning to $\rho \alpha$.

Mathematical properties of model (R) can be found in appendix A.3. The solutions of model (R) are shown to be close to the solution of model (E) in appendix A.4.

This is model (R) that is used for discretization and implementation in the code.

3.5.2 Numerical scheme for the hyperbolic part of the model: Fractional-step method

3.5.2.1 Principle

The relaxation model (R) is solved according to the relaxation scheme as proposed by Saurel & Abgrall (1999a). This is a "fractional-step" method. This means that the time step for the resolution of model (R) is divided into two steps. Firstly there is a transport step to transport the conservative variables omitting the relaxation term in the equation for α (3.82). This is the equivalent to temporarily considering that the relaxation time is infinite or that the relaxation process is "paused". Secondly, the solution obtained at the first step is "relaxed" towards the pressure equilibrium. This restores the pressure equilibrium. Now this is equivalent to considering that the relaxation time becomes zero. In this step the equations that are solved are the one of model (R) with no momentum source terms and for which ϵ tends to zero. To sum up, solving (R) with this fractional-step method amounts to solving an approximation of model (E) firstly by considering an infinite relaxation time and transporting the variables and secondly by considering a zero relaxation time. Finally, the approximation we make is that the global relaxation time is equal to the time step. So this method is only accurate for small time steps. This is not limiting because as the numerical methods for the source terms are explicit and the model compressible, the time step will be small anyway. Let us remark that for a second order Runge-Kutta method the fractional method is repeated twice in each time step.

3.5.2.2 Transport step

During this step the system of conservation equations associated to model (R) is integrated considering the source terms from volume forces, viscous effects and capillary effects. However, the relaxation source term in equation (3.82) is not taken into account in this step. This is the equivalent to considering an infinite relaxation time (or a zero relaxation speed). The system that has to be integrated is thus a system of balance equations in the form:

$$\frac{\partial W}{\partial t} + \frac{\partial F}{\partial x} + \frac{\partial G}{\partial y} + \frac{\partial H}{\partial z} = S \quad (3.87)$$

$W = {}^t (\rho\alpha, \tilde{\rho}_1, \tilde{\rho}_2, \rho u, \rho v, \rho w)$ being the vector of conservative variables, F the vector flux along x , G the flux along y , H the flux along z and S the source term, which only has components in the equations of momentum balance:

$$S = S^{visc} + S^{surfens} + S^{ext} = \nabla \cdot (\tau^D + \tau^C) + \rho(g - \gamma_e) \quad (3.88)$$

This leads to the resolution of a system of conservation laws for the variables W , using the finite volume method over a cartesian grid (SLOSH is able to deal with

unstructured grid but for sake of simplicity we present the methods for a cartesian grid):

$$C_{i,j,k} = [x_{i-\frac{1}{2}}, x_{i+\frac{1}{2}}] \times [y_{j-\frac{1}{2}}, y_{j+\frac{1}{2}}] \times [z_{k-\frac{1}{2}}, z_{k+\frac{1}{2}}] \quad (3.89)$$

The numerical unknowns are $w_{i,j,k}$ defined by the volume-averaged continuous variables:

$$w_{i,j,k} = \frac{1}{|C_{i,j,k}|} \int_{C_{i,j,k}} W dV \quad (3.90)$$

Plus the quantity $S_{i,j,k}$ is defined as:

$$S_{i,j,k} = \frac{1}{|C_{i,j,k}|} \int_{C_{i,j,k}} S dV \quad (3.91)$$

The volume integration of the system (3.87) using Ostrogradski theorem leads to the following semi-discrete scheme:

$$\frac{\partial w_{i,j,k}}{\partial t} + \sum_{faces} \frac{1}{|C_{i,j,k}|} \int_{face} (F\mathbf{e}_x + G\mathbf{e}_y + H\mathbf{e}_z) \cdot \mathbf{n}_{face} dS \quad (3.92)$$

where the sum \sum_{faces} refers to the faces of the cell $C_{i,j,k}$ and where the integral \int_{face} concerns each one of these faces. By setting these fluxes to be constant over a face, one obtains:

$$\int_{face} (F\mathbf{e}_x + G\mathbf{e}_y + H\mathbf{e}_z) \cdot \mathbf{n}_{face} dS \approx (f\mathbf{e}_x + g\mathbf{e}_y + h\mathbf{e}_z) \cdot \mathbf{n}_{face} |F| \quad (3.93)$$

where f , g , h are numerical flux functions depending on the unknowns $w_{i,j,k}$ in the cells on both sides of the considered face. In the case of a structured grid this leads to:

$$\frac{\partial w_{i,j,k}}{\partial t} = S_{i,j,k} - \left(\frac{f_{i+\frac{1}{2},j,k} - f_{i-\frac{1}{2},j,k}}{\Delta x_i} + \frac{g_{i,j+\frac{1}{2},k} - g_{i,j-\frac{1}{2},k}}{\Delta y_j} + \frac{h_{i,j,k+\frac{1}{2}} - h_{i,j,k-\frac{1}{2}}}{\Delta z_k} \right) \quad (3.94)$$

where Δx_i , Δy_j and Δz_k are the (non constant) local space steps in each direction and where $f_{p,j,k}$ refers to the flux through the face of abscissa x_p on the j th line of the grid. The fluxes $f_{i+\frac{1}{2},j,k}$, $g_{i,j+\frac{1}{2},k}$ and $h_{i,j,k+\frac{1}{2}}$ through considered faces located respectively at $i + \frac{1}{2}$, $j + \frac{1}{2}$ and $k + \frac{1}{2}$ are numerically approximated by the numerical flux functions $f(w_{i,j,k}, w_{i+1,j,k})$, $g(w_{i,j,k}, w_{i,j+1,k})$ and $h(w_{i,j,k}, w_{i,j,k+1})$, which depend on the states in the cells on both sides of the considered faces. These flux functions are detailed further.

Time scheme The scheme on which relies the time progression from w^n to w^{n+1} according to the equation (3.94) is the Two-step Runge Kutta scheme:

$$\begin{aligned} w_{i,j,k}^{n+\frac{1}{2}} &= w_{i,j,k}^n + \frac{\Delta t^n}{2} S_{i,j,k}^n - \frac{\Delta t^n}{2} \left(\frac{f_{i+\frac{1}{2},j,k}^n - f_{i-\frac{1}{2},j,k}^n}{\Delta x_i} + \frac{g_{i,j+\frac{1}{2},k}^n - g_{i,j-\frac{1}{2},k}^n}{\Delta y_j} + \frac{h_{i,j,k+\frac{1}{2}}^n - h_{i,j,k-\frac{1}{2}}^n}{\Delta z_k} \right) \\ w_{i,j,k}^{n+1} &= w_{i,j,k}^n + \Delta t^n S_{i,j,k}^{n+\frac{1}{2}} - \Delta t^n \left(\frac{f_{i+\frac{1}{2},j,k}^{n+\frac{1}{2}} - f_{i-\frac{1}{2},j,k}^{n+\frac{1}{2}}}{\Delta x_i} + \frac{g_{i,j+\frac{1}{2},k}^{n+\frac{1}{2}} - g_{i,j-\frac{1}{2},k}^{n+\frac{1}{2}}}{\Delta y_j} + \frac{h_{i,j,k+\frac{1}{2}}^{n+\frac{1}{2}} - h_{i,j,k-\frac{1}{2}}^{n+\frac{1}{2}}}{\Delta z_k} \right) \end{aligned} \quad (3.95)$$

where $\Delta t^n = t_{n+1} - t_n$ is the time step calculated at each iteration using the following CFL condition:

$$\Delta t^n = CFL \min_{i,j} \left(\frac{\Delta x_i}{|u_{i,j,k}| + c_{i,j,k}}, \frac{\Delta y_i}{|v_{i,j,k}| + c_{i,j,k}}, \frac{\Delta z_i}{|w_{i,j,k}| + c_{i,j,k}} \right) \quad (3.96)$$

with $u_{i,j,k}$ (respectively $v_{i,j,k}$, respectively $w_{i,j,k}$) the velocity along x (respectively y , respectively z) in the cell $C_{i,j,k}$, $c_{i,j,k}$ the local speed of sound, and CFL a constant.

Note: The source terms will be treated thanks to an explicit scheme.

Space scheme First it is important to consider a scheme that ensures masses positivity. Now an exact scheme on stationary contact discontinuities, in line with a grid line, particularly verifies this condition. Among the exact schemes on stationary contact discontinuities, one presents a small numerical diffusion: the Godunov scheme.

The Godunov space scheme consists in taking as numerical flux function, the flux corresponding to the exact solution of the Riemann problem associated to the model (R), with the state in the cells on both sides of the interface considered as the initial condition:

$$f_{i+\frac{1}{2},j,k} = f(w_{i,j,k}, w_{i+1,j,k}) = F\left(w^R(0; w_{i,j,k}, w_{i+1,j,k})\right) \quad (3.97)$$

where w^R is the solution of the Riemann problem associated to model (R) (see equation (A.33)) taken at $x/t = 0$ and with the initial condition $W_g = w_{i,j,k}$, and $W_d = w_{i+1,j,k}$. The numerical fluxes $g_{i,j+\frac{1}{2},k}$ and $h_{i,j,k+\frac{1}{2}}$ are built the same way.

The second order in space is obtained thanks to the MUSCL method along with the slope limiter called monotonized central. In practice instead of calculating $f_{i+\frac{1}{2}} = f(w_{i,j,k}, w_{i+1,j,k})$, $g_{i,j+\frac{1}{2},k} = g(w_{i,j,k}, w_{i,j+1,k})$ and $h_{i,j,k+\frac{1}{2}} = (w_{i,j,k}, w_{i,j,k+1})$, the MUSCL method consists in computing:

$$\begin{aligned} f_{i+\frac{1}{2}} &= f(w_{i,j+\frac{1}{2}s_i,k}, w_{i+1,j-\frac{1}{2}s_{i+1},k}) \\ g_{j+\frac{1}{2}} &= f(w_{i,j+\frac{1}{2}s_j,k}, w_{i,j+1-\frac{1}{2}s_{j+1},k}) \\ h_{i+\frac{1}{2}} &= f(w_{i,j+\frac{1}{2}s_i,k}, w_{i+1,j-\frac{1}{2}s_{i+1},k}) \end{aligned} \quad (3.98)$$

$$(3.99)$$

where s_i , s_j and s_k are the limited slopes defined by:

$$\begin{aligned} s_i &= \text{moncen}(\Delta_{+,x}(w_{i,j,k}), \Delta_{-,x}(w_{i,j,k})) \\ s_j &= \text{moncen}(\Delta_{+,y}(w_{i,j,k}), \Delta_{-,y}(w_{i,j,k})) \\ s_k &= \text{moncen}(\Delta_{+,z}(w_{i,j,k}), \Delta_{-,z}(w_{i,j,k})) \end{aligned} \quad (3.100)$$

$$(3.101)$$

where:

$$\text{moncen}(a, b) = \max(\text{sign}(ab), 0) \min(m|a|, \frac{|a+b|}{2}, m|b|) \quad (3.102)$$

the parameter m ranging between 1 and 2. In practice, this parameter controls the "steepness" of the limiter. Here it is set to $m = 1.8$.

At this stage, given the conservative variables at time t_n , the scheme allows to compute the conservative variables at time t_{n+1} : $W^{n+1} = {}^t(\rho\alpha, \tilde{\rho}_1, \tilde{\rho}_2, \rho u, \rho v, \rho w)$, which all depend on the "natural variables" at time t_{n+1} : $V^n = {}^t(\alpha, \rho_1, \rho_2, u, v, w)$. However, the volume fraction obtained in function of the conservative variables $\alpha^{n+1} = \frac{\rho\alpha^{n+1}}{\tilde{\rho}_1^{n+1} + \tilde{\rho}_2^{n+1}}$ (thanks to the definition of ρ) does not correspond to the pressure equilibrium. Therefore it is necessary to update it through the relaxation step.

3.5.2.3 Relaxation Step

This step is the second step of the fractional-step method performed here. The following system must be solved for ϵ tending towards zero:

$$\frac{\partial}{\partial \tau} \begin{pmatrix} \alpha \\ \tilde{\rho}_1 \\ \tilde{\rho}_2 \\ \rho u \\ \rho v \\ \rho w \end{pmatrix} = \begin{pmatrix} \frac{P_2 - P_1}{\epsilon} \\ 0 \\ 0 \\ 0 \\ 0 \\ 0 \end{pmatrix} \quad (3.103)$$

No momentum source terms are used because the transport step has already been done. It is obvious that only α varies through this step. Now one knows (see section 3.4.4) that when $\epsilon \rightarrow 0$ the volume fraction α solution of this system tends to the unique "equilibrium volume fraction" defined by equation (3.65).

In the particular case where the form of the equations of state allows us to calculate the equilibrium volume fraction explicitly, this relaxation step simply consists in updating the new volume fraction in each cell. In this case there is no numerical scheme within itself. In cases where the equilibrium volume fraction is not calculated explicitly one will need to use a numerical scheme to solve the above mentioned system.

The resolution of the Riemann problem associated with model (R) is described in appendix A.5.

3.5.3 Numerical scheme for the diffusion term

The scheme used to discretize the right side terms viscous force terms in the momentum equation of model (R) is described in this section. This term is the divergence of the viscous stress tensor, it reads:

$$S^{visc} = \nabla \cdot \tau^D = \nabla \cdot (\mu(\nabla \underline{V} + {}^t \nabla \underline{V})) \quad (3.104)$$

The term $\nabla \cdot (\mu({}^t \nabla \underline{V}))$ is considered negligible compared to the term $\nabla \cdot (\mu(\nabla \underline{V}))$

By integrating the divergence over the cell C_{ij} , one obtains the following discretization

scheme:

$$\begin{aligned}
S_{i,j}^{visc} = & \frac{1}{\Delta x_i} \left[\left(\mu \frac{\partial u}{\partial x} \right)_{i+1/2,j} - \left(\mu \frac{\partial u}{\partial x} \right)_{i-1/2,j} + \left(\mu \frac{\partial u}{\partial y} \right)_{i,j+1/2} - \left(\mu \frac{\partial u}{\partial y} \right)_{i,j-1/2} \right] \underline{e}_x \\
& + \frac{1}{\Delta y_i} \left[\left(\mu \frac{\partial v}{\partial x} \right)_{i+1/2,j} - \left(\mu \frac{\partial v}{\partial x} \right)_{i-1/2,j} + \left(\mu \frac{\partial v}{\partial y} \right)_{i,j+1/2} - \left(\mu \frac{\partial v}{\partial y} \right)_{i,j-1/2} \right] \underline{e}_y
\end{aligned} \tag{3.105}$$

where (u, v) are the velocities in the reference frame $(\underline{e}_x, \underline{e}_y)$. Then we discretize these terms by the following scheme:

$$\left(\frac{u}{x} \right)_{i+1/2,j} = \mu_{i+1/2,j} \frac{u_{i+1,j} - u_{i,j}}{\Delta x} \tag{3.106}$$

where $\mu_{i+1/2,j}$ is the viscosity reconstructed at the cell's face. This reconstructed viscosity must depend on the viscosity in neighbouring cells:

$$\mu_{i+1/2,j} = \bar{\mu}(\mu_{i,j}, \mu_{i+1,j}) \tag{3.107}$$

Moreover, the function $\bar{\mu}$ must verify $\bar{\mu}(\mu, \mu) = \mu$, which corresponds to the fact that a zone where α is constant, the viscosity at the face must be the one of the fluid present in both neighbouring cells in order to be consistent with one-phase Navier-Stokes equations. The choice of viscosities reconstructed at faces is such that the scheme exactly preserves piecewise linear velocity fields. That is the plane Couette type flows. More precisely, let us consider the two-phase flow defined by the following velocity field:

$$\underline{V}_{exact} = u_{exact} \underline{e}_x = \left(u_0 + \frac{\tau_0}{\mu(y)} (y - y_0) \right) \underline{e}_x \tag{3.108}$$

with

$$\mu(y) = \begin{cases} \mu_1 & \text{if } y \geq y_0 \\ \mu_2 & \text{if } y \leq y_0 \end{cases} \tag{3.109}$$

and where τ_0 is the shear at the interface located in $y = y_0$:

$$\tau_0 = \mu_1 \frac{u}{y} (y = y_0^+) = \mu_2 \frac{u}{y} (y = y_0^-) \tag{3.110}$$

The latter relation represents the equilibrium of the stresses at the interface. Moreover, let us suppose that at the interface the line $y = y_0$ is precisely located on a mesh line, which we assume to be regular (Δy constant). Let us write the two source terms corresponding to cells $C_{i,j}$ and $C_{i,j+1}$ located on each side of the interface:

$$\Delta y^2 S_{j+1}^{visc} \cdot \underline{e}_x = \mu_{j+3/2} (u_{j+2} - u_{j+1}) - \mu_{j+1/2} (u_{j+1} - u_j) \tag{3.111}$$

$$\Delta y^2 S_j^{visc} \cdot \underline{e}_x = \mu_{j+1/2} (u_{j+1} - u_j) - \mu_{j-1/2} (u_j - u_{j-1}) \tag{3.112}$$

where column indices i were omitted, everything being constant along x . To affirm that the scheme exactly respects the considered flow is equivalent to saying that both these source terms must be zero. The velocity profile being piecewise linear, we have:

$$u_j = \frac{1}{V(C_{i,j})} \int_{C_{i,j}} u_{exact} dV = u_{exact} \left(y_0 - \frac{\Delta y}{2} \right) \quad (3.113)$$

and the same way we have:

$$u_{j-1} = u_{exact} \left(y_0 - \frac{3\Delta y}{2} \right) \quad (3.114)$$

$$u_{j+1} = u_{exact} \left(y_0 + \frac{\Delta y}{2} \right) \quad (3.115)$$

$$u_{j+2} = u_{exact} \left(y_0 + \frac{3\Delta y}{2} \right) \quad (3.116)$$

from which we deduce by replacing u_{exact} by its expression the different velocities:

$$u_{j+2} - u_{j+1} = \frac{\tau_0}{\mu_1} \Delta y \quad (3.117)$$

$$u_j - u_{j-1} = \frac{\tau_0}{\mu_2} \Delta y \quad (3.118)$$

$$u_{j+1} - u_j = \tau_0 \left(\frac{1}{\mu_{j+1}} + \frac{1}{\mu_j} \right) \frac{\Delta y}{2} \quad (3.119)$$

We have accounted that cells $C_{i,j+1}$ and $C_{i,j+2}$ are both located above the interface and that therefore $\mu_{j+2} = \mu_{j+1} (= \mu_1)$. The same way we obtain $\mu_{j-1} = \mu_j (= \mu_2)$. This remark also allows us to write both viscosities at faces $J + 3/2$ and $j - 1/2$:

$$\mu_{j+3/2} = \bar{\mu}(\mu_{j+1}, \mu_{j+2}) = \mu_{j+1} = \mu_1 \quad (3.120)$$

$$\mu_{j-1/2} = \bar{\mu}(\mu_j, \mu_{j-1}) = \mu_j = \mu_2 \quad (3.121)$$

Going back over the discrete balance (3.112), we obtain:

$$\mu_1 \frac{\tau_0}{\mu_1} \delta y - \mu_{j+1/2} \tau_0 \frac{\Delta y}{2} \left(\frac{1}{\mu_j} + \frac{1}{\mu_{j+1}} \right) = 0 \quad (3.122)$$

$$\mu_{j+1/2} \tau_0 \frac{\Delta y}{2} \left(\frac{1}{\mu_j} + \frac{1}{\mu_{j+1}} \right) - \mu_2 \frac{\tau_0}{\mu_2} \delta y = 0 \quad (3.123)$$

This is the harmonic average of viscosities in the cells that are adjacent to the considered face. One can generalise this reasoning to the case of non-regular meshes. And one obtains the following viscous fluxes scheme (for instance for $\mu \partial_x u$):

$$\left(\mu \frac{\partial u}{\partial x} \right)_{i+1/2,j} = \frac{\mu_{i+1,j} \mu_{i,j} (\Delta x_{i+1} + \Delta x_i) 2(u_{i+1,j} - u_{i,j})}{\Delta x_{i+1} \mu_i + \Delta x_i \mu_{i+1} \Delta x_{i+1} + \Delta x_i} \quad (3.124)$$

The treatment for the sources terms is explicit. Thus there is a stability condition associated to the viscous source term. The stability of such a discretization has not

been exhaustively studied. However the discrete time step has to be lower than the acoustic time scale:

$$\Delta t \leq \frac{\Delta x}{c} \quad (3.125)$$

because the method is fully explicit. The time step must also be lower than the time scale corresponding to the viscosity for the viscous term to be stable:

$$\Delta t \leq \frac{\Delta x^2}{2\nu} \quad (3.126)$$

3.6 Conclusion

In this chapter, the numerical methods for the simulation of wave breaking have been reviewed. We described the models found in the literature for two-phase free-surface flows. The original model used in SLOSH has been derived and compared to existing ones. We showed that it belongs to the class of models called multifluid models. Finally, the numerical methods used in SLOSH have been presented.

This sets the context from which we made an extension of the model presented in chapter 4.

Chapter 4

Extended model

4.1 Introduction

In the bibliographic review in chapter 2 we insisted on the fact that the simulation of wave impacts requires to take into account the presence of air is within water (dispersed-phase flow). In chapter 3 we presented the original model. Although this model is appropriate for the simulation of two-phase flows in the limit of separated-phase flows, it is not suitable for cases of dispersed-phase flows. As the mixture sound speed in model (R) defined by equation (A.25) does not properly models the physical mixture sound speed. Figure 4.1 shows both mixture sound speed in model (R) and physical mixture sounds speed (Wood 1941). One can see that the sound speed in model (R) is

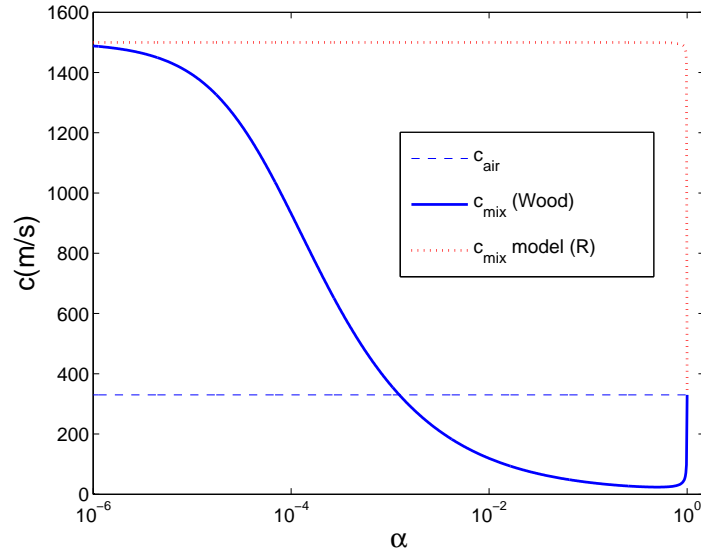


Figure 4.1: Air-water mixture sound speed, comparison between model (R) and physical.

only representative of the physical one when volume fraction is close to 0 or 1. I.e. it is relevant for separated-phase flows only. Therefore a more accurate model is required to properly estimate pressure fields in dispersed-phase flows like wave impact.

Moreover, as wave impact is a case mixing separated-phase limit (presence of the free surface) and dispersed-phase limit (presence of air within water), another necessary feature for a new model is the ability to distinguish the gas phase included in the liquid phase from the gas above the free surface. Indeed this feature will allow to set a particular behaviour to the gas phase trapped in water like subgrid scale models for the rise of bubbles. This is a prospective approach and it will not be implemented in this work yet.

In this chapter we propose an improvement of the model previously presented in chapter 3. The first section presents the mathematical features that we added in the model. The second section deals with the numerical implementation of this model.

4.2 Principle

We consider the physical situation of a wave-impact flow in which there are three distinct viscous fluids: the air above the free surface, the water and the air within water. We model this physical situation by a general mixture composed of fluid 1 and fluid 2. Fluid 1 is air above the free surface. Fluid 2 is the mixture of air below the free surface that we call fluid "a" and water that we call fluid "w". The scheme in figure 4.1 shows the hierarchy of phase compositions. So the improvement from model (R) is to consider that fluid 2 itself is a mixture. Let us note that in this configuration fluids 1 and 2 are still flowing separately, but fluids "a" and "w" flow dispersedly.

For the derivation of the mathematical model, we assume that we are at the macroscopic scale defined in section 3.4.2, thus the control volume V_{tot} mentioned in this chapter refers to the volume over which the average process is undertaken. We assume no phase change and isothermal flow. Moreover both fluids are supposed barotropic. In this context $\alpha = \frac{V_1}{V_{tot}}$ is the volume fraction of fluid 1 in a control volume containing a mixture of fluid 1 and 2. Let us introduce $\beta = \frac{V_a}{V_2}$ the volume fraction of air in fluid 2. An let $y = \frac{m_a}{m_2}$ be the mass fraction of air in fluid 2.

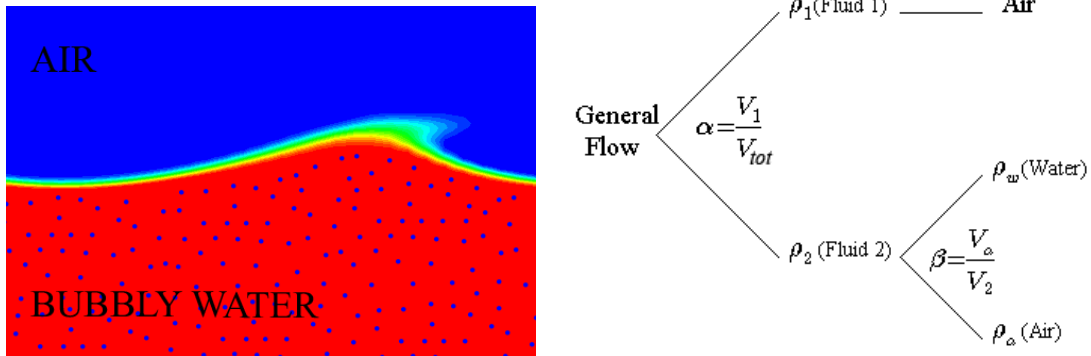


Table 4.1: Scheme of the extended model principle.

For sake of clarity, we introduce the following notations:

$$\begin{aligned}
\tilde{\rho}_1 &= \alpha\rho_1 \\
\tilde{\rho}_2 &= (1 - \alpha)\rho_2 \\
\tilde{\rho}_a &= \beta\rho_a \\
\tilde{\rho}_w &= (1 - \beta)\rho_w
\end{aligned} \tag{4.1}$$

From these definitions:

$$\tilde{\rho}_a = \beta\rho_a = y\rho_2 = y\frac{\tilde{\rho}_2}{1 - \alpha} \tag{4.2}$$

$$\tilde{\rho}_w = (1 - \beta)\rho_w = (1 - y)\rho_2 = (1 - y)\frac{\tilde{\rho}_2}{1 - \alpha} \tag{4.3}$$

4.3 Governing equations

The new model presented here is an improvement of the model (E) presented in chapter 3 (equations (3.69)) on which the original version of SLOSH was based.

4.3.1 Conservation equations

As the idea of this new model is add a third phase, it requires an extra mass conservation equation: the transport of the mass of fluid a (air within fluid 2) regarding the general mixture, $\frac{m_a}{V_{tot}} = \tilde{\rho}_2 y$ (using definitions), which is governed by:

$$\frac{\partial y}{\partial t} + \underline{V} \cdot \nabla(y) = 0 \tag{4.4}$$

Equation (4.4) can be written in conservative form by multiplying it by $\tilde{\rho}_2$ and adding the product of y and the mass conservation equation for fluid 2 (equation (4.7)). This leads to a conservation equation for the mass of fluid a:

$$\frac{\partial(\tilde{\rho}_2 y)}{\partial t} + \nabla \cdot (\tilde{\rho}_2 y \underline{V}) = 0 \tag{4.5}$$

The assumption of no slip between fluid 1 and fluid 2 mentioned in chapter 3, is also made here for fluid a and fluid w. Thus the velocity field is still unique. It is noted \underline{V} .

Therefore, the conservative variables are $\tilde{\rho}_1$, $\tilde{\rho}_2$, $\tilde{\rho}_2 y$ and $\rho \underline{V}$, where $\rho = \alpha\rho_1 + (1 - \alpha)\rho_2$. And the governing conservation equations of the model read:

$\frac{\partial \tilde{\rho}_1}{\partial t} + \nabla \cdot (\tilde{\rho}_1 \underline{V}) = 0$	(4.6)
$\frac{\partial \tilde{\rho}_2}{\partial t} + \nabla \cdot (\tilde{\rho}_2 \underline{V}) = 0$	(4.7)
$\frac{\partial(\tilde{\rho}_2 y)}{\partial t} + \nabla \cdot (\tilde{\rho}_2 y \underline{V}) = 0$	(4.8)
$\frac{\partial \rho \underline{V}}{\partial t} + \nabla \cdot (\rho \underline{V} \otimes \underline{V} + P(\tilde{\rho}_1, \tilde{\rho}_2, \tilde{\rho}_2 y) \underline{I}) = \nabla \cdot \underline{\tau}^D + \underline{F}$	(4.9)

The mixture for density reads: $\rho = \alpha\rho_1 + (1 - \alpha)\rho_2$ (4.10)

with $\rho_2 = \beta\rho_a + (1 - \beta)\rho_w$ (4.11)

The mixture for viscosity reads: $\mu = \alpha\mu_1 + (1 - \alpha)\mu_2$ (4.12)

with $\mu_2 = \beta\mu_a + (1 - \beta)\mu_w$ (4.13)

The mixture for pressure reads: $P = \alpha P_1 + (1 - \alpha)P_2$ (4.14)

with $P_2 = \beta P_a + (1 - \beta)P_w$ (4.15)

4.3.2 Pressure equilibria

The original model was closed by assuming the pressure equilibrium between fluid 1 and fluid 2, which allowed for the computation of the volume fraction α . This equation remains in the new model, it reads:

$$\boxed{P_1 = P_2} \quad (4.16)$$

In this new model, the mass conservation of fluid a is ensured by equation (4.5). However, another variable is introduced, the mass (or volume) fraction of fluid a: y (or β). Thus one more equation is required in order to close the model. For sake of coherence we set:

$$\boxed{P_a = P_w} \quad (4.17)$$

4.3.3 Transformation equations

In this section we introduce the transformation equations associated with each phase. One can notice that we do not use the terminology "equations of state" because it would imply to provide equations that describe all states that each fluid can undertake independently from the transformation path. And thus it would involve the internal energy of each phase. However as long as we do not consider the Navier-Stokes energy conservation equation for the motion of the phases, we implicitly assume that for all transformations the internal energy is constant. However the expression "equation of state" will be used by abuse in this document.

4.3.3.1 Equation of state of fluid 1

Equation of state of fluid 1 is taken to be linear around a reference state. It reads:

$$\boxed{p_1(\rho_1) = P_{10} + c_{10}^2(\rho_1 - \rho_{10})} \quad (4.18)$$

c_{10} is the sound speed in fluid 1 at P_{10} . Equation (4.18) can be rewritten upon conservative variables $\tilde{\rho}_1$ and α using notations (4.1):

$$p_1(\tilde{\rho}_1, \alpha) = P_{10} + c_{10}^2\left(\frac{\tilde{\rho}_1}{\alpha} - \rho_{10}\right) \quad (4.19)$$

4.3.3.2 Equation of state of air within fluid 2

Fluid "a" (pure air) within fluid 2 is assumed to behave according to a polytropic law:

$$\boxed{p_a(\rho_a) = \frac{P_{a0}}{\rho_{a0}^k} \rho_a^k} \quad (4.20)$$

Equation (4.20) can be rewritten upon conservative variable $y\tilde{\rho}_2$, and, α and β using relation (4.2):

$$p_a(y\tilde{\rho}_2, \alpha, \beta) = \frac{P_{a0}}{\rho_{a0}^k} \left(\frac{y\tilde{\rho}_2}{\beta(1-\alpha)} \right)^k \quad (4.21)$$

4.3.3.3 Equation of state of water within fluid 2

Pure water within fluid 2 is assumed to behave linearly around a constant reference state (P_{w0}, ρ_{w0}) , which reads:

$$\boxed{p_w(\rho_w) = P_{w0} + c_{w0}^2(\rho_w - \rho_{w0})} \quad (4.22)$$

where c_{w0} is the sound speed in pure water at P_{w0} . Equation (4.22) can be rewritten upon conservative variables $\tilde{\rho}_2$ and $y\tilde{\rho}_2$, and, α and β using relation (4.3):

$$p_w(\tilde{\rho}_2, y\tilde{\rho}_2, \alpha, \beta) = P_{w0} + c_{w0}^2 \left(\frac{(1-y)\tilde{\rho}_2}{(1-\beta)(1-\alpha)} - \rho_{w0} \right) \quad (4.23)$$

4.3.3.4 Resulting equation of state of fluid 2

Equation of state of fluid 2 follows by combining equations of state of pure air and pure water within fluid 2 to pressure closure equation (4.15):

$$\boxed{p_2(\rho_a, \rho_w, \beta) = \beta \frac{P_{a0}}{\rho_{a0}^k} (\rho_a)^k + (1-\beta) \left[P_{w0} + c_{w0}^2(\rho_w - \rho_{w0}) \right]} \quad (4.24)$$

It is useful for further developments to rewrite equation (4.24) upon conservative variables $\tilde{\rho}_2$ and $y\tilde{\rho}_2$, and, α and β using relations (4.2) et (4.3), this form reads:

$$p_2(\tilde{\rho}_2, y\tilde{\rho}_2, \alpha, \beta) = \beta \frac{P_{a0}}{\rho_{a0}^k} \left(\frac{y\tilde{\rho}_2}{\beta(1-\alpha)} \right)^k + (1-\beta) \left[P_{w0} + c_{w0}^2 \left(\frac{(1-y)\tilde{\rho}_2}{(1-\beta)(1-\alpha)} - \rho_{w0} \right) \right] \quad (4.25)$$

Now we are going to derive an expression for P_2 that only involve ρ_2 and y . From equation (4.24) and the definition of $\tilde{\rho}_2$ one can obtain:

$$p_2(\rho_2, y, \beta) = \beta \frac{P_{a0}}{\rho_{a0}^k} \left(\frac{y\rho_2}{\beta} \right)^k + (1-\beta) \left[P_{w0} + c_{w0}^2 \left(\frac{(1-y)\rho_2}{(1-\beta)} - \rho_{w0} \right) \right] \quad (4.26)$$

Now in order for ‘beta to vanish one needs to express β upon ρ_2 and y). One can achieve this by using the pressure equilibrium equation $P_a = P_w$. When developing the equations of states, it reads:

$$\frac{P_{a0}}{\rho_{a0}^k} \left(\frac{y\rho_2}{\beta} \right)^k = P_{w0} + c_{w0}^2 \left(\frac{(1-y)\rho_2}{(1-\beta)} - \rho_{w0} \right) \quad (4.27)$$

The solution β of this equation only depends on ρ_2 and y because the rest is constant. The problem is that this equation is implicit for β .

Let us try the particular case $k = 1$, which is simpler. Equation (4.27) becomes a second degree polynomial:

$$\beta^2 (P_{w0} - c_{w0}^2 \rho_{w0}) - \beta \left(P_{w0} + c_{w0}^2 (1-y)\rho_2 - c_{w0}^2 \rho_{w0} + \frac{P_{a0}}{\rho_{a0}} y\rho_2 \right) + \frac{P_{a0}}{\rho_{a0}} y\rho_2 = 0 \quad (4.28)$$

of which the Δ reads:

$$\Delta = \left(P_{w0} + c_{w0}^2 (1-y)\rho_2 - c_{w0}^2 \rho_{w0} + \frac{P_{a0}}{\rho_{a0}} (y\rho_2) \right)^2 - 4(P_{w0} - c_{w0}^2 \rho_{w0}) \frac{P_{a0}}{\rho_{a0}} (y\rho_2) \quad (4.29)$$

which leads to the expression for β as a function of ρ_2 and y :

$$\beta(\rho_2, y) = \frac{(P_{w0} + c_{w0}^2 (1-y)\rho_2 - c_{w0}^2 \rho_{w0} + \frac{P_{a0}}{\rho_{a0}} (y\rho_2)) \pm \sqrt{\Delta}}{2P_{w0} - 2c_{w0}^2 \rho_{w0}} \quad (4.30)$$

Now from equation (4.26), one obtains an analytical expression for P_2 upon ρ_2 and y :

$$p_2(\rho_2, y) = \frac{P_{a0}}{\rho_{a0}^k} y\rho_2 + \left(\frac{P_{w0} - c_{w0}^2 \rho_{w0} - c_{w0}^2 (1-y)\rho_2 - \frac{P_{a0}}{\rho_{a0}} y\rho_2 \pm \sqrt{\Delta}}{2P_{w0} - 2c_{w0}^2 \rho_{w0}} \right) \left[P_{w0} + c_{w0}^2 \left(\frac{(1-y)\rho_2}{(1-\beta)} - \rho_{w0} \right) \right] \quad (4.31)$$

However this is only valid for $k = 1$. Equation (4.31) is plotted in figure 4.2 for several fixed values of y .

The equation of state of fluid 2 in the case of $k = 1.4$ can be computed numerically.

4.3.4 Acoustics of the bubbly water (fluid 2)

The objective for this study is to represent pressure variations in the liquid phase due to wave impacts that may be large. However, as a first step, it is necessary to ensure that linear perturbations of pressure are well represented. Large pressure variations will be investigated further in a validation case in chapter 5. Also, this section aims to validate acoustics behaviour of the new model. Like in the original model, fluids 1 and 2 are still flowing separately in the new model. But the latter is designed for the simulation of dispersed air in the liquid phase (fluid 2). So we investigated the acoustic propagation in the mixture of air and water represented by fluid 2.

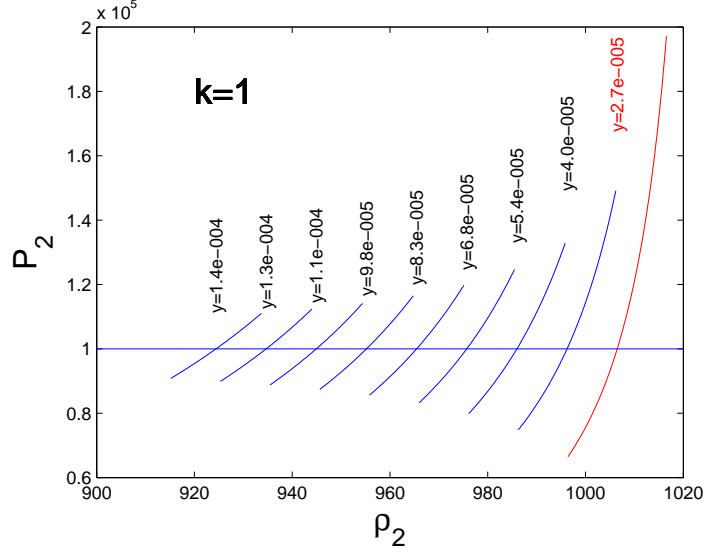


Figure 4.2: Resulting equation of state of fluid 2 for several fixed values of y .

The definition of sound speed in fluid 2 at atmospheric pressure P_0 is:

$$c_{20}^2 \equiv \left. \frac{\partial P_2}{\partial \rho_2} \right|_{\rho_{20}} \quad (4.32)$$

where the pressure in fluid 2 reads (equation (4.15)):

$$P_2 = \beta P_a(\rho_a) + (1 - \beta) P_w(\rho_w) \quad (4.33)$$

Let us derive equation (4.33) upon ρ_2 :

$$\frac{\partial P_2}{\partial \rho_2} = \beta \frac{\partial P_a(\rho_a)}{\partial \rho_2} + (1 - \beta) \frac{\partial P_w(\rho_w)}{\partial \rho_2} + (P_a - P_w) \frac{\partial \beta}{\partial \rho_2} \quad (4.34)$$

$$\frac{\partial P_2}{\partial \rho_2} = \beta \frac{\partial P_a(\rho_a)}{\partial \rho_a} \frac{\partial \rho_a}{\partial \rho_2} + (1 - \beta) \frac{\partial P_w(\rho_w)}{\partial \rho_w} \frac{\partial \rho_w}{\partial \rho_2} + (P_a - P_w) \frac{\partial \beta}{\partial \rho_2} \quad (4.35)$$

As $\rho_a = \frac{y\rho_2}{\beta}$ and $\rho_w = \frac{(1-y)\rho_2}{1-\beta}$, equation (4.35) becomes:

$$\frac{\partial P_2}{\partial \rho_2} = \frac{\partial P_a(\rho_a)}{\partial \rho_a} y \frac{\beta - \rho_2 \frac{\partial \beta}{\partial \rho_2}}{\beta} + \frac{\partial P_w(\rho_w)}{\partial \rho_w} (1 - y) \frac{(1 - \beta) + \rho_2 \frac{\partial \beta}{\partial \rho_2}}{(1 - \beta)} + (P_a - P_w) \frac{\partial \beta}{\partial \rho_2} \quad (4.36)$$

Now replacing y and $(1 - y)$ by their expression upon ρ_a and ρ_w , we have:

$$\frac{\partial P_2}{\partial \rho_2} = \frac{\partial P_a(\rho_a)}{\partial \rho_a} \rho_a \left(\frac{\beta}{\rho_2} - \frac{\partial \beta}{\partial \rho_2} \right) + \frac{\partial P_w(\rho_w)}{\partial \rho_w} \rho_w \left(\frac{(1 - \beta)}{\rho_2} + \frac{\partial \beta}{\partial \rho_2} \right) + (P_a - P_w) \frac{\partial \beta}{\partial \rho_2} \quad (4.37)$$

Now to obtain sound speed as defined by equation (4.32), one needs to take equation (4.37) at the particular standard state (P_{20}, ρ_{20}) . This leads to introduce the sound speeds in air $c_{a0}^2 = \left. \frac{\partial P_a}{\partial \rho_a} \right|_{P_0}$ and water $c_{w0}^2 = \left. \frac{\partial P_w}{\partial \rho_w} \right|_{P_0}$. Accounting for $P_a = P_w$, we have the following expression for the sound speed in fluid 2:

$$\boxed{c_{20}^2 = c_{a0}^2 \rho_{a0} \left(\frac{\beta_0}{\rho_{20}} - \left. \frac{\partial \beta_0}{\partial \rho_2} \right|_{\rho_{20}} \right) + c_{w0}^2 \rho_{w0} \left(\frac{(1 - \beta_0)}{\rho_{20}} + \left. \frac{\partial \beta_0}{\partial \rho_2} \right|_{\rho_{20}} \right)} \quad (4.38)$$

Let us emphasize that the sound speed is the speed of a linear pressure perturbation around a given reference state. Here the reference state is the standard state used is the standard state (P_{20}, ρ_{20}) . This is the reason why subscript "0" is used.

Now we need an expression for $\left. \frac{\partial \beta}{\partial \rho_2} \right|_{\rho_{20}}$. It is obtained by rewriting the pressure equilibrium between air and water (equation (4.17)) upon ρ_2 using relations (4.2) and (4.3):

$$\frac{P_0}{\rho_{a0}^k} \left(\frac{y \rho_2}{\beta} \right)^k = P_0 + c_{w0}^2 \left(\frac{(1 - y) \rho_2}{(1 - \beta)} - \rho_{w0} \right) \quad (4.39)$$

and by taking its derivative:

$$\frac{P_0}{\rho_{a0}^k} k \left(\frac{y \rho_2}{\beta} \right)^{k-1} \left(y \frac{\beta - \rho_2 \frac{\partial \beta}{\partial \rho_2}}{\beta^2} \right) = c_{w0}^2 \left((1 - y) \frac{(1 - \beta) + \rho_2 \frac{\partial \beta}{\partial \rho_2}}{(1 - \beta)^2} \right) \quad (4.40)$$

This leads to:

$$\frac{\partial \beta}{\partial \rho_2} = \frac{\beta(1 - \beta)^2 \frac{P_0}{\rho_{a0}^k} k \left(\frac{y \rho_2}{\beta} \right)^{k-1} y - \beta^2 c_{w0}^2 (1 - y)(1 - \beta)}{\beta^2 c_{w0}^2 \rho_2 (1 - y) + (1 - \beta)^2 \frac{P_0}{\rho_{a0}^k} k \left(\frac{y \rho_2}{\beta} \right)^{k-1} y \rho_2} \quad (4.41)$$

and at $\rho_2 = \rho_{20}$, we obtain:

$$\left. \frac{\partial \beta}{\partial \rho_2} \right|_{\rho_{20}} = \frac{\beta_0(1 - \beta_0)^2 \frac{P_0}{\rho_{a0}^k} k \left(\frac{y \rho_{20}}{\beta_0} \right)^{k-1} y - \beta_0^2 c_{w0}^2 (1 - y)(1 - \beta_0)}{\beta_0^2 c_{w0}^2 \rho_{20} (1 - y) + (1 - \beta_0)^2 \frac{P_0}{\rho_{a0}^k} k \left(\frac{y \rho_{20}}{\beta_0} \right)^{k-1} y \rho_{20}} \quad (4.42)$$

Replacing $\frac{y \rho_2}{\beta_0}$ by ρ_{a0} (see equations (4.1)) and $\frac{P_0}{\rho_{a0}^k} k \rho_{a0}^{k-1}$ by c_{a0}^2 (derivative of equation (4.20)), we have:

$$\left. \frac{\partial \beta}{\partial \rho_2} \right|_{\rho_{20}} = \frac{\beta_0(1 - \beta_0)^2 c_{a0}^2 y - \beta_0^2 c_{w0}^2 (1 - y)(1 - \beta_0)}{\beta_0^2 c_{w0}^2 \rho_{20} (1 - y) + (1 - \beta_0)^2 c_{a0}^2 y \rho_{20}} \quad (4.43)$$

Then replacing $(1 - y)$ by $\frac{(1 - \beta_0) \rho_{w0}}{\rho_{20}}$ and y by $\frac{\beta_0 \rho_{a0}}{\rho_{20}}$ (see equations (4.1)) leads to:

$$\boxed{\left. \frac{\partial \beta}{\partial \rho_2} \right|_{\rho_{20}} = \frac{\beta_0(1 - \beta_0)}{\rho_{20}} \frac{c_{a0}^2 \rho_{a0} - c_{w0}^2 \rho_{w0}}{\beta_0 \rho_{w0} c_{w0}^2 + (1 - \beta_0) \rho_{a0} c_{a0}^2}} \quad (4.44)$$

Finally, by replacing expression (4.44) in equation (4.38), one obtains the sound speed in fluid 2 as a function of β_0 , ρ_2 and constants. It reads:

$$\frac{1}{\rho_{20}c_{20}^2} = \frac{\beta_0}{\rho_{a0}c_{a0}^2} + \frac{(1-\beta_0)}{\rho_{w0}c_{w0}^2} \quad (4.45)$$

Thus the expression for sound speed c_{20} in the model corresponds exactly to Wood's (1941) formula.

Wood's (1941) law is plotted in chapter 2 in figure 2.15. The reader will note that this example presents the derivation of the sound speed at standard pressure P_0 , which represents the speed of linear pressure perturbation around standard state, but similarly it can be computed around any reference state $(P_{ref}, \rho_{2,ref})$.

4.4 Numerical implementation

As described in section 3.5.2 the original numerical method is a fractional-step method. This means that at each step of the second order Runge-Kutta method, two steps are performed: a transport step and a relaxation step. For details on both steps refer to section 3.5.2. We extended the original method to fulfil the requirements of the new model.

4.4.1 Transport step: numerical flux (Godunov)

In the transport step of the fractional-step method an additional conservation equation is included: the transport equation (4.8) for the mass of fluid "a" within fluid 2. This modification does not lead to particular difficulty except for the Godunov part of the solver. Indeed, the transport step requires to compute the numerical fluxes of conservative variables through cell faces. In the computation of these fluxes, we first need the densities at the face, RHO_1 and RHO_2 . They are given by the resolution of the Riemann problem detailed in appendix A.5. Then the total pressure at the face is needed. It reads $P = \alpha_1 P_1 + \alpha_2 P_2$. Therefore P_1 and P_2 are need at the considered face. P_1 depends on RHO_1 through the equation of state of fluid 1 (equation (4.18)). But the expression of P_2 in equation (4.25) cannot be used directly because the Godunov scheme in SLOSH has been developed to deal with linear equations of state. Thus we use a local and instantaneous linear approximation of fluid-2 equation of state:

$$P_2 = P_{2,ref} + c_{2,ref}^2 (RHO_2 - \rho_{2,ref}) \quad (4.46)$$

RHO_2 given by the resolution of the Riemann problem detailed in appendix A.5. However the reference state $(P_{2,ref}, \rho_{2,ref}, c_{2,ref})$, which has to be local (for each cell) and instantaneous (for each time step of the Runge-Kutta method), must be given a definition.

For $P_{2,ref}$, we take the arithmetic mean of the pressures at the previous time step in the cells at the left and right sides of the considered face: $P_{2,L}$ and $P_{2,R}$. In the same way, for $\rho_{2,ref}$, we take the arithmetic mean of the densities at the previous time step in the cells at the left and right sides of the considered face: $\rho_{2,L}$ and $\rho_{2,R}$.

Now, for $c_{2,ref}$, we chose to take the arithmetic mean of the sound speed associated to the state in the cells at the left and right sides of the considered face at the previous time step: $c_{2,L}$ and $c_{2,R}$.

$c_{2,L}$ is computed through the equation defining the sound speed in fluid 2 (equation (4.45)) using the state at the previous time step in the cell at the left side of the considered face: $(\rho_{2,L}, \beta_2, P_{2,L}, \rho_{a,L}, c_{a,L}, \rho_{w,L}, c_{w,L})$, where $c_{a,L}$ is computed through the equation of state of fluid a, $c_{a,L} = \sqrt{\frac{k P_{2,L}}{\rho_{a,L}}}$, which is the derivative of equation (4.20) taken in the cell at the left side of the face, and where $c_{w,L}$ is equal to the constant $c_{w,0}$ (as in the linear equation of state of fluid w, equation (4.22)).

In the same way $c_{2,R}$ is computed through equation (4.45) using the state at the previous time step in the cell at the right side of the considered face: $(\rho_{2,R}, \beta_2, P_{2,R}, \rho_{a,R}, c_{a,R}, \rho_{w,R}, c_{w,R})$.

4.4.2 Relaxation step

In the section 4.4.1, we presented the computation for the transport step within the fractional-step method. Now the conservative variables $\tilde{\rho}_1, \tilde{\rho}_2, \tilde{\rho}_2 y$ et $\rho \underline{V}$ are known. It is then necessary to compute values of α and β that satisfy the pressure equilibria (4.17) and (4.16). This will allow us to compute the natural variables $\rho_1 = \frac{\tilde{\rho}_1}{\alpha}$, $\rho_2 = \frac{\tilde{\rho}_2}{1-\alpha}$, $\rho_a = \frac{\tilde{\rho}_a}{\beta}$ and $\rho_w = \frac{\tilde{\rho}_w}{1-\beta}$. and the pressures. In order to achieve this, it is necessary to solve the system formed by pressure equilibrium equations (equations (4.17) and (4.16)). In the following, we rewrite these two equilibria upon conservative variables.

Firstly, the pressure-equilibrium equation between air and water within fluid 2 (equation (4.17)) reads, using equations of state (4.21) and (4.23) involving conservative variables:

$$\frac{P_0}{\rho_{a0}^k} \left(\frac{y \tilde{\rho}_2}{\beta(1-\alpha)} \right)^k = P_0 + c_{w0}^2 \left(\frac{(1-y) \tilde{\rho}_2}{(1-\beta)(1-\alpha)} - \rho_{w0} \right) \quad (4.47)$$

Equation (4.47) involves the unknowns α and β , constants $(P_0, \rho_{a0}, c_{w0}, \rho_{w0}, k)$ and conservative variables $\tilde{\rho}_2$ and $\tilde{\rho}_2 y$ that have been computed during transport step. Thus equation (4.47) constitutes a first equation that will be of use to compute α et β . The left part of equation (4.47) is a decreasing function and the right part is an increasing function, then the solution β is unique.

Secondly, the other equation involving α and β is the pressure equilibrium equation between fluid 1 and fluid 2 (equation (4.16)). In equation (4.16), the computation of P_1 is easily achieved by using the equation of state of fluid 1 (4.19). However, the expression of P_2 through equation (4.25) is too complex to be used here. Instead, we replace P_2 by P_w , which are exactly equal as all the pressures have been relaxed at the previous time step. Indeed, $P_2 = \beta P_a + (1-\beta)P_w$ (equation (4.15)) and $P_a = P_w$ (equation (4.17)), thus $P_2 = \beta P_a + (1-\beta)P_w = P_w$. Then we rewrite the pressure equilibrium between fluid 1 and fluid 2 (4.16) in:

$$P_1 = P_w \quad (4.48)$$

This trick is useful because P_w has the advantage of being simple linear equation of state. Now pressure equilibrium between fluid 1 and fluid 2 reads, by replacing with

equations of state (4.19) and (4.23):

$$\boxed{P_{10} + c_{10}^2 \left(\frac{\tilde{\rho}_1}{\alpha} - \rho_{10} \right) = P_{w0} + c_{w0}^2 \left(\frac{(1-y)\tilde{\rho}_2}{(1-\beta)(1-\alpha)} - \rho_{w0} \right)} \quad (4.49)$$

Equation (4.49) constitutes the second necessary equation for computing α et β . The relation between β and α through equation (4.49) can be found explicitly.

The computation of α et β through equations (4.47) and (4.49) is achieved by using implementing a Newton-Raphson method generalized to systems of two equations.

4.5 Conclusion

In this chapter, we have presented how we extended the model in the SLOSH code. We added a third phase, within fluid 2, that allows for the simulation of dispersed mixture of air and water as fluid 2. The governing equations have been augmented of one transport equation. New equations of state have been introduced to allow for an accurate representation of mixtures of air and water. Finally, we presented the extension to the original numerical methods present in the SLOSH code necessary to account for the new model.

Chapter 5

Extended model: Validation

5.1 Introduction

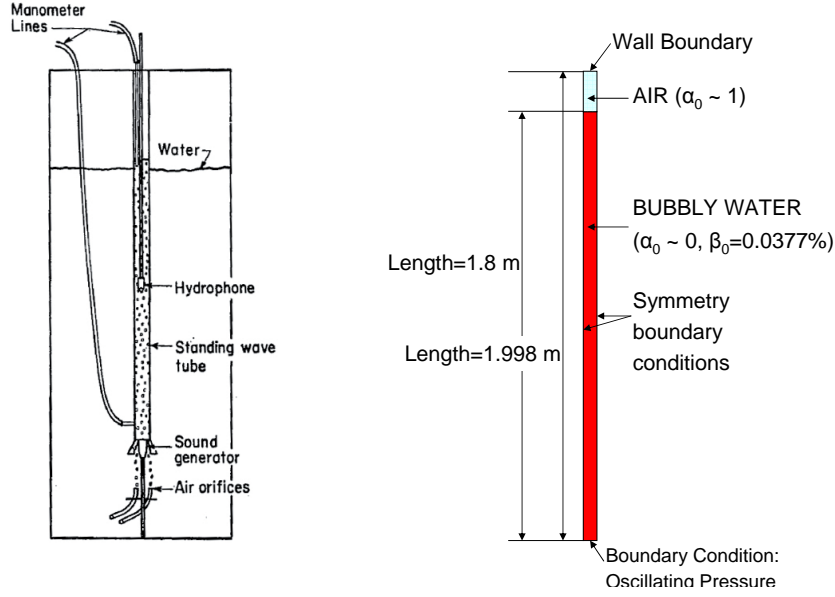
This chapter is devoted to the validation process of the numerical model presented in chapter 4. We carried out these tests in order to assess its ability to represent physical processes that are necessary for an accurate description of wave impacts on structures. Firstly, we analyse the accuracy of the code in terms of the propagation of an acoustic wave in a mixture of air and water. Secondly, the accuracy of the code for representing the propagation of a shock wave is investigated. Indeed, as shown in chapter 2, it has been highlighted in the literature that shock waves can form below the wave impact zone. Therefore a good representation of such a critical phenomenon is of first importance. Finally, we compare the free surface dynamics of a deep-water breaking wave obtained by our model to simulations from an incompressible model, which ensures the accuracy of the model concerning complex breaking wave situations.

5.2 Acoustic wave propagation in a bubbly liquid

5.2.1 Set-up

The aim of this section is to analyse the accuracy of the code in the modelling of an acoustic-wave propagation in a homogeneous bubbly liquid. For this purpose we measure the speed of sound and the attenuation of a pressure wave in a mixture of air and water. The chosen reference case is the experiment carried out by Silberman (1957) whose experimental apparatus is represented in figure 5.1(a). This experiment consists in a vertical circular-cross-section column containing water whose internal diameter is 7.62 cm and whose upper side is open to the atmosphere. Bubbles are introduced at the bottom of the column and rise towards the free surface. A transducer is placed at the bottom of the column. This transducer generates pressure waves propagating towards the free surface. The free surface is located at 1.80 m above the transducer. Sound pressure measurements are made at the centre of the column with hydrophones.

The corresponding numerical set-up is represented in figure 5.1(b). This is a one dimensional representation of the experimental set-up of Silberman (1957). Let us



(a) Silberman's experimental set-up. (b) Corresponding numerical set-up.

Figure 5.1: Silberman (1957) case's scheme.

note that as the water column undergoes a hydrostatic pressure profile, the subscript "0" is used to distinguish values taken at atmospheric pressure. The numerical column (figure 5.1(b)) is filled with a mixture of air and water, represented by fluid 2, up to 1.80-m-high as in the experiment. The upper part is filled with pure air, represented by fluid 1, over a vertical length of 0.198 m. So the total length of the column is 1.998 m as presented in figure 5.1. This set-up allows us to represent the presence of the atmosphere above the free surface but over a small vertical distance to avoid adding too many computation cells. In the lower part, fluid-1 volume fraction $\alpha_0(z)$ is uniformly set to 10^{-9} , which is almost zero so that fluid 1 is practically absent. The reader will note that due to the numerical method both fluid 1 and fluid 2 must be present everywhere in the domain, although only in small proportions. In the upper part, fluid-1 volume fraction $\alpha_0(z)$ is uniformly set to $1 - 10^{-9}$ whose is almost 1 so that fluid 2 is practically absent. The initial spatial distribution of fluid-1 volume fraction at atmospheric pressure is:

$$\alpha_0(z) = \begin{cases} 10^{-9} & \text{for } 0 < z < 1.8 \\ 1 - 10^{-9} & \text{for } 1.8 < z < 1.998 \end{cases} \quad (5.1)$$

Fluid 2 is a mixture of air (fluid a, whose density is $\rho_{a0} = 1.33 \text{ kg.m}^{-3}$, and sound speed is $c_{a0} = 340 \text{ m.s}^{-1}$) and water (fluid w, which density is $\rho_{w0} = 1027 \text{ kg.m}^{-3}$, and sound speed is $c_{w0} = 1500 \text{ m.s}^{-1}$). Fluid-a (air) mass fraction y is uniformly set to $y = 4.89795 \cdot 10^{-7}$. Thus, close to the free surface where the pressure is the atmospheric pressure, the air volume fraction is $\beta_0 = 3.77 \cdot 10^{-4}$, which is a value used by Silberman (1957). It is important to notice that due to hydrostatic pressure variation, $\beta_0(x)$

decreases from the free surface to the bottom.

Fluid 1 is an approximation of air controlled by a linear equation of state ($\rho_{10} = 1.33 \text{ kg.m}^{-3}$, $c_{10} = 340 \text{ m.s}^{-1}$).

The upper boundary condition is a wall. At the side boundaries symmetry conditions are used. The bottom boundary is an oscillation inflow condition, which allows us to generate a pressure oscillation at the bottom of the numerical domain over the whole duration of the simulation. The amplitude of the pressure wave is small (around 3 Pa) in order to stay within the acoustic limit. The frequency of the oscillations are varied within the [374 – 12384] Hz interval. The pressure wave that is generated at the bottom of the column propagates upwards, is partly reflected at the free surface. Then it propagates back downwards and is reflected at the bottom. Then it is reflected back and forth and is damped on both upward and downward courses.

Figure 5.2(a) shows an example of an instantaneous pressure field obtained for a forcing frequency of 2012 Hz. The bottom of the column where the wave is generated is on the left-hand side. The free surface being located at $Z = 1.80 \text{ m}$ one can see that in the here displayed case the pressure wave front has not reached the free surface yet. When it does it will be reflected partially and the reflected wave will superimpose itself with the incident one. One can notice very small oscillations on the wave front that are due to a numerical disturbance. The peak values decrease with Z and the min values increase, thus the amplitude of the wave decreases with altitude Z , which is a damping effect.

Figure 5.2(b) shows an example of the root mean square pressure (RMS) fluctuation field, which is defined by:

$$Prms = \sqrt{(P(z, t) - P_{hyd}(z))^2} \quad (5.2)$$

where P is the pressure, P_{hyd} is the hydrostatic component of the pressure and $\overline{A(t)}$ is the time average of $A(t)$. The RMS operator allows for a statistical description that does not depend on time. The amplitude of the RMS signal increases with Z for the shown frequency. In this case the amplitude is the strongest closest to the free surface where the reflected wave superimposes with the incident wave. However this is not always the case as in some cases the amplitude decreases with Z . It depends on the attenuation coefficient value. An essay of explanation is proposed here. Let us note A_1 , the amplitude of the incident wave at the bottom, A_2 its amplitude at the free surface, (if we assume a total reflection A_2 is also the amplitude of the reflected wave at the free surface) and B_1 the amplitude of the reflected wave reaching the bottom. By assuming that the attenuation through the column does not depend on the amplitude, one can write:

$$\frac{B_1}{A_2} = \frac{A_2}{A_1} = \gamma \quad (5.3)$$

where γ is the ratio of the amplitudes at each end of the liquid domain. When both the incident and the reflected waves superimpose the total amplitude is $A_1 + B_1$ at the bottom and $2A_2$ at the free surface. So the fact that the total amplitude is greater at the bottom than at the free surface reads:

$$A_1 + B_1 > 2A_2 \quad (5.4)$$

which can be written upon γ using equation (5.3):

$$\gamma^2 - 2\gamma + 1 > 0 \quad (5.5)$$

This is a second degree inequality whose corresponding polynomial has a unique positive root. Therefore for attenuation coefficients γ below $1 + \sqrt{2}$, the total amplitude increases with Z whereas for γ above $1 + \sqrt{2}$ the total amplitude decreases with Z .

Figure 5.2(b) shows that the pressure wave is almost entirely reflected at the free surface. However we noticed some small pressure oscillations in the air part above the free surface. This can be noticed in the right part of figure 5.2(b). These small oscillations are the part of the pressure wave that is transmitted to the air domain. In order for this wave not to disturb the position of the free surface too much, we chose a length aspect ratio between liquid and air domains that prevents transmitted pressure waves from the bubbly part to resonate in the air part. In effect, such a phenomenon can, when its amplitude increases by resonance effect, stimulate the bubbly part of the column.

One can notice that the shape of the signal indicates that it is close to stationary near the free surface because the latter permits an almost full reflection of the wave. Whereas the signal is far from stationary near the bottom because the pressure stimulation is superimposed on the reflected damped wave coming back downwards it.

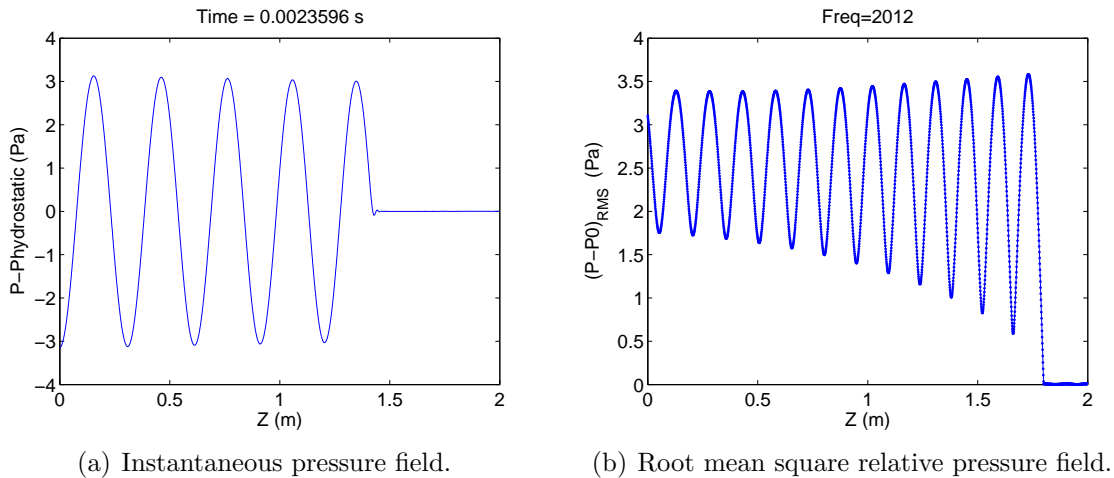


Figure 5.2: Pressure field example

5.2.2 Sound speed

In this section numerical sound speeds for different frequencies and different air content are compared to analytical results and experimental data.

Figure 5.3(a) shows a plot of sound speed within the mixture at a constant air volume fraction $\beta = 3.77 \cdot 10^{-4}$ at frequencies well below bubble resonance frequency $f_0 = 2738$ Hz (see Commander & Prosperetti 1989). Computed sound speeds are measured with a precision of 4 m/sec. Sound speed is almost constant as expected and close to theoretical and experimental sound speed values.

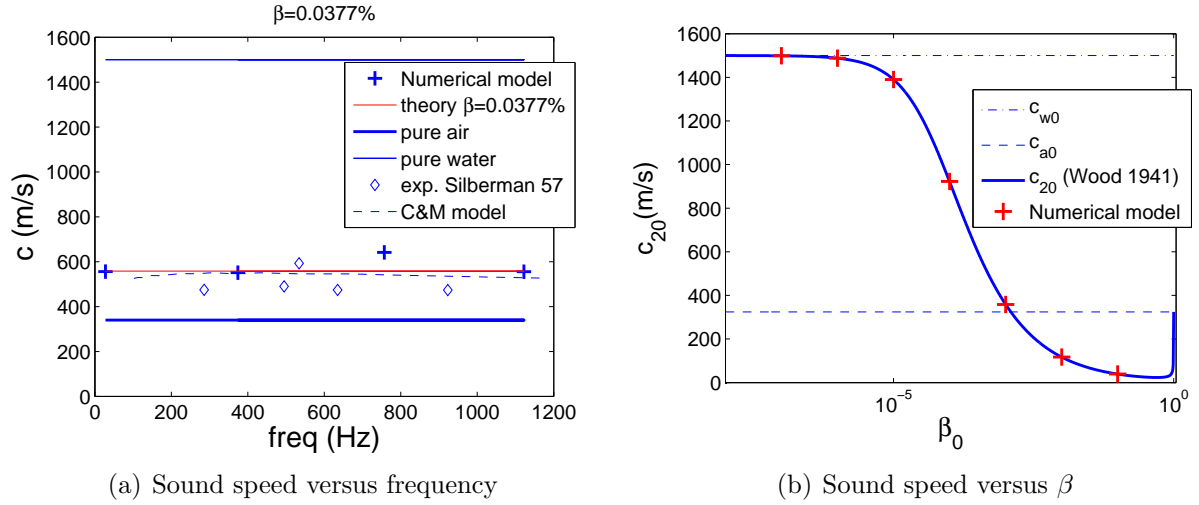


Figure 5.3: Sound speed versus frequency and air content.

Figure 5.3(b) shows a plot of sound speed versus air volume fraction β . This graph shows a fair agreement of sound speed with Wood's law.

This test shows that the numerical model represents the speed of sound in a mixture of air and water with good accuracy.

5.2.3 The influence of grid resolution

In this section, a case for which pressure wavelength equals domain length (mode 1) is run for different mesh sizes. For that purpose, a mode 1 pressure wave is set as the initial condition in the liquid domain. Different mesh refinements are tested in order to estimate what resolution is necessary for the numerical attenuation to no longer interfere with the physical attenuation. The wave attenuation at a node or antinode in figure 5.2(b) can be estimated by:

$$Att = \frac{4f}{nc} \operatorname{atanh} \left(\frac{Prms_{min}}{Prms_{max}} \right) \quad (5.6)$$

where f is the frequency of the temporal signal, c is the sound speed in the medium, n is the number of quarter wavelength from the free surface to the node or antinode in question. $Prms_{min}$ and $Prms_{max}$ are the min and max of $Prms$ at the considered node or antinode, obtained by assuming linear variation of the maxima of $Prms$ and the minima of $Prms$ over each half-wavelength interval. For instance, when considering a node, $Prms_{min}$ is the value of $Prms$ at the node, and $Prms_{max}$ is found by linear interpolation between the values of $Prms$ and the two neighbouring antinodes. The value of such attenuation for several grid resolutions is plotted in figure 5.4. The attenuation decreases exponentially with the resolution. Figure 5.4 shows that a criterion for attenuation to be physical attenuation is to set the resolution to at least 50 cells per wavelength.

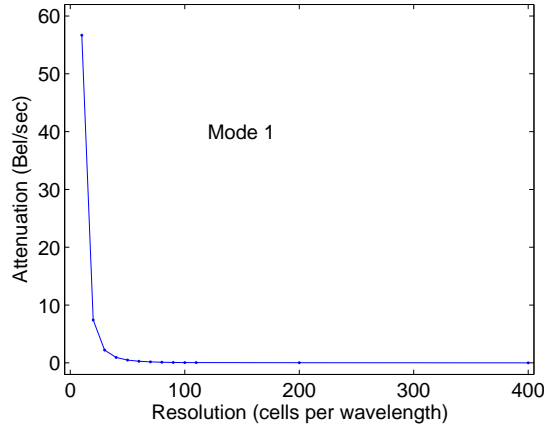


Figure 5.4: Wave attenuation versus resolution for a standing linear pressure wave, $\beta = 3.77 \cdot 10^{-4}$.

5.2.4 Wave attenuation

This section aims to present the analysis of viscous attenuation of a linear pressure wave. In a mixture of air and water, the presence of bubbles can severely increase dissipation processes. Indeed, it has been shown in the literature that pressure waves pulsating at frequencies around bubble resonance frequency undertake greater dissipation than away from this frequency. However as the numerical model developed here does not take into account the bubbles as separated entities, we do not expect such an increase in the dissipation for frequencies around bubble resonance frequency.

Figure 5.5 represents the attenuation, as defined by equation (5.6), versus elevation in the column for a forcing frequency of 2012 Hz. This figure shows that attenuation is not constant and varies with altitude. It increases exponentially from the bottom to the free surface.

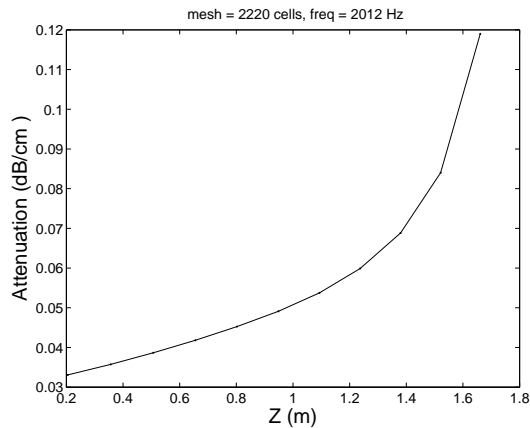


Figure 5.5: Attenuation versus altitude, $\beta = 3.77 \cdot 10^{-4}$, frequency = 2012 Hz .

In figure 5.6, attenuation is plotted versus frequency. The dots represent the experimental points by Silberman (1957). The line represents the model by Commander

& Prosperetti (1989). The bars represent the minimum and maximum values of attenuation in the computations, as attenuation varies with altitude as shown in figure 5.5. As a matter of fact, Silberman's (1957) attenuation values are not well defined as they do not mention if they consider minimum, maximum, average or another value for the attenuation estimation. The green bars are for a 222-cell mesh and the blue bars correspond to a 2220-cell mesh, meshes which provide a resolution of at least 50 cells per pressure wave length.

One can see that theoretical attenuation first increases gently with frequency (200 - 2000 Hz). Then attenuation increases faster (2000-3000 Hz) and reaches its maximum around the fundamental bubble resonance frequency f_0 . Then it decreases strongly (3000-10 000 Hz) and then with a gentle negative slope (10 000 - 100 000 Hz). The theoretical model from Commander & Prosperetti (1989) and experimental data from Silberman (1957) show good agreement.

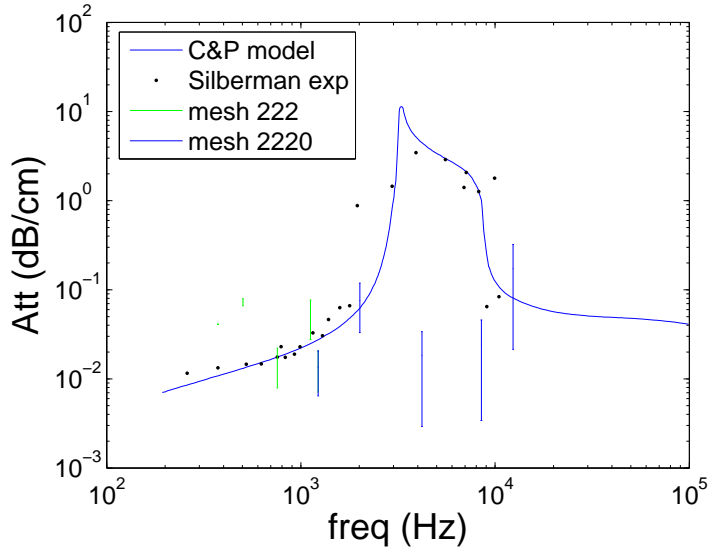


Figure 5.6: Attenuation versus frequency, $\beta = 3.77 \cdot 10^{-4}$.

The numerical results are in good agreement with both experimental and theoretical data for frequencies below and above bubble resonance frequency. However our model underestimates attenuation at frequencies around bubble resonance frequency. This was an expected result as our model does not take into account bubble resonance mechanisms. Therefore our model globally gives good agreement to experimental results, except for the range of frequencies [2000 – 9000] Hz around bubbles resonant frequency. For frequency 1228 Hz, both results from 222-cell and 2220-cell meshes are plotted and they are superimposed. Thus one can note there is no effect of the mesh.

5.3 Shock tube

Shock waves are likely to happen around the wave impact zone (Peregrine et al. 2005). Therefore it is necessary to assess the ability of the numerical model to represent the

propagation of a shock wave. For that purpose, a classic test case is run, the shock tube, which comes from gas dynamics applications.

The configuration is a one dimensional tube divided into two inner parts by a membrane. The left part is filled with a particular fluid at high pressure, and the right part is filled with another fluid at low pressure. At the beginning of the test the membrane is broken and a pressure jump and/or a rarefaction wave propagates through the tube.

In order to represent the situation of the propagation of a shock wave, we consider a shock tube filled with fluid 2 (so fluid 1 is almost absent: $\alpha = 1 \cdot 10^{-9}$), which is a mixture of air and water. The air mass fraction y is identical in both left and right parts of the tube corresponding to air volume fraction β_0 values ranging between 10^{-4} and 0.1.

Numerical results are compared to the analytical solution recently proposed by Franquet (2006) and Saurel, Le Metayer, Massoni & Gavrilyuk (2007) for a mixture shock tube. This solution has the particularity of providing Hugoniot type shock relations for mixtures. It is derived in appendix A.6. It is important to notice that this analytical model is not totally equivalent to our numerical model. Indeed, in the analytical one both fluids are represented by Stiffened Gas equations of state. Whereas in our numerical model the equations of state are a polytropic equation for fluid a and a linear equation for fluid w as presented in chapter 4. Moreover, there is an energy conservation equation, whereas the numerical model only represents dynamics. But this is the closest theoretical model for shock tube we found in the literature. Some discrepancies can thus be expected around the contact discontinuity and will be discussed below.

For this first case, the initial air mass fraction in both parts of the tube is $y_0 = 1.3118 \cdot 10^{-5}$. This mass fraction, at atmospheric pressure, corresponds to an air volume fraction of $\beta = 0.01$.

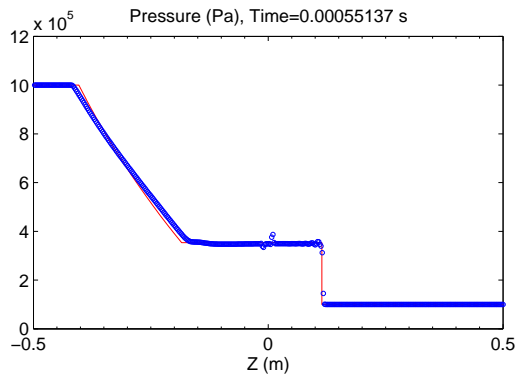
	P (Pa)	y	ρ_a ($kg.m^{-3}$)	ρ_w ($kg.m^{-3}$)	β	u ($m.s^{-1}$)
Left	10^6	$1.3118 \cdot 10^{-5}$	6.908	1027.4	0.00194716	0
Right	10^5	$1.3118 \cdot 10^{-5}$	1.33	1027	0.01	0

The results are shown in figure 5.7. The agreement between the simulation and the analytical solution is good.

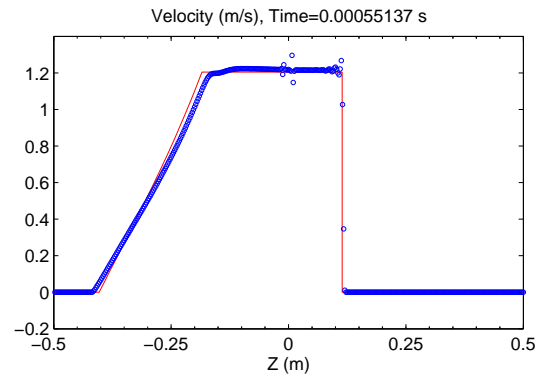
The shock wave (at $Z = 0.1142$ m) has an accurate location and an accurate velocity.

The solution between the rarefaction wave and the shock wave (-0.1844 m $<$ Z $<$ 0.1142 m) is globally accurate. One can note a slight discrepancy at the right of the contact discontinuity ($0 <$ Z $<$ 0.1142 m) particularly in the graphs for β , density of fluid a and density of fluid 2. Indeed, in the analytical model densities depend on internal energy (through Stiffened Gas equation), which is not the case in the numerical model. And as no continuity of internal energy is required at the interface, the densities also undertake a jump. Although left and right internal energies are initially different, they would have reached the same value if the thermodynamic paths undertaken by the left and right parts of the interface were the same. But it is not the case as a shock is a highly dissipative process in which the loss of kinetic energy generates an increase in heat and therefore in internal energy. This implies a jump in densities at the contact discontinuity.

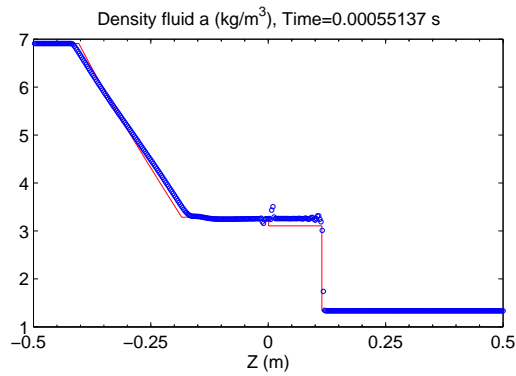
One can notice oscillation at the contact discontinuity. This is certainly due to a



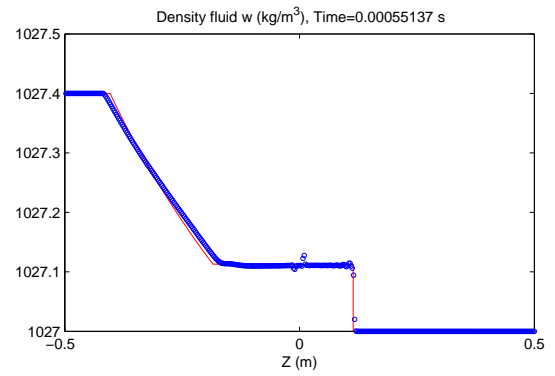
(a) Pressure



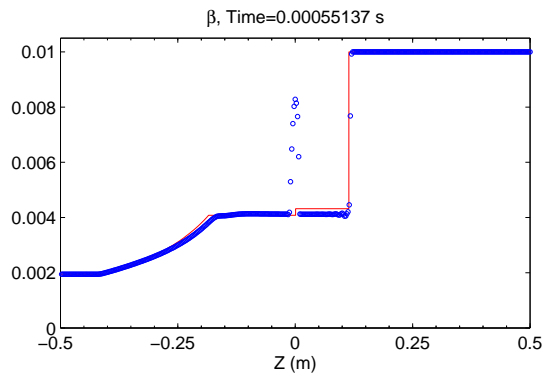
(b) Velocity



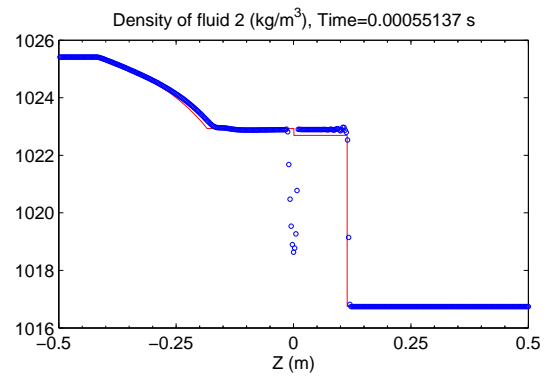
(c) Density of fluid a



(d) Density of fluid w



(e) β



(f) Density of mixture (fluid 2)

Figure 5.7: Comparison of a numerical simulation of the mixture shock tube with 800 cells to the analytical solution, for $P_L/P_R = 10$ and $\beta_0 = 0.01$.

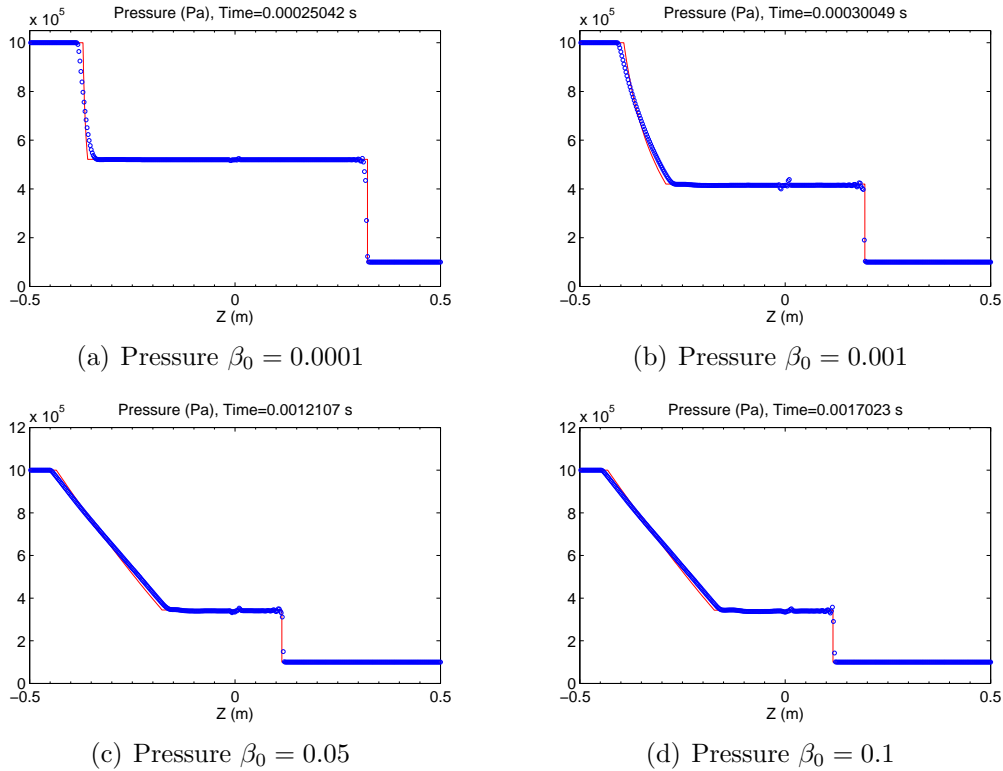


Figure 5.8: Comparison of the numerical simulation of the mixture shock tube with 800 cells to the analytical solution, for $P_L/P_R = 10$ and different values of β_0 .

lack of exactitude in the Riemann solver we developed. Indeed, the Godunov method we implemented relies on a linear equation of state, so we made the assumption that the previous time step state is close enough to current time step state to linearly extrapolate the current state from it (see section 4.4). This generates an oscillation at the contact discontinuity.

However as the main interest of this study is to characterize pressure field dynamics, this is not of first importance.

One can also notice that the rarefaction wave is a little wider than the analytical one. This implies that its front is less steep, which is characteristic of a numerical diffusion process.

Then, we run the same case for different air mass fractions. The focus is on the pressure as this is what is of interest in this study as the mechanism likely to cause damage to a coastal structure. Results are shown in figure 5.8. The agreement between numerical simulations and analytical solution is good whatever the air mass fraction.

One can see some slight spurious oscillations around the interface.

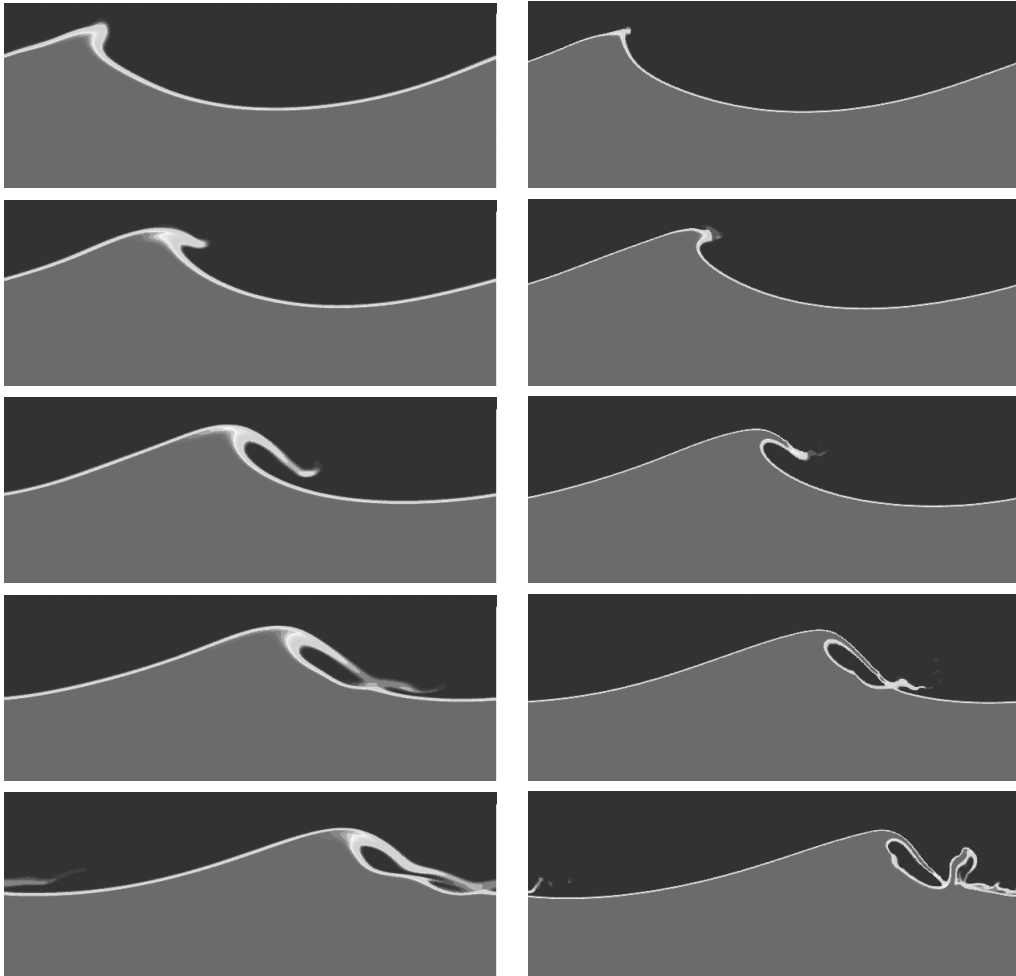


Figure 5.9: Free-surface dynamics, comparison between our model (left) and Duval's (2007) model (right) for the breaking of Stokes wave ($Re = 10^4$, steepness=0.45) for non-dimensional times: $\frac{t}{T} = \{0.5719, 0.6369, 0.7019, 0.7669, 0.8319, 0.8969, 0.9619, 1.0269, 1.0919\}$.

5.4 Deep water breaking Stokes Wave at the incompressible limit

This section aims to validate the numerical model for a breaking wave configuration. We chose a Stokes wave breaking in deep water. The representation of complex free surface dynamics by our code is compared to an incompressible numerical model based on a one-fluid model with a Volume-Of-Fluid (VOF) method proposed by Duval (2007). The simulation is initialized with a propagating Stokes wave solution with fluid 1 representing air above free surface and fluid 2 representing liquid below free surface. The steepness of the wave is chosen so that the breaking process is expected to occur soon. In order to properly compare it to the incompressible model, our model is run in the limit of fluid 2 being pure water. This is achieved by setting fluid-"a" mass fraction (air) within liquid phase (fluid 2) to almost zero, $y = 1.2987 \cdot 10^{-10}$, which corresponds at atmospheric pressure to a volume fraction of $\beta = 10^{-7}$. It is important to notice that our methods being explicit, we set the sound speeds in equations of state of fluid "w" and fluid 1 to 70 m/s in order to limit the computation time. This value however verifies a criterion for incompressibility defined by Chantepredrix (2004). The incompressible Navier-Stokes model is run on a uniform 512x512 cells mesh whereas our simulation is run on a 200x375 cells mesh for the same CPU reason.

This comparison is shown in figure 5.9.

The results from our model are in global agreement with the incompressible model results. The overturning and the formation of the air pocket in the curl are accurate. The diffusion is observed to be stronger in our model. This is probably due to the use of a coarser mesh.

The splash up in our simulation has a weaker energy compared to the incompressible case. This may be due to the coarser mesh that, by making stronger diffusion of this thin jet, reduces the mass in the jet, and thus its momentum. Another explanation may be that the incompressibility criterion mentioned above for our model, is not valid. In this way, the compressibility is responsible for smoothing the dynamics of the jet rebound which is less elastic.

5.5 Conclusion

In this chapter we focused on the validation of our numerical model. Firstly, we chose a case for testing basic acoustics in a gas/liquid mixture in our code. This test led to very good agreement between our model and the experiment. Secondly we chose to test our code regarding the propagation of a shock wave in a gas/liquid mixture. Our model showed good agreement with the theory. Finally, we ran a test case to assess the ability of our model to represent complex free surfaces as in wave breaking. The results from our code showed good agreement with the result from a classic incompressible model.

Chapter 6

Wave impact on a wall

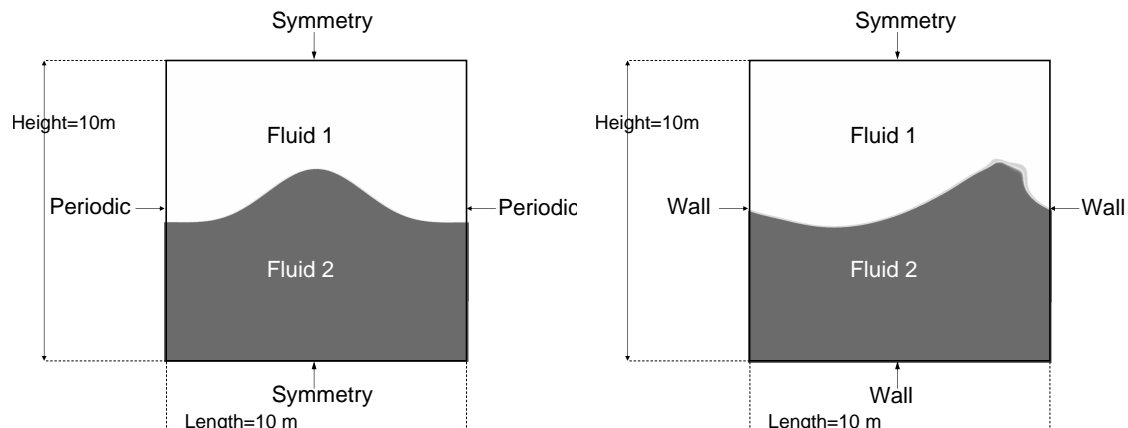
6.1 Introduction

In this chapter we present the results from our simulations of wave impacts on a vertical wall. Section 6.2 aims to present the numerical set-up we used for generating wave impacts on a wall. In section 6.3 we present the results concerning the dynamics of the wave impacts. In this section we will describe the details of the free-surface dynamics, particularly the different features of the entrapment of an air pocket against the wall. In section 6.4 we investigate the forces generated by the wave impact. We will first focus on the effect of the impact parameters on the forces applied on the wall. Finally we will draw attention to the existence of vertical pressure gradients strong enough to lift up a concrete block located in front of the wall.

6.2 Numerical set-up for impact

Ideally, we would have simulated the shoaling of the wave on a sloping bottom and then the breaking and the impact. However, for practical CPU reasons we could not perform the simulation of the propagation of the approaching wave. Therefore we chose an unstable third order Stokes wave as the initial condition. The computational domain is a square (figure 6.1), its size equals the wavelength. Its wavelength is $\lambda = 10\text{ m}$ and its steepness is $ka = 0.55$ where k is its wave number and a its amplitude. The wave period is $T = 2.2175\text{ s}$ and the still water level (SWL) is 5 m . The domain above the free surface is filled with fluid 1, which is air governed by the linear equation of state (equation (4.18) page 61) with $P_{10} = 10^5\text{ Pa}$, $\rho_{10} = 1.334\text{ kg/m}^3$, $c_{10} = 340\text{ m/s}$. The domain below the free surface is filled with fluid 2, which is a mixture of fluid w and fluid a . Fluid w is water governed by the linear equation of state (4.22) (page 62) with $P_{w0} = 10^5\text{ Pa}$, $\rho_{w0} = 1027\text{ kg/m}^3$, $c_{w0} = 1500\text{ m/s}$ and fluid a is air governed by the polytropic equation of state (4.20) (page 62) with $P_{a0} = 10^5\text{ Pa}$, $\rho_{a0} = 1.334\text{ kg/m}^3$, $k = 1.4$.

The mesh we used is a 200×375 cells mesh. The horizontal dimension of a cell is constant $\Delta x = 0.05\text{ m}$. The vertical dimension of a cell varies with the altitude z . From the bottom, the first cell has a vertical dimension of $7.20 \cdot 10^{-2}\text{ m}$, then the vertical



(a) First set of boundary conditions. $t/T = 0$. (b) Second set of boundary conditions. $t/T = 0.2706$.

Figure 6.1: Numerical set-ups.

size of the cells decreases with z according to a geometric progression with a common ratio of 0.98618 up to $z = 4\text{ m}$. Then from $z = 4\text{ m}$ to $z = 7\text{ m}$ the vertical dimension of the cells is constant and equals $1.67 \cdot 10^{-2}\text{ m}$. Finally, from $z = 7\text{ m}$ to $z = 10\text{ m}$, the vertical dimension of the cells increases with z according to a geometric progression with a common ratio of 1.0141.

The time step is re-evaluated by the code at each time step by the CFL condition in equation (3.96) (page 53). It depends on the highest sound speed among all the cells at a given time, and therefore on the volume fraction of air in fluid 2.

We simulate the impact of the wave on the right side wall using two stages. The first stage is the simulation of the destabilization of the initial Stokes wave and the initiation of breaking. This first stage lasts until the "breaking point", which is defined as being the first moment a part of the wave front becomes vertical. This stage begins at $t/T = 0$ and finishes at $t/T = 0.2706$. For this stage a first set of boundary conditions is used (figure 6.1(a)). Symmetry conditions are set at the top and bottom boundaries of the domain and periodic conditions are set at the left and right boundaries. For a symmetry condition the state in the ghost cell is the same as the state in the adjacent cell except that the normal velocities are opposite. The velocity in the ghost cell thus reads: $\underline{V} - (\underline{V} \cdot \underline{n}_f)\underline{n}_f$ where \underline{V} is the velocity in the adjacent cell and \underline{n}_f is the unit vector normal to the boundary face. For periodic conditions the state in the ghost cell at the right side of the domain is set to the state in the boundary cell at the left side and vice versa. The periodic boundary conditions allow for the propagation of the wave as if the domain had an infinite length. This first stage is unique for all the simulations presented in this chapter. At the end of this first stage we obtain a "periodic" solution for a wave that is about to break as shown in figure 6.1(b).

The second stage is the impact phase, where the wave breaks on the vertical wall. It begins at $t/T = 0.2706$ and is finished by the end of the simulation $t/T = 0.5411$. For this stage a second set of boundary conditions is used (figure 6.1(b)). A symmetry condition is used at the upper boundary. The left, bottom and right boundaries are

	$D = 0.10$	$D = 0.08$	$D = 0.06$	$D = 0.04$
$\beta = 0.001$		x		
$\beta = 0.01$		x		
$\beta = 0.05$	x	x	x	x

Table 6.1: Investigated parameters values.

now wall conditions. For a wall condition, the state in the ghost cell is the same as the state in the adjacent cell except that the velocity reads: $-\underline{V}$ where \underline{V} is the velocity in the adjacent cell.

At the beginning of this second stage, we were able to set different values for the air mass fraction y in the liquid phase in order to avoid recomputing the first phase for each investigated case. This implies that we assumed that the air content has a negligible influence on the propagation of the wave in the first stage. Figure 6.5 shows the superimposition of the free surface for all three values of beta at the same given time before the impact. One can notice that the air content has effectively a very small influence on the free surface dynamics before the impact. In order to achieve the change in y we recomputed the field variables corresponding to the wanted value of y from the state arising from the first stage, and used those new field variables as the initial state for the second stage.

At the beginning of this second stage, we were also able to set different impact conditions. Let us define the "breaking distance" D as the dimensionless distance from the wall at which the breaking point occurs. It is non-dimensionalized by the wave length λ . In order to simulate the impact for different values of the breaking distance, we introduced a horizontal shift in the solution between the first stage and the second stage. As the solution arising from the first stage is periodic, such a horizontal shift does not imply any disturbance in the solution. This second stage is repeated for each investigated case.

In this way we investigated, for a constant breaking distance $D = 0.08$, 3 levels of aeration in fluid 2, $y = [1.3000 \cdot 10^{-6}; 1.3118 \cdot 10^{-5}; 6.8348 \cdot 10^{-5}]$ corresponding to $\beta_0 = [0.001; 0.01; 0.05]$ at atmospheric pressure. And we investigated for a constant value of the air content $\beta = 0.05$, 4 values for the breaking distance $D = [0.10; 0.08; 0.06; 0.04]$. The investigated cases are shown in table 6.1. In the following, when not mentioned, the default value of D is 0.08. We chose these values of β because they allow for the investigation of a wide range of compressibility. Indeed, for these air content values the corresponding sound speeds in fluid 2 are respectively $c_{20} = [358.7; 116.99; 53.54] \text{ m/s}$. We chose the values of the breaking distance D for the impact to correspond to the "well developed plunging breakers" type in the classification of (Schmidt et al. 1992) (figure 2.1 page 7) or to the "plunging breaker" types in the classification of (Oumeraci et al. 1993) (figure 2.2(b) or 2.2(c) page 7), because these types are reported to be some of the most violent ones as the highest values of pressure at the wall are observed for these types. We sought to investigate the effect of a slight change in D on the impact dynamics and on the resulting forces. In our simulations the wave front was never vertical on its full height thus the "perfect breaking" of Nagai (1960) (figure 2.3 page 8) was not observed.

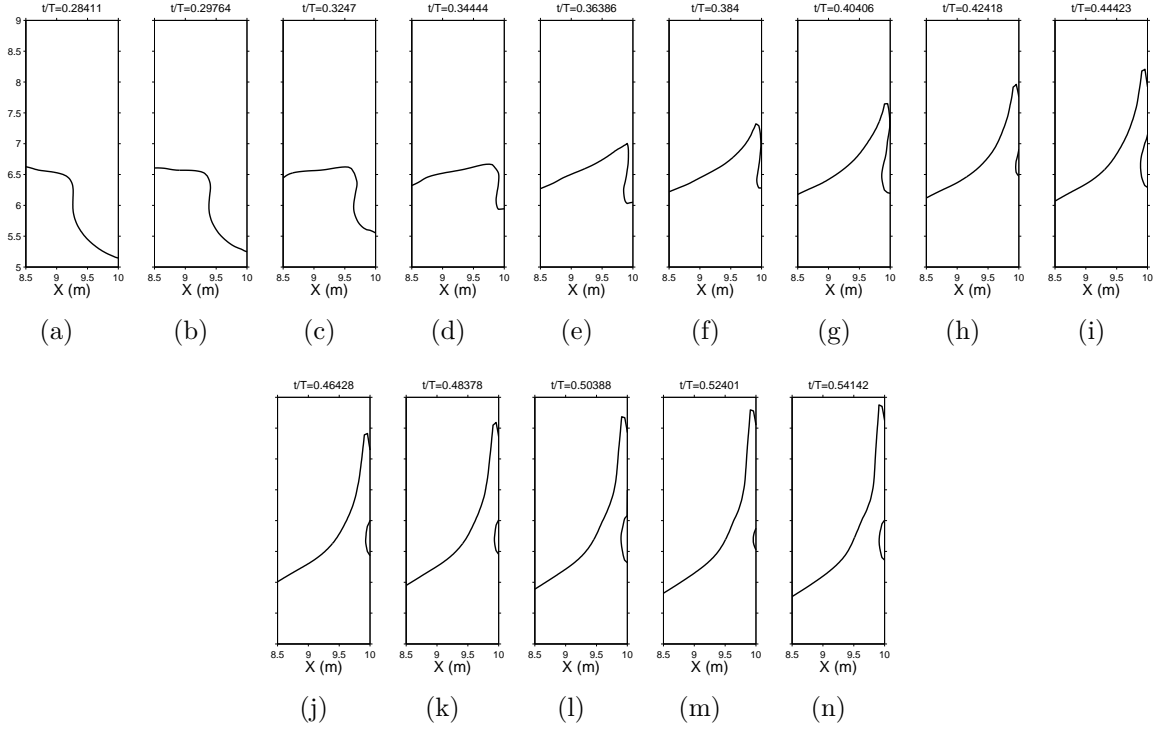


Figure 6.2: Free-surface profiles at impact for $\beta = 0.001$ and $D = 0.08$.

6.3 Wave impact dynamics

In this section we investigate the dynamics of the flow at the wave impact. The free surface dynamics is studied first and then the pressure field is analysed. Let us remark that in the following the times are non-dimensionalized by the wave period T .

6.3.1 Free-surface dynamics

Figures 6.2 to 6.8 show the free surface profiles close to the wall between $X = 8.5 \text{ m}$ and $X = 10 \text{ m}$ for all simulated cases. The time span for these figures is from the first record we have after the beginning of the second simulation stage to the end of the second simulation stage.

Let us remark that the free surface is defined as the interface between fluid 1 and fluid 2 which is mathematically defined as the jump in the volume fraction which varies continuously at the interface due to numerical diffusion. In the following, the numerical free-surface is defined as the iso- $\alpha = 0.5$ line.

The value of beta increases through figures 6.2, 6.3 and 6.4.

Let us focus on the description of the case $\beta = 0.001$ and $D = 0.08$ (figure 6.2). Figures 6.2(a) to 6.2(e) show the wave overturning and entrapping an air pocket against the wall. In figure 6.2(f) the wave crest enters in contact with the wall. After that, the wave crest jet is deflected in an upward jet along the wall. The jet continues to rise up the wall until the end of the simulation but its ascending velocity seems to decrease with time. Let us draw attention to the fact that the time of contact between the free

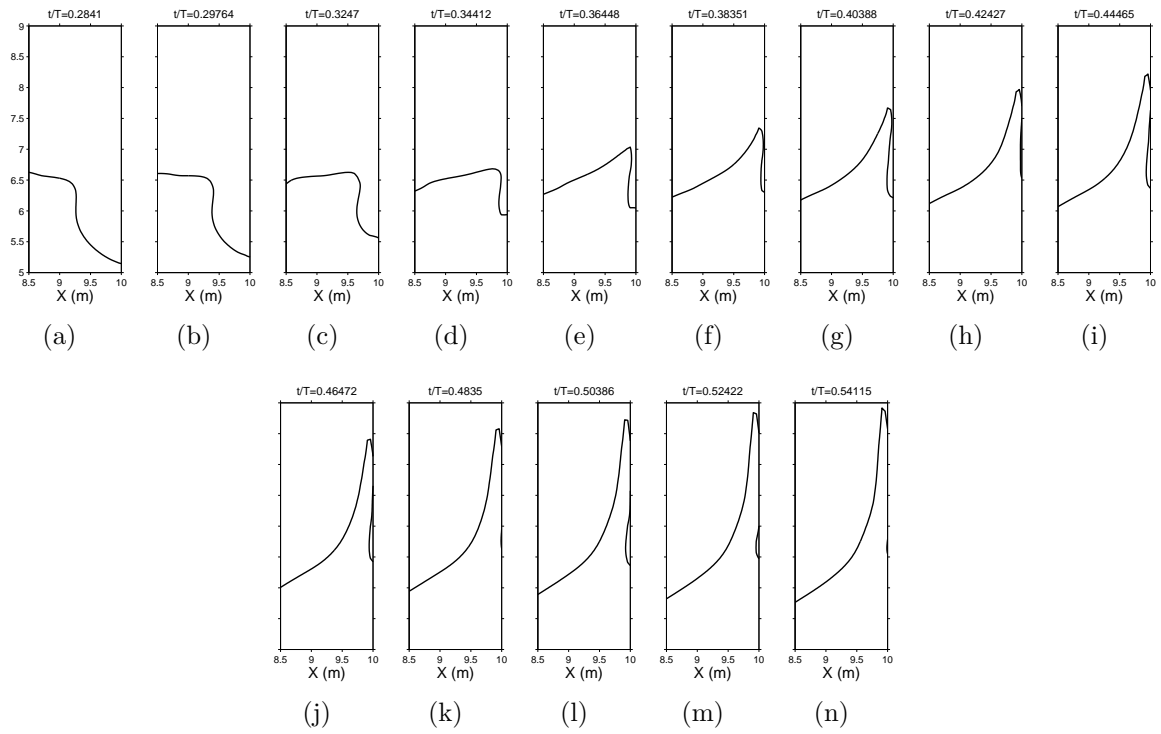


Figure 6.3: Free-surface profiles at impact for $\beta = 0.01$ and $D = 0.08$.

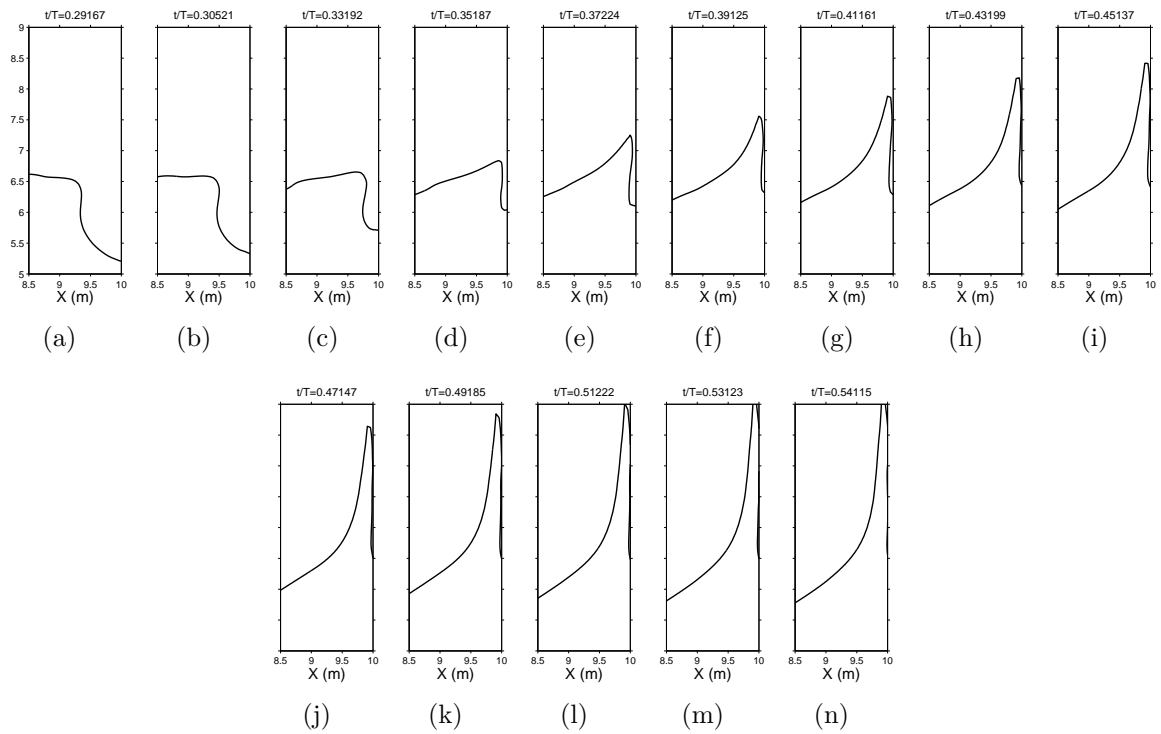


Figure 6.4: Free-surface profiles at impact for $\beta = 0.05$ and $D = 0.08$.

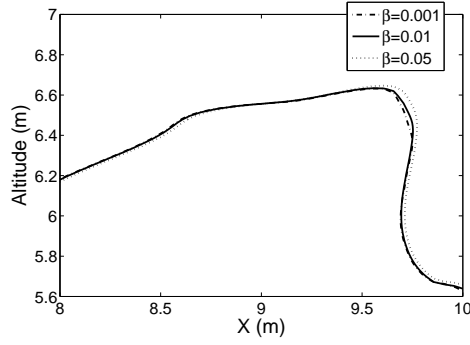


Figure 6.5: Influence of β on the free-surface position before the impact, $t = 0.3292$ and $D = 0.08$.

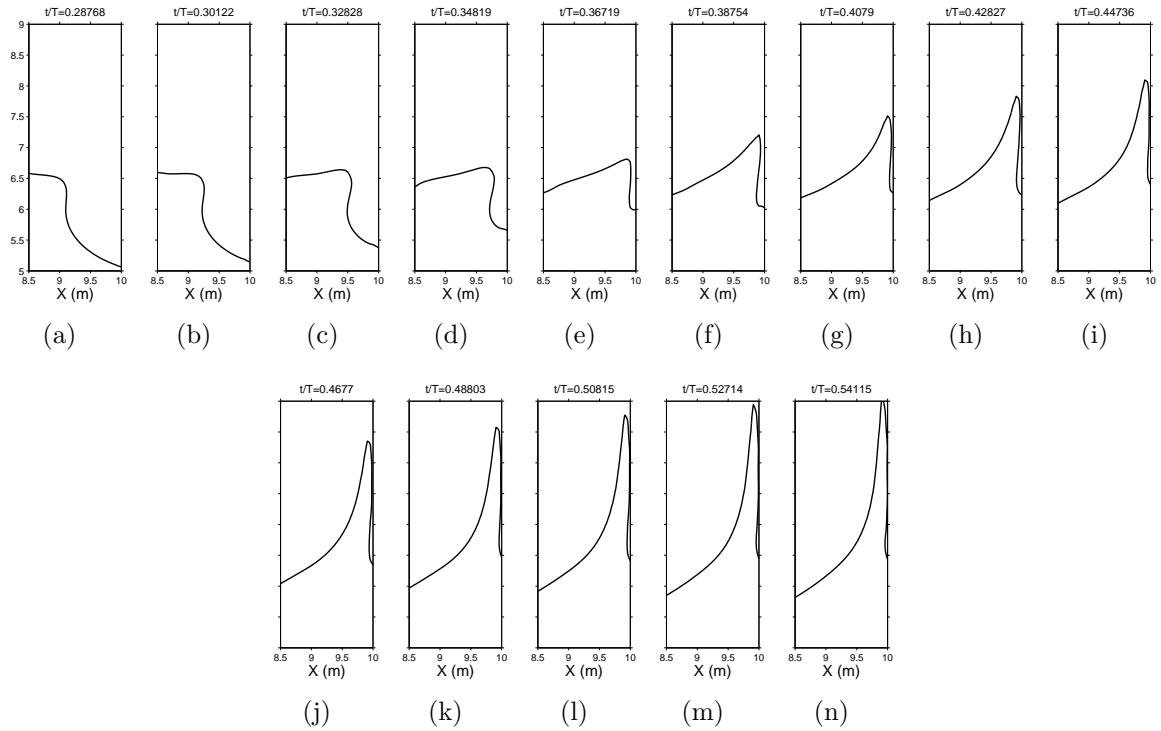


Figure 6.6: Free-surface profiles at impact for $\beta = 0.05$ and $D = 0.10$.

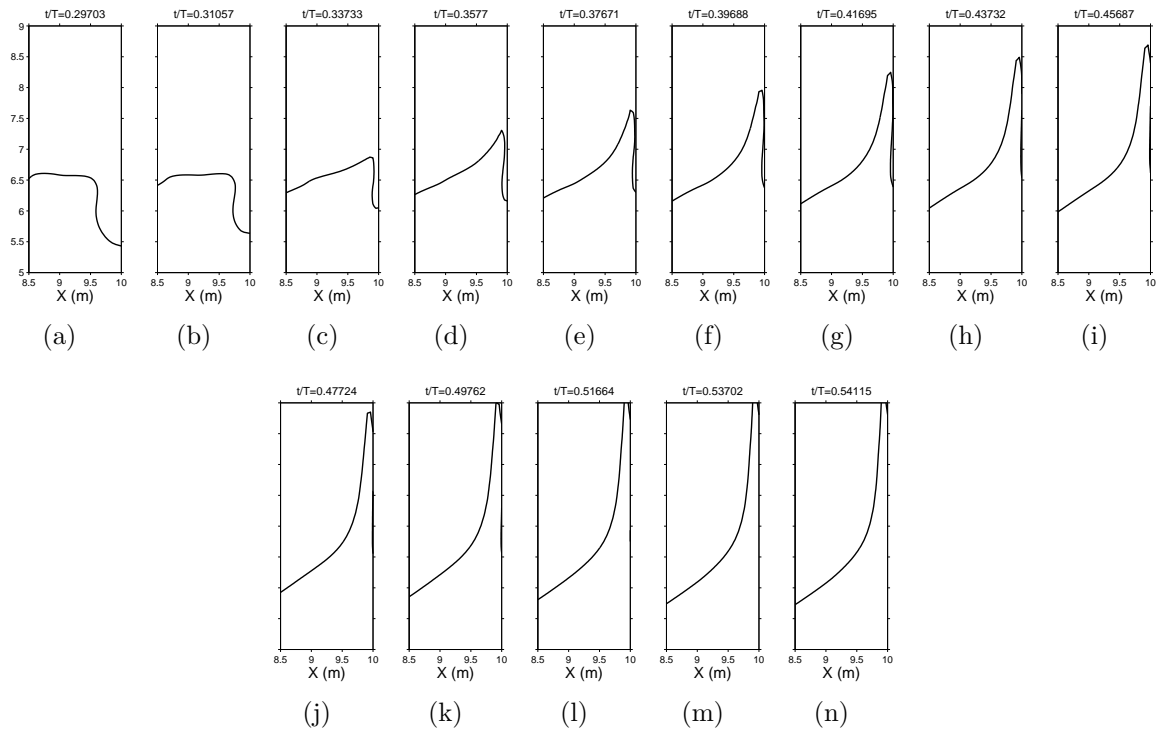


Figure 6.7: Free-surface profiles at impact for $\beta = 0.05$ and $D = 0.06$.

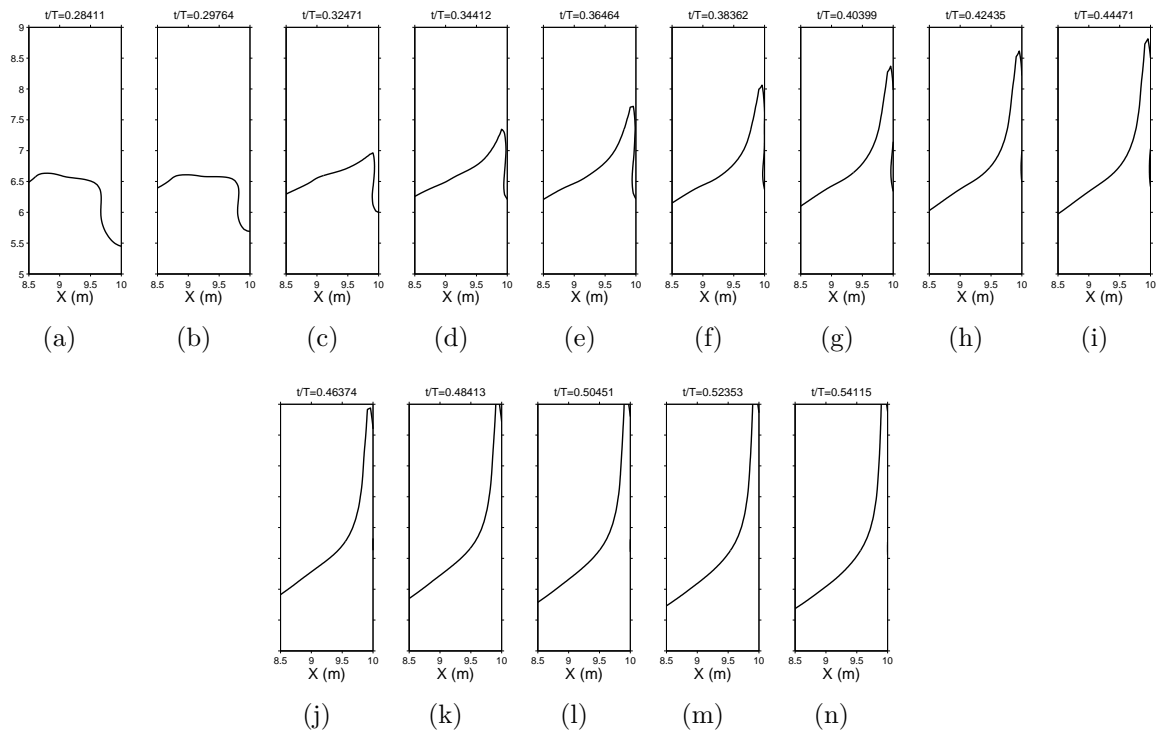


Figure 6.8: Free-surface profiles at impact for $\beta = 0.05$ and $D = 0.04$.

surface and the wall is very dependent on the iso- α value we chose to define the free surface. Moreover, it will be shown in section 6.3.5 that the time of maximum pressure at the wall, which currently defines the "impact time" in the literature, does not equal the time of contact between the free surface and the wall found here.

From figure 6.2(f) to 6.2(n), the horizontal dimension of the air pocket alternately increases (figures 6.2(f) to 6.2(g), 6.2(h) to 6.2(i), 6.2(j) to 6.2(l) and 6.2(m) to 6.2(n)) and decreases (figures 6.2(g) to 6.2(h), 6.2(i) to 6.2(j) and 6.2(l) to 6.2(m)).

For $\beta = 0.01$ and $D = 0.08$ (figure 6.3) the contact between the free surface and the wall seems to occur at the same time as for the previous case, which was expected as we showed that the influence of β is small before impact. However, the entrapped pocket has a smaller horizontal dimension and its shape is more stretched in the vertical direction as one can see between figure 6.2(l) and 6.3(l).

For $\beta = 0.05$ and $D = 0.08$ (figure 6.4) the contact between the free surface and the wall seems to occur at the same time as for the previous cases. The entrapped pocket has a lower horizontal dimension than for $\beta = 0.01$ as one can see between figure 6.3(l) and 6.4(l). Therefore the volume of the entrapped air pocket seems to decrease with β .

D decreases through figures 6.6,6.4,6.7 and 6.8. So the approaching wave can be seen to be closer to the wall in figures 6.6(a),6.4(a),6.7(a) and 6.8(a). For $\beta = 0.05$ and $D = 0.08$ (figure 6.4) the contact between the free surface and the wall seems to occur earlier than for the larger D value ($D = 0.10$). Indeed, the contact between the free surface and the wall for the case ($\beta = 0.05, D = 0.10$) seems to occur at $t/T = 0.4079$ (figure 6.6(g)), whereas for the case ($\beta = 0.05, D = 0.08$) it seems to occur at $t/T = 0.39125$ (figure 6.4(f)). For the case ($\beta = 0.05, D = 0.06$) the contact between the free surface and the wall seems to occur at $t/T = 0.37671$ (figure 6.7(e)). And for the case ($\beta = 0.05, D = 0.04$) the contact between the free surface and the wall seems to occur at $t/T = 0.34412$ (figure 6.8(d)). Therefore the time of contact between the free surface and the wall increases with D .

The horizontal dimension of the air pocket also increases with D . Indeed, one can see this feature by comparing figures 6.6(j), 6.4(j), 6.7(j) and 6.8(j).

6.3.2 The vertical jet along the wall

One can see in figures 6.2 to 6.8 that eventually there is a jet going upward against the wall. In this section we want to determine the altitude reached by this jet in function of the two parameters (β and D).

We saw in chapter 2 that two mechanisms for the generation of a vertical jet along the wall are highlighted in the literature. The first one is when the waterline (point of contact between the free surface and the wall) rises up along the wall and generates such a vertical jet. This phenomenon is often called "sloshing". The second one is when the vertical jet is generated by the wave crest hitting the wall and being deflected upward to follow a new vertical upward trajectory along the wall. This phenomenon is the classic fluid mechanics problem of a jet deflection by a plane. At the limit between these two mechanisms, there is the case where the waterline and the wave crest reach the same altitude on the wall at the same time. This is the "flip-through" impact type

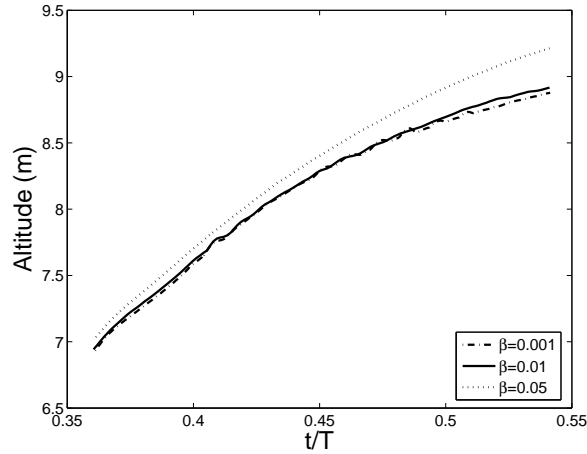


Figure 6.9: Influence of the air content on the altitude of the vertical jet at the wall, for $D = 0.08$.

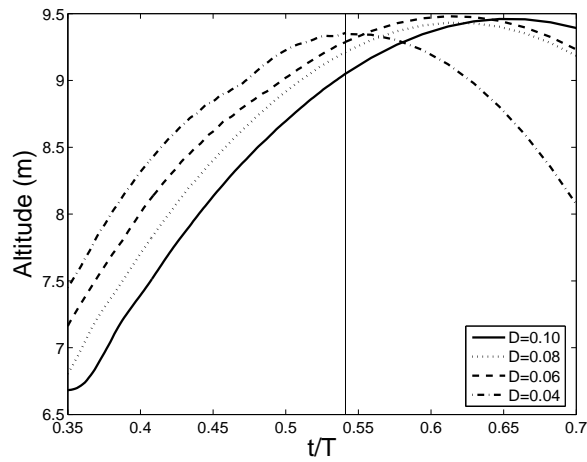


Figure 6.10: Influence of D on the altitude of the liquid jet at the wall. Extrapolated data after the end of simulations (vertical line).

of Cooker & Peregrine (1992) reviewed in chapter 2. But we have seen above that for all our cases the wave front has a concave shape and there is the entrapment of an air pocket. This implies that the wave crest hits the wall at an altitude that the waterline could not have reached in the first place. Therefore the mechanism that generates this vertical jet in all our cases is the second one (deflected jet).

In figure 6.9, one can see that the altitude of the jet at a given time increases with β .

Regarding the influence of D on the altitude of the jet, it is more difficult to compare the simulations. Indeed, as we change the value of D , the beginning of the rising of the jet along the wall is not the same. Moreover, we did not simulate long enough to see the jet course falling back down. Thus we propose here to assume that the trajectory of the maximum position of the jet verifies a second order polynomial and we extrapolate the data after the maximum simulated time. Figure 6.10 shows the simulated data and

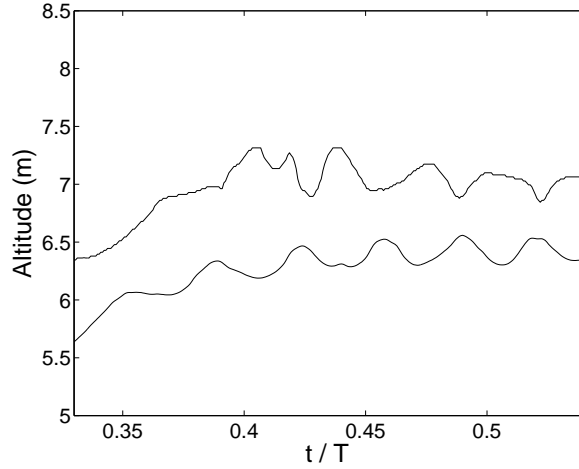


Figure 6.11: Air-pocket lower and upper extremities position at the wall for $\beta = 0.001$ and $D = 0.08$.

the interpolated data for the altitude of the jet for all values of D . For the simulated data in figure 6.10, at a given time the altitude of the jet decreases with D . For the interpolated data in figure 6.10, the maximum variation in the maximum altitude attained by the jet is of 1.5 % (between $D = 0.06$ and $D = 0.04$).

Therefore we can conclude that the maximum altitude attained by the vertical jet along the wall increases with β but is almost not influenced by a variation in D .

6.3.3 The air pocket

In section 6.3.1 we noticed some oscillations in the horizontal dimension of the entrapped air pocket. For example, for $\beta = 0.001$ the horizontal dimension of the air pocket presents obvious oscillations. From figure 6.2(g) to 6.2(h) its volume decreases, then it increases from figure 6.2(h) to 6.2(i), and it decreases again from figure 6.2(j) to 6.2(k).

One can also observe such an oscillation in the case $\beta = 0.01$ (figure 6.3). However it is less obvious for the cases with $\beta = 0.05$, whatever the value of D . One may see in figures 6.4, 6.7 and 6.8 that the pocket sometimes seems to totally disappear. But this is only an effect of the choice of the iso- α value for the definition of the numerical free-surface.

An important point to notice is that the numerical model does not account for the fragmentation of the air pocket. Indeed, the fragmentation process implies a relative motion between both fluids at small scale and our code has been developed under the assumption of no slip between fluids (see section 3.4.4).

In order to estimate the oscillation in the volume of the air pocket, the time evolution of the position of the air-pocket extremities for the case $\beta = 0.001$ and $D = 0.08$ is plotted in figure 6.11. One can see that the extremities' oscillations are out of phase. The air pocket thus experiences an oscillation in its vertical size. One can also notice that the air pocket has an upward motion until $t/T = 0.4$ and then stabilizes at a constant altitude.

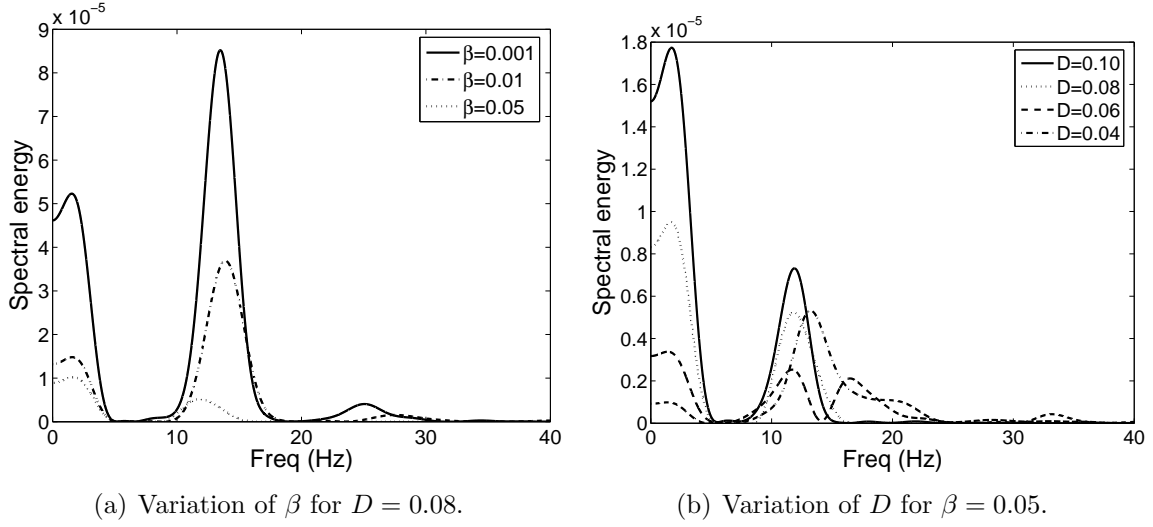


Figure 6.12: Fourier transforms of waterline position.

Figure 6.12 shows the Fourier transforms of the air-pocket lower extremity position for all the cases. There are two dominant frequencies for all the investigated parameters values except for $D = 0.06$ in figure 6.12(b) where 3 peaks are observed. The low frequency is constant with β and D . This frequency seems to be due to the global upward motion (or the average derivative) (as seen in figure 6.11) of the pocket.

The frequency value of the second peak (figure 6.12) varies with the parameters β and D . Let us try to estimate the natural frequency of oscillation of the entrapped air pocket. The frequency of an air pocket can be estimated by using the following equation which gives the natural frequency of the adiabatic pulsation of a spherical bubble (Leighton 1994):

$$f_0 = \frac{1}{2\pi R_0} \sqrt{\frac{3\gamma P_0}{\rho_{20}}} \quad (6.1)$$

where R_0 is the steady state radius, γ is the specific heat ratio of air and P_0 the atmospheric pressure. ρ_{20} is the density of fluid 2 at atmospheric pressure. As ρ_{20} depends on β , the variation of beta we investigated implies a noticeable variation in f_0 . However equation (6.1) is for a spherical bubble and one can see in figures 6.2 to 6.8 that the air pocket in our cases has a lens shape. But we can use this equation as an approximation by replacing R_0 by a typical length scale of the air pocket.

(Oumeraci, Partensky & Tautenhain 1992) proposes another way to compute the natural oscillation frequency of an air pocket through the simple relationship:

$$f_0 = \frac{k_a}{2R_0} \quad (6.2)$$

where $k_a = 5.35 \text{ m/s}$ is a coefficient established by (Oumeraci et al. 1992).

From the air-pocket extremities positions, we can estimate the vertical dimension of the pocket. Then we use equation (6.1) and (6.2) with half of the pocket height as R_0 . We obtain the values for R_0 and the deduced frequencies in tables 6.2 and 6.3. The estimated size of the pocket increases with β (table 6.2) and increases

	$\beta = 0.001$ $D = 0.08$	$\beta = 0.01$ $D = 0.08$	$\beta = 0.05$ $D = 0.08$
Estimated R_0 (m)	0.346	0.467	0.605
f_0 (eq. (6.1))(Hz)	9.55	7.07	5.46
f_0 (eq. (6.2))(Hz)	7.74	5.72	4.42
Simulations high frequency (Hz)	13.5	14	11.8

Table 6.2: Estimation of the pocket natural frequency for all the β values and $D = 0.08$.

	$D = 0.10$ $\beta = 0.05$	$D = 0.08$ $\beta = 0.05$	$D = 0.06$ $\beta = 0.05$	$D = 0.04$ $\beta = 0.05$
Estimated R_0 (m)	0.617	0.605	0.556	0.373
f_0 (eq. (6.1))(Hz)	5.35	5.46	5.94	8.85
f_0 (eq. (6.2))(Hz)	4.34	4.42	4.81	7.17
Simulations high frequency (Hz)	12	11.8	11.7 and 16.5	13.2

Table 6.3: Estimation of the pocket natural frequency for all the D values and $\beta = 0.05$.

with D (table 6.3). In table 6.2 the results from the model in equation (6.1) are close to but a little larger than the ones from the model in equation (6.2). In table 6.3 the results from the model in equation (6.1) are a little smaller than the ones from the model in equation (6.2), but the values are close. The characteristic length we take for our air pocket is approximative and its shape is not spherical. Although the higher frequency in the spectra in figure 6.12 and the theoretical frequencies do not compare quantitatively, their order of magnitude is the same thus this frequency might be related to the oscillation of the air pocket.

In figure 6.12(a) the amplitude of the first peak and the amplitude of the second peak decrease with β .

In figure 6.12(b) the amplitude of the first peak increases with D . The amplitude of the second peak also increases with D except for the case $D = 0.04$ for which the energy is split between a second and a third peak whose amplitude is therefore lower.

A distinct third peak can be distinguished for most of the cases. This might indicate the presence of a higher frequency mode. Higher frequencies might be generated when the pocket is split in two parts as for instance in figure 6.4(n).

6.3.4 Flow Mach number

In this section the aim is to evaluate the Mach number in the flow. (Peregrine & Thais 1996) mentioned that the vertical jet rising along the wall may be supersonic in the case of "flip-through" impact. Although our cases are not of the "flip-through" type, we want to know if the waterline reaches a supersonic velocity.

When observing the velocity field from our simulations, we saw that the location where the velocity magnitude records highest values is in the air pocket, close to the wall. So there is no use in computing a Mach number throughout the whole domain. We only computed a Mach number based on the vertical velocity of the waterline and

	$\beta = 0.001$ $D = 0.08$	$\beta = 0.01$ $D = 0.08$	$\beta = 0.05$ $D = 0.08$
Max Mach	0.0494	0.1883	0.2177

Table 6.4: Mach number for all β values.

	$\beta = 0.05$ $D = 0.10$	$\beta = 0.05$ $D = 0.08$	$\beta = 0.05$ $D = 0.06$	$\beta = 0.05$ $D = 0.04$
Max Mach	0.1819	0.2177	0.2639	0.4563

Table 6.5: Mach number for all D values.

the sound speed in the liquid mixture at standard pressure. It reads:

$$\text{Mach} = \frac{\text{Waterline velocity}}{c_{20}(\beta_0)} \quad (6.3)$$

We show in table 6.4, the maxima of the Mach number for all β values. The maximum Mach number increases with β .

We show in table 6.5, the maxima of the Mach number for all β values. The maximum Mach number decreases with D .

The maximum Mach number value we found is 0.45 for the case with the largest air content and the smallest breaking distance. So we conclude that there are no supersonic flows for the wave-impact type we simulated. However, a flow is usually considered incompressible when the Mach number stays below 0.3 and we showed that in the case of our simulations we find values that go beyond this threshold. This indicates the importance of simulating wave impacts with compressible models.

6.3.5 Spatio-temporal pressure evolution

Let us introduce a new field variable, P' which is obtained by removing the hydrostatic pressure from the pressure field. By doing this we only consider the unsteady contribution within the pressure field. However, computing the hydrostatic pressure requires us to use the position of the free surface. And when the wave overturns, a unique free surface for a given abscissa cannot be defined. It becomes even more difficult when an air pocket is entrapped and eventually splits. When the free-surface is multivalued we based the computation of this variable on the lowest altitude of the free surface for a given abscissa. Therefore one must be careful when interpreting this variable P' .

Figure 6.13 shows a time sequence of the P' field for $\beta = 0.05$ and $D = 0.08$. In figure 6.13(a) at $t/T = 0.3451$, one can see a positive pressure perturbation (P' is around $10^5 Pa$) in the bubbly liquid around the air pocket. At this time there is an area of negative P' at the foot of the wall. In figure 6.13(b) at $t/T = 0.3750$, the pressure perturbation in the bubbly liquid has propagated downward and seaward as a circular wave. At these times there is an area of negative pressure perturbation at the location where the positive perturbation was located. In figure 6.13(c) at $t/T = 0.3804$, the circular compression wave has reached the bottom close to the wall and its amplitude intensifies when the bottom is reached, certainly because the reflected wave

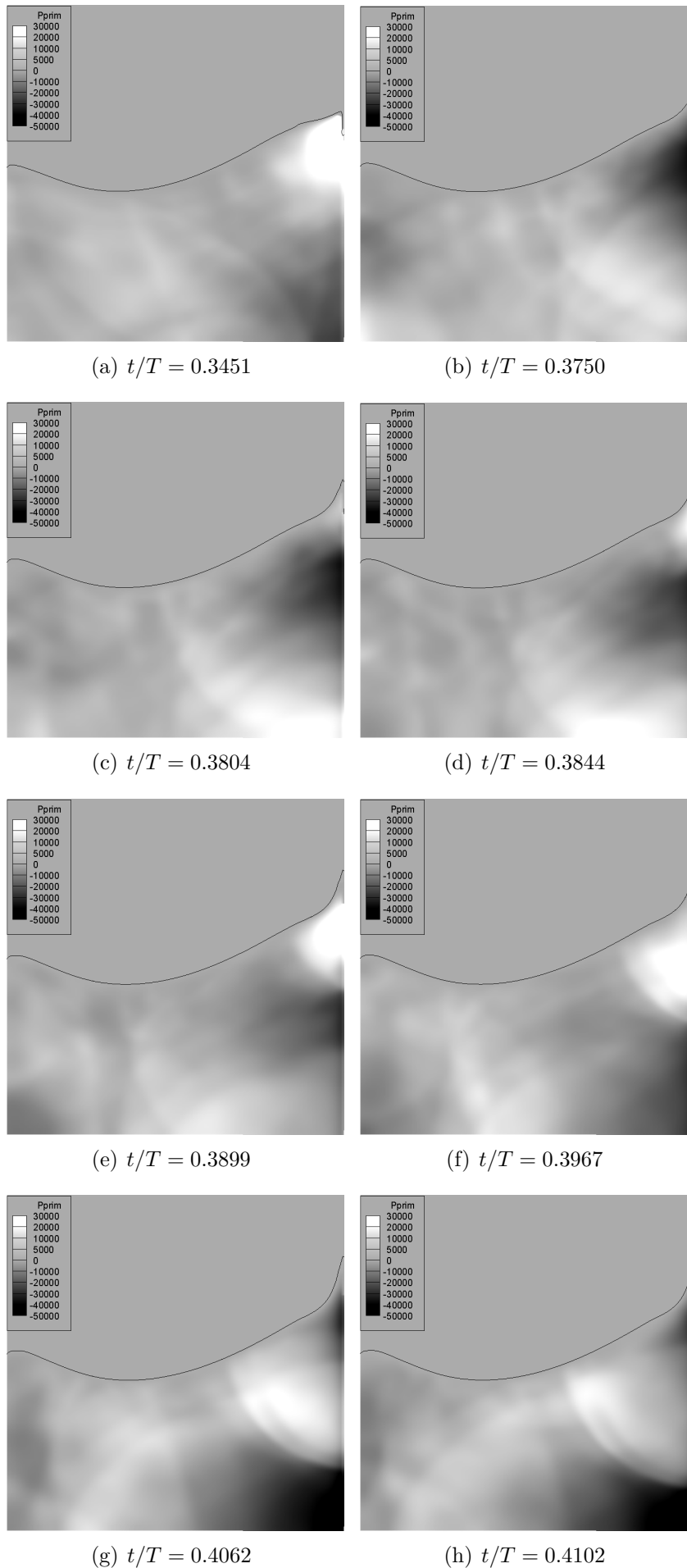


Figure 6.13: Relative Pressure field sequences for $\beta = 0.05$ and $D = 0.08$.

superimposes itself to the incident wave. In figure 6.13(d), a second positive pressure perturbation (around $4 \cdot 10^4 Pa$) occurs in the bubbly liquid around the location of the air pocket. And the compression wave at the bottom has moved seaward. Then in figures 6.13(e) and 6.13(f), this secondary positive perturbation propagates downward and seaward in the bubbly liquid, starting to become a circular wave. In figures 6.13(g) and 6.13(h), this second circular wave is fully developed and continues to propagate downward and seaward in the bubbly liquid. We chose not to show further snapshots in time because from $t/T = 0.4102$ the primary wave has been reflected back on to the left wall and is returning back to the middle of the domain to meet the secondary wave.

In this case, there are simultaneous opposite pressure perturbations at the altitude of the air pocket and at the foot of the wall.

6.3.6 Evolution of the pressure distribution at the wall: Oscillations

In the following, we call "pressure" the magnitude $P - P_0$, which is the absolute pressure from which we remove the constant atmospheric pressure.

Figure 6.14 shows the time evolution of the pressure distribution at the wall for all β values and for $D = 0.08$.

For the $\beta = 0.001$ case, one can see in figure 6.14(a) that the pressure at the wall presents several extrema around 1 m above the still water level (SWL). These extrema are localized in space. One can see that the pressure at this altitude oscillates, indeed the pressure on the wall at a given altitude alternates between being negative and positive. The first maximum is reached for $t/T = 0.3466$ at the altitude of 6.034 m, and has a value of $(1.181 \cdot 10^5 Pa)$. In the following we will call "primary maximum" the first occurrence of a pressure maximum. One can notice that in figure 6.2 the free surface (which is defined as the $\text{iso-}\alpha = 0.5$ line) has not made contact with the wall for $t/T = 0.3466$ yet, which is the time of occurrence of the first pressure maximum.

Figure 6.15(a) shows a zoom in the impact zone at the time of the primary maximum and the altitude of the primary maximum. One can notice in figure 6.15(a) that the altitude of the primary maximum is just below the lower extremity of the air pocket.

For the $\beta = 0.01$ case, one can see in figure 6.14(b) that the primary maximum occurs a little earlier than for the previous case, around $t/T = 0.3468$ at the altitude of 5.97 m and has the value $1.11 \cdot 10^5 Pa$. The altitude of the primary maximum is just below the bottom of the air pocket (figure 6.15(b)).

For the $\beta = 0.05$ case, in figure 6.14(c), the primary maximum seems to occur even earlier, at around $t/T = 0.3465$, at the altitude of 5.97 m. The altitude of the primary maximum is just below the bottom of the air pocket (figure 6.15(c)). The primary maximum pressure value is $1.10 \cdot 10^5 Pa$. The primary maximum value is much larger than the other positive values of the oscillation. The oscillation is more damped than for the previous cases. One can notice a great pressure ($1.117 \cdot 10^5 Pa$) at the bottom of the wall for $t/T = 0.5312$. An important feature to notice in figure 6.14(c) is that just after the primary maximum, at the moment of the following negative maximum,

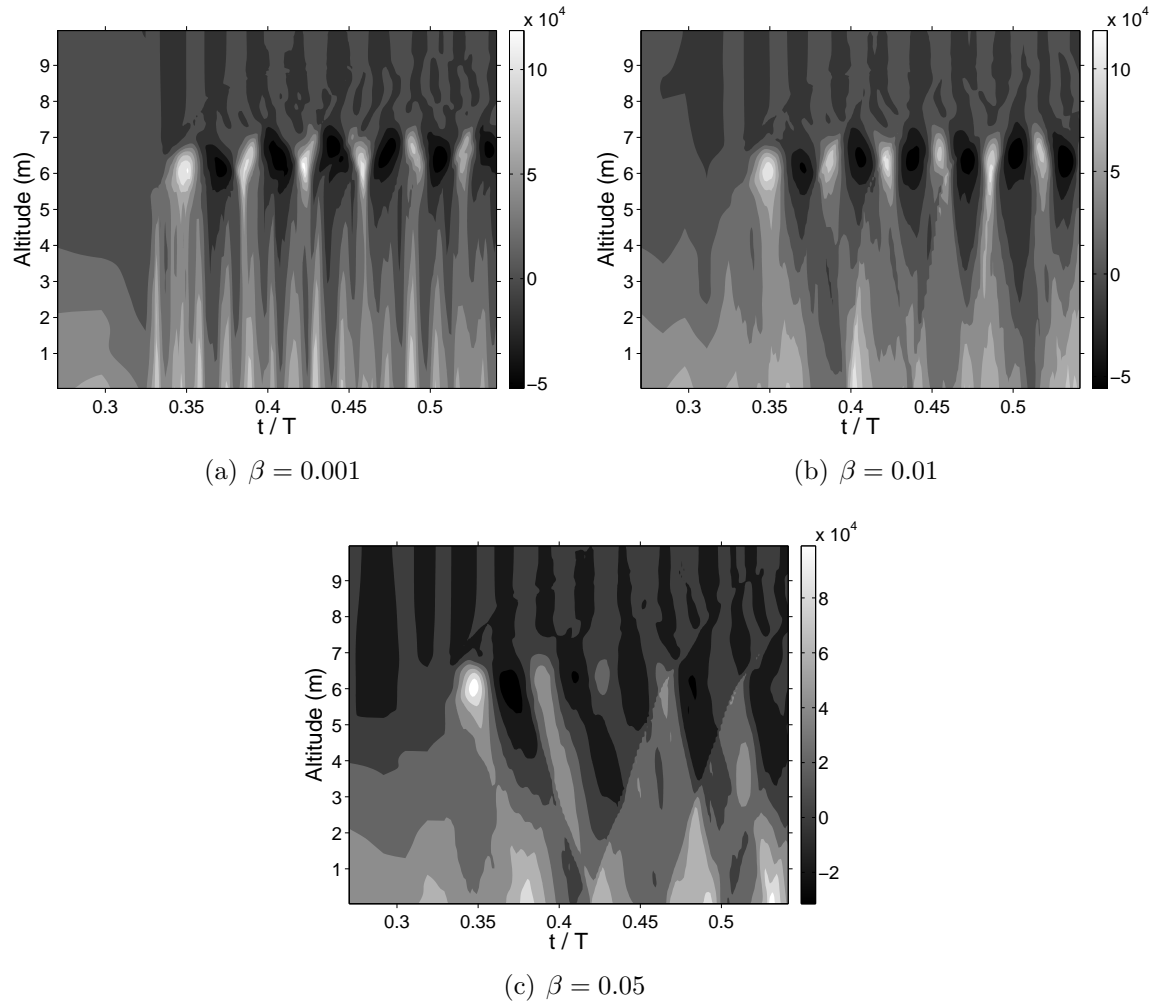


Figure 6.14: Evolution of the distribution of pressure $P - P_0$ at the wall for all β values and for $D = 0.08$.

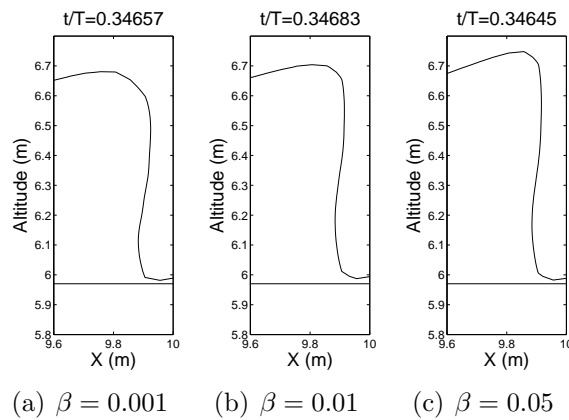


Figure 6.15: Free-surface position (dotted line) and altitude of the primary maximum pressure at the wall (solid line) for all β values and $D = 0.08$.

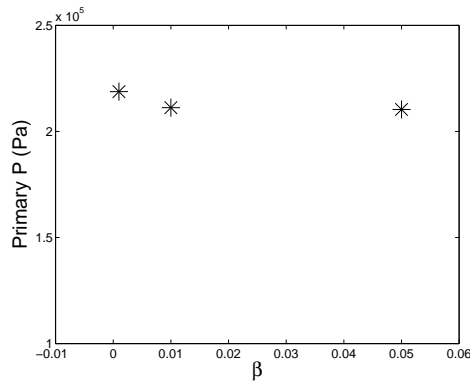


Figure 6.16: Primary pressure P maximum value for all β values and $D = 0.08$.

the pressure at the bottom of the wall is great. At this time there is a strong pressure gradient directed upward.

Another important feature, particularly visible in figure 6.14(a) and 6.14(b), is that the pressure extrema have an ascending movement until $t/T = 0.4$ and then stabilize at a constant altitude. This movement was also observed for the location of the air pocket in section 6.3.3, which indicates that the pressure extrema "follow" the air pocket.

When looking at the three figures 6.14, one can see that the maximums of pressure generate pressure waves that propagate downward along the wall. In the analysis of the global pressure field in section 6.3.5, we already remarked this feature and mentioned that for the case $\beta = 0.05$, there can be simultaneous opposite pressure perturbations at the altitude of the air pocket and at the foot of the wall. For the lowest value of β (0.001), the wave propagates very rapidly (the trajectories are almost vertical in figure 6.14(a)) because the sound speed is high. Thus the high pressures at the bottom occur well before the low pressures at the altitude of the air pocket do. Then when β increases the sound speed decreases, thus the pressure waves generated by each maximum propagate more slowly. So the trajectories for the case $\beta = 0.01$ in figure 6.14(b) are more inclined than the case $\beta = 0.001$. But the high pressures at the bottom still occur too early to be synchronous with the low pressures at the altitude of the air pocket. The trajectories for the case $\beta = 0.05$ in figure 6.14(c) are even more inclined than the case $\beta = 0.01$. In this case, although the high pressures at the bottom are not exactly synchronous with the low pressures at the altitude of the air pocket, one can see in figure 6.14(c) that there can be times for which a high pressure at the bottom and a low pressure at the altitude of the air pocket occur simultaneously.

Therefore, the occurrence of simultaneous opposite pressure perturbations at the altitude of the air pocket and at the foot of the wall strongly depends on the sound speed, and thus on the air content.

Globally, we can see that the time of occurrence of the primary maximum does not seem to vary with β but this was expected as we saw that the free-surface dynamics are independent from β . Figure 6.16 shows the value of pressure for the primary maximum. This pressure maximum decreases only slightly with β . It decreases of 3.5% from $\beta = 0.001$ to $\beta = 0.01$ and of 0.5% from $\beta = 0.01$ to $\beta = 0.05$. Figure 6.16 shows that the aeration level has almost no influence on the maximum pressure

at the wall. This confirms the results of (Bullock et al. 2007) (section 2.4.2.2 page 23) who found that both a low and high level of entrained air can create high pressures of similar magnitude. However, our conclusion may be specified in the sense that in our study we are in the presence of both air entrapment and air entrainment. Therefore we can specify our conclusion with the following: in the presence of the entrapment of an air pocket the level of entrained air does not have a large influence on the primary maximum pressure.

Regarding the magnitude of the primary pressures, we found another important feature that should be highlighted. For the mesh used (described in section 6.2), the horizontal dimension of the cells is 0.05 m and the interface diffuses over 4 to 5 cells. So in our simulations the wave crest jet experiences an important diffusion and its momentum is thus reduced. Therefore, in quantitative terms, the pressure maxima we found on the wall is certainly underestimated because of the numerical diffusion of the wave crest jet.

Finally, we can also conclude that the maximum pressure on the wall is not necessarily attained at the time of the primary maximum but can be attained later for another pressure maximum. The altitude of the primary maximum does not experience large variations with β . Indeed, the primary maximum pressure at the wall occurs in the air pocket as mentioned above. Thus the mechanism of generation of the primary maximum is likely to be a high pressure in the pocket. And as the free-surface dynamics and particularly the size and location of the pocket does not vary with β , neither does the altitude of the primary maximum pressure.

Figure 6.17 shows the time evolution of the pressure distribution on the wall for all values of D . For the $D = 0.10$ case (figure 6.17(a)), the primary maximum occurs at $t/T = 0.3645$, at the altitude of 5.987 m . The altitude of the primary maximum is above the bottom of the air pocket (figure 6.18(a)). The primary maximum pressure value is $1.147\ 10^5\text{ Pa}$. The primary maximum value is much larger than the other positive values of the oscillation. One can notice in figure 6.17(a) that just after the primary maximum, at the moment of the following negative maximum, the pressure at the bottom of the wall is large. At this time there is a strong pressure gradient directed upward. Figure 6.17(b), for the $D = 0.08$ case, is the same as figure 6.14(c) and has already been described above. It is just recalled here to compare the different values for D .

For the $D = 0.06$ case (figure 6.17(c)), the primary maximum occurs at $t/T = 0.3292$, at an altitude of 6.00 m . The altitude of the primary maximum is above the bottom of the air pocket (figure 6.18(c)). The primary maximum value is $1.027\ 10^5\text{ Pa}$ and is much larger than the other positive values of the oscillation. The same feature as in the $D = 0.06$ and $D = 0.08$ cases, that is to say a strong pressure gradient directed upward just after the primary maximum. One can notice large oscillating pressure values at the bottom of the wall. Particularly for $t/T = 0.5126$ it reaches $(1.048\ 10^5\text{ Pa})$.

For the $D = 0.04$ case (figure 6.17(d)), the primary maximum occurs at $t/T = 0.3112$, at an altitude of 6.00 m . The altitude of the primary maximum is above the bottom of the air pocket (figure 6.18(d)). The primary maximum value is $1.031\ 10^5\text{ Pa}$ and is larger than the other positive values of the oscillation. The same feature as in the $D = 0.10$ and $D = 0.08$ cases, that is to say a strong pressure gradient directed upward just after

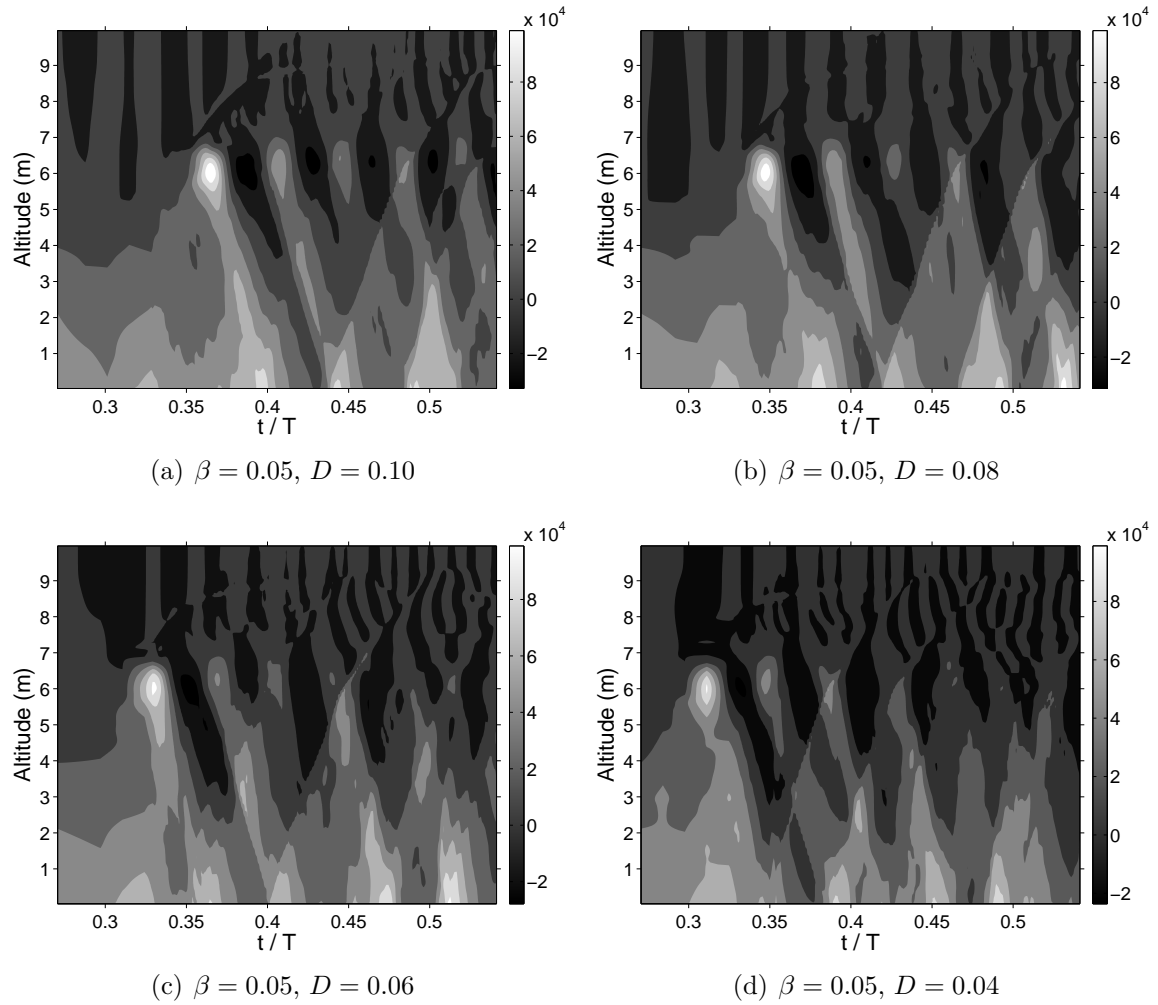


Figure 6.17: Evolution of the distribution of pressure $P - P_0$ at the wall for all D values.

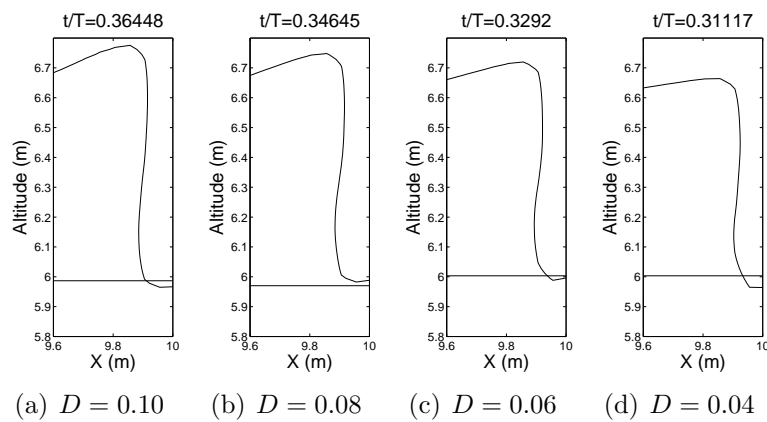


Figure 6.18: Free-surface position (dotted line) and altitude of the primary maximum pressure at the wall (solid line) for all D values and $\beta = 0.05$.

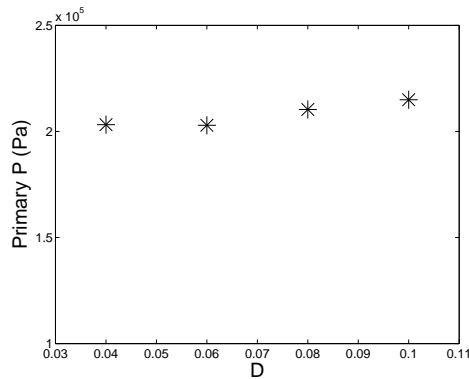


Figure 6.19: Primary pressure P maximum value for all D values.

the primary maximum. One can notice large oscillating pressure values at the bottom of the wall. Particularly for $t/T = 0.5126$ it reaches $(1.048 \cdot 10^5 \text{ Pa})$.

When looking at these three figures 6.17, one can see the same feature mentioned above that is that the maximums of pressure generate pressure waves that propagate downward along the wall. However β does not vary here, which implies that the pressure waves propagate with the same speed. Moreover, we saw that the value used here $\beta = 0.05$ is the most critical in the sense that there can be simultaneous opposite pressure perturbations at the altitude of the air pocket and at the foot of the wall. One can see this feature in figure 6.18. Therefore the occurrence of simultaneous opposite pressure perturbations at the altitude of the air pocket and at the foot of the wall does not depend on the breaking distance D at least in the considered range.

Globally, the time of occurrence of the primary maximum increases with D . The value of the primary maximum increases by 5% from $D = 0.04$ to $D = 0.10$. The pressure value for the primary maximum slightly increases with D (figure 6.19). It increases by 5.5% from $D = 0.04$ to $D = 0.10$. Therefore, in terms of pressure at the wall, an impact for which the wave breaks at a larger distance from the wall (larger values of D) is a little more critical than when the wave breaks closer to the wall, for the range of D we investigated.

The fact that the primary maximum pressure at the wall could be due to the air pocket is coherent with some studies in the literature. Indeed, Bagnold (1939) mentioned that "shock pressures occur only when the shape of the advancing wave front is such as to enclose an air cushion between it and the wall". Richert (1968), Partensky (1988) and Hattori et al. (1994) observed the most severe pressures at the wall when the wave hits the wall with a shape somewhere between the perfect breaking and the case with a very thin lens shaped air pocket. Oumeraci et al. (1995) found that the case with a large air pocket (figure 2.2(b)) resulted in the highest pressures, although the case with a small air pocket (figure 2.2(c)) gave the largest overall forces.

Regarding the altitude of the primary maximum pressure, Kirkgoz (1982), Partensky (1988) and Allsop, Vicinanza & McKenna (1996) found cases where the primary maximum was found above SWL. And (Oumeraci et al. 1995) reported that for the flip-through case, and for the small and large air-pocket cases, the maximum pressure also occurred at SWL. However, in our simulation cases we cannot confirm this as the

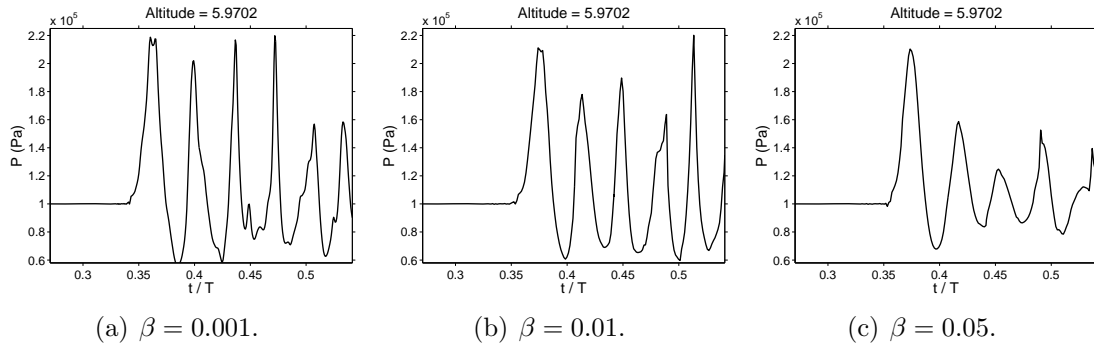


Figure 6.20: Pressure P history on the wall at the altitude of the first maximum pressure for all β values and for $D = 0.08$.

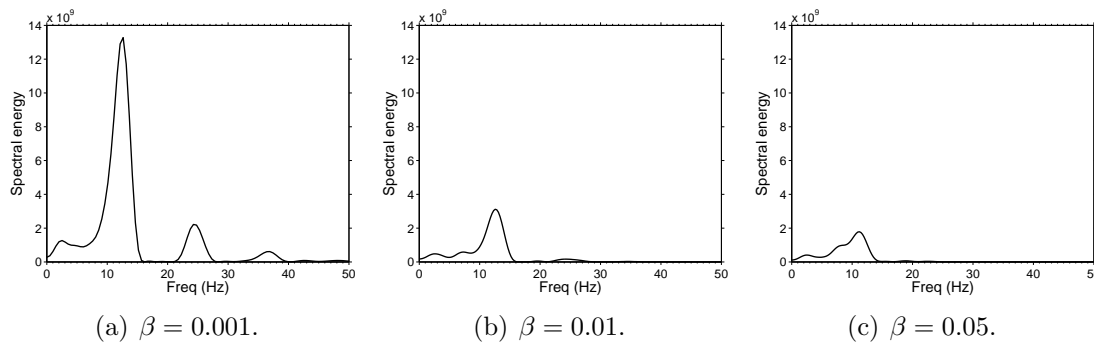


Figure 6.21: Fourier transform of the pressure history at the location of primary maximum pressure for all β values and for $D = 0.08$.

altitude we found for the primary maximum is 1 m above SWL.

Figure 6.20 shows the pressure history on the wall at the altitude of the primary maximum pressure for each value of β . We can see the oscillation observed in section 6.3.6. In figure 6.20 one can clearly see there are sub-atmospheric pressures after the primary maximum pressure. In their experiment, Bullock et al. (2007) also observed sub-atmospheric pressures for cases with $\beta \geq 0.05$. They specified that these sub-atmospheric pressures occur by the end of the first phase of expansion of the air pocket and they mentioned that similar behaviour has also been observed in previous studies (Oumeraci et al. 1993, Hattori et al. 1994, Walkden, Crawford, Bullock, Hewson & Bird 1996). Figure 6.21 shows the Fourier transform of the curves in figure 6.20. One can see that there is a clear dominant frequency in the three graphs in figure 6.21. These dominant frequencies correspond to the oscillation of the maximum pressure at the wall mentioned above. In figure 6.21(a), the dominant frequency is 12.6 Hz , in figure 6.21(b) it is 12.6 Hz , and in figure 6.21(c) it is 11.2 Hz . These frequencies compare well with the frequency of oscillation of the air-pocket volume estimated in section 6.3.3 (table 6.2). Therefore the oscillation of the pressure at the wall at the altitude of the air pocket seems to be due to the oscillation of the air pocket. This means that the pressure maxima at the wall are due to compressions of the air pocket and that the pressure minima at the wall are due to expansions of the air pocket (see for

	$\beta = 0.001$	$\beta = 0.01$	$\beta = 0.05$
c_{20} (m/s)	358.7	116.99	53.54
Dominant frequency (Hz)	12.6	12.6	11.2
f_l (Hz) (longitudinal mode)	17.94	5.85	2.68
f_t (Hz) (transverse mode)	35.87	11.70	5.35

Table 6.6: Eigen frequencies in the liquid domain.

a comparison example figures 6.14(a) and 6.11). This confirms what has been observed experimentally by Bullock et al. (2007).

Now let us evaluate the frequencies of the pressure wave reflected by the walls in the liquid domain. Indeed, when a maximum pressure occurs at the wall it propagates in the domain and is likely to be reflected off the left wall boundary or off the bottom wall boundary. Let us consider the longitudinal and transverse fundamental acoustic modes of the fluid-2 domain, which may be approximated by a rectangle whose length is the length of the domain and whose height is the still water depth. The longitudinal mode is not realistic in the sense that we were forced to use an artificial wall boundary on the left-hand side of the domain instead of a non-reflecting boundary condition. Thus this longitudinal mode might be a spurious mode in this study. The eigen frequency for the longitudinal mode reads $f_l = \frac{c_{20}}{2L}$. For the transverse (vertical) mode, we consider the still water level, H_{SWL} , as the length scale. This mode may correspond to a reflection of the pressure wave on the bottom in front of the structure. The eigen frequency for the transverse mode reads $f_t = \frac{c_{20}}{2H_{SWL}}$. One might wonder how the acoustic waves established in the liquid domain interact with the flow dynamics after the primary maximum pressure event and particularly with the air pocket dynamics. Let us remark that using the sound speed at standard pressure c_{20} to compute these frequencies is an approximation, because, as the pressure decreases with the altitude in the liquid, the sound speed is not constant in the domain. Through this approximation the acoustic-wave refraction is neglected. The values of f_l and f_t are shown in table 6.6.

For the $\beta = 0.001$ case, the frequency f_t seems to be present in the spectrum as one can see an energy peak around 36 Hz in figure 6.21(a). But its energy is much lower than the energy of the dominant frequency. Thus we can be sure that the dominant frequency on the wall at the altitude of the air pocket is not forced by a transverse steady wave in the liquid domain. This implies that the mechanism that generates these pressure oscillations is the free oscillation of the air pocket. This is confirmed by the fact mentioned above that the movement of the pressure extrema on the wall is the same as the movement of the air pocket.

For the $\beta = 0.01$ case, the dominant frequency is 12.6 Hz, the transverse mode frequency f_l is 5.85 Hz and the longitudinal mode frequency f_t is 11.70 Hz. The dominant frequency and f_t are very close and undistinguishable in figure 6.21(b). We can conclude that in this case the free oscillation of the air pocket might be forced by the transverse mode.

For the $\beta = 0.05$ case, the dominant frequency is 11.2 Hz and f_l and f_t are respectively 2.68 Hz and 5.35 Hz. In this case the transverse is not present in the

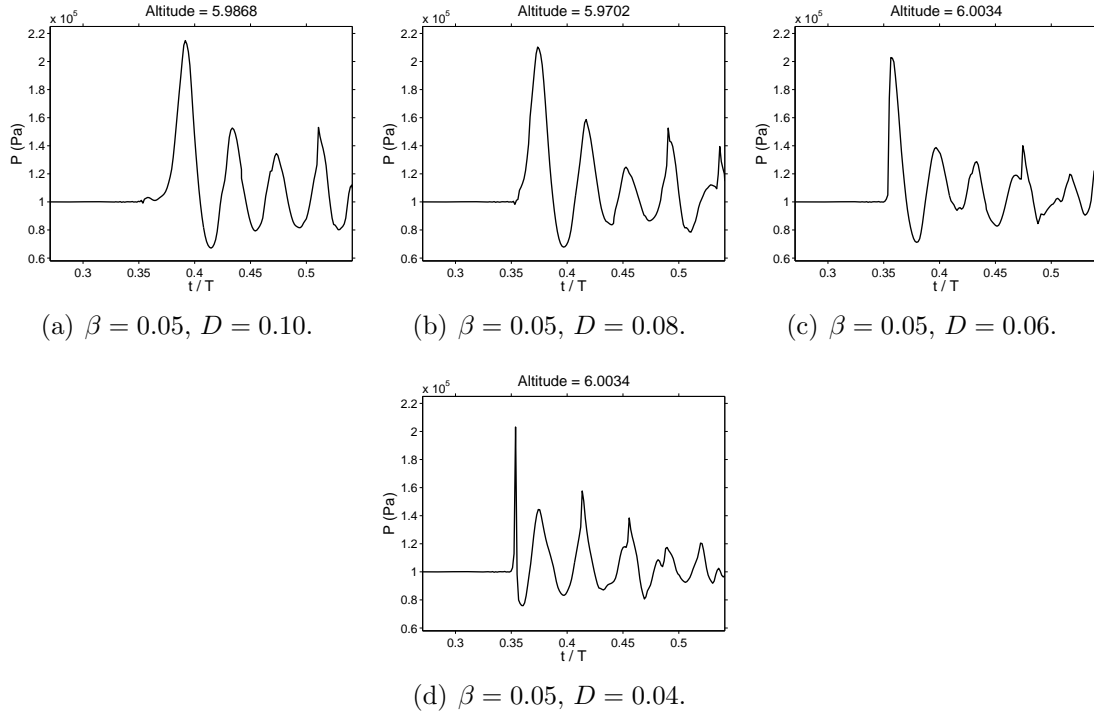


Figure 6.22: Pressure history on the wall at the altitude of the first maximum pressure for different D values and $\beta = 0.05$.

spectrum in figure 6.21(c). Thus the main pressure oscillation seems to be due to the free oscillation of the air pocket.

We can conclude that there are two physical oscillating mechanisms. The first mechanism is due to the oscillation of the air pocket. The second one is the transverse acoustic mode.

Figure 6.22 shows the pressure history on the wall at the altitude of the primary maximum pressure for each value of D . One can see the oscillation observed in section 6.3.6. Figure 6.23 shows the Fourier transform of the pressure histories in figure 6.22. One can see that there is a clear dominant frequency. For the case $D = 0.10$, the dominant frequency is 10.8 Hz . For the case $D = 0.08$, the dominant frequency is 11.2 Hz . And for the cases $D = 0.06$ and $D = 0.04$, the dominant frequency is 12.05 Hz . These frequencies compare very well with the frequency of oscillation of the air-pocket volume estimated in section 6.3.3 (table 6.3). This means that the oscillation of the pressure at the wall in these cases corresponds to the oscillation of the air pocket.

However, let us consider the frequency of the steady waves in the domain. For these cases the level of aeration is the same, $\beta = 0.05$. Thus the eigen frequencies f_l and f_t in the liquid domain are the ones in the last column of table 6.6, 2.68 Hz and 5.35 Hz respectively. For all D values, the dominant frequency value is not close to f_l and f_t . A frequency close to f_l seems to be present in the spectra (figure 6.23). Thus the spurious (longitudinal) mode may be interfering in these cases. No energy peak can be seen close to f_t in the spectra in figure 6.23, so it seems that in these cases the transverse mode does not play a dominant role.

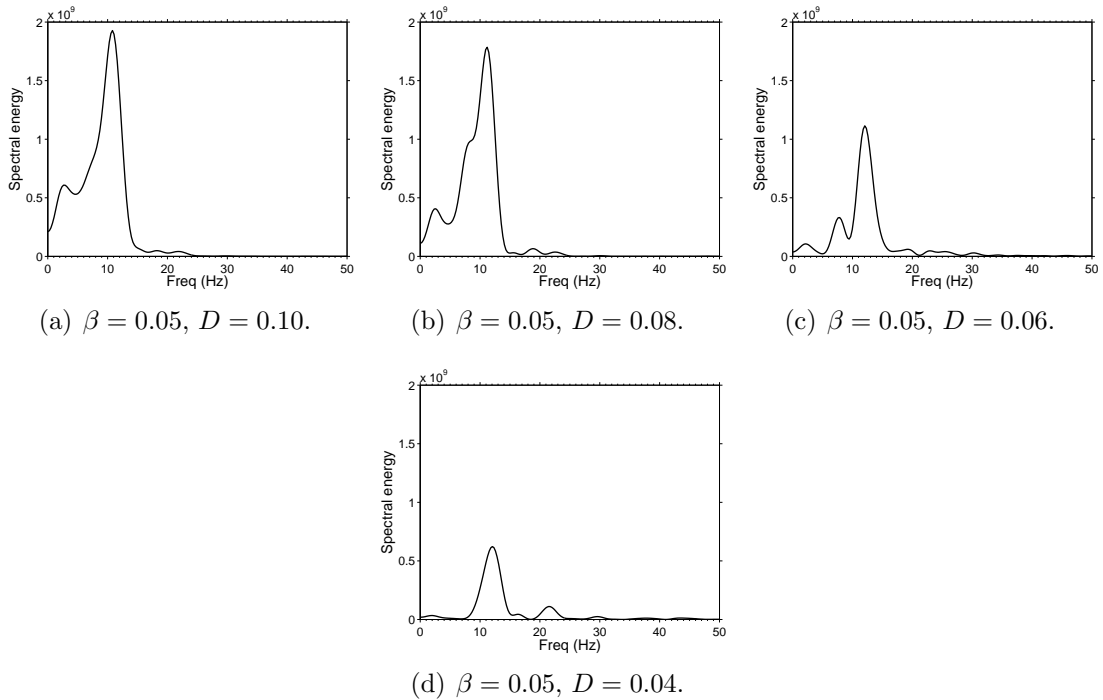
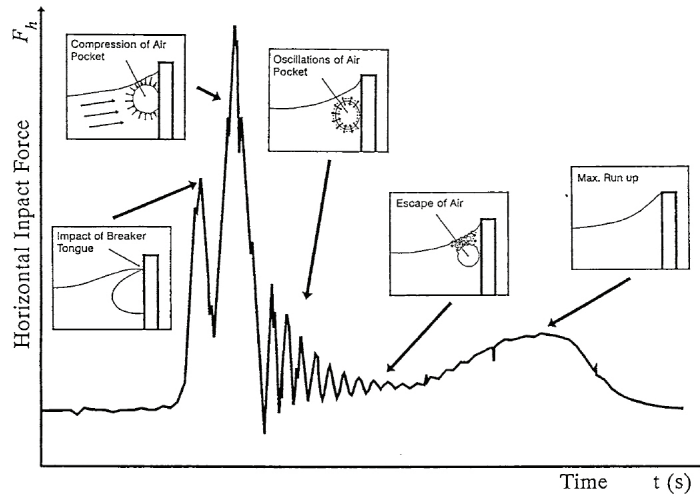
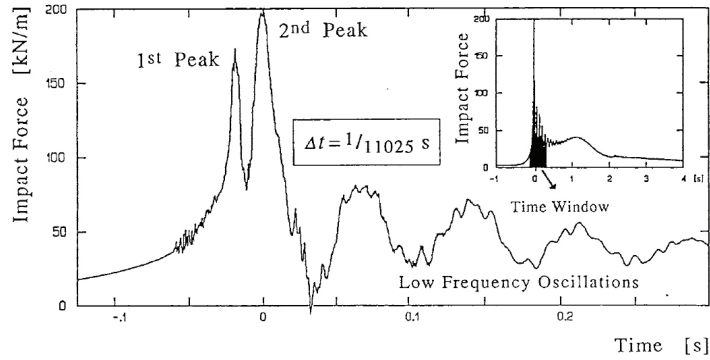


Figure 6.23: Fourier transform of the pressure history at the location of primary maximum pressure for all D values and $\beta = 0.05$.

Therefore we found that the strong pressure oscillations at the wall at the altitude of the air pocket are due to the air-pocket oscillation. Some studies found in the literature confirm this idea. Chan & Melville (1988) observed that the oscillations in the measured pressure at the wall are associated with the trapped air. Schmidt et al. (1992), in an attempt to explain the different aspects of the pressure history at the wall (figure 6.24(a)), mentioned that the oscillations in the pressure history are due to cyclic compressions and expansions of the entrapped air pocket. Moreover, the pressure histories we find at the wall can be related to the ones found by (Schmidt et al. 1992). The overall shape of the signal they show (figure 6.24(b)) is similar to our cases for $\beta = 0.05$. In their case there are two maxima at the beginning of the signal, whereas in our cases for $\beta = 0.05$ there is only one maximum. In our cases for $\beta = 0.001$ and $\beta = 0.01$ (figures 6.20(a) and 6.20(b)), we also see a "double peak maximum" at the time of the primary maximum. Schmidt et al. (1992) related the first maximum of the double peak to the impact of the wave crest on the wall and the second maximum to the compression of the air pocket (figure 6.24(a)). However the lack of precision of the definition of the wave crest at impact in our simulations prevents us from confirming this result. In addition the amplitudes of the maximum secondary pressure maxima in our cases with the largest β (figures 6.22(a) to 6.22(d)) decrease with time as in their case. In our cases the decrease in the amplitude is not constant. This may be due to the interference generated by the steady waves entrapped in the liquid domain. It is also certainly due to the fact that our simulations do not account for the fragmentation of the air pocket so the damping of the amplitude of the air-pocket oscillation is not



(a) Attempt of explanation for the different aspects of the pressure history at the wall, from Schmidt et al. (1992).



(b) Horizontal force history resulting from pressure integration, from a large scale model test of Schmidt et al. (1992). $T = 6.75$ s.

Figure 6.24: Figures from Schmidt et al. (1992).

as strong as in the experiment.

Schmidt et al. (1992) mentioned that the low frequency oscillations they observed after the pressure peak (figure 6.24(b)) are due to "cyclic compressions and expansions of the entrapped air pocket". The frequency they observed was 13.3 Hz. This is the dominant frequency we also observe in our pressure histories at the wall at the altitude of the air pocket (6.21 and 6.23) and in the oscillation of the air pocket (figure 6.12). Moreover, they deduce that the air pocket in their experiment has an equivalent diameter of $2R_0 = 0.4m$ through the relationship (6.2). The dimension of the air pocket they deal with has the same order of magnitude as our air pocket (tables 6.2 and 6.3). This confirms that the dominant oscillating mechanism present in our simulations is the oscillation of the air pocket.

In figure 6.25 we plotted the frequency of to the main peak in the Fourier transforms of figures 6.21 and 6.23. One can see that the frequency of the pressure oscillations decreases with β . In figure 6.25(b) one can see that the frequency decreases with D .

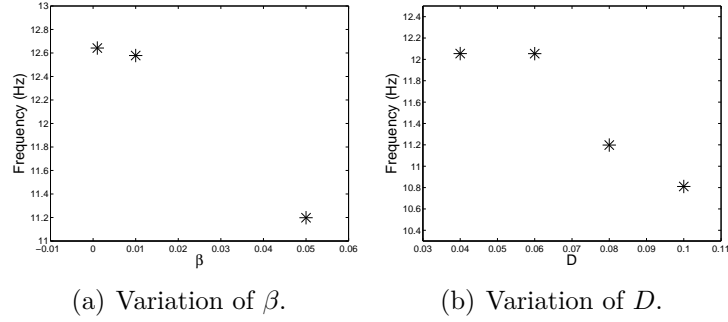


Figure 6.25: Dominant frequency for all the simulated cases.

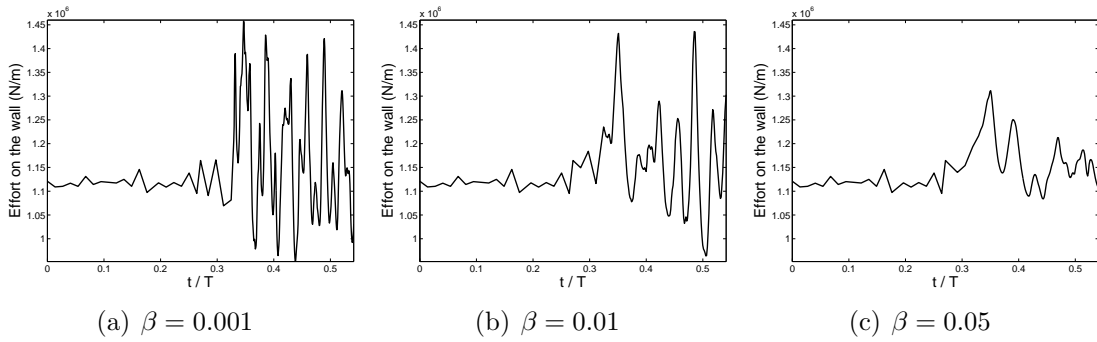


Figure 6.26: Lineic effort on the wall for all β values and for $D = 0.08$.

This can be explained by the fact that the increase in D increases the size of the air pocket, thus its eigen frequency decreases with D .

6.4 Forces

In this section the aim is to study the forces generated by the wave impact on the wall. In section 6.4.1 we investigate the forces induced on the wall. And in section 6.4.2 we estimate whether or not the pressure gradients at the wall generated by the wave impact are strong enough to lift a concrete block.

6.4.1 Forces on the wall

We computed the overall force applied on the wall, by integrating the pressure distribution, including the hydrostatic part. Figures 6.26 and 6.27 show the time evolution of the lineic horizontal force applied on the wall, respectively for all β values and all D values. The first maximum in each case occur at the time of the primary maximum pressure introduced in section 6.3.6. The hydrostatic lineic forces which are the ones observed before the impact are approximately 1.11×10^6 N/m. One can see that after the time of the primary maximum pressure, the force on the wall oscillates around the hydrostatic force value. The amplitude of this oscillation decreases when β increases (figures 6.26(a) to 6.26(c)). This means that in terms of mechanical constraints on the

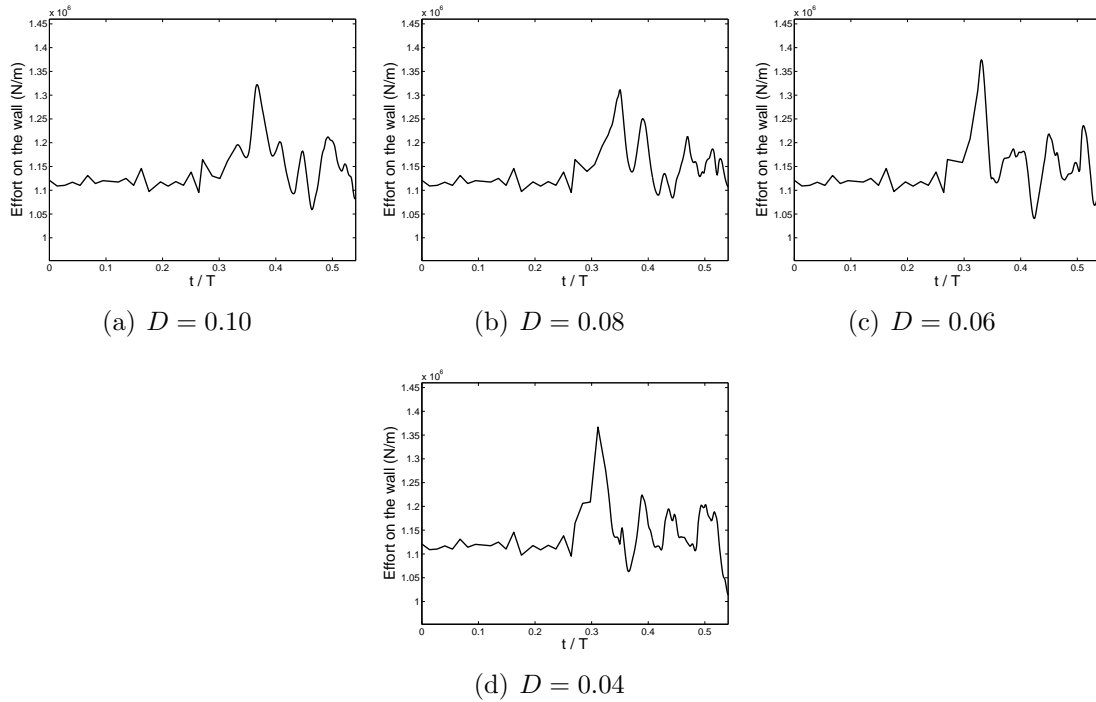


Figure 6.27: Lineic effort on the wall for all D values and for $\beta = 0.05$.

structure the most critical situation is for a low air content.

Moreover, these can be compared to the force history of Schmidt et al. (1992) in figure 6.24(b). For the lowest β values (figure 6.26(a)) the force history we compute presents an entertained oscillation. This differs from the case of Schmidt et al. (1992) for which they find a double maximum at the beginning of the history and then a damped oscillation. Our cases for the highest β value (figures 6.26(c) and 6.27) present a first maximum and then a damped oscillation as in the case of Schmidt et al. (1992).

In the same way, we computed the moment at the foot of the wall. Figures 6.28 and 6.29 show the time evolution of the moment applied on the wall, respectively for all β values and all D values.

In table 6.7, we show the minimum and maximum values of the force and of the

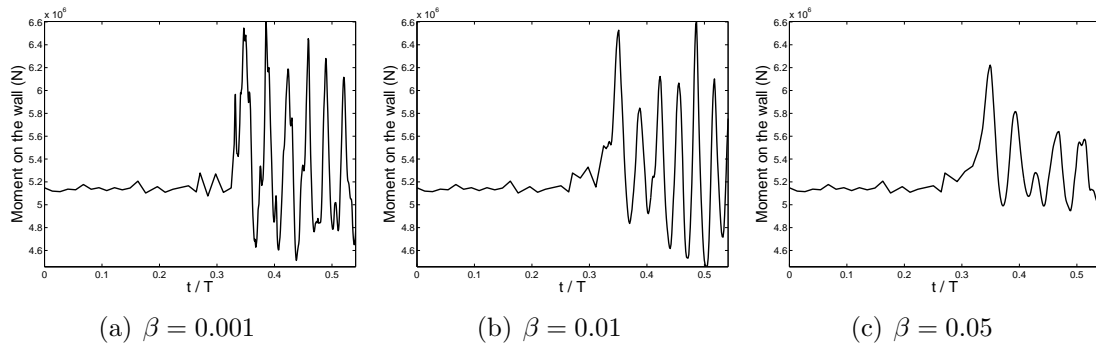


Figure 6.28: Lineic moment on the wall for all *beta* values.

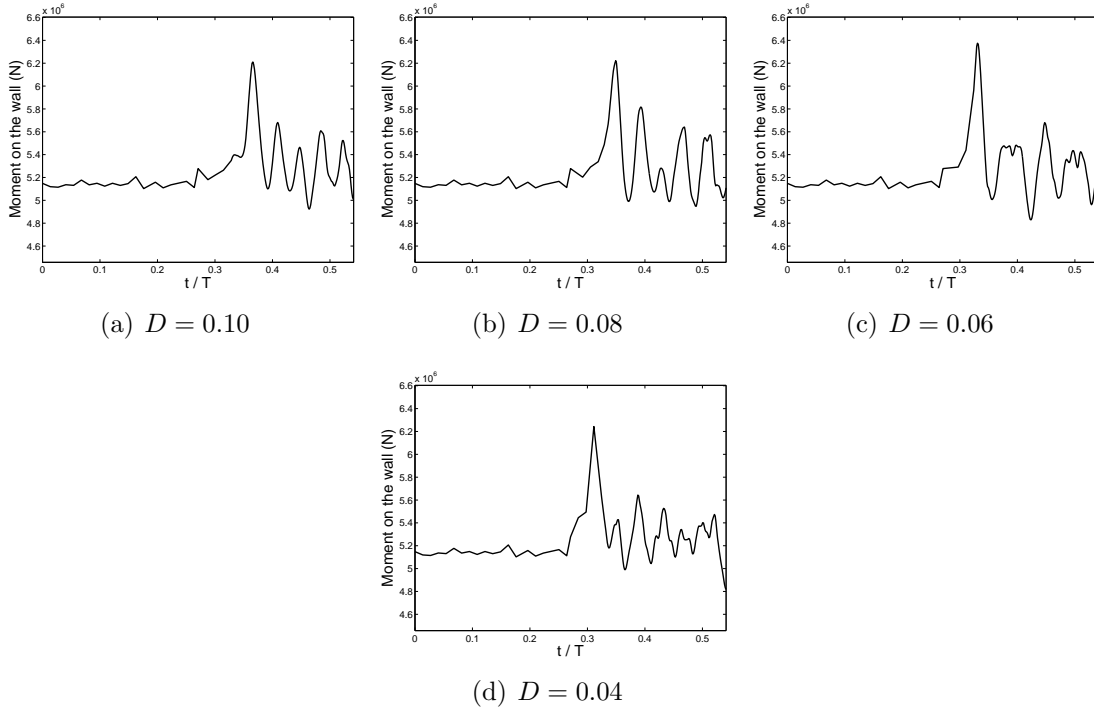


Figure 6.29: Lineic moment on the wall for D values and for $\beta = 0.05$.

	$\beta = 0.001$	$\beta = 0.01$	$\beta = 0.05$
Max force (kN/m)	1457.79	1435.92	1311.43
Time of max force (wave periods)	0.34657	0.48486	0.35052
Min force (kN/m)	952.07	963.88	1083.77
Time of min force (wave periods)	0.43797	0.50522	0.4433
Max moment (kN)	6601.21	6603.99	6222.49
Time of max moment (wave periods)	0.38539	0.48622	0.34916
Min moment (kN)	4512.51	4457.36	4947.64
Time of min moment (wave periods)	0.43797	0.50386	0.48914

Table 6.7: Forces values on the wall for all β values.

	$D = 0.10$	$D = 0.08$	$D = 0.06$	$D = 0.04$
Max force (kN/m)	1322.26	1311.43	1374.51	1366.90
Time of max force (wave periods)	0.36719	0.35052	0.33055	0.31117
Min force (kN/m)	1059.19	1083.77	1040.31	1013.34
Time of min force (wave periods)	0.46363	0.4433	0.42374	0.54115
Max moment (kN)	6210.79	6222.49	6375.42	6243.21
Time of max moment (wave periods)	0.36583	0.34916	0.33055	0.31117
Min moment (kN)	4922.88	4947.64	4829.27	4817.15
Time of min moment (wave periods)	0.46363	0.48914	0.42374	0.54115

Table 6.8: Forces values on the wall for all D values.

moment on the wall for all β values. We also show the times at which these extrema occur.

The value of the maximum force on the wall decreases with β . The maximum force does not occur at the same time for all β values.

In the case $\beta = 0.001$, the maximum force on the wall occurs at the time of the primary maximum pressure (section 6.3.6). In the case $\beta = 0.01$, the maximum force on the wall occurs later than the primary maximum pressure, $\Delta t/T = 0.1380$. In this case, the second highest force occurred at the time of the primary maximum pressure, and its amplitude is 1432 kN/m . In the case $\beta = 0.05$, the maximum force on the wall occurs a little later than the primary maximum pressure, $\Delta t/T = 0.0041$. Then a large force is found at approximately the same time of the primary maximum pressure for all β values.

The minimum force increases with the air content.

The maximum moment is the same for the $\beta = 0.001$ and $\beta = 0.01$, but is smaller for $\beta = 0.05$. The time of occurrence of the maximum moment for $\beta = 0.01$ is different from the other cases, but the same remark made for the force applies for the moment.

In table 6.8, we show the minimum and maximum values of the force and of the moment on the wall and their time of occurrence for all D values.

The maximum force on the wall does not vary much with D . However, the time of occurrence of the maximum force increases with D .

The maximum moment does not vary much with D . The time of occurrence of the maximum moment increases with D .

The Fourier transforms of the force histories at the wall have been computed (figure 6.30 and figure 6.31). There is a common maximum frequency in all the three spectra 13 Hz which is the frequency of oscillation of the air pocket found in section 6.3.5. This frequency is the dominant frequency for $\beta = 0.001$ and $\beta = 0.05$, but not in the other cases. This means that there is a mechanism other than the oscillation of the air pocket that applies a force on the wall. For the cases $\beta = 0.05$ and $D = 0.08$ (figure 6.30(c) or 6.31(b)) and $\beta = 0.05$ and $D = 0.10$ (figure 6.31(a)), the dominant frequency is close to the frequency of the longitudinal acoustic mode in the liquid domain 2.68 Hz (table 6.6), thus for these cases we cannot conclude on the dominant mechanism. For the cases $\beta = 0.05$ and $D = 0.06$ (figure 6.31(c)) and $\beta = 0.05$ and $D = 0.04$ (figure 6.31(d)), the dominant frequency is around 7.5 Hz , which is close to the frequency of

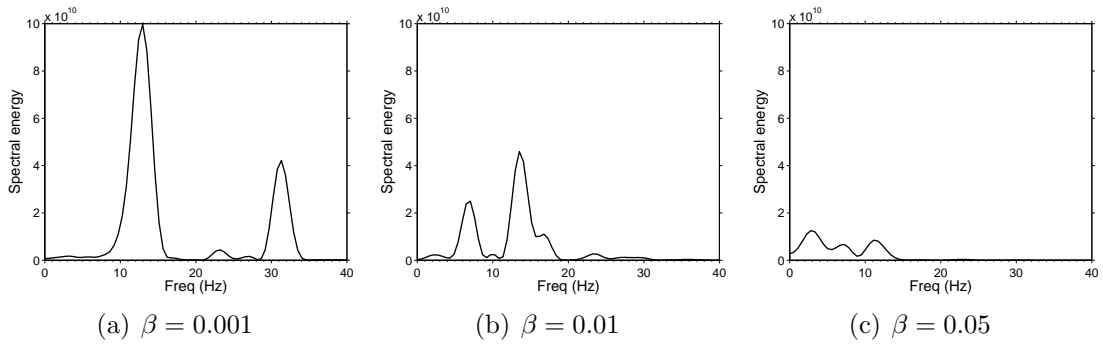


Figure 6.30: Fourier transform of the forces on the wall for all β values and $D = 0.08$.

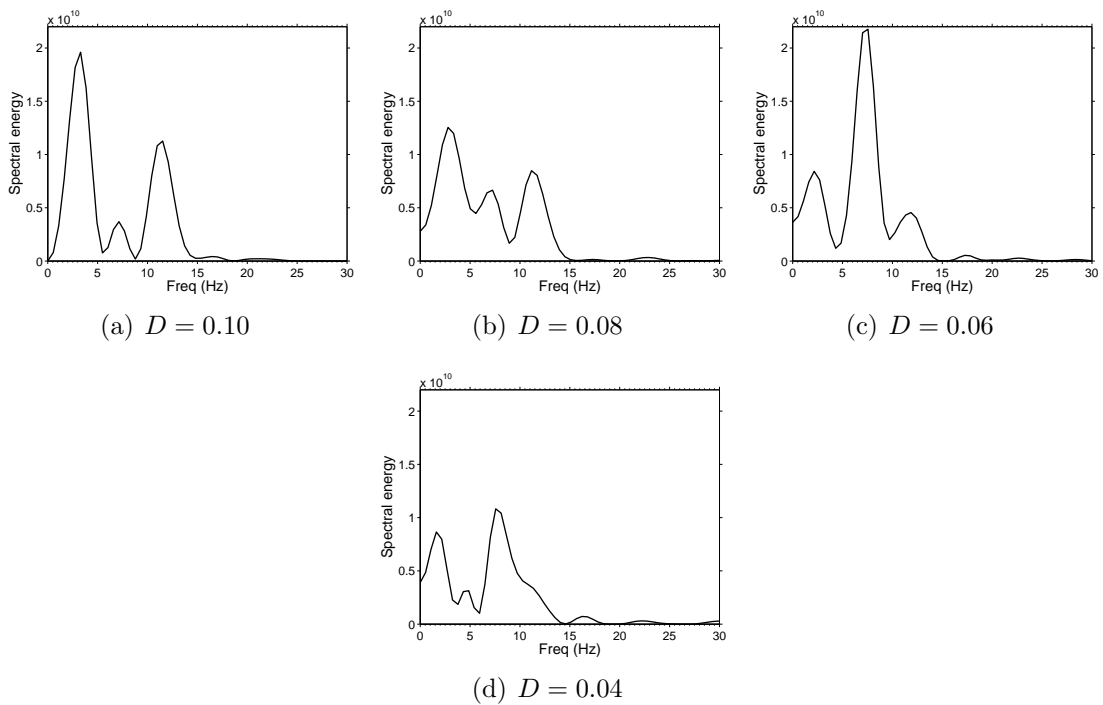


Figure 6.31: Fourier transform of the forces on the wall for all D values and for $\beta = 0.05$.

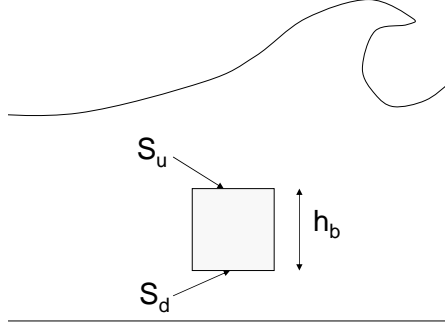


Figure 6.32: Definition scheme of an immersed block.

the transverse acoustic mode. So the dominant mechanism might be the transverse mode but we cannot conclude definitely.

6.4.2 Estimation of the forces on an object located in front of the wall

As we mentioned in section 6.3.6, there can be occurrences of a simultaneous high pressure at the foot of the wall and low pressure at the altitude of the primary maximum. This is critical for possible movements of lying objects, like an armour unit. Therefore, in this section, we evaluate if there are vertical pressure gradients large enough to raise an object made of concrete.

First, let us derive a pressure-gradient condition for a concrete block to be lifted up. So let us consider a block made of concrete, whose density is $\rho_b = 2500 \text{ kg/m}^3$. Such a block is under the influence of its own weight force, which reads: $\rho_b V g$ where V is its volume and g is gravity. When such a block is immersed, it is also under the influence of a pressure force. To compute this pressure force in a simple manner, let us say that this block has an elementary, parallelepiped shape, and is arranged so that its 3 directions are vertical and horizontal, as schemed in figure 6.32. Let S be the surface of the horizontal face of the block. The total pressure in the ambient liquid medium at the altitude of the upward face being noted P_u , the pressure force applied to the upward face reads: $P_u S$. In the same way, the force applied to the downward face reads: $P_d S$. The pressure force applied to the object reads $F_p = (P_d - P_u) S = \Delta P S$. Therefore to lift a block requires that: $\Delta P S \geq \rho_b V g$. Let h_b be the height of the block, we have $V = h_b S$, so the above condition reads:

$$\Delta P \geq \rho_b h_b g \quad (6.4)$$

The curve in figure 6.33 gives the value of $\rho_b h_b g$ that has to be exceeded for a block to be lifted up.

More generally, we can say that if the pressure difference over a certain vertical distance Δz is greater than the threshold value $\rho_b g \Delta z$, a block of the same vertical

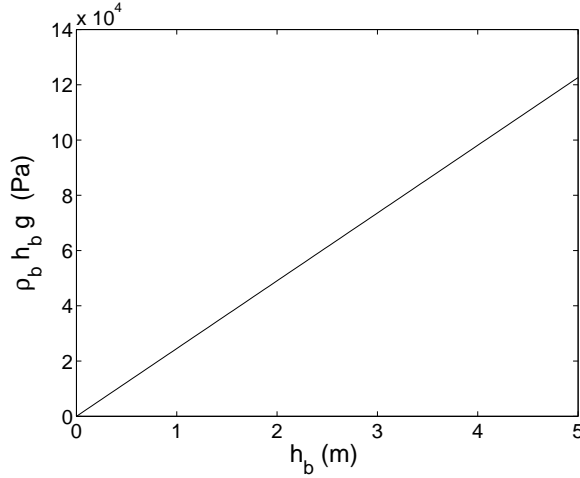


Figure 6.33: Pressure variation threshold to exceed for the lifting of a concrete block.

dimension can be lifted up. This condition reads:

$$\frac{\Delta P}{\Delta z} \geq \rho_b g \quad (6.5)$$

Thus we evaluate in the following if there are locations and times for which this condition is verified in simulated cases in the vicinity of the wall. In order to achieve this, we performed moving averages along a vertical profile close to the wall. These averages are based on several chosen distances.

Figures 6.34 to 6.36 represent the altitude on the wall and the time at which the pressure gradient verifies the criterion (6.5) for various values of Δz . In figure 6.35(a) the moving average is computed for a Δz of 1 m. In figure 6.35(b) the moving average is computed for a Δz of 2 m, etc.

In the $\beta = 0.001$ and $\beta = 0.01$ cases, for $\Delta Z = [1; 2; 3]$ (figure 6.34 and 6.35), one can see that the threshold is exceeded after the time of the impact and at several altitudes. One can see by comparing this with figure 6.11 that these altitudes seem to be alternately the lower extremity and the higher extremity of the air pocket. A block being on top of an armour layer, very close to the wall and to the free surface, may be influenced by these gradients.

It is different for the largest value of air content $\beta = 0.05$ (figure 6.36) for which there is a particular feature. In this case the threshold is exceeded for a ΔZ of 1 m at the altitude of the lower extremity of the air pocket, and from $t/T = 0.38$ up to $t/T = 0.41$ the threshold is exceeded in a zone descending through time along the wall. At the final time of this descending course ($t/T = 0.41$), the threshold is exceeded at 1.15 m from the bottom. Therefore a block located above an altitude of 1.15 m could be lifted up.

There is the same feature for the cases $D = 0.10$ and $D = 0.06$ for a $\Delta Z = 1$ (figures 6.37 and 6.38). This means that the pressure gradients along the wall have the potential strength to rise 1-m-high concrete bodies even if they are well below the free-surface. In the case $D = 0.04$ (figure 6.39), this feature is not visible as the threshold is exceeded but only close to the free surface.

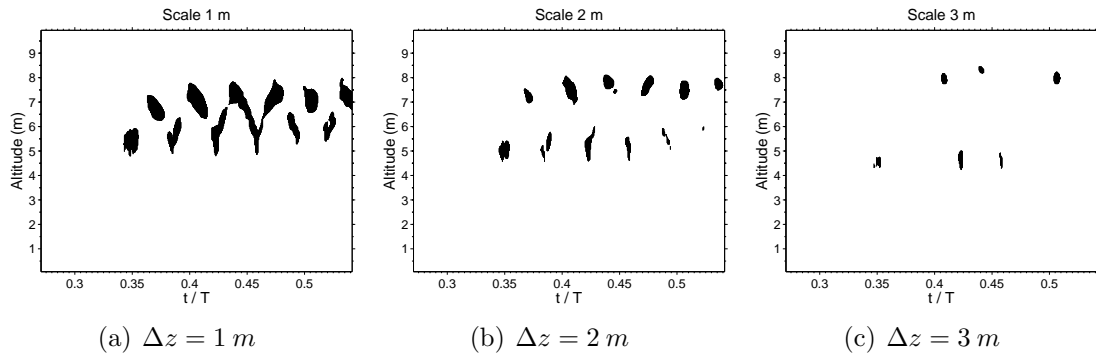


Figure 6.34: $\beta = 0.001$ and $D = 0.08$.

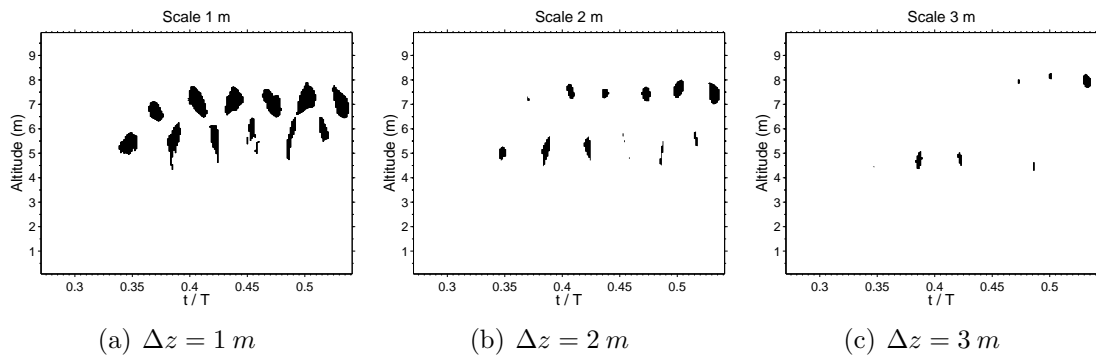


Figure 6.35: $\beta = 0.01$ and $D = 0.08$.

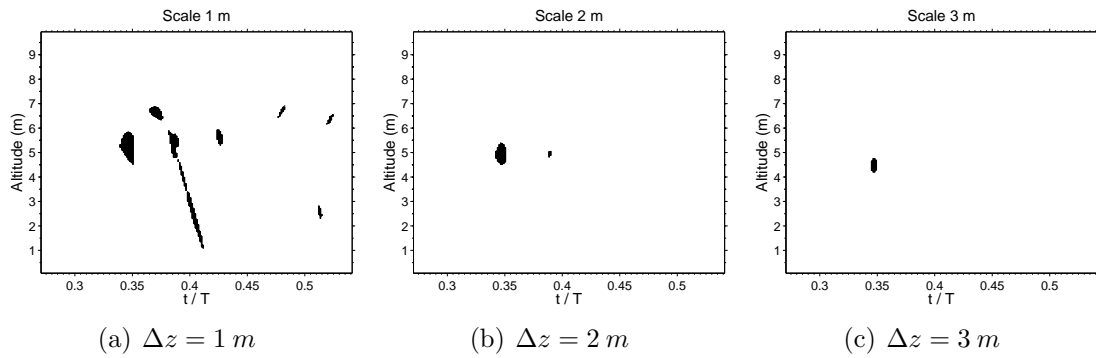


Figure 6.36: $\beta = 0.05$ and $D = 0.08$.

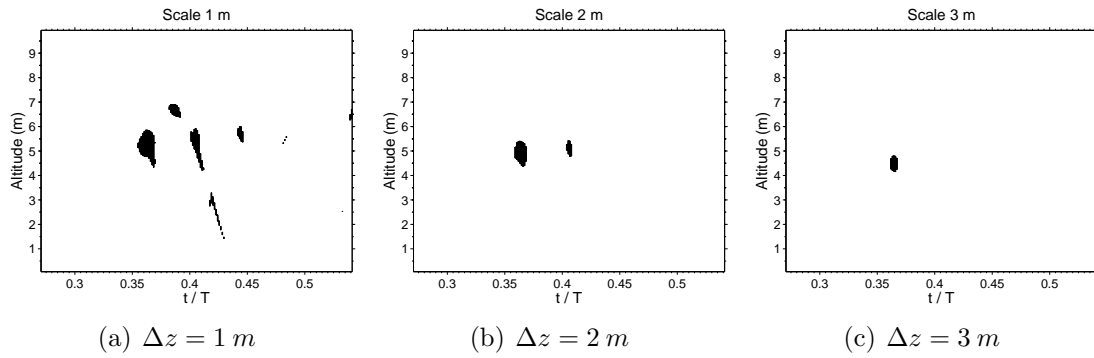


Figure 6.37: $D = 0.10$ and $\beta = 0.05$.

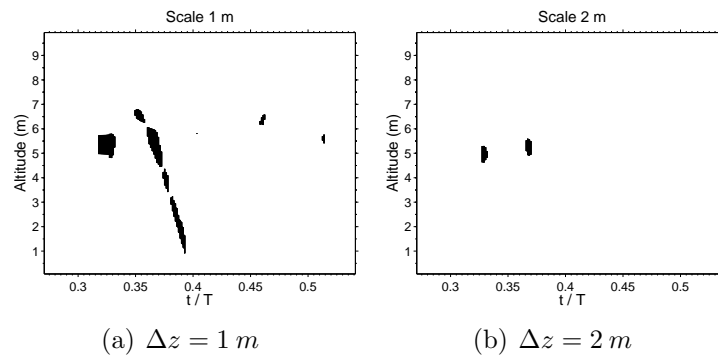


Figure 6.38: $D = 0.06$ and $\beta = 0.05$.

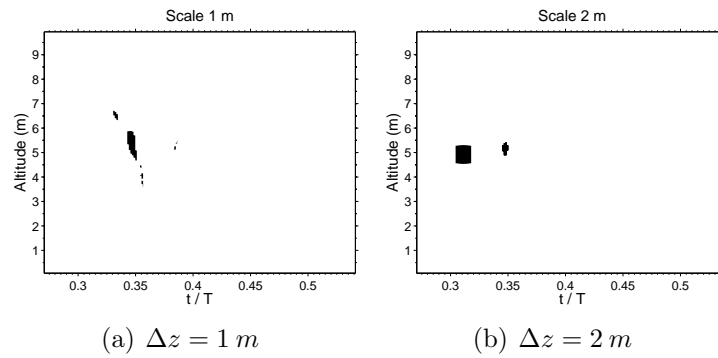


Figure 6.39: $D = 0.04$ and $\beta = 0.05$.

	$\beta = 0.001$	$\beta = 0.01$	$\beta = 0.05$
	$D = 0.08$	$D = 0.08$	$D = 0.08$
Max scale	6.2	4.5	4.3
Altitude	3.156	4.1113	3.7566
Time	0.4221	0.3862	0.3465

Table 6.9: Maximum scale over which the gradient is larger than the threshold for all β values.

	$D = 0.10$	$D = 0.08$	$D = 0.06$	$D = 0.04$
	$\beta = 0.05$	$\beta = 0.05$	$\beta = 0.05$	$\beta = 0.05$
Max scale (m)	4	4.3	2.8	2.9
Altitude (m)	3.8535	3.7566	4.4619	4.5449
Time	0.3631	0.3465	0.3292	0.3112

Table 6.10: Maximum scale over which the gradient is larger than the threshold for all D values.

The most critical situations are for a high aeration level and medium D value.

Table 6.9 shows the values of the maximum scale over which the moving average exceeds the threshold for all β values. This maximum scale decreases with β .

Table 6.10 shows the values of the maximum scale over which the moving average exceeds the threshold for all D values. This maximum scale increases with D .

Globally, we found that the maximum vertical scale over which a strong pressure gradient can occur decreases with β . However, the strong gradients are at a lower altitudes in front of the wall for high values of β , which is more critical in the sense that it can remove blocks from the bottom of the wall or from the top of an armour layer. We also found that the maximum vertical scale over which a strong pressure gradient can occur increases with the breaking distance. Therefore among the cases we investigated the most critical are those for which the wave breaks further seaward.

6.5 Conclusion

In this chapter we presented the results from the simulations of wave impacts on a vertical wall. We showed that the variation of the aeration level has a limited influence on the free-surface dynamics before the impact. In all studied cases an entrapment of an air pocket is observed. We observed that the volume of the air pocket decreases with the air content and increases with the breaking distance. This pocket has an ascending motion before it stabilizes at a certain altitude. We highlighted that the maximum pressure at the wall occurs inside the entrapped air pocket just above its lower extremity. We showed that the pressure oscillations at the wall are due to two physical mechanisms: the free oscillation of the air pocket and the transverse acoustic mode in the liquid domain. We showed that the primary maximum pressure value is not influenced much by the variation of the aeration level. For the values of the breaking distance we investigated, the primary maximum pressure value does not vary

much. Then we studied the forces applied to the wall. We showed that the breaking distance has a limited influence on the maximum force and that an increase in the air content level tends to reduce the maximum force on the wall. Finally we draw attention to the fact that the pressure gradients along the wall are sufficient to lift concrete blocks of different heights.

Chapter 7

Conclusion and perspectives

The aim of this work is to study wave impacts and for this purpose a numerical model capable of simulating the flow of an air and water mixture occurring in a wave impact on a wall was developed.

We reviewed the incompressible and compressible approaches available in the literature.

The original compressible multifluid model developed by (Chanteperdrix 2004) was unable to simulate the correct acoustic properties of an air/water mixture, for it was made to simulate separated-phase flows. Thus we extended this model in order to account for proper acoustics in a mixture. We achieved this improvement by adding a third phase in the model that accounts for the presence air within water as a dispersed phase.

Then we tested the ability and restrictions of this new multifluid model to represent different physical processes taking place in the dynamics of aerated-water-wave impacts on a wall. Firstly, we considered the propagation of an acoustic wave in a bubbly mixture. We compared the results from our code to experimental results and an analytical theory and showed that our code is capable to accurately represent acoustic wave propagation in such a mixture in terms of celerity and attenuation. However, the code does not account for the increase in attenuation due to bubble resonance. Secondly, we addressed the problem of the propagation of a shock wave in an air/water mixture by the simulation of a shock tube. Although we found some discrepancies at the contact discontinuity, the capturing of the shock and the simulation of its properties were in very good agreement with the analytical solution. Finally, we verified the ability of our code to simulate wave breaking. We compared its results with the results from an incompressible flow model. Despite the fact that the code cannot fully reach the incompressible limit, we found a good agreement in terms of free-surface dynamics.

Simulations of wave impacts on a vertical wall including the entrapment of an air pocket have been performed. We varied the volume fraction of air in the liquid medium from 0.001 to 0.05 and we varied the breaking distance from 0.04 to 0.10 wavelengths. We showed that the variation of the aeration level in the liquid medium has not much influence on the free-surface dynamics before the impact. However we observed that the volume of the air pocket decreases with the air content and increases with the breaking distance. In all our cases the air pocket had an ascending then stabilizing trajectory

on the vertical wall. We showed that the maximum pressure at the wall occurs just above the lower extremity of the entrapped air pocket. We showed that the pressure oscillations at the wall are due to two physical mechanisms: the free oscillation of the air pocket and the transverse acoustic mode in the liquid domain. We found that the value of the maximum impact pressure at the wall is hardly influenced by the variations of the air content nor by the variations of the breaking distance we investigated.

Finally, we showed that there can be simultaneous low pressures at the altitude of the air pocket and high pressures at the bottom of the wall. The simultaneity is influenced by the amount of entrained air in the liquid. Indeed the air content modifies the celerity at which the high pressures propagates down to the bottom and consequently it modifies the synchronous aspect of the eigen pressure oscillations between the bottom and the free surface and the oscillation of the air pocket. We then highlighted the existence of pressure gradients along the wall that are sufficiently strong to lift concrete blocks of different heights. Although we showed that the height of the blocks that can be lifted up decreases with the air content, the strongest gradients occur at lower altitudes in front of the wall for a high air content. This feature can be critical for composite breakwaters with an armour layer reaching the foot of the wall. We also showed that the height of the lifted blocks increases with the breaking distance.

Now let us propose a few directions for future research following this work.

For the wave impact simulations, we were forced to use an artificial wall boundary at the left of the domain instead of a non-reflecting boundary condition. A first improvement would be to implement a non-reflective boundary type in the code to avoid spurious steady pressure waves in the liquid domain.

Another improvement in the numerical set-up is to simulate the approaching wave shoaling over a sloping bottom in order to improve the initial condition for the wave impact simulations. However this require to reduce the CPU time required by the code. This can be achieved by the parallelization of the code. Such a numerical improvement will also allow for a more systematic analyse in different physical configurations by sweeping a larger range of aeration levels and breaking distances.

A physical feature that the code doest not account for is the fragmentation of the entrapped air pocket. This problem led to maintained oscillations of the air pocket whereas the oscillation are damped in reality. To represent the fragmentation the code must be improved to allow for relative velocity between phases at the small scale. The extension of this study to 3D computations will allow for instabilities of the air pocket in the horizontal direction which will also give a better representation of the fragmentation processes. 3D simulations will also enrich the configuration as the impact will be influenced by the angle at which the crest line reaches the wall. And the pressure distribution on the wall and within its vicinity will undoubtedly be modified in a 3D context.

Finally, situations with more complex structure geometries must be investigated. In this direction, there are lots of parameters that need to be explored like for instance the wall inclination or the inclusion of cracks of several geometries in the wall. Recent research in this field has proven it to be a promising direction (Muller et al. 2003, Wolters & Müller 2004). A step at the foot of the wall could be added. Several block

units could also be added. More generally, the effect of a macro porous structure in front of the wall like a real armour layer needs to be investigated. Now that the presence of strong gradients has been highlighted, the natural continuation is to estimate how they could be influenced by the presence of lying objects. Ideally, a similar code with the ability to simulate the movement of solid objects due to fluid movements could be used to quantify the forces on a block.

Appendix A

Appendices

A.1 Similarities between pressure equilibrium and the transport equation for the volume fraction

Proposition 1:

For every couple $(\tilde{\rho}_1, \tilde{\rho}_2)$ de $\mathbb{R}^{+} \times \mathbb{R}^{+*}$ and for every equation-of-state couple (p_1, p_2) verifying both following conditions:*

- *both laws $p_1(\rho_1)$ and $p_2(\rho_2)$ are C^1 strictly increasing over \mathbb{R}^+ ,*
- *each law $p_1(\rho_1)$ and $p_2(\rho_2)$ admit a infinite limit when the density tends to the infinity,*

equation (3.65) admits a unique solution that is the equilibrium volume fraction $\alpha = \alpha_(\tilde{\rho}_1, \tilde{\rho}_2)$ included between 0 and 1.*

Moreover, in the case of C^1 solution of the model formed by equations of mass conservation (3.4) and momentum balance (3.5), the equilibrium volume fraction α_ obeys the following partial derivatives equation:*

$$\frac{\partial \alpha_*}{\partial t} + \underline{V} \cdot \nabla \alpha_* = K(\alpha_*, \rho_1, \rho_2) \nabla \cdot \underline{V} \quad (\text{A.1})$$

with:

$$K(\alpha_*, \rho_1, \rho_2) = \alpha_*(1 - \alpha_*) \frac{\rho_2 c_2^2 - \rho_1 c_1^2}{\alpha_* \rho_2 c_2^2 + (1 - \alpha_*) \rho_1 c_1^2} \quad (\text{A.2})$$

and:

$$\rho_1 = \frac{\tilde{\rho}_1}{\alpha_*}, \quad \rho_2 = \frac{\tilde{\rho}_2}{(1 - \alpha_*)} \quad (\text{A.3})$$

where c_k is the reference sound speed in fluid k , ρ_k is the density of fluid k .

In brief one can say that equation (A.1) is equivalent to equation (3.65) for regular solutions of equations (3.4) and (3.5).

Notes:

1. In the case of infinitely thin interfaces, the factor $\alpha_*(1 - \alpha_*)$ in the right member is identically zero.
2. Equation (A.1) can be written:

$$\frac{\partial \alpha_*}{\partial t} + \nabla(\alpha_* \underline{V}) = \frac{\alpha_*}{\rho_1 c_1^2 \rho c_*^2} \nabla \cdot \underline{V} \quad (\text{A.4})$$

where c_* is the "mixture sound speed" defined by $\frac{1}{\rho c_*^2} = \frac{\alpha_*}{\rho c_1^2} + \frac{(1 - \alpha_*)}{\rho c_2^2}$, making $\frac{1}{\rho c_*^2}$ the "mixture compressibility".

This equation can be interpreted as the mass conservation of fluid 1. In the parts of the domain where the fluid 2 is present (where α_* is almost 0), the volume fraction of the fluid 1 is conserved. However, in the parts of the domain where the fluid 1 is absent (where α_* is almost 1), the "loss of mass" is inversely proportional to the sound speed in fluid 1.

Proof:

Let us set function ϕ :

$$\varphi(\alpha, \tilde{\rho}_1, \tilde{\rho}_2) = p_1\left(\frac{\tilde{\rho}_1}{\alpha}\right) - p_2\left(\frac{\tilde{\rho}_2}{1-\alpha}\right) \quad (\text{A.5})$$

φ is defined for all α strictly included between 0 and 1 and for all couple $(\tilde{\rho}_1, \tilde{\rho}_2)$, $\tilde{\rho}_1 > 0$, $\tilde{\rho}_2 > 0$. Both masses $\tilde{\rho}_1$ and $\tilde{\rho}_2$ being set, let us call $\tilde{\varphi}$ the function associating α to $\tilde{\varphi}(\alpha) = \varphi(\alpha, \tilde{\rho}_1, \tilde{\rho}_2)$.

This function is strictly decreasing as long as it is the sum of two strictly decreasing functions, the first one being the composition of a strictly increasing function (p_1) (assumption) by a strictly decreasing function $\tilde{\rho}_1/\alpha$ ($\tilde{\rho}_1$ being set), the second one being the composition of a strictly increasing function ($-p_2$) (assumption) by a strictly increasing function $\tilde{\rho}_2/(1-\alpha)$.

Otherwise, when α tends to 0 (respectively to 1), $\tilde{\varphi}(\alpha)$ tends to $+\infty$ (resp. $-\infty$), as an assumption on the pressure law p_1 (resp. p_1).

Put together, these two properties prove that $\tilde{\varphi}$ is zero once and only once at $\alpha = \alpha_*$. This deduction being valid for all couple $(\tilde{\rho}_1, \tilde{\rho}_2)$, it implicitly defines the function $\alpha_*(\tilde{\rho}_1, \tilde{\rho}_2)$ such as:

$$\varphi(\alpha_*(\tilde{\rho}_1, \tilde{\rho}_2), \tilde{\rho}_1, \tilde{\rho}_2) = 0 \quad (\text{A.6})$$

Moreover, a corollary of the *theorem of implicit functions* ensures of the same regularity for α_* than for φ and gives the partial derivatives:

$$\begin{aligned} \frac{\partial \alpha_*}{\partial \tilde{\rho}_1} &= -\frac{\frac{\partial \varphi}{\partial \tilde{\rho}_1}}{\frac{\partial \varphi}{\partial \alpha}} \\ \frac{\partial \alpha_*}{\partial \tilde{\rho}_2} &= -\frac{\frac{\partial \varphi}{\partial \tilde{\rho}_2}}{\frac{\partial \varphi}{\partial \alpha}} \end{aligned} \quad (\text{A.7})$$

Thus one can write:

$$\begin{aligned} \frac{\partial \alpha_*}{\partial t} &= \frac{\partial \alpha_*}{\partial \tilde{\rho}_1} \frac{\partial \tilde{\rho}_1}{\partial t} + \frac{\partial \alpha_*}{\partial \tilde{\rho}_2} \frac{\partial \tilde{\rho}_2}{\partial t} \\ &= -\left(\frac{\partial \alpha_*}{\partial \tilde{\rho}_1} \nabla(\tilde{\rho}_1 \underline{V}) + \frac{\partial \alpha_*}{\partial \tilde{\rho}_2} \nabla(\tilde{\rho}_2 \underline{V}) \right) \quad (\text{mass conservation}) \\ &= -\underline{V} \cdot \left(\frac{\partial \alpha_*}{\partial \tilde{\rho}_1} \nabla(\tilde{\rho}_1) + \frac{\partial \alpha_*}{\partial \tilde{\rho}_2} \nabla(\tilde{\rho}_2) \right) - \left(\tilde{\rho}_1 \frac{\partial \alpha_*}{\partial \tilde{\rho}_1} + \tilde{\rho}_2 \frac{\partial \alpha_*}{\partial \tilde{\rho}_2} \right) \nabla \cdot \underline{V} \\ &= -\underline{V} \cdot \nabla \alpha_* - \left(\tilde{\rho}_1 \frac{\partial \alpha_*}{\partial \tilde{\rho}_1} + \tilde{\rho}_2 \frac{\partial \alpha_*}{\partial \tilde{\rho}_2} \right) \nabla \cdot \underline{V} \end{aligned} \quad (\text{A.8})$$

going from the second line to the third being only possible for C_1 solutions $(\tilde{\rho}_1, \tilde{\rho}_2, \underline{V})$. Then let us set:

$$K = -\left(\tilde{\rho}_1 \frac{\partial \alpha_*}{\partial \tilde{\rho}_1} + \tilde{\rho}_2 \frac{\partial \alpha_*}{\partial \tilde{\rho}_2} \right) \quad (\text{A.9})$$

In order to reveal the expression of K , one needs to calculate $\frac{\partial \alpha_*}{\partial \tilde{\rho}_1}$ and $\frac{\partial \alpha_*}{\partial \tilde{\rho}_2}$. Let us use the corollary mentioned above to first calculate the partial derivatives of $\varphi(\alpha, \tilde{\rho}_1, \tilde{\rho}_2) =$

$p_1(\frac{\tilde{\rho}_1}{\alpha}) - p_2(\frac{\tilde{\rho}_2}{1-\alpha})$:

$$\begin{aligned}\frac{\partial \varphi}{\partial \tilde{\rho}_1} &= \frac{c_1^2}{\alpha} \\ \frac{\partial \varphi}{\partial \tilde{\rho}_2} &= -\frac{c_2^2}{(1-\alpha)} \\ \frac{\partial \varphi}{\partial \alpha} &= -\frac{\tilde{\rho}_1}{\alpha^2} c_1^2 - \frac{\tilde{\rho}_2}{(1-\alpha)^2} c_2^2\end{aligned}\tag{A.10}$$

because $c_k^2 \equiv \frac{\partial p_k}{\partial \rho_k}$. This leads to the following partial derivatives of α_* :

$$\begin{aligned}\frac{\partial \alpha_*}{\partial \tilde{\rho}_1} &= \frac{\frac{c_1^2}{\alpha}}{\frac{\tilde{\rho}_1}{\alpha^2} c_1^2 + \frac{\tilde{\rho}_2}{(1-\alpha)^2} c_2^2} \\ \frac{\partial \alpha_*}{\partial \tilde{\rho}_2} &= -\frac{\frac{c_2^2}{(1-\alpha)}}{\frac{\tilde{\rho}_1}{\alpha^2} c_1^2 + \frac{\tilde{\rho}_2}{(1-\alpha)^2} c_2^2}\end{aligned}\tag{A.11}$$

Thus K can be written:

$$K = -\left(\tilde{\rho}_1 \frac{\partial \alpha_*}{\partial \tilde{\rho}_1} + \tilde{\rho}_2 \frac{\partial \alpha_*}{\partial \tilde{\rho}_2}\right)\tag{A.12}$$

$$= \alpha_*(1-\alpha_*) \frac{\rho_2 c_2^2 - \rho_1 c_1^2}{\alpha_* \rho_2 c_2^2 + (1-\alpha_*) \rho_1 c_1^2}\tag{A.13}$$

multiplying numerator and denominator by $\alpha_*(1-\alpha_*)$ and setting $\rho_1 = \tilde{\rho}_1/\alpha_*$ and $\rho_2 = \tilde{\rho}_2(1-\alpha_*)$.

A.2 Mathematical properties of the model (E)

Model (E) was derived earlier (section 3.4.4). We remind it here:

$$\frac{\partial \tilde{\rho}_1}{\partial t} + \nabla \cdot (\tilde{\rho}_1 \underline{V}) = 0\tag{A.14}$$

$$\frac{\partial \tilde{\rho}_2}{\partial t} + \nabla \cdot (\tilde{\rho}_2 \underline{V}) = 0\tag{A.15}$$

$$\frac{\partial \rho \underline{V}}{\partial t} + \nabla \cdot (\rho \underline{V} \otimes \underline{V} + P \underline{I}) = \nabla \cdot (\mu (\nabla \underline{V} + {}^t \nabla \underline{V})) + \rho \underline{g} + \underline{M}_m\tag{A.16}$$

$$\text{with } P(\tilde{\rho}_1, \tilde{\rho}_2) = \alpha p_1\left(\frac{\tilde{\rho}_1}{\alpha}\right) + (1-\alpha) p_2\left(\frac{\tilde{\rho}_2}{1-\alpha}\right)\tag{A.17}$$

$$\text{and } \alpha \text{ such as } p_1\left(\frac{\tilde{\rho}_1}{\alpha}\right) = p_2\left(\frac{\tilde{\rho}_2}{1-\alpha}\right)\tag{A.18}$$

The model (E) is hyperbolic. The eigenvalues of the kinematic matrix are $u - c_*$, c_* , $u + c_*$, where the "mixture sound speed" c_* is defined by:

$$\frac{1}{\rho c_*^2} = \frac{\alpha}{\rho_1 c_1^2} + \frac{1-\alpha}{\rho_2 c_2^2}\tag{A.19}$$

This shows that c_* is positive ensuring that eigenvalues are real. Now by introducing the isothermal compressibility coefficient of the fluid k :

$$\chi_{T,i} \equiv -\frac{1}{V} \frac{\partial V}{\partial P} = \frac{1}{\rho} \frac{\partial \rho}{\partial P} = \frac{1}{\rho c^2} \quad (\text{A.20})$$

$$(\text{A.21})$$

(as by differentiating $\rho V = m$ one obtains $\partial V = -\frac{V}{\rho} \partial \rho$) it leads to a mixture law in the form of the mixture law for density (equation (3.52)):

$$\chi_{T,*} = \alpha \chi_{T,1} + (1 - \alpha) \chi_{T,2} \quad (\text{A.22})$$

There is a Lax entropy and associated flux for the model (E). This is another important property of hyperbolic conservation-laws system is the existence of a Lax entropy endowing it with thermodynamic consistency. The couple of functions (S_*, H_*) such as:

$$S_*(\tilde{\rho}_1, \tilde{\rho}_2, \rho u) = \frac{1}{2} \rho u^2 \tilde{\rho}_1 f_1 \left(\frac{\tilde{\rho}_1}{\alpha} \right) + \tilde{\rho}_2 f_2 \left(\frac{\tilde{\rho}_2}{1 - \alpha} \right) \quad (\text{A.23})$$

$$H_*(\tilde{\rho}_1, \tilde{\rho}_2, \rho u) = u (S(\tilde{\rho}_1, \tilde{\rho}_2, \rho u) + P(\tilde{\rho}_1, \tilde{\rho}_2))$$

where α is the equilibrium volume fraction defined by $p_1(\frac{\tilde{\rho}_1}{\alpha}) = p_2(\frac{\tilde{\rho}_2}{1-\alpha})$ and with f_1 and f_2 verifying:

$$f_1' = \alpha^2 \frac{p_1}{\tilde{\rho}_1^2} \quad \text{and} \quad f_2' = (1 - \alpha)^2 \frac{p_2}{\tilde{\rho}_2^2} \quad (\text{A.24})$$

is a usual couple of Lax entropy for the model (E).

The magnitude $\rho f = \tilde{\rho}_1 f_1 + \tilde{\rho}_2 f_2$ is exactly the *mixture volume density of free energy* and corresponds to the work of pressure forces. The proposition mentioned above is thus an expected result for an isothermal model, indeed it represents the second principle of thermodynamics: the total energy (including the kinetic energy) is a neg-entropy for a isothermal system.

For details about mathematical proof of these propositions, see (Chanteperdrix 2004).

A.3 Mathematical properties of the model (R)

The model (R) is hyperbolic. The eigenvalues of the corresponding linear model are considered, the linearization being performed relatively to the "natural variables" $V = {}^t(\alpha, \rho_1, \rho_2, \underline{V})$.

Eigenvalues of the kinematic matrix of model (R) are $u - c$, c , $u + c$, the eigenvalues u being of multiplicity two, and the mixture sound speed c being defined by:

$$\rho c^2 = \alpha \rho_1 c_1^2 + (1 - \alpha) \rho_2 c_2^2 \quad (\text{A.25})$$

There is a Lax entropy and associated flux for the model (R). The existence of a Lax entropy is necessary to ensure the thermodynamic consistency of the model (R). If the small parameter ϵ is positive, the couple of functions (S, H) :

$$\begin{aligned} S(\alpha, \rho_1, \rho_2, \rho u) &= \frac{1}{2}\rho u^2 + \alpha\rho_1 f_1(\rho_1) + (1 - \alpha)\rho_2 f_2(\rho_2) \\ H(\alpha, \rho_1, \rho_2, \rho u) &= u (S + P(\alpha, \rho_1, \rho_2)) \end{aligned} \quad (\text{A.26})$$

with f_1 and f_2 two functions of ρ_1 and ρ_2 respectively verifying:

$$f_1'(\rho_1) = \frac{p_1(\rho_1)}{\rho_1^2} \quad \text{and} \quad f_2'(\rho_2) = \frac{p_2(\rho_2)}{\rho_2^2} \quad (\text{A.27})$$

is a usual couple of Lax entropy for the model (R). This result does not depend on the shape of the equations of state $p_k = p_k(\rho_k)$. The convexity of both entropies is proven by Chantepredrix (2004) using the fact that the equilibrium volume fraction α minimizes the entropy S of the model (R), giving this way a accurate meaning to the appellation "equilibrium" for the model (E): the pressure equilibrium is not only an arbitrary choice of closure (see section 3.4.4) but corresponds to the minimization of the total free energy. For details about mathematical proof of these propositions, see (Chantepredrix 2004).

Although it has been shown here that model (E) and model (R) result from the same assumptions but undertaken in a different order, there is another manner to show how they relate to each other. This is done by a Chapman-Enskog development and can be found in appendix A.4.

A.4 Connection between models (E) and (R): Chapman-Enskog type development

As we mentioned the fact that the model (R) is appropriate for numerical implementation as it is hyperbolic and consistent in terms of thermodynamics, it is now relevant to show that its solutions are close to the solutions of the model (E). The objective of this section is to show that the model (R) constitutes an accurate approximation of the model (E) within the meaning of asymptotic analysis. This result will justify the use of the model (R) for the numerical resolution of the model (E).

To connect both model (E) and (R), let us consider the formal asymptotic development of the relaxation model (R) at first order in ϵ , and this in terms of Chapman-Enskog development as it is carried out by (Coquel & Perthame 1998).

Thus let us consider a solution $W^\epsilon = {}^t(\alpha^\epsilon, \tilde{\rho}_1^\epsilon, \tilde{\rho}_2^\epsilon, \rho^\epsilon \underline{V}^\epsilon)$ of the relaxation model (R) close to a solution of equilibrium model within the meaning that α^ϵ is set to:

$$\alpha^\epsilon = \alpha_* + \epsilon\alpha_1^\epsilon + O(\epsilon^2) \quad (\text{A.28})$$

α_* being solution of the pressure equilibrium closure law (3.65) of the model (E). Thus the following result is shown:

Proposition 2:

At the first order in ϵ , the relaxation model is formally equivalent to the following system:

$$\frac{\partial}{\partial t} \begin{pmatrix} \tilde{\rho}_1^\epsilon \\ \tilde{\rho}_2^\epsilon \\ \rho^\epsilon \underline{V}^\epsilon \end{pmatrix} + \nabla \cdot \begin{pmatrix} \tilde{\rho}_1^\epsilon \underline{V}^\epsilon \\ \tilde{\rho}_2^\epsilon \underline{V}^\epsilon \\ \rho^\epsilon \underline{V}^\epsilon \times \underline{V}^\epsilon + P_*(\tilde{\rho}_1^\epsilon, \tilde{\rho}_2^\epsilon) \underline{I} \end{pmatrix} = \begin{pmatrix} 0 \\ 0 \\ \epsilon \nabla (\eta(\alpha_*, \tilde{\rho}_1^\epsilon, \tilde{\rho}_2^\epsilon) \nabla \cdot \underline{V}^\epsilon) \end{pmatrix} \quad (\text{A.29})$$

with:

$$\alpha^\epsilon = \alpha_* - \epsilon \left(\frac{\alpha_*^2 (1 - \alpha_*)^2 K}{(1 - \alpha_*)^2 \tilde{\rho}_1^\epsilon c_1^2 + \alpha_*^2 \tilde{\rho}_2^\epsilon c_2^2} \right) \nabla \cdot \underline{V}^\epsilon \quad (\text{A.30})$$

where α_ is solution of the pressure equilibrium closure law (3.65), K is given by equation (A.2) and η is the following function:*

$$\eta(\alpha, \tilde{\rho}_1, \tilde{\rho}_2) = \frac{\alpha^2 (1 - \alpha)^2 (\tilde{\rho}_1 + \tilde{\rho}_2)}{(1 - \alpha)^2 \tilde{\rho}_1 c_1^2 + \alpha^2 \tilde{\rho}_2 c_2^2} (c^2 - c_*^2) \quad (\text{A.31})$$

Notes:

1. A necessary condition for the obtained system to be well written, i.e. to constitute a parabolic approximation of the equilibrium model (E) is that the function η must be positive, that is:

$$c_*^2 \leq c^2 \quad (\text{A.32})$$

This relationship is verified in this case. Indeed, thanks to equation (A.25) and (A.19), one see that $(\rho_2 c_2^2 - \rho_1 c_1^2)K$ must be positive, what is immediate in view of the expression of K , equation (A.2). The connection between (R) and (E) is thus well established: a solution of the model (R), close to a solution of the model (E), is a solution at the first order in ϵ of a system constituting a parabolic approximation of the model (E). This result is fundamental for the numerical implementation as it ensures, at least formally, that the numerical resolution of the model (R) for initial conditions compatible with the pressure equilibrium equation (3.65), the obtained solution will actually be a solution of the model (E) except for the terms of ϵ order.

2. The source term of the momentum balance equation being proportional to $\alpha(1 - \alpha)$ through η , which is a viscosity term, will play a role only at the interface.
3. The volume fraction α^ϵ is uncoupled from the rest of the system. Indeed, once the system (A.29) is solved, α^ϵ becomes computable by (A.30).
4. It is relevant to notice that η is dimensionless whereas ϵ has the dimension of a dynamic viscosity, (Pa.s).

For details about mathematical proof of these propositions, see (Chantepedrix 2004).

A.5 Resolution of the Riemann problem associated with model (R)

The objective here is to introduce the following one-dimensional (one dimension being enough to build the scheme) Riemann problem associated with model (R):

$$\left\{ \begin{array}{l} \frac{\partial W}{\partial t} + \frac{\partial F(W)}{\partial x} = 0 \\ \text{where } W = {}^t (\rho\alpha, \tilde{\rho}_1, \tilde{\rho}_2, \rho u) \\ \text{and } F(W) = {}^t (\rho\alpha u, \tilde{\rho}_1 u, \tilde{\rho}_2 u, \rho u^2 + \alpha p_1 + (1 - \alpha)p_2), \\ \text{with the initial condition:} \\ W(x, 0) = \begin{cases} W_g, & \text{if } x < 0 \\ W_d, & \text{if } x > 0 \end{cases} \end{array} \right. \quad (\text{A.33})$$

Chanteperdrix (2004) shows that the 1-curves of shock and rarefaction (détente) can be written:

$$u_1 = u_g + \theta_g(P), \text{ with } \theta_g(P) = \begin{cases} c_g \log\left(\frac{P_g - \tilde{P}_{0,g}}{P - \tilde{P}_{0,g}}\right) & \text{if } P \leq P_g \\ -\frac{P - P_g}{\sqrt{\rho_g(P - \tilde{P}_{0,g})}} & \text{if } P > P_g \end{cases} \quad (\text{A.34})$$

The same way the 3-curves of shock and rarefaction can be written:

$$u_3 = u_d + \theta_d(P), \text{ with } \theta_d(P) = \begin{cases} -c_d \log\left(\frac{P_d - \tilde{P}_{0,d}}{P - \tilde{P}_{0,d}}\right) & \text{if } P \leq P_d \\ \frac{P - P_d}{\sqrt{\rho_d(P - \tilde{P}_{0,d})}} & \text{if } P > P_d \end{cases} \quad (\text{A.35})$$

In practice, given two states W_g and W_d , solving the Riemann problem (A.33) consists in computing two intermediary states W_g^* and W_d^* respectively linked to W_g by a 1-wave (shock or rarefaction) and to W_d by a 3-wave (shock or rarefaction). Moreover, both states W_g^* and W_d^* are linked together by a 2-contact-discontinuity, that is to say they verify: -matching of the velocities: $u_g^* = u_d^* = u^*$, -matching of the pressures: $P_g^* = P_d^* = P^*$.

A.6 An analytical solution for a multiphase shock tube

The analytical solution for the mixture shock tube is based on a two-phase model with a unique velocity field and a unique pressure field (pressure equilibrium) from Kapila et al. (2001) and under the assumption of chemical inertia and that heat transfer into

the shock layer is negligible:

$$\begin{aligned}
\frac{\partial \alpha_1}{\partial t} + \underline{V} \cdot \nabla \alpha_1 &= \frac{\rho_2 c_2^2 - \rho_1 c_1^2}{\frac{\rho_1 c_1^2}{\alpha_1} + \frac{\rho_2 c_2^2}{\alpha_2}} \nabla \cdot \underline{V} \\
\frac{\partial (\alpha \rho)_1}{\partial t} + \nabla \cdot ((\alpha \rho)_1 \underline{u}) &= 0 \\
\frac{\partial (\alpha \rho)_2}{\partial t} + \nabla \cdot ((\alpha \rho)_2 \underline{u}) &= 0 \\
\frac{\partial (\rho \underline{u})}{\partial t} + \nabla \cdot (\rho \underline{u} \otimes \underline{u}) + \nabla p &= 0 \\
\frac{\partial (\rho E)}{\partial t} + \nabla \cdot ((\rho E + p) \underline{u}) &= 0
\end{aligned} \tag{A.36}$$

with $\rho = \sum_k \alpha_k \rho_k$ the mixture density and $\rho E = \sum_k \alpha_k \rho_k e_k + \rho \frac{\underline{u} \cdot \underline{u}}{2}$ the mixture total energy and where α_k , ρ_k , c_k represent volume fraction, density and sound speed in phase k and e_k is its internal energy, which is controlled by the equation of state $e_k = e_k(p, \rho_k)$.

This model is called a reduced model and is obtained by expressing the pressure equilibrium condition $p_1(\rho_1, s_1) = p_2(\rho_2, s_2)$ in a differential form with an isentropic constraint along the fluid trajectories (Murrone & Guillard 2005).

This model represents a two-phase mixture evolving with a unique velocity and a unique pressure, but with two temperatures and two entropies. The equation of state of both phases is the Stiffened Gas equation, which reads:

$$p_k(\rho_k, e_k) = (\gamma_k - 1) \rho_k e_k - \gamma_k p_{\infty, k} \tag{A.37}$$

where the coefficient γ_k and $p_{\infty, k}$ are characteristic of the thermodynamic behaviour of the pure phase k . The first coefficient is the polytropic coefficient and the second one derives from a molecular attractive potential and represents the stiffness effects. These coefficients are obtained from the knowledge of sound speed c_0 and slope coefficient δ in the experimental Hugoniot curve for the considered material $\sigma = c_0 + \delta u$. (e.g LeMetayer, Massoni & Saurel 2004).

Under the assumption of a one dimensional problem, an exact Riemann solver is derived from this model.

Contact discontinuity:

The interface condition at the contact discontinuity are found to be:

$$\begin{aligned}
[u] &= 0 \\
[p] &= 0
\end{aligned} \tag{A.38}$$

where $[f] = f_R - f_L$ is the notation for the jump in f between a right state "R" and a left state "L" on both sides of the interface.

Rarefaction wave:

The Riemann invariants through the rarefaction wave are:

$$\begin{aligned} dp &= \pm \rho c du \\ dy_1 &= 0 \\ ds_1 &= 0 \\ ds_2 &= 0 \end{aligned} \tag{A.39}$$

which for the Stiffened Gas equation of state read:

$$\begin{aligned} dp &= \pm \rho c du \\ y_1 &= y_1^0 \\ \rho_k &= \rho_k^0 \left(\frac{p + p_{\infty,k}}{p^0 + p_{\infty,k}} \right)^{\frac{1}{\gamma_k}} \end{aligned} \tag{A.40}$$

where

$$\rho c = \left(\sum_k \frac{y_k}{\rho_k^2 c_k^2} \right)^{-\frac{1}{2}} = \left(\sum_k \frac{y_k^0}{\rho_k^{0^2} c_k^{0^2} \left(\frac{p+p_{\infty,k}}{p^0+p_{\infty,k}} \right)^{\frac{\gamma_k+1}{\gamma_k}}} \right)^{-\frac{1}{2}} \tag{A.41}$$

Shock wave:

The Rankine-Hugoniot relations are obtained by replacing the volume fraction equation by the internal energy equations of each fluid. Saurel et al. (2007) justify the proposition of Trunin (2001) who imposes the following relation for the jump in internal energy of each phase through a shock wave:

$$e_k^* - e_k^0 + \frac{p^* + p^0}{2} \left(\frac{1}{\rho_k^*} - \frac{1}{\rho_k^0} \right) = 0 \tag{A.42}$$

This leads to the following shock relations:

$$\begin{aligned} u &= u^0 \pm m \left(\frac{1}{\rho^0} - \frac{1}{\rho} \right) \\ p &= p^0 + m^2 \left(\frac{1}{\rho^0} - \frac{1}{\rho} \right) \\ y_k &= y_k^0 \\ \rho_k &= \rho_k^0 \frac{(\gamma_k + 1)(p + p_{\infty,k}) + (\gamma_k - 1)(p^0 + p_{\infty,k})}{(\gamma_k - 1)(p + p_{\infty,k}) + (\gamma_k + 1)(p^0 + p_{\infty,k})} \end{aligned} \tag{A.43}$$

where the mass-flowrate $m = \sqrt{\frac{p-p^0}{\frac{1}{\rho^0} - \frac{1}{\rho(p)}}}$ only depends on pressure because the mixture density $\frac{1}{\rho} = \sum_k \frac{y_k}{\rho_k(p)}$ only depends on pressure.

Numerical algorithm:

At a given location:

- if $p^* > p^0$, there is a shock wave and shock relations (A.43) are used to determine the state of the mixture behind this shock wave.
- if $p^* \leq p^0$, there is a rarefaction wave and Riemann invariants (A.41) are used to determine the state of the mixture behind this wave.

Material velocity reads: $u = u^0 \pm \Phi(p)$ with: $\Phi(p) = \frac{p-p^0}{m}$ for a shock wave and $\Phi(p) = \int_{p^0}^p \frac{dp}{\rho c}$ for a rarefaction wave. In the latter case a numerical integration is needed to compute $\Phi(p)$ and a Gauss-Legendre method is used: $\int_{p^0}^p \frac{dp}{\rho c} = \frac{p-p^0}{2} \sum_{k=1}^n \frac{\omega_k}{\rho c(x_k)}$ with $x_k = \frac{p+p^0}{2} + \frac{p-p^0}{2} \xi_k$ $\xi_k \in [-1; 1]$ $x_k \in [p^0; p]$ where ξ_k and ω_k are the abscissas and weights of Gauss-Legendre. A six-abscissa approximation is sufficient for this application. Whatever the wave configuration, the material velocity is determined by:

$$u_L^* = u_L - \Phi_L(p) u_R^* = u_R + \Phi_R(p) \quad (\text{A.44})$$

By combining relations (A.44) and the condition at contact discontinuity $u_L^* = u_R^* = u$, one obtains a unique equation depending on the after-shock pressure p^* :

$$u_R^* - u_L^* = u_R - u_L + \Phi_R(p) + \Phi_L(p) = 0 \quad (\text{A.45})$$

The equation (A.45) is non-linear, it is solved using a Newton-Raphson method. Once p^* is known, material velocity u^* is computed through relations (A.44) and other variables are computed using shock relations (A.43) or rarefaction wave relations (A.41) depending on the considered wave.

Bibliography

- Abgrall, R. (1996), ‘How to prevent pressure oscillations in multicomponent flow calculations: A quasi conservative approach’, *Journal Of Computational Physics* **125**, 150–160.
- Abgrall, R., Nkonga, B. & Saurel, R. (2003), ‘Efficient numerical approximation of compressible multi-material flow for unstructured meshes’, *Computers & Fluids* **32**, 571–605.
- Allaire, G., Clerc, S. & Kokh, S. (2002), ‘A five-equation model for the simulation of interfaces between compressible fluids’, *Journal of Computational Physics* **181**, 577–616.
- Allsop, N., Vicinanza, D. & McKenna, J. (1996), Wave forces on vertical and composite breakwaters, Technical report, Report SR 443, HR Wallingford.
- Anderson, D. M., McFaden, G. B. & Wheeler, A. A. (1998), ‘Diffuse-interface methods in fluid mechanics’, *Annual Review of Fluid Mechanics* **30**, 139–165.
- Baer, M. R. & Nunziato, J. W. (1986), ‘A two-phase mixture theory for the deflagration-to-detonation transition (ddt) in reactive granular materials’, *Int. J. Multiphase Flow* **12**(6), 861–889.
- Bagnold, R. A. (1939), ‘Interim report on wave pressure research’, *J. Inst. Civil Eng.* **12**, 201–226.
- Battjes, J. A. (1974), ‘Surf Similarity’, *Proc. of the 14th Coastal Eng. Conf. ASCE* pp. 466–480.
- Biausser, B., Grilli, S. & Fraunié, P. (2004), Numerical simulations of three-dimensional wave breaking by coupling of a vof method and a boundary element method, in ‘The Thirteenth (2003) International Offshore and Polar Engineering Conference’, Honolulu, Hawaii, USA.
- Bredmose, H., Brocchini, M., Peregrine, D. H. & Thais, L. (2003), ‘Experimental investigation and numerical modelling of steep forced water waves’, *Journal of Fluid Mechanics* **490**(-1), 217–249.
- Buckingham, M. (1997), ‘Sound Speed and Void Fraction Profiles in the Sea Surface Bubble Layer’, *Applied Acoustics* **51**(3), 225–250.

- Bullock, G. N., Crawford, A. R., Hewson, P. J., Walkden, M. J. A. & Bird, P. A. D. (2001), 'The influence of air and scale on wave impact pressures', *Coastal Engineering* **42**(4), 291–312. TY - JOUR.
- Bullock, G., Obhrai, C., Peregrine, D. & Bredmose, H. (2007), 'Violent breaking wave impacts. part 1: Results from large-scale regular wave tests on vertical and sloping walls', *Coastal Engineering* **54**, 602–617.
- Chan, E. S. & Melville, W. K. (1988), Deep-Water Plunging Wave Pressures on a Vertical Plane Wall, *in* 'Proc. of the Royal Society of London. Series A, Mathematical and Physical Sciences', Vol. 417, No 1852 (May 9, 1988), pp. 95–131.
- Chanteperdrix, G. (2004), Modélisation et simulation numérique d'écoulements diphasiques à interface libre. Application à l'étude des mouvements de liquides dans les réservoirs de véhicules spatiaux, PhD thesis, Ecole Nationale Supérieure de l'Aéronautique et de l'Espace, CNES/ONERA France.
- Christensen, E. D. (2006), 'Large eddy simulation of spilling and plunging breakers', *Coastal Engineering* **53**, 463 – 485.
- Cocchi, J. P. & Saurel, R. (1997), 'Journal of computational physics', *A Riemann problem based method for compressible multfluid flows* **137**, 265–298.
- Commander, K. W. & Prosperetti, A. (1989), 'Linear pressure waves in bubbly liquids: Comparison between theory and experiments', *The Journal of the Acoustical Society of America* **85**(2), 732–746.
- Cooker, M. J. & Peregrine, D. H. (1992), 'Wave impact pressure and its effect upon bodies lying on the sea bed', *Coastal Engineering* **18**(Issues 3-4), Pages 205–229.
- Cooker, M. & Peregrine, D. (1990a), A model for breaking wave impact pressures, *in* 'Proc. 22nd Int. Conf. Coastal Eng.', ASCE, Delft, pp. 1473–1486.
- Cooker, M. & Peregrine, D. (1990b), Violent water motion at breaking-wave impact, *in* 'Proc. 22nd Int. Conf. Coastal Eng.', ASCE, Delft, pp. 164–176.
- Cooker, M. & Peregrine, D. (1995), 'Pressure-impulse theory for liquid impact problems', *Journal of Fluid Mechanics* **297**, 193–214.
- Coquel, F., Gallouët, T., Hérard, J. & Seguin, N. (2002), 'Closure laws for a two-fluid two-pressure model', *Compte Rendu de l'Academie des Science de Paris, serie I* **334**, 1–6.
- Coquel, F. & Perthame, B. (1998), 'Relaxation of energy and approximate Riemann solvers for general pressure laws in fluid dynamics', *SIAM Journal of Numerical Analysis* **35**(6), 2223–2249.
- Cox, D. & Shin, S. (2003), 'Laboratory Measurements of Void Fraction and Turbulence in the Bore Region of Surf Zone Waves', *Journal of Engineering Mechanics* **129**(10), 1197–1205.

- Cox, S. J. & Cooker, M. J. (1999), ‘The motion of a rigid body impelled by sea-wave impact’, *Applied Ocean Research* **21**(3), 113–125.
- Cox, S. J. & Cooker, M. J. (2001), ‘The pressure impulse in a fluid saturated crack in a sea wall’, *Coastal Engineering* **42**, 241–256.
- Dalrymple, R. A. & Rogers, B. D. (2006), ‘Numerical modeling of water waves with the sph method’, *Coastal Engineering* **53**, 141–147.
- De Rouville, A. (1938), ‘Etats actuels des études internationales sur les efforts dus aux lames.’, *Ann. Ponts Chaussées* **108**, 5–113.
- Deane, G. (1997), ‘Sound generation and air entrainment by breaking waves in the surf zone’, *The journal of the acoustical society of America* **102**(5), 2671–2689.
- Deane, G. & Stokes, M. (1999), ‘Air Entrainment Processes and Bubble Size Distributions in the Surf Zone’, *Journal of Physical Oceanography* **29**(7), 1393–1403.
- Deane, G. & Stokes, M. (2002), ‘Scale dependence of bubble creation mechanisms in breaking waves’, *Nature* **418**, 839–844.
- Denny, D. F. (1951), ‘Further experiments on wave pressures’, *J. Inst. Civil Engrs* **35**, 330–345.
- Drew, D. A. (1983), ‘Mathematical modeling of two-phase flow’, *Ann. Rev. Fluid Mech.* **15**, 261–91.
- Drew, D. & Passman, S. (1998), *Theory of multicomponent fluids*, Applied Mathematical Science.
- Duval, M. (2007), Etude du deferlement d’une onde de Stokes et de la dissipation associée par simulation directe, PhD thesis, Institut National Polytechnique de Toulouse, Toulouse, France.
- Fedkiw, R. P., Aslam, T., Merriman, B. & Osher, S. (1999), ‘A non oscillatory eulerian approach to interfaces in multimaterial flows (The Ghost Fluid Method)’, *Journal of computational physics* **152**, 457–492.
- Franquet, E. (2006), Modelisation eulerienne d’écoulements multiphasiques en presence d’ondes de chocs, de detonations et d’interfaces materielles., PhD thesis, Universite Aix Marseille I - Universite de Provence, Marseille, France.
- Furhboter, A. (1986), ‘Model and prototype tests for wave impact and run-up on a uniform 1:4 slope’, *Coastal Engineering* **10**, 49–84.
- Gingold, R. & Monaghan, J. (1977), ‘Smoothed particle hydrodynamics- theory and application to non-spherical stars’, *Royal Astronomical Society, Monthly Notices* **181**, 375.

- Gomez-Gesteira, D., Cerqueiro, M., Crespo, C. & Dalrymple, R. A. (2005), ‘Green water overtopping analyzed with sph model’, *Ocean Engineering* **32**, 223–238.
- Gomez-Gesteira, M. & Dalrymple, R. A. (2004), ‘Using a three-dimensional smoothed particule hydrodynamics method for wave impact on a tall structure’, *Journal of Waterway, Port, Coastal and Ocean Engineering* **130**, 63–69.
- Grilli, S. T., Svendsen, I. A. & Subramanya, R. (1997), ‘Breaking criterion and characteristics for solitary waves on slopes’, *Journal of Waterway, Port, Coastal and Ocean Engineering* **123**(3), 102–112.
- Hattori, M., Arami, A. & Yui, T. (1994), ‘Impact wave pressure on vertical walls under breaking waves of various types’, *Coastal Engineering* **22**, 79–114.
- Hayashi, T. & Hattori, M. (1958), *Pressure of the breaker against the vertical wall*, Coastal Engr. in Japan.
- Helluy, P., Golay, F., Caltagirone, J.-P., Lubin, P., Vincent, S., Drevard, D., Marcer, R., Fraunié, P., Seguin, N., Grilli, S., Lesage, A.-C., Dervieux, A. & Allain, O. (2005), ‘Numerical simulations of wave breaking’, *Mathematical Modelling and Numerical Analysis* **39**(3), 591–607.
- Hieu, P. D. & Tanimoto, K. (2006), ‘Verification of a vof-based two-phase flow model for wave breaking and wave-structure interactions’, *Ocean Engineering* **33**(11-12), 1565–1588.
- Hirt, C. & Nichols, B. (1981), ‘Volume of fluid /VOF/ method for the dynamics of free boundaries’, *Journal of Computational Physics* **39**, 201–225.
- Hoque, A. & Aoki, S.-I. (2005), ‘Distributions of void fraction under breaking waves in the surf zone’, *Ocean Engineering* **32**, 1829–1840.
- Hsieh, D.-Y. & Plesset, M. S. (1961), ‘On the propagation of sound in a liquid containing gas bubbles’, *The Physics Of Fluids* **4**(8), 970–975.
- Hull, P. & Muller, G. (2002), ‘An investigation of breaker heights, shapes and pressures’, *Ocean Engineering* **29**(1), 59–79.
- Iribarren, C. R., N. C. (1949), Protection des ports, in ‘17th Int. Nay. Congr., Lisbon’, Section II. Comm. 4, p. 31:80.
- Iwata, K. & Kiyono, K. (1985), ‘Breaking of two components composite and irregular waves’, *Coastal Engineering in Japan* **28**, 71–87.
- Jacqmin, D. (1999), ‘Calculation of Two-Phase Navier-Stokes Flows Using Phase-Field Modeling’, *Journal of Computational Physics* **155**, 96–127.
- Jamet, D., Lebaigue, O., Coutris, N. & Delhaye, J. (2001), ‘The Second Gradient Method for the Direct Numerical Simulation of Liquid-Vapor Flows with Phase Change’, *Journal of Computational Physics* **169**, 624–651.

- Jamet, D., Vila, J., Villedieu, P. & Chantepedrix, G. (2003), 'Équations de bilan pour un modèle compressible avec prise en compte de la tension interfaciale', *in prep.*
- Kapila, A., Menikoff, R., Bdzil, J., Son, S. & Stewart, D. (2001), 'Two-phase modeling of deflagration-to-detonation transition in granular materials: Reduced equations', *Physics of Fluids* **13**(10), 3002–3024.
- Karim, M. F., Tanimoto, K. & Hieu, P. D. (2009), 'Modelling and simulation of wave transformation in porous structures using vof based two-phase flow model', *Applied Mathematical Modelling* **33**, 343–360.
- Karni, S. (1994), 'Multicomponent flow calculations by a consistent primitive algorithm', *Journal of Computational Physics* **112**, 31–43.
- Kirkgoz, M. S. (1982), 'Shock pressure of breaking waves on vertical walls', *J. Waterways, Port Ocean Engng Div ASCE* **108**, 81–95.
- Kirkgoz, M. S. (1991), 'Impact pressure of breaking waves on vertical and sloping walls', *Ocean Engineering* **18**(1/2), 45–59.
- Kirkgoz, M. S. (1995), 'Breaking wave impact on vertical and sloping coastal structures', *Ocean Engineering* **22**(1), 35–48.
- Kirkgoz, M. S. & Akoz, M. S. (2005), 'Geometrical properties of perfect breaking waves on composite breakwaters', *Ocean Engineering* **32**(16), 1994–2006.
- Kleefsman, K., Fekken, G., Veldman, A., Iwanowski, B. & Buchner, B. (2005), 'A volume-of-fluid based simulation method for wave impact problems', *Journal of Computational Physics* **206**, 363–393.
- Lamarre, E. & Melville, W. K. (1991), 'Air entrainment and dissipation in breaking waves', *Nature* **351**, 469–472.
- Lamarre, E. & Melville, W. K. (1992), 'Instrumentation for the measurement of void-fraction in breaking waves: laboratory and field results', *Journal of Oceanic Engineering* **17**(2), 204–215.
- Lamarre, E. & Melville, W. K. (1995), 'Instrumentation for the Measurement of Sound Speed near the Ocean Surface', *Journal of Atmospheric and Oceanic Technology* **12**, 317–329.
- Lamb, H. (1932), *Hydrodynamics*, 6th. edn. edn, Cambridge university Press.
- Lara, J., Garcia, N. & Losada, I. (2006), 'Rans modelling applied to random wave interaction with submerged permeable structures', *Coastal Engineering* **53**, 395–417.
- Lee, Y.-G. & Heo, J.-K. (2005), 'Simulating nonlinear waves on the free surface in surf zones with two-dimensional sloping beach', *Ocean Engineering* **32**, 57–84.

- Leighton, T. (1994), *The Acoustic Bubble*, Academic, London.
- LeMetayer, O., Massoni, J. & Saurel, R. (2004), ‘Elaboration des lois d’état d’un liquide et de sa vapeur pour les modèles d’écoulements diphasiques’, *Int. J. Thermal Sciences* **43**(3), 265–276.
- Lin, P. & Liu, P. L. F. (1998), ‘A numerical study of breaking waves in the surf zone’, *Journal of Fluid Mechanics* **359**(1), 239–264.
- Liu, E. Y. M. & Shao, S. (2002), ‘Simulation of near-shore solitary wave mechanics by an incompressible sph method’, *Appl. Ocean Res.* **24**, 275–286.
- Lo, E. Y. & Shao, S. (2002), ‘Simulation of near-shore solitary wave mechanics by an incompressible SPH method’, *Applied Ocean Research* **24**(5), 275–286.
- Losada, I. J., Lara, J. L., Christensen, E. D. & Garcia, N. (2005), ‘Modelling of velocity and turbulence fields around and within low-crested rubble-mound breakwaters’, *Coastal Engineering* **52**, 887–913.
- Lucy, L. (1977), ‘A numerical approach to testing the fission hypothesis’, *The Astronomical Journal* **8**(12), 1013–1024.
- Lugni, C., Brocchini, M., Dolcini, A., Palladino, F., Bulgarelli, U. & Faltinsen, O. (2005), An experimental investigation on the flip-through phenomenon., in ‘Proc. 20th International Workshop on Water Waves and Floating Body, Longyearbyen, The University Centre in Svalbard’.
- Lugni, C., Brocchini, M. & Faltinsen, O. M. (2006), ‘Wave impact loads: The role of the flip-through’, *Physics of Fluids* **18**(12), 122101–122118.
- Massoni, J., Saurel, R., Nkonga, B. & Abgrall, R. (2002), ‘Some models and eulerian methods for interface problems between compressible fluids with heat transfer’, *International Journal of Heat and Mass Transfer* **45**(6).
- Medina, J. R. & Hudspeth, R. T. (2000), ‘Discussion of "progression and variability of damage on rubble mound breakwaters"', *Journal of Waterway, Port, Coastal and Ocean Engineering* **126**(5), 268–270.
- Melby, J. A. & Kobayashi, N. (1998), ‘Progression and variability of damage on rubble mound breakwaters’, *J. Wtrwy., Port, Coast., and Oc. Engrg.* **124**(6), 286–294.
- Miche, M. (1944), ‘Le pouvoir réfléchissant des ouvrages maritimes exposés à l’action de la houle’, *Ann. Ponts Chaussées* **121**, 285–318.
- Monaghan, J. J. (1992), ‘Smoothed particle hydrodynamics’, *Annual Review of Astronomy and Astrophysics* **30**, 543–574.
- Monaghan, J. J. & Kos, A. (1999), ‘Solitary waves on a cretan beach’, *Journal of Waterway, Port, Coastal and Ocean Engineering* **125**, 145–154.

- Monahan, E. C. (1993), 'Occurrence and evolution of acoustically relevant sub-surface bubble plumes and their associated, remotely monitorable, surface whitecaps.', *Natural Physical Sources of Underwater Sound* pp. 503–517.
- Muller, G. & Wolters, G. (2000), Impact forces on the sea bed created by wave uprush, *in* 'Proceedings of the 4th International Conference on Coasts'.
- Muller, G., Wolters, G. & Cooker, M. (2003), 'Characteristics of pressure pulses propagating through water-filled cracks', *Coastal Engineering* **49**, 83–98.
- Murrone, A. & Guillard, H. (2005), 'A five equation reduced model for compressible two phase flow problems', *Journal of Computational Physics* **202**(2), 664–698.
- Nagai, S. (1960), 'Shock pressures exerted by breaking waves non breakwaters', *J. Waterways, Harbors Div. ASCE* **86**, 1–38.
- Obhrai, C., Bullock, G., Muller, G., Wolters, G., Peregrine, D., Bredmose, H. & Grüne, J. (2004), Violent wave impacts on vertical and inclined walls: large scale model tests., *in* 'Proc. 29th Int. Conf. on Coastal Engineering ASCE Lisbon'.
- Osher, S. & Sethian, J. A. (1988), 'Fronts propagating with curvature-dependent speed: Algorithms based on Hamilton-Jacobi formulations ', *Journal of Computation Physics* **79**, 12–49.
- Oumeraci, H. (1994), 'Review and analysis of vertical breakwater failures—lessons learned', *Coastal Engineering* **22**(1-2), 3–29.
- Oumeraci, H., Bruce, T., Klammer, P. & Easson, W. (1995), Piv-measurements of breaking wave kinematics and impact loading of caisson breakwaters, *in* '4th Int. Conf. Port Engng Dev. Countries 3', pp. 2394–2410.
- Oumeraci, H., Klammer, P. & Partensky, H. W. (1993), 'Classification of Breaking Wave Loads on Vertical Structures', *Journal of Waterway, Port, Coastal and Ocean Engineering* **119**(4), 381–397.
- Oumeraci, H. & Partensky, H. (1991), Breaking wave impact loading of caisson breakwaters, *in* 'Proc. Mast GG Workshop, Wave Impact Loading on Vertical Structures', Hannover.
- Oumeraci, H., Partensky, H. & Tautenhain, E. (1992), Breaking wave loads on vertical gravity structures, *in* 'Int. Conf. Offshore and Polar Eng., ISOPE'92, San Francisco'.
- Partensky, H.-W. (1988), Dynamic forces due to waves breaking at vertical coastal structures, *in* '2nd Int. Symposium on Wave Research and Coastal Engineering, University of Hanover'.
- Penrose, O. & Fife, P. (1993), 'On the relation between the standard phase-field model and a "thermodynamically consistent phase-field model', *Physica D* **69**, 107–113.

- Peregrine, D. (2006), *Personal communication* .
- Peregrine, D. H. (1983), ‘Breaking Waves on Beaches’, *Annual Review of Fluid Mechanics* **15**(1), 149–178.
- Peregrine, D. H. (2003), ‘Water-wave impact on walls’, *Annual Review of Fluid Mechanics* **35**, 23–43.
- Peregrine, D. H., Bredmose, H., Bullock, G., Obhrai, C., Muller, G. & Wolters, G. (2005), Violent water wave impact on a wall, *in* P. a. D.Henderson, ed., ‘in Rogue Waves, Proc. Aha Huliko a Hawaiian Winter Workshop’, pp. 155–159.
- Peregrine, D. H. & Kalliadasis, S. (1996), ‘Filling flow, cliff erosion and cleaning flows, journal of fluid mechanics’, **310**, 165–374.
- Peregrine, D. H. & Thais, L. (1996), ‘The effect of entrained air in violent water wave impacts’, *Journal of Fluid Mechanics* **325**, 377–397.
- Richert, G. (1968), Experimental investigation of shock pressures against breakwaters, *in* ‘Proc. 11th Conf. Coastal Engng.’, ASCE, pp. 954–973.
- Saurel, R. & Abgrall, R. (1999*a*), ‘A simple method for compressible multifluid flows’, *Siam J. Sci. Comput.* **21**(3), 1115–1145.
- Saurel, R. & Abgrall, R. (1999*b*), ‘A multiphase godunov method for compressible multifluid and multiphase flows’, *Journal of Computational Physics* **150**, 425–467.
- Saurel, R., Le Metayer, O., Massoni, J. & Gavrilyuk, S. (2007), ‘Shock jump relations for multiphase mixtures with stiff mechanical relaxation ’, *Shock Waves* **16**(3), 209–232.
- Saurel, R. & LeMetayer, O. (2001), ‘A multiphase model for compressible flows with interfaces, shocks, detonation waves and cavitation’, *Journal of Fluid Mechanics* **431**, 239–271.
- Scardovelli, R. & Zaleski, S. (1999), ‘Direct numerical simulation of free-surface and interfacial flow’, *Annual Review of Fluid Mechanics* **31**(1), 567–603.
- Schmidt, R., Oumeraci, H. & Partenscky, H. W. (1992), Impact loads induced by plunging breakers on vertical structures, *in* ‘Proc. 23rd Int. Conf. Coastal Engng.’, ASCE, Venice, pp. pp.1545–1558.
- Scott, J. C. (1975), ‘The role of salt in white-cap persistence’, *Deep sea Res.* **22**, 653–657.
- Shyue, K. M. (1998), ‘An efficient shock-capturing algorithm for compressible multi-component problems’, *Journal Of Computational Physics* **142**, 208.

- Silberman, E. (1957), ‘Sound velocity and attenuation in bubbly mixtures measured in stranding wave tubes’, *The journal of the Acoustical Society of America* **29**(8), 925–933.
- Song, C. & Sirviente, A. I. (2004), ‘A numerical study of breaking waves’, *Physics Of Fluids* **16**(7), 2649–2667.
- Stokes, M. & Deane (1999), ‘A new optical instrument for the study of bubbles at high void fractions within breaking waves’, *journal of Oceanic Engineering* **24**(3), 300–311.
- Terril, E., Melville, W. & Stramski, D. (2000), ‘A Broadband Acoustic Technique for Measuring Bubble Size Distributions: Laboratory and Shallow Water Measurements’, *Journal of Atmospheric And Oceanic Technology* **17**(2), 220–239.
- Terril, E., Melville, W. & Stramski, D. (2001), ‘Bubble entrainment by breaking waves and their influence on optical scattering in the upper ocean’, *Journal of Geophysical Research* **106**(C8), 16815–16823.
- Trunin, R. (2001), ‘Shock compression of condensed materials (laboratory studies)’, *Uspekhi Fizicheskikh Nauk* **171**(4), 387–414.
- Tsai, C. P., Chen, H. B., Hwung, H. H. & Huang, M. J. (2005), ‘Examination of empirical formulas for wave shoaling and breaking on steep slopes’, *Ocean Engineering* **32**, 469–483.
- Vagle, S. & Farmer, D. M. (1998), ‘A comparison of four methods for bubble size and void fraction measurements’, *Ieee Journal Of Oceanic Engineering* **23**(3), 211–222.
- Walkden, M., Crawford, A., Bullock, G., Hewson, P. & Bird, P. (1996), ‘Wave impact loading on vertical structures’, *Clifford, J.E. (Ed.), Advances in Coastal Structures and Breakwaters. Thomas Telford, London* pp. 273–286.
- Watanabe, Y. & Saeki, H. (1999), ‘Three-dimensional large eddy simulation of breaking waves’, *Coastal Engineering Journal* **41**, 281 – 301.
- Weggel, J. R. (1972), Maximum breaker height for design, *in* ‘13th ICCE’, pp. 419–432.
- Wemmenhove, R. (2006), Numerical simulation of hydrodynamic wave loading by a compressible two-phase model, *in* ‘European Conference on Computational Fluid Dynamics ECCOMAS CFD 2006’.
- Whillock, A. (1987), ‘Measurements of forces resulting from normal and oblique wave approaches to small scale seawalls’, *Coastal Engineering* **11**, 297–308.
- Wolters, G. & Müller, G. (2004), ‘The propagation of wave impact induced pressures into cracks and fissures’, *Geological Society, London, Engineering Geology Special Publications* **20**, 121–130.

- Wolters, G., Müller, G., Bullock, G., Obhrai, C., Peregrine, H. & Bredmose, H. (2005), Field and large scale model tests of wave impact pressure propagation into cracks., *in* S. World Scientific, ed., 'Proc. 29th Int. Conf. Coastal Engineering 2004', Vol. 4, pp. 4027–4039.
- Wood, A. (1941), *A textbook of sound*, G. Bell, London.
- Wood, D. J., Peregrine, D. H. & Bruce, T. (2000), 'Wave impact on a wall using pressure-impulse theory. i: Trapped air', *Journal of Waterway, Port, Coastal, and Ocean Engineering* **126**(4), 182–190. TY - JOUR.
- Yang, C. & Tryggvason, R. (1997), 'Dissipation of energy by finite-amplitude surface waves', *Computers and Fluids* **27**(7), 829–845.
- Zhang, S., Yue, K. P. & Tanizawa, K. (1996), 'Simulation of plunging wave impact on a vertical wall', *Journal of Fluid Mechanics* **327**, 221–254.